

Probing Cancer Targets and Therapeutic Mechanisms using Small Molecules

Yan Zhang

Submitted in partial fulfillment of the
requirements for the degree
of Doctor of Philosophy
in the Graduate School of Arts and Sciences

COLUMBIA UNIVERSITY

2019

© 2018

Yan Zhang

All Rights Reserved

ABSTRACT

Probing Cancer Targets and Therapeutic Mechanisms using Small Molecules

Yan Zhang

Small molecules are a powerful tool to illuminate biological mechanisms and assist in the identification and validation of therapeutic targets. *KRAS* is the single most frequently mutated oncogene in human cancer, with particularly high mutation frequencies observed in pancreas (95%), colon (45%), and lung (35%) cancer. However, despite three decades of effort, there is no clinical viable *KRAS* cancer therapy. The first part of this thesis focuses on exploring the potential of directly targeting the *KRAS* nucleotide binding site. Directly targeting oncogenic *KRAS* with small molecules in the nucleotide-binding site has had limited success due to the high affinity of *KRAS* for nucleotide GTP and the high cellular concentration of GTP. The strategy of generating engineered *KRAS* allele based on shape and covalent complementarity was exploited herein to address this challenge. Using fragment-based small molecule design, a cell-membrane-permeable covalent inhibitor able to irreversibly modify the engineered nucleotide-binding site of *KRAS* was developed. The second part of this thesis describes the investigation of the therapeutic potential of imidazole ketone erastin (IKE), a small molecule inhibitor of the cystine/glutamate antiporter system x_c^- , in a subcutaneous xenograft model of Diffuse Large B Cell Lymphoma (DLBCL). A biodegradable polyethylene glycol-poly(lactic-co-glycolic acid) nanoparticle formulation was employed to aid in the delivery of IKE to cancer cells *in vivo*. This IKE nanoparticle system showed improved tumor accumulation and therapeutic index relative to free IKE, indicating its potential for treating DLBCL. The final part of this thesis describes the study of lipid metabolism features of ferroptotic cell death using quantitative reverse transcription PCR (RT-qPCR) and mass spectrometry-based lipidomic analysis. In summary, this work illustrates how chemistry and chemical biology approaches can supplement existing efforts towards the design and discovery of new drugs for challenging targets, as well as aid in the study of therapeutic mechanisms.

Table of Contents

| | |
|--|----|
| List of Figures | v |
| List of Tables | ix |
| Chapter 1 Introduction | 1 |
| 1.1 Small molecule design as the tool to validate targets and probe biological mechanisms | 1 |
| 1.1.1 Advancement in target identification and small molecule design..... | 1 |
| 1.1.2 Fragment-based drug design | 2 |
| 1.2 RAS superfamily of small GTPases | 5 |
| 1.2.1 RAS plays a key role in cell signaling | 5 |
| 1.2.2 RAS isoforms | 7 |
| 1.2.3 Strategies for drug discovery in RAS and current progress | 9 |
| 1.3 Ferroptosis | 11 |
| 1.3.1 Classical view of cell death and new classification of cell death..... | 11 |
| 1.3.2 Molecular and pharmaceutical modulators of ferroptosis | 11 |
| 1.3.4 Labile iron regulation in ferroptosis | 15 |
| 1.3.5 Application of ferroptosis in therapeutics | 17 |
| 1.4 Lipid metabolism in ferroptosis | 18 |
| 1.4.1 Fatty acids structure, nomenclature, and effects on ferroptosis | 18 |
| 1.4.2 Involvement of phospholipids biosynthesis in ferroptosis | 19 |
| 1.4.3 Participation of lipid peroxidation in ferroptosis | 21 |
| 1.4.4 Mass spectrometry platform-based lipidomics analysis..... | 22 |
| 1.5 Application of nanoparticles in drug delivery | 24 |

| | |
|---|-----------|
| 1.5.1 Abnormal tumor vasculature offers both challenges and opportunities in drug delivery | 24 |
| 1.5.2 Perspectives on polymer-based nanoparticle design | 25 |
| 1.6 Overview of dissertation | 28 |
| Chapter 2: Design of Small Molecules that Compete with Nucleotide Binding to an Engineered Oncogenic KRAS Allele¹ | 29 |
| 2.1 Introduction | 29 |
| 2.2 Results..... | 31 |
| 2.2.1 Design of KRAS allele | 31 |
| 2.2.2 Functional study of the engineered KRAS allele and biophysical assay design | 34 |
| 2.2.3 <i>in silico</i> design of inhibitors | 38 |
| 2.2.4 Synthesis of ligand library..... | 44 |
| 2.2.5 Evaluation of small molecule activities in biophysical assays | 44 |
| 2.2.6 Evaluation of covalent binding of small molecules to KRAS* | 48 |
| 2.2.7 Inhibition effect of the compound on signaling pathway | 48 |
| 2.3 Conclusion and Discussion..... | 52 |
| 2.4 Methods | 54 |
| Chapter 3: Pharmacokinetic and Pharmacodynamic Study of IKE²..... | 78 |
| 3.1 Introduction | 78 |
| 3.2 Result | 80 |
| 3.2.1 DLBCL have differential sensitivity to IKE | 80 |
| 3.2.2 Pharmacodynamics study of IKE <i>in vitro</i> | 83 |
| 3.2.3 Pharmacokinetics (PK) and pharmacodynamics (PD) study of IKE <i>in vivo</i> | 87 |

| | |
|---|------------|
| 3.3 Conclusion and Discussion..... | 90 |
| 3.4 Methods | 91 |
| Chapter 4: <i>in vivo</i> Study of IKE Nanoparticle Formulation in Xenograft Model³ | 100 |
| 4.1 Introduction | 100 |
| 4.2 Results..... | 101 |
| 4.2.1 PLGA and PEG-PLGA nanoparticle system optimization | 101 |
| 4.2.2 IKE PEG-PLGA NPs have suitable properties to be applied <i>in vivo</i> | 106 |
| 4.2.3 Investigation of ferroptosis biomarker expression in IKE and IKE PEG-PLGA efficacy study | 109 |
| 4.3 Discussion | 113 |
| 4.4 Methods | 114 |
| Chapter 5 Untargeted Lipidomics Study of IKE Induced Ferroptosis⁴ | 119 |
| 5.1 Introduction | 119 |
| 5.2 Results..... | 120 |
| 5.2.1 Untargeted lipidomics study of IKE induced ferroptosis in cell culture | 120 |
| 5.2.2 Investigation of enzymes relating to IKE induced lipids change | 122 |
| 5.2.3 Untargeted lipidomics study of IKE induced ferroptosis <i>in vivo</i> | 124 |
| 5.3 Discussion | 128 |
| 5. 4 Methods | 131 |
| Chapter 6 Conclusions and Future Directions | 136 |
| 6.1 Target validation using protein engineering strategy | 136 |
| 6.1.1 Summary | 136 |

| | |
|--|------------|
| 6.1.2 Significance..... | 137 |
| 6.1.3 Future directions..... | 139 |
| 6.2 Application of IKE <i>in vivo</i>..... | 140 |
| 6.2.1 Summary | 140 |
| 6.2.2 Significance..... | 141 |
| 6.2.3 Future directions..... | 142 |
| 6.3 Nanoparticles as drug carriers | 144 |
| 6.3.1 Summary | 144 |
| 6.3.2 Significance..... | 144 |
| 6.3.3 Future directions..... | 145 |
| 6.4 Identification of ferroptosis biomarkers..... | 146 |
| 6.4.1 Summary | 146 |
| 6.4.2 Significance..... | 148 |
| 6.4.3 Future directions..... | 148 |
| Reference | 151 |

List of Figures

| | |
|---|----|
| Figure 1. 1 Schematic overview of Venetoclax (ABT-199) discovery..... | 5 |
| Figure 1. 2 Schematic overview of RAS signaling pathways..... | 7 |
| Figure 1. 3 Schematic illustration of pathways regulating ferroptosis..... | 14 |
| Figure 1. 4 The summary of structure-and-activity relationship study of erastin analogs..... | 15 |
| Figure 1. 5 Schematic overview of iron metabolism in ferroptosis | 16 |
| Figure 1. 6 Schematic of phospholipids structure in different classes and the hydrolysis sites of different phospholipases..... | 21 |
| | |
| Figure 2. 1 Schematic overview of protein engineering strategies to validate KRAS..... | 30 |
| Figure 2. 2 Representation of KRAS G12V (PDB code: 4TQ9) and engineered KRAS* structures..... | 33 |
| Figure 2. 3 Sequence alignment of RAS and small GTPases superfamily | 33 |
| Figure 2. 4 A BRAF-RBD pull down assay proved that only GTP-bound but not GDP-bound KRAS* could bind with BRAF..... | 34 |
| Figure 2. 5 Nucleotide exchange of GTP in KRAS protein..... | 35 |
| Figure 2. 6 Schematic of establishing a stable transfected engineered cell line | 36 |
| Figure 2. 7 Western blot indicated the overexpression of RAS in <i>KRAS</i> ^{G12V} MEFs and <i>KRAS</i> * MEFs..... | 37 |
| Figure 2. 8 <i>RAS</i> mRNA level measurement by RT-qPCR..... | 37 |
| Figure 2. 9 Schematic principle of fluorescence polarization assay. | 38 |
| Figure 2. 10 Screen of fragments in biophysical assay..... | 39 |
| Figure 2. 11 Fragment-based small molecule design targeting KRAS* nucleotide binding site..... | 40 |
| Figure 2. 12 Combinatorial library design..... | 41 |
| Figure 2. 13 YZ0711 ligand interaction diagram..... | 42 |
| Figure 2. 14 Watermap performed on YZ0711 bound KRAS* | 43 |
| Figure 2. 15 Synthesis route of compound YZ0711 | 44 |
| Figure 2. 16 The structure and activity relationship of selected covalent inhibitors..... | 45 |

| | |
|---|----|
| Figure 2. 17 Binding affinity test of covalent inhibitors in fluorescence polarization assay | 46 |
| Figure 2. 18 Analysis of compounds' cellular activities and cell membrane permeabilities | 47 |
| Figure 2. 19 Exchange rate of BODIPY-GTP by small molecule YZ0711 in KRAS | 47 |
| Figure 2. 20 YZ0711 covalently labels KRAS* but not KRAS G12V | 49 |
| Figure 2. 21 Desthiobiotin-GTP pull down assay suggested YZ0711 occupied KRAS* nucleotide binding site covalently | 50 |
| Figure 2. 22 YZ0711 specifically inhibited KRAS* MEFs proliferation | 50 |
| Figure 2. 23 YZ0711 disrupted KRAS*-BRAF interaction..... | 51 |
| Figure 2. 24 YZ0711 inhibited RAS-MAPK pathway..... | 52 |
| | |
| Figure 3. 1 Chemical structure of erastin and imidazole-ketone-erastin (IKE). | 79 |
| Figure 3. 2 Pathways regulating sensitivity of DLBCLs to IKE..... | 80 |
| Figure 3. 3 Test of DLBCL sensitivity to IKE using cell viability assay | 81 |
| Figure 3. 4 <i>CBS</i> , <i>SLC7A11</i> , and <i>FTL</i> gene expression levels in different sensitivity groups of DLBCL... | 82 |
| Figure 3. 5 Measurement of GSH level in IKE treated SUDHL-6 cells..... | 83 |
| Figure 3. 6 Measurement of lipid peroxidation level in IKE treated SUDHL-6 cells using flow cytometry | 84 |
| Figure 3. 7 Measurement of MDA level in SUDHL-6 cells using immunofluorescence | 85 |
| Figure 3. 8 IKE induced ferroptosis marker change in a time-dependent way..... | 86 |
| Figure 3. 9 <i>SLC7A11</i> , <i>CHAC1</i> , and <i>PTGS2</i> are specific for IKE-induced ferroptosis | 86 |
| Figure 3. 10 Caspase-3 activity measurement using Apo-ONE assay and western blot | 87 |
| Figure 3. 11 PK/PD study of IKE in NCG mice bearing SUDHL-6 xenograft | 89 |
| Figure 3. 12 Analysis of ferroptosis gene biomarkers in tumor tissues of IKE treated SUDHL-6 xenografts..... | 89 |
| Figure 3. 13 Measurement of MDA level in tumor tissues of IKE treated SUDHL-6 xenografts using immunofluorescence | 90 |

| | |
|--|-----|
| Figure 3. 14 Measurement of 8-OHdG level in tumor tissues of IKE treated SUDHL-6 xenografts using immunofluorescence | 91 |
| Figure 4. 1 Principles of nanoparticle formulation using microfluidic system..... | 102 |
| Figure 4. 2 Optimization of organic phase in PEG-PLGA nanoparticle formulation..... | 103 |
| Figure 4. 3 Optimization of concentration step in PEG-PLGA and PLGA nanoparticle formulation..... | 104 |
| Figure 4. 4 Optimization of IKE loading in nanoparticles..... | 104 |
| Figure 4. 5 Nanoparticles' size and surface potential parameters..... | 105 |
| Figure 4. 6 IKE PEG-PLGA nanoparticles have enhanced cellular activity comparing with free IKE. .. | 106 |
| Figure 4. 7 IKE and IKE NPs inhibited tumor growth in NCG mice bearing SUDHL6 xenografts | 107 |
| Figure 4. 8 Measurement of IKE accumulation in tumor tissues..... | 108 |
| Figure 4. 9 Measurement of PTGS2 level in tumor tissues from efficacy study by immunofluorescence | 109 |
| Figure 4. 10 Measurement of MDA level in tumor tissues from efficacy study by immunofluorescence | 111 |
| Figure 4. 11 Measurement of MDA level in tumor tissues from efficacy study by TBARS assay | 111 |
| Figure 4. 12 Measurement of 8-OHdG in tumor tissues from efficacy study by immunofluorescence ... | 112 |
| Figure 4. 13 Measurement of cleaved-caspase 3 abundance in tumor tissues from efficacy study | 112 |
| Figure 4. 14 Schematic overview of IKE-induced ferroptosis..... | 114 |
| Figure 5. 1 Untargeted lipidomics study in SUDHL-6 cells..... | 121 |
| Figure 5. 2 Expression level of genes involving lipid metabolism | 123 |
| Figure 5. 3 Schematic view of fatty acid biosynthesis, lipids remodeling, and arachidonic acid oxidation | 123 |
| Figure 5. 4 Untargeted lipidomics study <i>in vivo</i> | 125 |
| Figure 5. 5 Metscape network analysis of lipids identified in IKE treatment <i>in vivo</i> | 126 |
| Figure 5. 6 Gene expression analysis <i>in vivo</i> | 127 |

Figure 5. 7 Lethality and sensitivity effects evaluation of lipids 127

List of Tables

| | |
|--|-----|
| Table 1. 1 KRAS mutation frequencies in different cancers | 6 |
| Table 2. 1 Representation of different engineered alleles of KRAS and the evaluation of pocket sizes and stabilities | 32 |
| Table 3. 1 IKE distribution in plasma through IP, IV and PO administration routes | 88 |
| Table 3. 2 IKE distribution in plasma and tumor tissue through IP administration..... | 88 |
| Table 4. 1 Percentage of tumor growth inhibition by IKE and IKE NP | 108 |

ACKNOWLEDGEMENTS

There are many people who have provided me with mentorship, support, help and friendship over my graduate school career that I would like to acknowledge. First, I would like to thank my advisor, Brent Stockwell, for his consistent support and feedback through my entire graduate study. I have learned far more than what I could have ever imagined with his mentorship. Thank you for guiding my scientific development, encouraging my creativity, providing me with limitless opportunities to explore different scientific disciplines, and fostering an innovative and collaborative lab culture.

I am fortunate to come to an amazing lab and work with all wonderful people in Stockwell lab. Stockwell group is composed of scientists from a diverse scientific background. It is being a true pleasure to learn from each other and work on multidisciplinary projects together. Specifically, I would like to thank Dr. Marie-Hélène Larraufie for teaching me about computational-aided small molecule design techniques, getting me started in Stockwell lab, and provided a lot of help in the engineered KRAS project. I would like to thank Leila Musavi for teaching me protein purification, Nen Pagano for teaching me cell culture work, Huizhong Feng for teaching me protein crystallization, Anna Kaplan for teaching me everything I know about biophysical evaluation of small molecules in protein, Pieter Bos for helping me in synthetic aspects of ferrostatin analogs and computational chemistry techniques, Arie Zask for constant help in synthetic organic chemistry and helping me edit part of my thesis, and Tal Hirschhorn and Niki von Krusenstiern for helping me edit my thesis. I would like to thank Hui Tan, Jacob Daniels, Fereshteh Zandkarimi, and Hengrui Liu for their contribution in the IKE project. Hui has been incredibly helpful in nanoparticle formulation, mouse efficacy study, and cell work. Jacob has put a lot of time helping me optimize the mouse xenograft study and mass spectrometry analysis, I would also like to thank him for critically reading and editing my thesis. Fereshteh has helped me understand untargeted lipidomics study, the field I have never worked before. Hengrui Liu has helped me finish immunofluorescence analysis of all efficacy samples.

I would like to acknowledge the researchers I have collaborated with outside of the Stockwell lab. I am grateful to Dr. Lewis Brown and Dr. Hermanth Akkiraju for their help on mass spectrometry

analysis in the engineered KRAS project. I am grateful to Dr. Owen O'Connor for providing diffuse large B cell lymphoma cancer cell lines, Dr. Koji Uchida for providing the monoclonal anti-MDA antibody, and Dr. Lewis Brown for supporting the untargeted lipidomics study in the IKE project.

I would like to thank my committee member, Dr. Richard Friesner and Dr. Ann McDermott, for serving on my committee for the last five years, as well as Dr. Wei Min, Dr. Neel Shah, and Dr. Simon Cheng for serving on my defense committee. I greatly appreciate their time and feedback on my projects, as well as their support on my career development.

I am also very grateful for all the administrative support I have received from our lab manager Elise Jiang, computer support- Anthony Gomez, and the administrators of the Department of Chemistry including Alix Lamia, Alison Doyle, Socky Lugo, and Dani Farrell.

I deeply appreciate the educators and the education I received prior to beginning my PhD. I would like to thank Dr. Wei He for the constant mentorship he extended to me during my time in his lab at Tsinghua University and beyond, and my mathematics and science teachers in elementary school, middle school, and high school for fostering my love to science.

Finally, I would like to express my gratitude to my friends, classmates, and family who have offered me friendship and support over the years. I am especially thankful to my parents for supporting all the decisions I made. I would never have enjoyed so many opportunities without their encouragement and love.

To my parents

Chapter 1 Introduction

1.1 Small molecule design as the tool to validate targets and probe biological mechanisms

1.1.1 Advancement in target identification and small molecule design

Small molecules can be discovered by screening chemical libraries for changes of protein activities (target-based) or desired phenotypes in cell or organism-based assays (phenotypic). For the last 30 years, the pharmaceutical industry has widely used target-based screens to identify medicines for specific diseases. There are many successes using this strategy, for example, the discovery of Gleevec (imatinib) which selectively inhibits BCR-ABL and revolutionized the treatment of chronic myeloid leukemia. However, this approach is limited in exploring new mechanisms of action and more disease-relevant models. Phenotypic screening allows identifying biologically active small molecules in an unbiased way, which means the targets could be any protein or biologic and the small molecules could use different actions such as agonist/antagonist, protein-protein interaction inhibitor, and allosteric inhibitor. Analysis of FDA approved drugs between 1999 and 2008 revealed that there are 75 first-in-class drugs among the 259 approved agents, 37% of them are from phenotypic screening, 23% are from target-based screening, 7% are modified natural products, the rest 33% are biologics¹. Giving the high need for new medicines based on new mechanisms of action, there is a resurgence of phenotypic screening despite the complexity of identifying targets, discovering suitable biomarkers, and establishing dose-response relationships using this approach.

Although target-based and phenotypic screening have different methodologies and criteria during drug discovery, both approaches face the problems of target identification and validation, and small molecule design. Fortunately, there are many technologies aiding the above processes. First, target identification and validation is greatly facilitated by the advancement of genetic technologies including siRNA, zinc finger nucleases (ZFN), transcription activator-like effector nucleus (TALEN), meganucleases, and CRISPR-Cas9 system¹. Second, the improvement of phenotypic screening in stem-

cell and primary-cell, and 3D and micro-physiological culture systems enables the application of more disease-relevant models in high-throughput screens. Third, ‘omics’ analysis including genomics, transcriptomics, proteomics, and metabolomics combined with bioinformatics provides multi-dimensional parameters on small molecule modulation. At the same time, high-throughput medicinal chemistry, beads chemistry, and new synthetic methods enable synthesizing small molecules more efficiently. Finally, computational chemistry and structural biology techniques, especially, cryo-electron microscopy (Cryo-EM), greatly accelerate drug design processes and are now an indispensable tool in small molecule design.

Small molecule design and drug discovery is an interdisciplinary research involving computational and medicinal chemistry, biophysics, genomics, proteomics, cell and molecular biology, and pharmacology. Chemical biology sits at the intersection of these disciplines and is an essential component of modern drug discovery. For example, chemical biology provides small molecule tools to identify and validate new targets, methodologies for disease-relevant phenotypic screens, approaches for designing therapeutic agents, and profiling targets and side effects through chemical proteomics. We anticipate seeing these efforts promote preclinical drug discovery and illuminate new paradigms for developing novel therapies.

1.1.2 Fragment-based drug design

There are different approaches to obtain chemical starting points in small molecule design, for example, from existing drugs or natural products/ligands with known biological clinical activities, high-throughput screening (HTS), and fragment-based drug discovery (FBDD). Among these approaches, HTS is one of the dominant paradigms for discovering new molecules in the pharmaceutical industry. However, the chemical space is unimaginably large, an estimate of 10^{63} molecules can be formed with up to 30 C, N, O, S atoms². The current global screening collection has around 10^8 molecules³, which represent only a very tiny fraction of possible chemical space. Besides, HTS libraries contain molecules that have inappropriate physical properties such as high lipophilicity, poor solubility, and tendency of aggregation, leading to production of false positives results. Thus, recent HTS has focused on screening

‘drug-like’ compounds with pharmacophores known to exhibit desirable biological activities to eliminate false positives.

FBDD has emerged as a complementary approach to HTS. FBDD is based on screening a collection of low molecular weight molecules (fragments, MW < 300 Da) to increase “hit” identification rates, followed by either linking the two fragments bound to adjacent pockets of the protein target or elaborating the initial fragments by adding functional chemical groups to increase the complexity, selectivity, and potency of the small molecule. Compared with HTS which screens more complex moieties, FBDD has higher hit rates because of less possibilities of fragments to form mismatches with the receptor⁴. Besides, the chemical space is around 10^8 with up to 11 C, N, O and F atoms (MW < 160)⁵, thus, a relatively small library of fragments is required to represent the chemical space. Furthermore, it is easier to control the physical parameters of lead compounds developed from small and efficiently binding fragments than from more complex molecules which might contain non-essential groups for binding⁶.

Common strategies used in FBDD screening include fluorescence-based thermal shift, NMR spectrometry, X-ray crystallography, mass spectrometry, surface plasmon resonance (SPR), and virtual screening. The development of leads from FBDD requires the integration of structural biology, synthesis, computational chemistry, and biophysics. There are many cases of developing clinical candidates using this pipeline, for example, Vemurafenib (PLX4032) which targets BRAF^{V600E} kinase, Venetoclax (ABT-199) which targets BCL-2 (B cell CLL/lymphoma 2), and Onalespib (AT13387) which targets molecular chaperone HSP90. A brief overview of Venetoclax design will be described here to show how the FBDD approach facilitate drug discovery (**Figure 1.1**).

Venetoclax is the first protein-protein interaction inhibitor, the first apoptosis-targeting therapeutic for cancer, and the second FBDD-derived drug approved by FDA⁷. It mimics BH3-only proteins and binds to the hydrophobic groove of BCL-2 proteins thus inhibiting BCL-2 activity and restoring apoptotic cell death in cancer cells. To discover initial fragments, NMR spectroscopy screening of a fragment library was performed on BCL-X_L protein, which has high sequence similarity to BCL-2. As a result, two fragments bound to the adjacent pockets of the BCL-X_L (**Figure 1.1A**) were identified⁸.

The discovery of acylsulfonamide as a linker followed by parallel synthesis led to the development of Compound 1, which could occupy both of the adjacent pockets (**Figure 1.1B**). Further structure-based design produced ABT-737 and ABT-263, which have high affinity for both BCL-2 and BCL-X_L and prevent cancer cell proliferation in a BAX- and BAK-dependent manner⁹. However, inhibiting BCL-X_L resulted in a decrease of platelets, and BAX- and BAK-mediated thrombocytopenia, which limits the dose of ABT-263 in patients. Therefore, a small molecule with higher selectivity to BCL-2 over BCL-X_L was required to eliminate the thrombocytopenia side effect. Researchers solved this challenge with the structural guidance of BCL-2 small molecule cocrystal structures and developed ABT-199 as a BCL-2 selective inhibitor. ABT-199, which has an indazole group, is 100-fold more potent to BCL-2 than BCL-XL (K_i for BCL-2 is 0.01 nM, K_i for BCL-XL is 46 nM). This drug is now used in treating chronic lymphocytic leukemia and small lymphocytic lymphoma.

FBDD is not only used in pharmaceutical industry, but also widely exploited by academic groups for the development of chemical tools. Fragment libraries are commercially available. Both the library and the screening costs are within the budget of academic research groups. Particularly, virtual screening (*in silico* docking) has been widely used for enriching compounds pool and analyzing binding modes. *In silico* docking performs a recursive search and evaluation algorithm on a collection of ligand confirmations until the convergence to the minimum energy is reached¹⁰. A scoring function based on the electrostatic and van der Waals energies, as well as penalizing interactions, is then used to rank the ligands¹⁰. The top-scoring fragments can be refined *in silico* again to improve characterization of ligand-receptor interactions and physical properties before selecting hits for pharmacological evaluation, which provides an effective and inexpensive way to enrich compounds. Collectively, virtual screening and FBDD offer a complementary approach to HTS and will keep advancing the field of drug discovery.

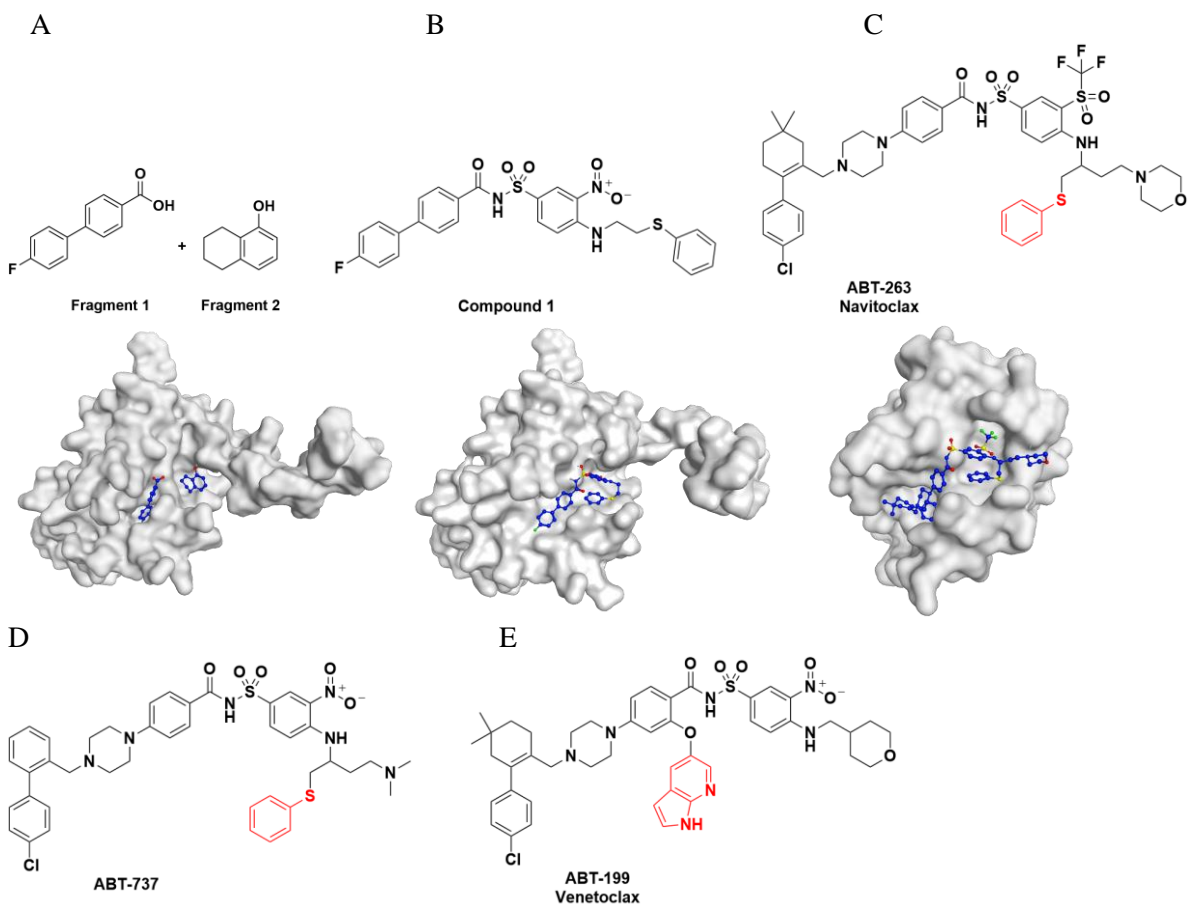


Figure 1. 1 Schematic overview of Venetoclax (ABT-199) discovery.

(A) Structure of fragments and co-crystal of fragments bound to BCL-X_L (PDB: 1YSG) (B) Structure of compound 1, which was designed based on the two fragments, and co-crystal of compound 1 bound to BCL-X_L (PDB: 1YSI) (C) Structure of ABT-263 and co-crystal of ABT-263 bound to BCL-2 (PDB: 4LVT) (D) Structure of ABT-737 (E) Structure of ABT-199

1.2 RAS superfamily of small GTPases

1.2.1 RAS plays a key role in cell signaling

The RAS superfamily proteins are small membrane-associated guanosine triphosphatases (GTPases) consisting of more than 150 GTP-binding proteins that play key roles in the regulation of cell growth and survival¹¹. There is speculation that several members of this family, including RAS, RAC1, RHOA and RHEB proteins, could serve as effective targets in multiple diseases. For example, around

30% of human cancers are driven by *RAS* oncogenes, specifically, pancreatic (71%), colorectal (42%), and lung (20%) cancers (**Table 1.1**). *KRAS* is the most frequently mutated (86%) among the three *RAS* isoforms¹². The *RAS* protein functions as a molecular switch, cycling between a GTP-bound active state and a GDP-bound inactive state (**Figure 1.2**). There are two classes of regulators catalyzing the exchange between these two states: i) Guanine nucleotide exchange factors (GEFs) including son of sevenless homologue (SOS) and *RAS* guanyl nucleotide-releasing protein (*RASGRP*), which catalyze GDP release from *RAS* ii) GTPase-activating proteins (GAPs), which catalyze the hydrolysis of GTP to GDP. Upon binding with GTP, the conformation of *RAS* switch I region (residues 30-38) and switch II region (residues 60-76) change substantially to enable *RAS* binding with effectors. As a result, pathways including RAF-MEK-ERK, PI3 kinase-AKT-mTOR, and RalGDS (*RAL* guanine nucleotide-dissociation stimulator) -*RAL* are activated to mediate cell survival, proliferation, vehicle trafficking and cytoskeletal organization.

Table 1. 1 *KRAS* mutation frequencies in different cancers

| | %<i>KRAS</i> | %<i>HRAS</i> | %<i>NRAS</i> | %All <i>RAS</i> |
|-----------------|---------------------|---------------------|---------------------|------------------------|
| Pancreas | 71 | 0 | <1 | 71 |
| Colon | 35 | 1 | 6 | 42 |
| Lung | 19 | <1 | 1 | 20 |

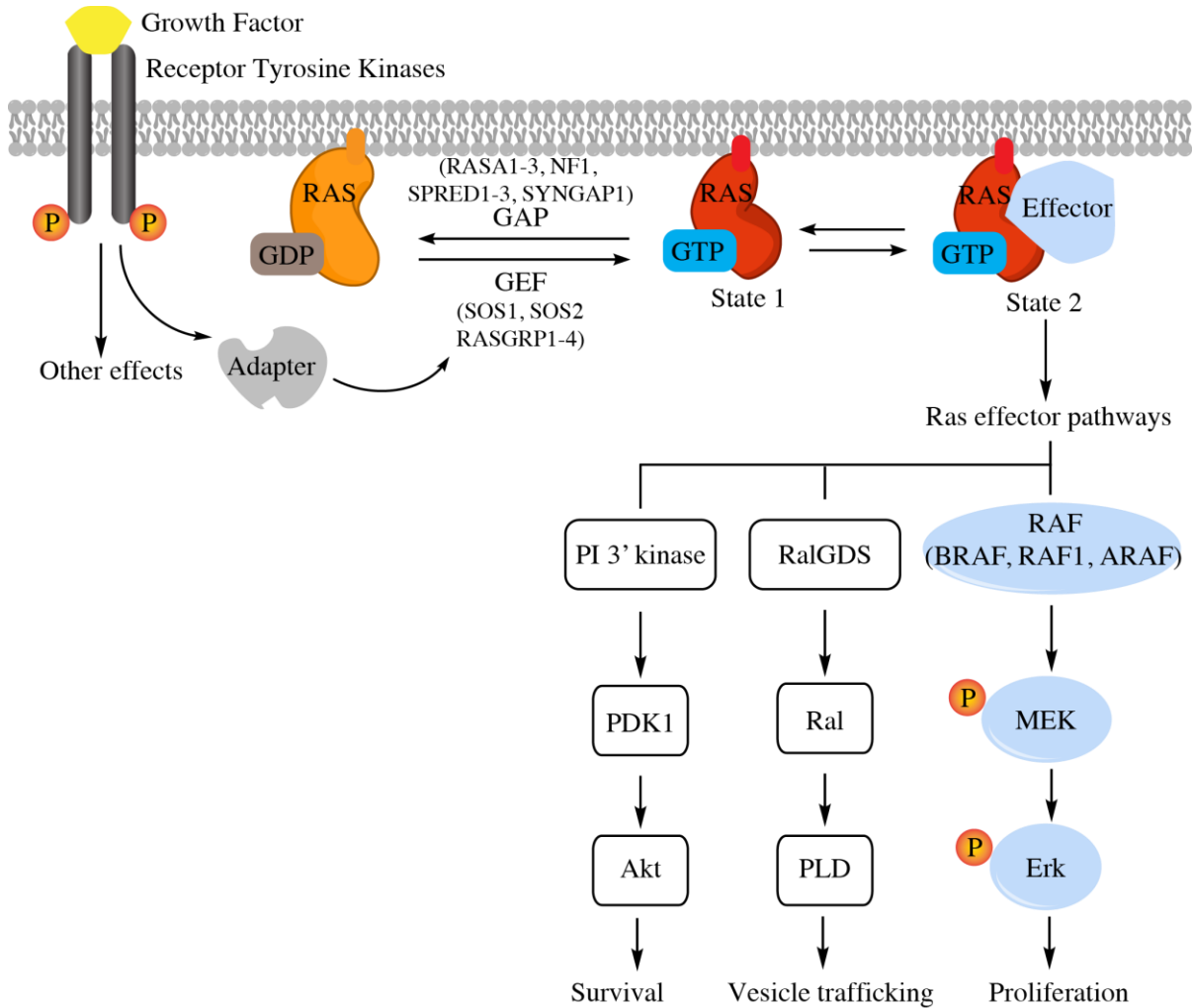


Figure 1. 2 Schematic overview of RAS signaling pathways.

The exchange of GDP-bound RAS to GTP-bound RAS is mediated by GEF including SOS1, SOS2, and RASGRP1-4. The hydrolysis of GTP is catalyzed by GAP. GTP-bound RAS has two states and only the state 2 is able to interact with PI3' kinase, RalGDS, and RAF effectors to stimulate the downstream signaling pathways.

1.2.2 RAS isoforms

RAS isoforms are encoded by three genes (*HRAS*, *KRAS*, and *NRAS*), while *KRAS* has two splice variants, resulting in a total of four proteins, *HRAS*, *NRAS*, *KRAS4A* and *KRAS4B*. These three RAS

isoforms are not identical in aspects of structure, post-translational modifications, distribution, function, and mutation rates in different cancers.

First, the four RAS proteins are composed of a highly homologous catalytic domain (the G domain, 92-98% sequence identity) and a flexible C-terminal hypervariable region (HVR) which contains the membrane anchor sequence such as the CAAX box (“A” refers to an aliphatic residue)¹³. Because of the significant difference in HVR across the RAS isoforms, they possess different post-translational modifications and subcellular localizations. For example, HRAS, NRAS, and KRAS4A can undergo prenylation and palmitoylation at the first and second cysteine in the CAAX box, which facilitates their shuttle between the plasma membrane and the endomembrane. KRAS4B lacks the second cysteine in the CAAX box, thus, could not have such localization modification. In addition, the polybasic sequence in KRAS4A and poly-lysine sequence in KRAS4B enhance their membrane anchoring through electrostatic interactions, which are different from HRAS and NRAS. The multiple membrane-anchoring mechanisms possessed by RAS isoforms leads to the difficulty of developing a single drug to inhibit RAS localization.

Second, KRAS, NRAS, and HRAS have different tissue distribution and physiological functions. While *Hras* or *Nras*-deficient mice are born and grow normally, *Kras* deficient embryos have abnormal ventricular walls, increased motoneurons death, fetal liver defects, and anemia, and eventually die during the embryonic period, which suggests *Kras* is essential for normal mouse embryogenesis¹⁴⁻¹⁵. A later study demonstrated that modification of *Kras* gene to express HRAS protein supports normal embryonic development despite inducing cardiovascular pathology in adult mice, indicating KRAS protein is not essential in embryogenesis but has a unique role in specific tissue homeostasis¹⁶. Because of the important localization role of different RAS isoforms, especially KRAS, target validation of RAS using genetic tools have many differences than those using pharmacological tools.

Finally, RAS isoforms have distinct roles in cancer as shown by cancer-type-specific mutational profiles. For example, there is near-exclusive mutation of *KRAS* in pancreas, lung, and colon cancer; while, *HRAS* mutations are predominant in neck and head squamous cell carcinoma; *NRAS* mutations are predominant in cutaneous melanoma and acute myelogenous leukemia (AML). The most frequently

mutated sites in RAS are residues 12 and 13 in the phosphate-binding loop (P-loop, residues 10-17) and residue 61 in switch II, both regions are around the nucleotide-binding pocket. Oncogenic mutations in RAS impair its intrinsic and GAP-mediated GTP hydrolysis, resulting in the accumulation of RAS-GTP that constitutively activates RAS downstream signaling.

1.2.3 Strategies for drug discovery in RAS and current progress

Despite the prevalence of RAS mutations in cancer, mutant RAS has remained an intractable target for decades. RAS function relies on membrane targeting, GTP binding, protein-protein interaction and the activation of downstream pathways. Thus, there are different strategies targeting RAS accordingly. First, RAS targeting could be achieved by direct inhibition including disrupting RAS localization on the membrane, decreasing GTP-bound RAS, and blocking RAS-effector interactions, which will be discussed in detail in the following section. Second, there are indirect inhibition approaches which include inhibiting RAS downstream signaling pathways, inhibition of RAS synthetic lethal interactors, and inhibition of metabolic targets relating to RAS. The indirect strategies could be challenging due to genetic context, complex feedback mechanisms, intrinsic resistance, and drug potency.

To disrupt RAS membrane anchoring, at least six farnesyltransferase inhibitors (FTIs) have been tested in clinical trials, however, none of them have achieved the expected activity against tumors¹⁷. One reason is that FTIs are able to inhibit HRAS function but not other isoforms because HRAS prenylation is exclusively modified by farnesyltransferase, while the other three isoforms have alternative membrane-anchoring mechanisms such as geranylgeranyltransferase I-mediated prenylation¹⁸. Another reason is that more than 30 proteins including the RAS and RHO family proteins require post-translational farnesylation for localization. As a consequence, FTIs have a small therapeutic window and could not be used in treating HRAS-mutation driven cancers¹⁷.

Considering the high concentration of GTP in the cell (~0.5 mM) and the picomolar binding affinity of GTP to RAS, designing compounds competing with nucleotide binding is challenging. The esterified electrophilic GDP analog showed some specificity to KRAS G12C, but the compound was not potent enough, and inhibited ERK and AKT phosphorylation at 100 μM ¹⁹. Based on the above facts, decreasing GTP-bound RAS through inhibition of GEF such as SOS1 and SOS2 is more feasible. A variety of methods including virtual, NMR-based, fragment-based, and peptidomimetic screens have been attempted to disrupt RAS-GEF binding and have discovered some hits including small molecules targeting the catalytic site of SOS1²⁰, and a α -helix that mimic α -helices on SOS protein surface²¹⁻²². At the same time, there are some previously unknown binding pockets on RAS that have been discovered, for example, a hydrophobic pocket in SOS CDC25 domain adjacent to RAS switch II region²³.

With the advancement of computational chemistry, designing small molecules targeting protein-protein interactions (PPI) in RAS is viable. A PPI inhibitor could be designed to either directly target RAS and block the effector binding, or target the RAS-binding domain (RBD) on effectors. For instance, a pan-RAS inhibitor MEW3144, which was designed to interact with adjacent sites in switch I and switch II regions of KRAS, exhibited nanomolar activity in cancer cell lines. The molecule showed tumor-suppression effects in the MDA-MB-231 (*KRAS G12D*) subcutaneous xenograft model²⁴⁻²⁵. Alternatively, a RAS-mimetic small molecule rigosertib inhibits RAF-RAS interaction by binding to the RAS-binding domain (RBD) of RAF kinases²⁶. Rigosertib is currently in phase III clinical for the treatment of myelodysplastic syndromes (MDS), which is active either as a single agent or in combination with Azacytidine.

Recently, a covalent allosteric binding strategy showed the feasibility of targeting a specific KRAS mutant, KRAS-G12C^{13, 27-29}. This type of electrophile aims to stabilize the inactive KRAS G12C and block GTP binding. KRAS-G12C-selective inhibitor ARS-1620 showed tumor suppression effect in six subcutaneous cell line-derived *p.G12C* tumor models and patient-derived tumor xenografts (PDX) harboring *KRAS p.G12C* but not *p.G12V*, *p.G12D*, and wild-type tumor models, indicating the potency and selectivity of this small molecule to *KRAS-G12C* mutant²⁹. The design of KRAS-G12C-selective

inhibitors requires intensive structure-based drug design efforts. For example, an orally available KRAS-G12C inhibitor MRTX849 was developed by analyzing >150 cocrystal structures and synthesizing >2000 discrete small molecules³⁰. MRTX849 will prove whether the covalent allosteric binding strategy could be translated to clinic.

1.3 Ferroptosis

1.3.1 Classical view of cell death and new classification of cell death

Cell death is of fundamental importance in life and plays essential roles in regulating organism development, tissue homeostasis, immune system, stress and defense response. The balance between cell death and cell survival/proliferation controls physiological and pathological settings in life. Thus, the investigation of molecular mechanisms that regulate multiple cell death pathways is key to understanding disease development and to discover new therapeutics³¹⁻³². For a long time, morphotypes has been employed to classify cell death into three types: apoptosis, autophagy, and necrosis. With the increasing number of cell death mechanisms discovered, the Nomenclature Committee on Cell Death (NCCD) has updated cell death definitions based on molecular aspects³³. Cell death is divided into the accidental cell death, which is caused by extreme physical, chemical, or mechanical insults, and regulated cell death (RCD), which is dependent on signal transduction and can be modulated pharmacologically or genetically. For example, apoptosis, the first well characterized RCD, is initiated by extracellular or intracellular microenvironmental perturbations and regulated by executioner caspases. Besides apoptosis, there are several other regulated cell death pathways discovered in last two decades. For instance, ferroptosis was named by Stockwell and colleagues in 2012 to describe a regulated cell death driven by iron-dependent lipid peroxidation that can be inhibited by iron chelators and lipophilic antioxidants³³⁻³⁷.

1.3.2 Molecular and pharmaceutical modulators of ferroptosis

Ferroptosis can be induced by both reduced glutathione (GSH) depletion and glutathione peroxidase 4 (GPX4) inactivation (**Figure 1.3**). Ferroptosis has two key regulators, system x_c^- and GPX4. System x_c^- mediates the import of cystine which is intracellularly reduced to cysteine, a necessary component of reduced glutathione (GSH) biosynthesis in cells. GPX4 reduces lipid peroxides by consuming GSH. Inhibition of system x_c^- or GPX4 could enhance lipid peroxidation thus leading to ferroptotic cell death, while iron chelators and antioxidants could inhibit lipid peroxidation and rescue ferroptotic cell death. In this section, the essential components of ferroptosis will be discussed to show how ferroptosis is distinct from other regulated cell death pathways.

GSH is an important antioxidant that eliminates cellular damage caused by reactive oxygen species. GSH depletion has features of increased lipid peroxidation, 8-hydroxy-2-deoxyguanosine (8-OHdG) formation, chromosomal giant DNA fragmentation, and membrane integrity loss³⁸⁻⁴⁴. GPX4 reduces membrane phospholipid hydroperoxides by consuming GSH to suppress ferroptosis. The inactivation or depletion of GPX4 would cause lipid hydroperoxides accumulation. For example, the kidney of *Gpx4*^{-/-} mice had increased levels of di-oxygenated species of PC (PC-OOH), PE (PE-OOH), and CL (CL-OOH) compared with control mice⁴⁵. In addition to the above molecular modulators, several other pathways also contribute to modulate cell sensitivity to ferroptosis. NRF2 transcription factor controls the expression of specific types of iron-signaling genes and antioxidant genes, and promotes resistance to ferroptosis³⁴. Ferroptosis sensitivity is also modulated by the stress-responsive transcription factor and canonical tumor suppressor protein p53. The role of p53 in ferroptosis is different depending on the context. For instance, acetylation-defective p53 sensitizes cells to ferroptosis, independently of cell-cycle arrest, apoptosis and senescence⁴⁶. However, stabilization of wild type p53 was proved to delay the onset of ferroptosis in response to cystine deprivation⁴⁷. And, some results suggest that p53 suppresses ferroptosis by blocking dipeptidyl-peptidase-4 activity⁴⁸. Defining the context during the investigation of ferroptosis molecular modulators is thus important.

In addition to the endogenous molecular modulators, there are many ferroptosis pharmaceutical modulators including both inducers and inhibitors. Ferroptosis inducers could be classified according to

the targets. Class 1 ferroptosis inducers include glutamate, sulfasalazine, sorafenib, as well as erastin and erastin analogs, which inhibit the cystine (Cys₂)/glutamate (Glu) antiporter system x_c⁻ resulting in cystine deprivation and subsequent GSH depletion^{34-35, 49-52}. Among these inducers, sorafenib is the only clinically-approved anticancer drug which was first discovered to be a multi-kinase inhibitor then identified to have system x_c⁻ inhibition activity in multiple cancer cell lines⁵³. Moreover, canonical hallmarks of apoptosis, such as pro-caspase-3 cleavage and poly (ADP ribose) polymerase 1 (PARP 1) cleavage, did not occur in sorafenib induced cell death, implying that the anticancer effect of sorafenib is not through apoptosis⁵³. Class 2 ferroptosis inducers include RSL3, ML162, and DPI compounds, which inhibit GPX4 directly to induce ferroptosis. For example, RSL-3 is a nanomolar small molecule inhibitor which covalently modifies the selenocysteine residue in GPX4. Class 3 ferroptosis inducers, which include FIN56 and CIL56, induce ferroptosis by depleting GPX4 and at the same time, depleting coenzyme Q₁₀ (CoQ₁₀) through mevalonate pathway. Also, there are more compounds including FINO₂, statins, silica-based nanoparticles, and ferric ammonium citrate, which induce lipid peroxidation and ferroptosis through various mechanisms.

There are three principle events in free radical-mediated peroxidation. The first step is the initiation through hydrogen atom transfer. Second is the propagation cycle including reaction of the lipid radical with molecular oxygen to produce a lipid peroxy radical, followed by fragmentation, rearrangement, and cyclization of the lipid peroxy radical. The third step is the termination reaction of forming nonradical products⁵⁴. Inhibition of either step one or step two would inhibit ferroptosis³⁴. Class 1 ferroptosis inhibitors are iron-chelators such as deferoxamine and deferiprone, which eliminate cellular free irons and prevent Fenton chemistry mediated-lipid peroxidation. Class 2 ferroptosis inhibitors are deuterated-polyunsaturated fatty acids (D-PUFAs). PUFA peroxidation is initiated by hydrogen atom abstraction at the bis-allylic site. PUFAs deuterated at the bis-allylic sites prevent the hydrogen atom transfer because of the isotope effect. Class 3 ferroptosis inhibitors are antioxidants, including the naturally occurring ones, Vitamin E (α -tocopherol) and CoQ₁₀, and the synthetic small molecules, Ferrostatin-1 (Fer-1) and lipostatin-1 (Lip-1), which inhibit ferroptosis by reducing the reactive oxygen

species. Fer-1 and Lip-1 function as radical-trapping antioxidants, and are more reactive in inhibiting oxidations in phosphatidylcholine (PC) lipid bilayers comparing to Vitamin E, which is consistent with the potency of these three inhibitors in ferroptosis⁵⁵.

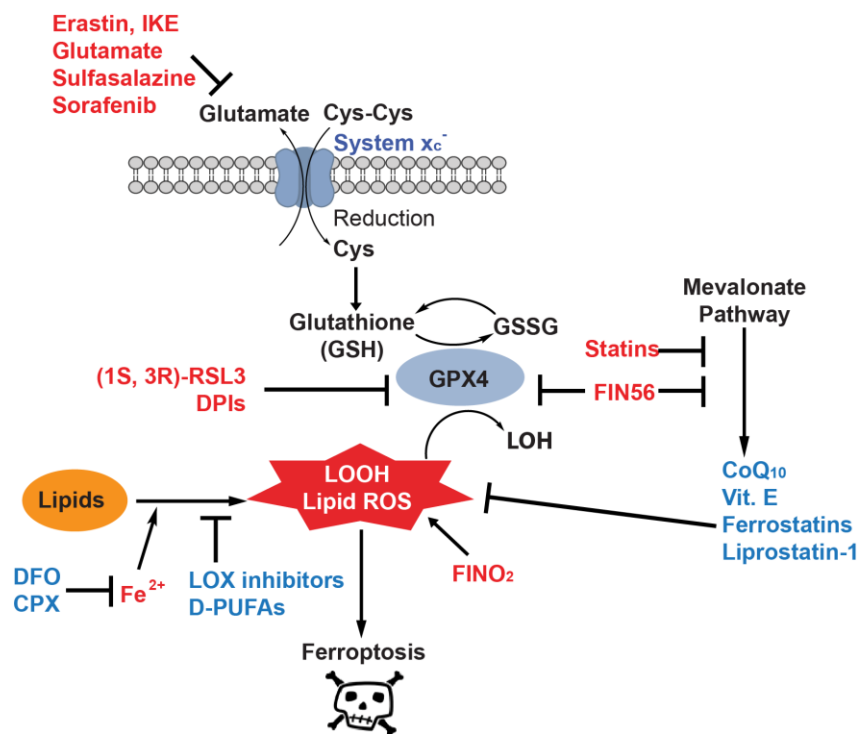


Figure 1. 3 Schematic illustration of pathways regulating ferroptosis.

Ferroptosis inducers are colored as red. Ferroptosis inhibitors are colored as blue.

1.3.3 Structure and activity relationship study of erastin analogs

Erastin (Eradicate RAS-and Small T transformed cells) was discovered by phenotypic screening of cell lines expressing mutant HRAS⁵⁶. Structure-and-activity relationship study of erastin analogs have demonstrated that the quinazolinone and imidazole group (highlighted as red) are amenable to a wide range of substitutions or bioisosteric replacements to tune the binding affinity and water solubility (**Figure 1.4**)^{52, 57}. While, the piperazine and chloro-benzyne methoxy groups (highlighted as black) are essential for the binding. For example, even the substitution of chlorine with fluorine on the benzyne methoxy group would decrease the binding affinity for more than twenty fold⁵². Besides, the introduction

of carbonyl group largely increases erastin analogs' binding affinity which probably results from the reversible covalent reaction of carbonyl group and lysine residues to form the Schiff base. In addition, the substitution of isopropyl group on methoxy benzyne ring (highlighted as blue) enhances metabolic stability. Overall, imidazole-ketone-erastin (IKE) is the most potent and metabolically stable analog of erastin synthesized thus far^{52, 57}.

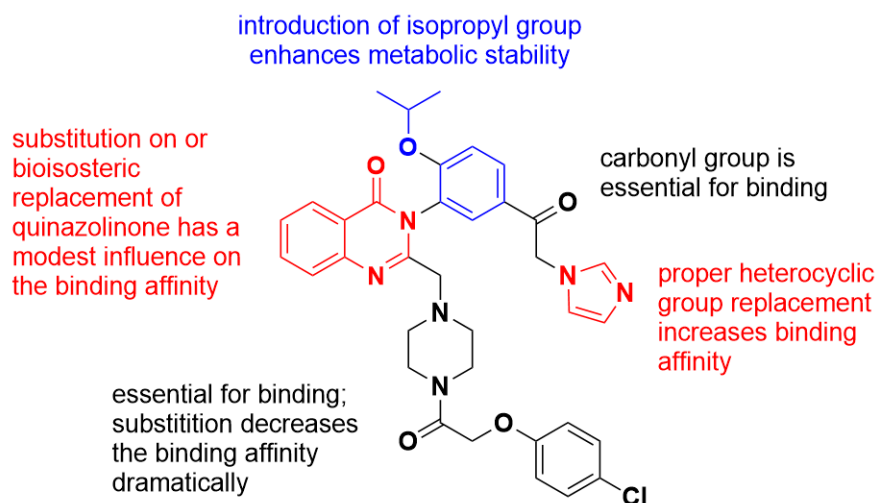


Figure 1. 4 The summary of structure-and-activity relationship study of erastin analogs (IKE structure is presented in the figure)

1.3.4 Labile iron regulation in ferroptosis

Labile iron pool is capable of catalyzing lipid peroxidation through Fenton reactions and has been proved to be required during ferroptosis. There is a speculation that regulating labile iron pool through iron import, export, metabolism, and storage would affect the cellular sensitivity to ferroptosis.

Iron metabolism is very fine tuned. Iron is imported to cells by transferrin receptor (TFR) upon loading on transferrin (TF) (**Figure 1.5**). Cellular labile iron pool is kept at the lowest enough level to protect cells from oxidative stress. The excess iron is either stored in ferritin or effluxed by ferroportin. Investigation to the links between ferroptosis and autophagy revealed that autophagy promotes ferroptosis

through ferritin degradation and labile iron release⁵⁸. Inhibition of nuclear receptor coactivator 4 (NCOA4) or knockdown of autophagy-related 5 (ATG5) and ATG7, which mediate iron release from ferritin, suppressed erastin-induced ferroptosis. A RNA interference experiment proved that knock down of iron-sulfur cluster biosynthetic enzyme NFS1 in low oxygen condition (3% O₂) limits iron-sulfur cluster availability and activates the iron-starvation response, which further leads to glutathione biosynthesis inhibition and triggers ferroptosis⁵⁹. At the same time, the author found that lung adenocarcinoma cell lines are dependent on high levels of NFS1 to prevent oxidative damage and ferroptosis. More work is needed toward understanding the relationship of labile iron, oxygenation, and ferroptosis so that key regulators controlling cell sensitivity to ferroptosis could be revealed.

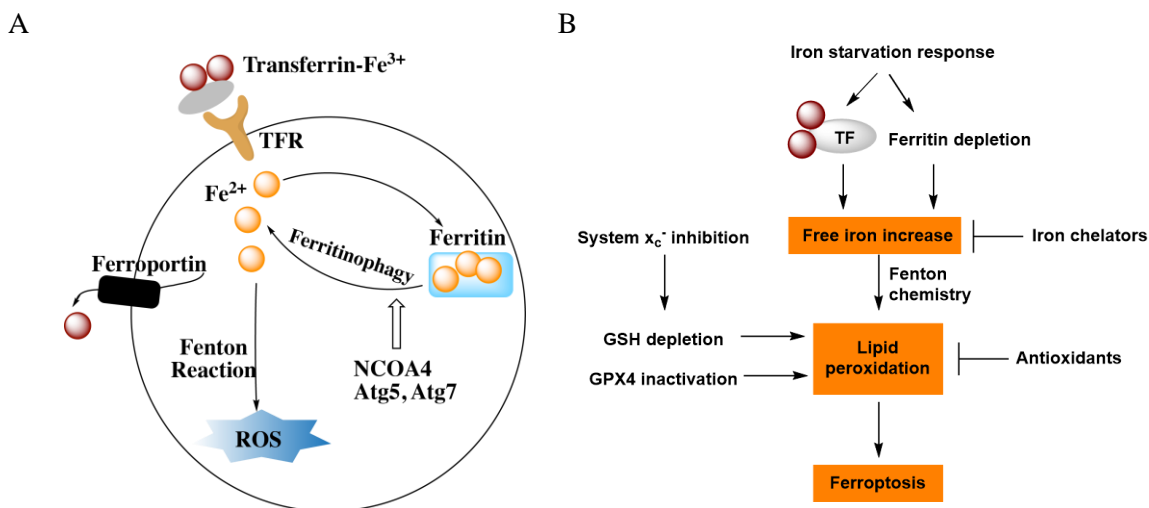


Figure 1. 5 Schematic overview of iron metabolism in ferroptosis

(A) Overview of iron absorption and metabolism. Fe³⁺ is carried by circulating apo-Transferrin (TF) in plasma to form diferric TF. The Transferrin-(Fe³⁺)₂ is imported by cell surface transferrin receptor (TFR). Fe³⁺ is released by endocytosing followed by reduction to Fe²⁺ to enter cellular labile iron pool. Excess iron is stored in ferritin or effluxed by ferroportin. Autophagy promotes ferroptosis through degradation of ferritin mediated by nuclear receptor coactivator 4 (NCOA4) and autophagy-related proteins (ATGs). (B) The relationship between iron regulation and ferroptosis. GPX4 inactivation and glutathione (GSH) depletion, induced by system x_c⁻ inhibition, produce oxidative stress to cells, which results in free iron-mediated- or enzyme-mediated-lipid peroxidation. Iron chelators and antioxidants prevent ferroptosis by decreasing free iron and lipid peroxides in cells individually. Increasing labile iron pool through activating transferrin (TF) and decreasing ferritin will increase cells sensitivity to ferroptosis.

1.3.5 Application of ferroptosis in therapeutics

Ferroptosis is a regulated cell death nexus linking metabolism and disease. The diverse ferroptosis pharmacology modulators provide important tools to investigate different types of diseases.

Increasing evidence suggests that ferroptosis is involved in brain injury and neurodegenerative diseases, which includes Huntington's disease, Alzheimer's disease, and Parkinson's disease. Analysis of brain tissues identified increased iron levels, oxidative stress, GSH levels, and lipid peroxidation in neurodegenerative diseases⁶⁰⁻⁶⁵. Besides, ferroptosis inhibitors such as antioxidants, including CoQ₁₀ and Vitamin E, entered in clinical studies and have been proved to slow or reduce neurodegenerative diseases⁶⁵. For example, a 2 years study of CoQ₁₀ in 300 patients with mild to moderate stage Alzheimer's disease has proved dose-related benefits on patients' cognition⁶⁶. Moreover, the ferroptosis inhibitor Fer-1 has shown the inhibition of cell death in cellular models of Huntington's disease and periventricular leukomalacia, indicating the potential application of ferrostatin analogs in brain injury and neurodegenerative diseases⁶⁷.

Small molecules-induced ferroptosis has shown tumor inhibition effect in cell culture. Specific types of cancer cell lines are especially sensitive to ferroptosis due to their dependence on ferroptosis regulators, such as the dependence on system x_c⁻ for B cell-derived lymphomas⁵¹, GPX4 for renal cell carcinomas (RCC)^{51, 68}, and ACSL4 for subtypes of breast cancer cell lines⁶⁹⁻⁷². Targeting ferroptosis might be hold potential benefit for treating these types of cancers. The obvious strategy is to inhibit tumor cell growth using single ferroptosis inducer. For example, cells of clear-cell renal cell carcinoma (ccRCC), which is intrinsically resistant to chemotherapy and radiation therapy, possess a lineage-specific vulnerability to ferroptosis inducer RSL3⁷³. Other strategies could be the combination of therapies including chemotherapy, radiation therapy and oxygenation therapy. For example, the ferroptosis inducer erastin synergizes with several chemotherapies, including cisplatin, temozolomide, adriamycin and doxorubicin in cell culture studies⁷⁴⁻⁷⁸. Moreover, oxygenation therapy, which could enhance free radical generation, might further elevate oxidative stress in tumor cells by combining with ferroptosis inducers.

Furthermore, ferroptosis regulator system x_c^- is not only a critical regulator in cysteine metabolism but also essential in glutamate signaling. System x_c^- is widely distributed in macrophages, liver, kidney, and brain. Exploring potential application of IKE in glutamate signaling and neuroscience is also of therapeutic interest. For example, the excess glutamate secreted by system x_c^- is associated with cancer-induced bone pain in distal breast cancer metastases. A system x_c^- inhibitor capsazepine showed the potential of preventing cancer-induced bone pain in a murine model mimicking human metastatic breast cancer to the bone⁷⁹.

Collectively, targeting ferroptosis could be an alternative option to treat neurodegenerative diseases and cancers including cancers that are intrinsically resistant to conventional chemotherapy or radiotherapy.

1.4 Lipid metabolism in ferroptosis

Ferroptosis is an iron-dependent and lipid peroxidation-induced cell death which can be rescued by antioxidants. Lipid metabolism is heavily involved in ferroptosis execution⁸⁰. Given by the complexity of lipid metabolism, I will introduce fatty acids structure and the effects of specific fatty acids on ferroptosis, followed by discussion of phospholipids biosynthesis and lipid peroxidation in ferroptosis. Finally, I will describe the application of mass spectrometry in untargeted lipidomics and the progress of mass spectrometry based lipidomics study in ferroptosis.

1.4.1 Fatty acids structure, nomenclature, and effects on ferroptosis

Fatty acids (FA) exist in mammalian cells both as free fatty acids (FFA) and esters, the latter ones include phospholipids, glycolipids, and triacylglycerols. Most of the naturally occurring fatty acids (FAs) are unbranched and have diverse carbon (C)-chain length and number of double bonds. FAs with chain-lengths of 11-20 carbons are classified as long chain fatty acids. FAs with >20 carbons are called very-

long chain fatty acids, which are less abundant than long chain fatty acids. Depending on the number of double bonds in the FAs, they can be classified into saturated FAs (SFAs), monounsaturated FAs (MUFAs), or polyunsaturated FAs (PUFAs). Because of the complexity of FAs structures, they are often named using the form of $C:D$, $n-x$ (or $\omega-x$), where C is the number of carbon atoms in the FA, D is the number of double bonds in the fatty acid, n (or ω) represents counting the double bond from the terminal methyl carbon toward the carbonyl carbon, and x is the position of the first double bond. For example, arachidonic acid is termed as 20:4, $n-6$ or 20:4, $\omega-6$. FA from the same $n-x$ series are likely to share a biosynthetic pathway.

Free FA and FA esters not only function as energy sources, but also serve as components of cell membranes, protein post-translational modifications, and messengers in signaling transduction⁸¹. Emerging evidence has indicated lipids and lipid metabolism heavily involved in ferroptosis and regulated cell death⁸⁰. It has been reported that fatty acids could trigger or potentialize ferroptosis. For example, PUFAs such as arachidonic acid, γ -linolenic acid, linoleic acid, cardiolipin, cholesterol, and ceramide enhanced ferroptosis and cell membrane integrity loss^{39, 82}. Particularly, the addition of arachidonic acid reduced caspase-3 activity, decreased cellular ATP level, mitochondrial membrane potential, and activated 12-lipoxygenase protein expression in C6 rat glioma cells⁴³. However, the MUFA oleic acid interestingly protects against lipid peroxidation in ferroptosis, which might because oleic acid does not have bisallylic sites, which are the sites vulnerable for lipid peroxidation initiation^{39, 82-83}.

1.4.2 Involvement of phospholipids biosynthesis in ferroptosis

Phospholipids are a major component of cell membranes, and are responsible for maintaining the structural integrity of cells. An *in silico* model of membrane dynamics suggests that ferroptosis induces changes in various membrane properties including thickness, fluidity, permeability, and curvature, which is in alignment with experimental results⁸⁴.

Biosynthesis of phospholipids is divided to two different pathways, the *de novo* pathway (Kennedy pathway) by using acyl-CoA and diacylglycerol, and the remodeling pathway (Lands' cycle) by using acyl-CoA and lysophospholipids⁸⁵. In the *de novo* pathway, acetyl-CoA carboxylases (ACC) catalyze the conversion of acetyl-CoA to malonyl-CoA followed by FA synthase (FASN) and FA elongase (ELOVLs)-mediated elongation to synthesize long chain FA-CoA. Then, long chain FA-CoA are converted to lysophospholipids (LPA) by glycerol-3-phosphate acyltransferase (GPAT) with the expense of glycerol-3-phosphate (G3P). Fatty acids are esterified to form phospholipids in an asymmetric manner. Saturated (SFA) and monounsaturated FAs (MUFA) are usually esterified at the *sn*-1 position, while, polyunsaturated FAs (PUFA) including arachidonic acid and eicosapentaenoic acid are mainly located at the *sn*-2 position.

Lysophospholipid acyltransferases (LPTs), such as lysophosphatidylcholine acyltransferase (LPCAT), lysophosphatidylethanolamine acyltransferase (LPEAT) and lysophosphatidylserine acyltransferase (LPSAT), are involved in catalyzing phospholipids synthesis from lysophospholipids. There are different classes of phospholipases including phospholipase A₁ (PLA₁), phospholipase A₂ PLA₂, phospholipase C (PLC), phospholipase D (PLD), which catalyze the hydrolysis of phospholipids to lysophospholipids at *sn*-1, *sn*-2, *sn*-3, and phosphate sites respectively (**Figure 1.6**). Under oxidative stress, phospholipase activation protects cells by cleaving the oxidized PUFAs to maintain cell membrane integrity. LPCAT2, LPCAT3, and Group IVA phospholipase A₂ (LPA2G4A) specifically participate in arachidonic acid acylation or hydrolyzation reactions. Therefore, these three isoforms represent the essential enzymes in arachidonic acid-mediated oxidative stress and inflammation generation.

Genes encoding lipid biosynthesis enzymes have been proved to regulate cell sensitivity to ferroptosis. First, the depletion of acyl-CoA synthetase long-chain family member 4 (*ACSL4*), which catalyzes the conversion of free long-chain FA to FA-CoA esters, or *LPCAT3*, which mediates the conversion of LPC to PC, results in resistance to GPX4 inhibition⁸⁶. A genome-wide CRISPR-based genetic screen on Pfa1 cells and RSL3-resistant clones also discovered that *ACSL4* expression was dramatically decreased in the resistant clones⁶⁹. Second, untargeted lipidomics studies performed in

ferroptosis occurring cells have identified that there was accumulation of LysoPC and depletion of PUFA, indicating that lysophospholipid acyltransferases (LPTs) might be activated during ferroptosis to cleave the oxidized PUFA in phospholipids^{82, 86}.

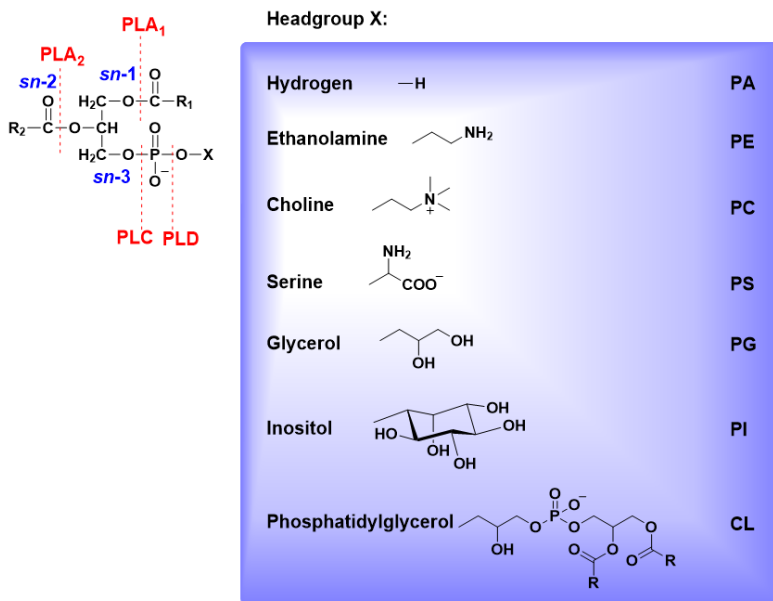


Figure 1. 6 Schematic of phospholipids structure in different classes and the hydrolysis sites of different phospholipases.

1.4.3 Participation of lipid peroxidation in ferroptosis

With the induction of oxidative stress, lipids can be oxidized via both enzymatic and non-enzymatic pathways. The enzymatic pathway relies on the catalysis by three main enzymes including cyclooxygenase (COX), lipoxygenase (LOX), and cytochrome P450 (CYP) isoforms. The non-enzymatic pathways include free radical-mediated oxidation and free radical independent non-enzymatic oxidation.

There are many classes of lipid peroxidation products. PUFA can form the intermediate oxygenated lipid derivatives including octadecanoids which are derived from 18-carbon PUFA, eicosanoids which are derived from 20-carbon PUFA, and docosanoids which are derived from 22-carbon

PUFA. The free radical-mediated oxidation products F_2 -isoprostanes and neuroprostanes, which are derived from arachidonates and docosahexanoates respectively, are well-characterized and often used as oxidative stress biomarkers *in vivo*⁸⁷. These intermediate derivatives can be degraded to secondary products including reactive carbonyl compounds such as aldehydes and dicarbonyls, and stable products such as ketones and alkanes. The reactive carbonyl compounds can further modify the proteins to form adducts that induce protein dysfunctions and other cellular responses. For example, 4-hydroxynoneal (4-HNE), 4-hydroxyhexenal (4-HHE), and malondialdehyde (MDA) can react with histidine (His), cysteine (Cys) or Lysine (Lys) residues to form stable Michael adducts⁸⁸. The reactive carbonyl compounds can be determined using TBA reactive substances (TBARS) assay, mass spectrometry, enzyme-linked immunosorbent assay (ELISA), as well as polyclonal or monoclonal antibodies against reactive carbonyl compounds-protein adducts to evaluate oxidative stress in cells and tissues.

Increasing evidence has shown the accumulation of specific lipid peroxides and participation of the associated enzymes during ferroptosis. A quantitative redox global phospholipidomics revealed that doubly and triply oxygenated species of PE are significantly increased in ferroptosis⁸⁹. PEs containing arachidonoyl (AA) and adrenoyl moieties (AdA) were identified as the preferred substrates for oxidation in ferroptosis⁹⁰. Inhibition of lipoxygenases (ALOXs) but not cyclooxygenases (COXs) and cytochrome P450 prevented RSL-3 induced ferroptosis⁹⁰. An independent research confirmed that both genetically silencing of *ALOX* (arachidonate lipoxygenase) genes and pharmaceutically inhibition of ALOX could lead to cells' resistance to ferroptosis⁸².

1.4.4 Mass spectrometry platform-based lipidomics analysis

Comprehensive analysis of lipids is full of challenges because of the structural complexity and low abundance of lipids and lipid oxidation products. First, lipids are composed of eight families containing around 1.68 million species⁹¹. Lipids formation is regio-, stereo-, and enantio-specific depending on the substrates, enzymes, and reaction conditions. The large variety of species, as well as

their complex structures, and biosynthesis/degradation pathways render complete lipid analysis incredibly difficult. Second, many types of lipids, especially lipids oxidation products, are not abundant *in vivo*, leading to the difficulties of detecting these types of lipids. Additionally some lipids are sensitive to oxidation which might result in artificial oxidation during sample preparation.

The mass spectrometry (MS) platform provides a high-throughput analytical tool to analyze complex lipids simultaneously in a single sample with high sensitivity and specificity^{89, 92}. MS is composed of 3 parts, an ion source, a mass analyzer, and a detector. The commonly used ionization methods include electrospray ionization (ESI), ESI tandem MS (MS/MS), atmosphere pressure chemical ionization (APCI), atmosphere pressure photoionization (APPI), desorption electrospray ionization (DESI), and matrix-assisted laser desorption ionization (MALDI)⁹¹. Each has its own advantages: (i) ESI could be used either in shotgun analysis to detect lipids at different modes by tuning pH value and adding specific ionization reagents or by coupling with separation techniques such as liquid chromatography (LC) and ultra-performance liquid chromatography (UPLC); (ii) ESI tandem MS (MS/MS) is able to analyze fragments of lipids thus providing double bond location information; (iii) APCI and APPI are more suitable for analyzing nonpolar lipids and are less susceptible to ionization suppression; (iv) DESI provides an ambient ionization method with minimal sample preparation which extracts sample locally and is widely used in direct tissue analysis; (v) MALDI is not generally suitable for lipid detection due to the lack of proper matrix, but the recent development of MALDI imaging mass spectrometry (MALDI-IMS) could possibly provide high resolution and accuracy of lipids distribution⁹³. The commonly used analyzers in lipidomics are quadrupole (Q), ion trap (IT), (quadruple) time of flight (Q)(TOF), TOF-TOF, Fourier-transform ion cyclotron resonance (FTICR), and orbitrap analyzer. The last four analyzers greatly accelerated the lipidomics research by allowing simultaneously analyzing multiple metabolites at high resolution without separation⁹⁴.

Mass spectrometry-based lipidomics studies have identified some trends of lipids change in ferroptosis. For example, metabolomic profiling of erastin-treated HT1080 cells has identified depletion of PUFAs including eicosapentaenoate (20:5 n-3), linoleate (18:2 n-6), linolenate (18:3 n-3/6), and

docosahexaenoate (22:6 n-3)⁶⁷. A quantitative redox lipidomics study proved PE oxidation in the endoplasmic-reticulum as an essential process in ferroptosis⁹⁰. In the future, the advancement of mass spectrometry-based imaging platform may yield even more information on lipids distribution in ferroptosis.

1.5 Application of nanoparticles in drug delivery

1.5.1 Abnormal tumor vasculature offers both challenges and opportunities in drug delivery

A primary goal in designing cancer therapies is to accumulate therapeutic levels of a drug at the tumor site but not distribute in healthy tissues and organs. Tumors have abnormal vasculature, which offers both challenges and provides opportunities for new approaches in drug delivery. In this section, I will first illustrate the general features of tumor vasculature and then discuss challenges of delivering conventional cancer therapies and how nanoparticles can offer new approaches to deliver chemotherapeutics.

Normal vasculature is arranged in a hierarchy of evenly spaced, well-differentiated vessels, with most of the cells in human body within a few cell diameters of a blood vessel, which allows for the efficient delivery of oxygen and nutrients to the cells. The rapid proliferation of tumor cells, however, results in abnormal blood vessels that are irregular and leaky in tumors, preventing efficient oxygen and nutrient delivery to tumors⁹⁵⁻⁹⁶. As a result, tumors have a characteristic hypoxic and low-nutrient microenvironment. In addition, solid tumors have defective lymphatic systems, leading to high interstitial pressure in tumors which limits the extravasation of macromolecules and the accumulation of metabolites, including lactic and carbonic acids, that leads to an acidic microenvironment. The dysfunctional vessel also hinders the delivery of small-molecule and macromolecular therapies to tumor cells that are distant from functional blood vessels⁹⁷.

The effectiveness of anticancer drugs relies on efficient penetration in tumor tissue to reach a therapeutic concentration. Conventional drugs are often hindered by problems such as water solubility, metabolic stability, cell membrane permeability, and the ability to penetrate solid tumors. Nanoparticle carriers are often able to overcome these limitations. For instance, free drugs may diffuse across tumor tissue nonspecifically, while nanoparticles have increased tumor accumulation due to the enhanced permeability and retention (EPR) effect, whereby the large pore openings in defective angiogenesis and dysfunctional lymphatic drainage in tumor microenvironment leads to the specific accumulation of nanoparticles in tumors⁹⁸. Currently, FDA-approved nanoparticle formulations, including Abraxane®, an albumin-based formulation of paclitaxel, Nanoxel®, a nanoliposome containing paclitaxel, and Doxil®, a nanoliposome containing doxorubicin, are being used in the clinic. All these nanoparticle formulations have decreased systemic toxicity compared to the parent drug.

1.5.2 Perspectives on polymer-based nanoparticle design

The design of nanoparticles for drug delivery requires precise control of the composition, size, shape, and surface properties. Both natural materials and synthetic materials can be used in the synthesis of nanoparticles; although natural materials have the advantages of abundance, high biocompatibility and biodegradability, nanoparticle materials are dominated by synthetic materials due to the precise control of the physicochemical properties offered by synthetic materials. In particular, the FDA-approved, biodegradable polyester poly(lactic acid) (PLA) and poly(lactide-*co*-glycolide) (PLGA) grafted with poly(ethylene glycol) (PEG) have been widely used. As such polymers are less likely to induce toxicity, immune responses, and chronic inflammation. PEG offers the additional benefit of having a hydrophilic surface, which prevents the aggregation and phagocytosis of nanoparticles, prolonging the nanoparticle circulation time in plasma. Moreover, biodegradability ensures complete degradation of the material and release of drug by multiple mechanisms, including surface and bulk erosion and diffusion (**Figure 1.7**).

Nanoparticles used in drug delivery typically have diameters ranging from 20 nm to 200 nm⁹⁹. This represents an ideal size for nanoparticles as the cutoff size of extravasation into tumors is around 400

nm and particles larger than 200 nm or smaller than 20 nm are rapidly cleared by liver, kidney, or spleen (**Figure 1.8**). Finally, diffusion-mediated penetration is inversely correlated with the particle size, thus smaller nanoparticles have greater tumor penetration ability. For these reasons, it is important that nanoparticles are designed with a diameter no smaller than 20 nm to ensure enhanced tumor accumulation.

The shape of nanoparticles influences their cellular uptake, circulation lifetime, and *in vivo* fates⁹⁹. For example, discoidal nanoparticles are more prone to tumbling and oscillatory effects in vasculature, thus increasing nanoparticle-cell wall contact and possibility of extravasation⁹⁹. Polymer-based nanoparticles are mostly spherical nanoparticles, which have smaller surface area comparing with discoidal and other non-spherical nanoparticles at the same size, which might be advantageous in tumor penetration¹⁰⁰.

The surface of nanoparticles offers additional means to achieve specific targeting to tumors. Nanoparticles with a slightly positive or negative charge will not readily aggregate due to repulsion forces. A high positive surface charge, however, will lead to cellular toxicity and quick clearance by macrophages. In addition, modifying the surface with antibodies, peptides, and aptamers allows for specific targeting towards cells and tissues. For example, antibody-conjugated nanoparticles offer increased tumor accumulation by combining the advantages conferred by nanoparticles with their increased ability to penetrate tumors and with the ability to recognize specific cells.

Of course, there are more factors to consider during nanoparticle design, such as deformability and ease of production. Further understanding of biological processes governing the uptake, transportation, distribution, and excretion of nanoparticles will enable the innovations on developing new materials and formulation strategies to achieve enhanced drug delivery.

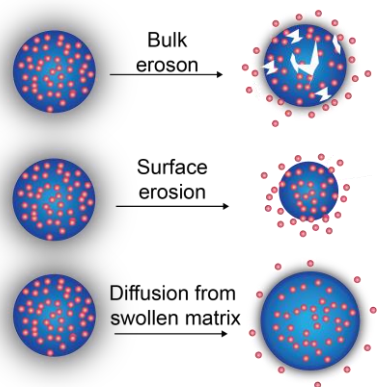


Figure 1. 6 Nanoparticles formed by biodegradable polymers have three drug releasing mechanisms

(1) bulk erosion by breaking down the whole matrix, (2) surface erosion by degrading or dissociation of polymers, (3) diffusion from swollen matrix

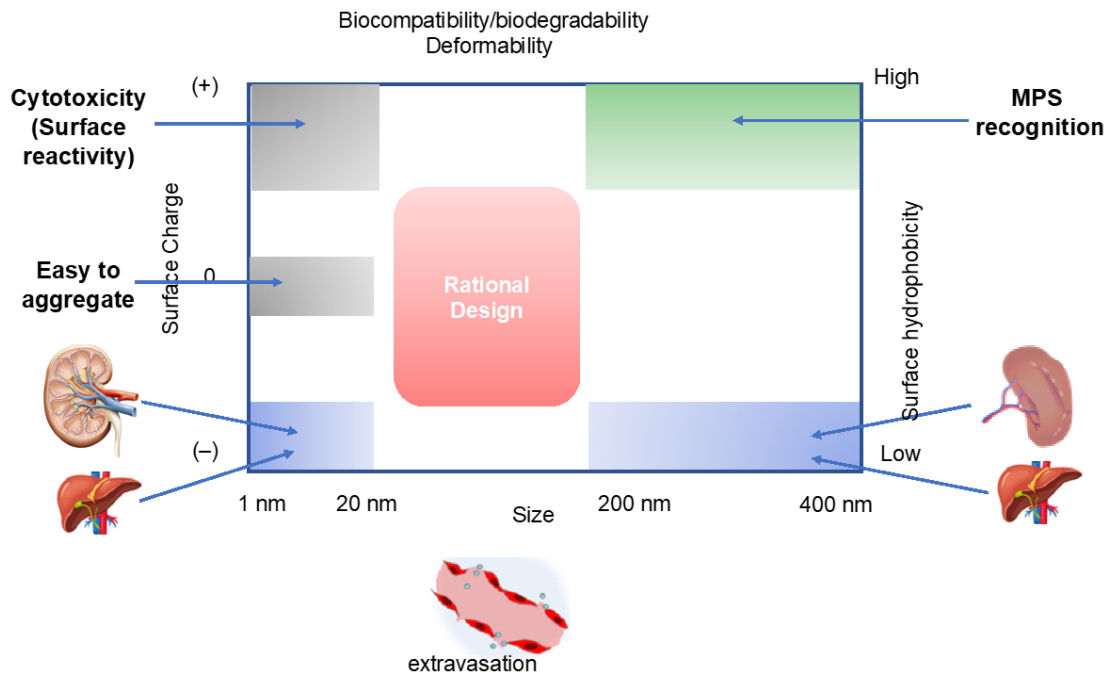


Figure 1. 7 Schematic overview of nanoparticle design used in drug delivery.

Nanoparticles used in drug delivery need to have size smaller than 200 nm but larger than 20 nm to enable extravasation and avoid quick clearance by kidney, spleen, and liver. The surface charge of nanoparticles need to be slightly positive or negative to avoid aggregation and cytotoxicity. The surface of nanoparticles should be hydrophilic to prevent mononuclear phagocytic system (MPS) recognition and clearance. Besides, the material used in nanoparticle formulation should be biocompatible and biodegradable to decrease the toxicity and possible immune responses and have some degree of deformability to enable nanoparticles' penetration to tumor tissue.

1.6 Overview of dissertation

The work described in this thesis employed computer based small molecule design in the target validation of KRAS, nanoparticle technology in the investigation of ferroptosis therapeutic potential *in vivo*, and untargeted lipidomics study in the characterization of lipid metabolism in ferroptosis. In the second chapter, I describe my work in design of small molecule that compete with nucleotide binding to an engineered oncogenic KRAS allele¹⁰¹. Using fragment based small molecule design, I successfully designed and synthesized a covalent inhibitor which can permanently modify the engineered KRAS and inhibit its downstream signaling in cells. In the third chapter, I investigated *in vitro* and *in vivo* pharmacodynamics of IKE, a metabolically stable, highly potent and selective system x_c^- inhibitor, using quantitative-RT-PCR, immunofluorescence, and metabolites measurement. Besides, I identified the differential sensitivities of a set of DLBCL cell lines to IKE and established a xenograft tumor model using a sensitive cell line, SUDHL-6. In the fourth chapter, I applied the principles of nanoparticle carrier design in the formulation of a biocompatible and biodegradable nanoparticle to deliver IKE *in vivo* and demonstrated the reduced toxicity with nanoparticle IKE formulation *in vivo*. In the fifth chapter, I analyzed the distinct lipids change of IKE-induced ferroptosis *in vitro* and *in vivo* with the help of my colleague on mass-spectrometry based lipidomics study. In addition, I identified the key enzymes participating in IKE-induced lipid metabolism change. In the final chapter, I consider the perspectives and future research directions suggested by the research described in the preceding chapters.

Chapter 2: Design of Small Molecules that Compete with Nucleotide Binding to an Engineered Oncogenic KRAS Allele¹

2.1 Introduction

RAS mutations are found in 30% of all human cancers, with *KRAS* the most frequently mutated among the three *RAS* isoforms (*KRAS*, *NRAS*, *HRAS*). However, directly targeting oncogenic *KRAS* with small molecules in the nucleotide-binding site has been difficult due to the high affinity of *KRAS* for GDP and GTP. We designed an engineered allele of *KRAS*, and a covalent inhibitor that competes for GTP and GDP. This ligand-receptor combination demonstrates that the high affinity of GTP/GDP for *RAS* protein can be overcome with a covalent inhibitor and a suitably engineered binding site. The covalent inhibitor irreversibly modifies the protein at the engineered nucleotide binding site and is able to compete with GDP and GTP. This provides a new tool for studying *KRAS* function and suggests strategies for targeting the nucleotide-binding site of oncogenic *RAS* proteins.

Generating engineered, inhibitable alleles of proteins to validate targets has proved successful for kinases and other proteins¹⁰²⁻¹¹¹. The essence of this strategy resides in the design of engineered alleles of the protein of interest that are sensitized to small-molecule inhibition, while being functionally indistinguishable from wild-type counterparts (Fig. 1A). Treatment with a complementary small-molecule probe can then provide selective, rapid, and dose-dependent inactivation of the protein of interest. More recently, Shah and co-workers reported a strategy for the selective inhibition and activation of an engineered H-Ras mutant by unnatural GDP and GTP analogues¹¹². However, future applications of that study were limited by using GDP analogues as molecular probes, which are inherently non-cell-permeable and not selective. Moreover, that study did not address the feasibility of designing drug-like small molecule that target engineered small GTPases.

¹This chapter is adapted from the manuscript: Zhang, Y.; Larraufie, M.-H.; Musavi, L.; Akkiraju, H.; Brown, L. M.; Stockwell, B. R., Design of small molecules that compete with nucleotide binding to an engineered oncogenic *KRAS* allele. *Biochemistry* **2018**, *57* (8), 1380-1389.

We aimed to address this issue by testing whether we could design a cell-permeable small molecule probe that would allow us to test the effects of pharmacological inhibition of suitably engineered small GTPases (**Figure 2.1**). We focused on the design of small molecules capable of inhibiting an engineered mutant allele of oncogenic KRAS (termed KRAS*). We were concerned that mutation of key conserved residues in KRAS might alter its natural nucleotide selectivity and important protein-protein interactions, making the mutant activated in a GEF-independent way and lose the switch function¹¹²⁻¹¹⁴, as first suggested for RAS (N116I)¹¹⁵. Shah and co-workers have reported, however, that H-RAS (L19A, N116A) mutations remain fully functional as the wild-type enzyme¹¹². We also demonstrated that the engineered inhibitable KRAS* allele we designed could bind to BRAF effector only after loading with GTP but not GDP. We report herein the computational design of a mutant engineered oncogenic allele of KRAS bearing an enlarged nucleotide binding site and a cysteine residue that can serve as a site for covalent targeting. We found that this mutant KRAS* was functionally indistinguishable from KRAS^{G12V} but could be selectively inhibited by a computationally designed covalent inhibitor.

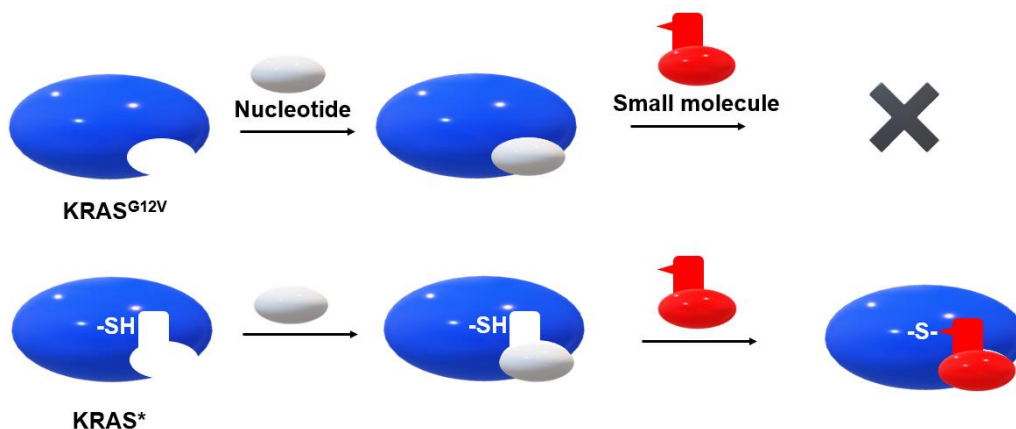


Figure 2. 1 Schematic overview of protein engineering strategies to validate KRAS.

The engineered KRAS* harbors an enlarged pocket and a cysteine residue, which enables selective targeting by a covalent small molecule. The KRAS* should be capable of binding with nucleotides and functional in cells to stimulate RAS downstream pathways. The covalent small molecule is expected to covalently lock the KRAS* in inactive state to disable KRAS* function but not interact with KRAS^{G12V} and other GTPases in cells.

2.2 Results

2.2.1 Design of KRAS allele

Small GTPases in the RAS family have a conserved binding site and share similar nucleotide-binding pockets¹¹⁶. Shah and co-workers demonstrated that mutation of L19 and N116, located on the backside of the HRAS GTP-binding site, to smaller alanine residues allowed access to a buried hydrophobic cavity. The crystal structure of KRAS^{G12V} in the GDP-bound conformation (4TQ9)¹¹⁷ was used as a template to model the influence of point mutations in the nucleotide-binding site. Prime and BioLuminate (Schrödinger) were used to calculate the change in structure and stability of the protein after introducing mutations (Table 2.1). N116 is necessary to be mutated to alanine to create a hydrophobic pocket around the nucleotide binding site. Besides, we would like to engineer a cysteine in the binding pocket to enable the covalent small molecule interaction. However, the single mutation of N116A combining with L19C is only able to generate a 4Å*3Å*4Å pocket, which is not big enough to facilitate the small molecule design. Thus, mutation of L19AN116AV114C or L19AN116AT144C would achieve the aim. Since V114 is in the middle of the cavity, which might be more versatile for binding with covalent inhibitors.

Residues 19 and 116 were mutated *in silico* and all residues within 10 Å of either mutation were minimized. A new hydrophobic cavity 3 Å wide and 10 Å long appeared in the nucleotide-binding site (**Figure 2.2**). We next wished to introduce a cysteine residue in the hydrophobic pocket that could then be used as a handle for covalent inhibition²⁵. Indeed, we envisioned that the use of covalent inhibitors might be key to be able to cope efficiently with the high cellular concentration of GTP (~1 mM)¹³. For that purpose, a cysteine residue (C114) that could be targeted by electrophilic moieties was installed in the backside of the engineered hydrophobic pocket. The stability of the engineered protein (KRAS*^{G12VL19AN116AV114C}, termed KRAS*) was predicted to have decreased energy of 52.96 kcal/mol.

Table 2. 1 Representation of different engineered alleles of KRAS and the evaluation of pocket sizes and stabilities

| | mutation | Pocket size (from MOE) | D stability (solvated) (kcal/mol) |
|----|-----------------|--|--|
| 1 | L19AN116A | 10Å*3Å*4Å | 37.92 |
| 2 | L19AN116C | No hydrophobic pocket around guanine nucleotide-binding site | 33.35 |
| 3 | L19AV114C | No hydrophobic pocket around guanine nucleotide-binding site | 38.94 |
| 4 | N116AL19C | 4Å*3Å*4Å | 36.39 |
| 5 | N116AV114C | Cys114 is not near to the pocket | 31.55 |
| 6 | N116AL23C | Cys23 is not near to the pocket | 29.14 |
| 7 | N116AL79C | Cys79 is not near to the pocket | 37.94 |
| 8 | N116AF156C | Cys156 is not near to the pocket | 38.27 |
| 9 | N116AV152C | Cys152 is not near to the pocket | 27.43 |
| 10 | N116AT144C | 4Å*3Å*3Å | 25.41 |
| 11 | L19AN16AV114C | 10Å*3Å*4Å | 52.96 |
| 12 | L19AN16AT144C | 10Å*3Å*4Å | 44.60 |
| 13 | L19AN16AL23C | Cys23 is not near to the pocket | 51.65 |
| 14 | L19AN16AL79C | 14Å*3Å*4Å | 59.89 |
| 15 | L19AN16AF156C | 11Å*3Å*4Å | 59.52 |
| 16 | L19AN116AV152C | 10Å*3Å*4Å | 48.04 |

D stability (solvated): Change in the stability of the protein due to the mutation, calculated using the Prime energy function with an implicit solvent term. The stability is defined as the difference in free energy between the folded state and the unfolded state. A positive value of the change means that the mutant is less stable than the original protein.

The predicted structure of the engineered protein showed that C114 was orientated to perform a nucleophilic attack on electrophilic moieties in the pocket (Figure 2.2). Importantly, the three mutated residues in KRAS* are in a conserved site among the GTPases, so they could potentially be translated to other members of the family (Figure 2.3).

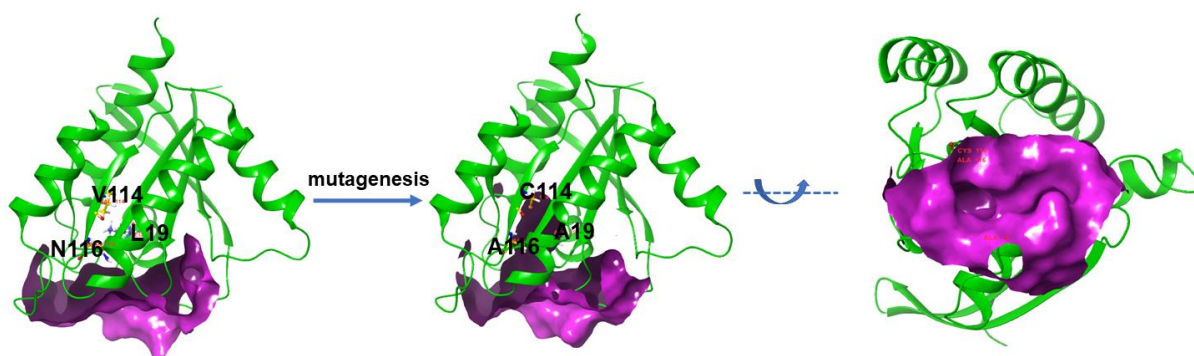


Figure 2. 2 Representation of KRAS G12V (PDB code: 4TQ9) and engineered KRAS* structures

(structure was minimized using Schrödinger Prime). Mutagenesis of L19AN116AV114C in KRAS G12V (KRAS^{G12V L19AN116AV114C}, termed KRAS*) created a hydrophobic pocket in the GDP/GTP binding site.

| | | <u>G1</u> | | <u>G4</u> |
|-------|----|---|-----|--|
| KRAS | 4 | YKL V VV G AVGV G K S AL T IQLI | 110 | PMVL V GN K CDLPSRTV |
| Arf1 | 18 | MRIL M V G LDGAG K TTVLYK L K | 120 | VLLVFAN K QDLPEAMS |
| Ran | 11 | FKLVL V GDGG T G K TTFVKRHL | 116 | PIVLCGN K VDIKDRKV |
| RhoA | 6 | KKLV I V G DGAC G K T CLLIVFS | 111 | PIIL V GN K KDLRND E H |
| RhoB | 6 | KKLV V V G DGAC G K T CLLIVFS | 111 | PIIL V AN K KDLRSDEH |
| Rab1A | 12 | FKLLL I GD S GV G K S CLLLRFA | 118 | NKLL V GN K CDLTT K V |
| Rheb | 7 | RKIA I L G YRS V G K SS L TIQFV | 113 | PIML V GN K KDLHM E RV |
| RalA | 15 | HKVIM V SGGG V G K SAL T LQFM | 121 | PFL L VGN K SDLE D KRQ |
| RalB | 15 | HKVIM V SGGG V G K SAL T LQFM | 122 | PLL V VGN K SDLE E RRQ |
| M-Ras | 14 | YKL V VV G DGG V G K SAL T IQFF | 120 | PMIL V AN K V D LMHL R K |
| Rit1 | 22 | YKL V ML G AG G V G K S AM T MQFI | 128 | PVVL V GN K SD L KQ L RQ |
| R-Ras | 30 | HKLV V V G GGG V G K SAL T IQFI | 136 | PVVL V GN K AD L ES Q RQ |
| Rap1A | 4 | YKL V VL G SGGG V G K SAL T VQFV | 110 | PMIL V GN K CDLE D ERV |

Figure 2. 3 Sequence alignment of RAS and small GTPases superfamily

(conserved residues are in BOLD). Mutated residues in KRAS* are conserved in small GTPases.

2.2.2 Functional study of the engineered KRAS allele and biophysical assay design

To verify that the engineered mutant allele functions well as a “switch”, KRAS* was loaded with GDP or GTP and incubated with RAF1 RBD (RAS binding domain) protein attached to glutathione Sepharose beads. The unbound KRAS* was removed during the washing step, while the bound KRAS* was quantified by immunoblotting with anti-RAS antibody. As expected, RAF 1 RBD specifically bound to GTP-loaded KRAS* but not GDP-loaded KRAS* (Figure 2.4).

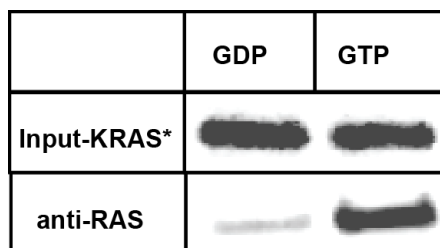


Figure 2. 4 A BRAF-RBD pull down assay proved that only GTP-bound but not GDP-bound KRAS* could bind with BRAF.

Purified GST-tag KRAS* was nuclear exchanged to GDP or GTP-bound form then incubate with BRAF-RBD followed by washing of non-specific binding and western blot for visualization of KRAS* abundance.

To prove that the KRAS* is not nucleotide-free analog of RAS as suggested for HRAS(N116I), we tested the binding of GDP and GTP by KRAS* and KRAS^{G12V} protein (Figure 2.5). Both KRAS* and KRAS^{G12V} were nucleotide exchanged to BODIPY-GTP, a fluorescent analog of GTP which have high polarization value when binds with protein and low polarization value in unbound form. BODIPY-GTP was displaced by GDP or GTP in both KRAS* and KRAS^{G12V}, indicating KRAS* retains nucleotide selectivity. Compared with KRAS^{G12V}, the faster nucleotide exchange rate of BODIPY-GTP to GTP or GDP might come from the low binding affinity between KRAS* and BODIPY-GTP.

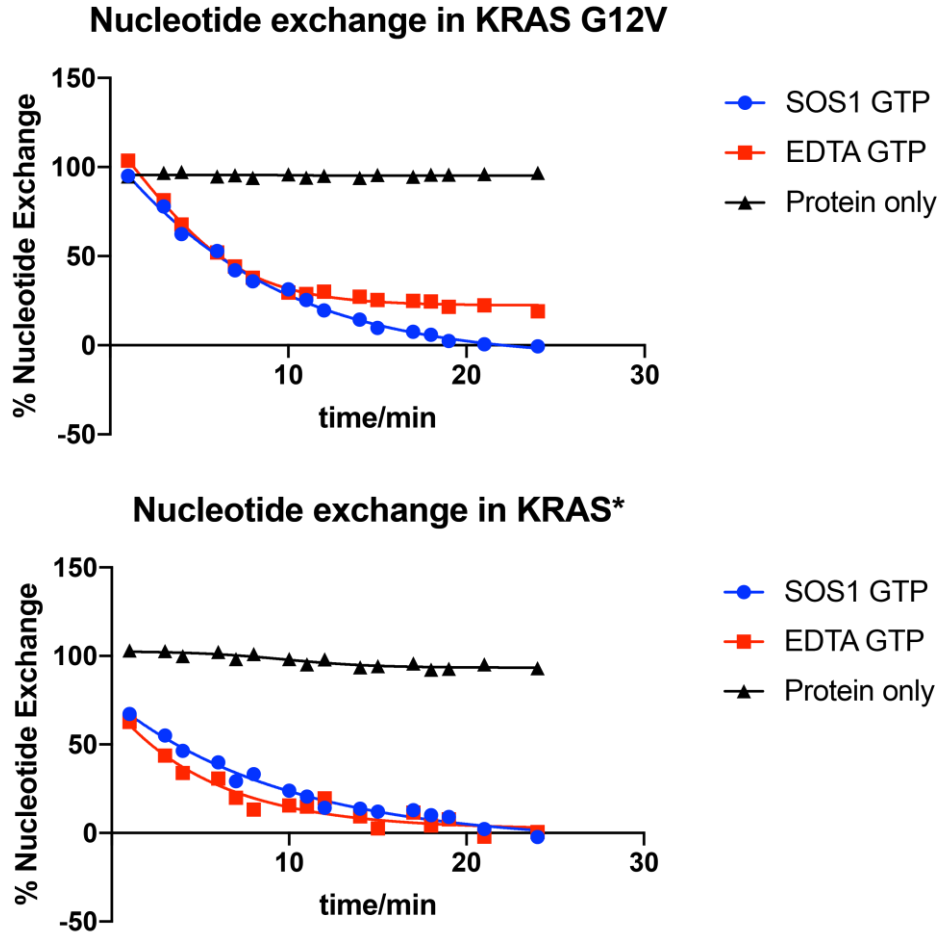


Figure 2. 5 Nucleotide exchange of GTP in KRAS protein

Nucleotide exchange of GTP in KRAS* is catalyzed by SOS1 and EDTA, same as what in KRAS G12V protein. The amount of exchanged GDP and GTP in KRAS^{G12V} is shown as function of time.

To further verify KRAS* function in cells, we used RAS-less MEFs. *K-Ras^{lox}(H-Ras^{-/-};N-Ras^{-/-};*K-Ras^{lox/lox};RETR^{ert/ert}*)* mouse embryonic fibroblasts (MEFs) were stably transfected with *KRAS** or *KRAS^{G12V}* alleles¹¹⁸. The MEFs were generated to carry null *HRAS* and *NRAS* alleles along with a floxed *KRAS* locus and a knocked-in inducible Cre recombinase. After transfection with *KRAS^{G12V}*, *KRAS**, or *BRAF^{V600E}-CAAX* individually, 4-hydroxytamoxifen was used to induce of Cre recombinase, resulting in the complete elimination of endogenous *KRAS* gene after two weeks (termed *KRAS** MEFs, *KRAS^{G12V}* MEFs, and *BRAF^{V600E}* MEFs) (Figure 2.6).

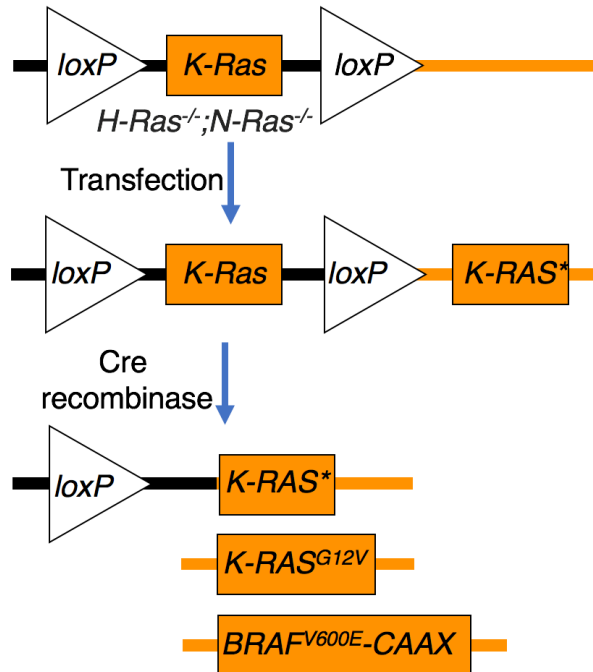


Figure 2. 6 Schematic of establishing a stable transfected engineered cell line

K-Ras^{lox}(H-Ras^{-/-};N-Ras^{-/-};K-Ras^{lox/lox};RERTn^{ert/ert}) mouse embryonic fibroblasts (MEFs) are transfected with *K-RAS**, *K-RAS^{G12V}*, *BRAF^{V600E-CAAX}* individually followed by activation of Cre recombinase by 4-hydroxy tamoxifen to knock out the endogenous *K-Ras*.

The ability of *KRAS** to activate RAF/MEK/ERK signaling was examined by measuring the abundance of phosphorylated ERK (pERK) and phosphorylated AKT (pAKT) in the transfected cell lines. Following EGF treatment, pERK and pAKT levels were increased in the transfected cell lines (Figure 2.7), demonstrating that the engineered mutations did not prevent *KRAS** from activating effector proteins. The EGF-dependent signal in *KRAS** MEFs also revealed that its binding to GTP was not GEF-independent as suggested for RAS (D119N)¹¹⁴.

KRAS mRNA levels were measured in the transfected cell lines by qPCR. We found that the *KRAS** mRNA was more abundant than the *KRAS^{G12V}* mRNA (Figure 2.8). Compared with the similar protein level of *KRAS* in *KRAS** MEFs and *KRAS^{G12V}* MEFs (Figure 2.7), that indicates *KRAS** may be less stable in cells, providing an advantage for rapidly inducing and removing this engineered protein from cells.

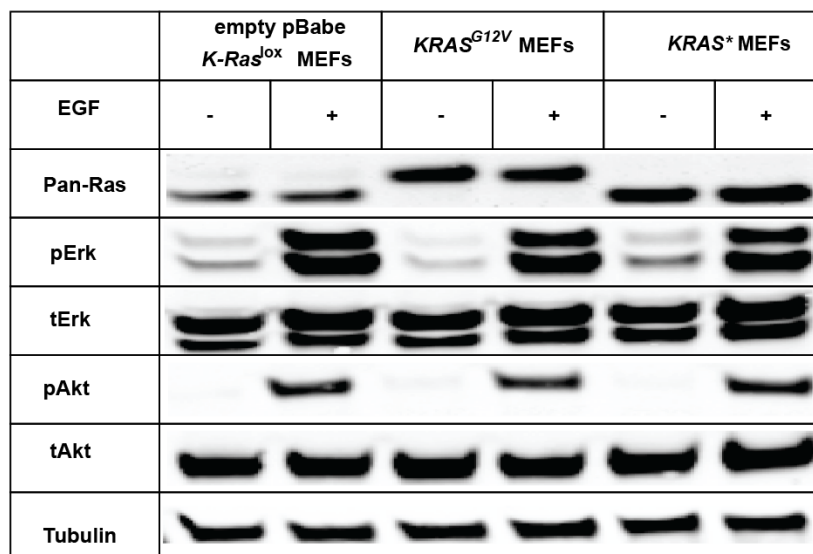


Figure 2. 7 Western blot indicated the overexpression of RAS in *KRAS*^{G12V} MEFs and *KRAS** MEFs.

“empty pBabe *K-Ras*^{lox} MEFs” represents the *K-Ras*^{lox} (*H-Ras*^{-/-}; *N-Ras*^{-/-}; *K-Ras*^{lox/lox}; *RERTn*^{ert/ert}) MEFs transferred with empty pBabe vector as a control. The RAS downstream signaling was activated upon EGF treatment in *K-Ras*^{lox} MEFs, *KRAS** MEFs, and *KRAS*^{G12V} MEFs.

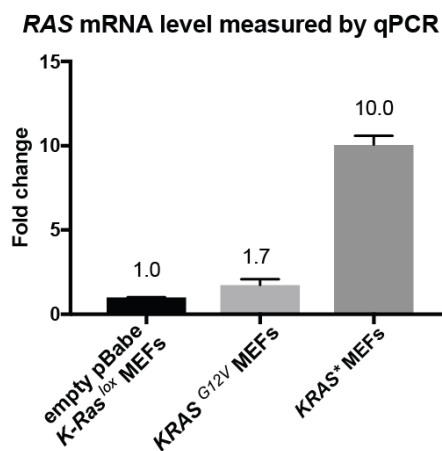


Figure 2. 8 *RAS* mRNA level measurement by RT-qPCR

RT-qPCR showed *KRAS* expression is 1.7-fold in *KRAS*^{G12V} MEFs, and 10-fold in *KRAS** MEFs comparing with empty pBabe *K-Ras*^{lox} MEFs.

To test the binding affinity of fragments and lead compounds, we developed an *in vitro* fluorescence polarization assay to test the ability of small molecules to displace BODIPY-GTP, a

fluorescent analog of GTP. In this assay, test compounds that were able to competitively replace BODIPY-GTP bound to KRAS* resulted in a decrease in the polarization of BODIPY-GTP (**Figure 2.9**).

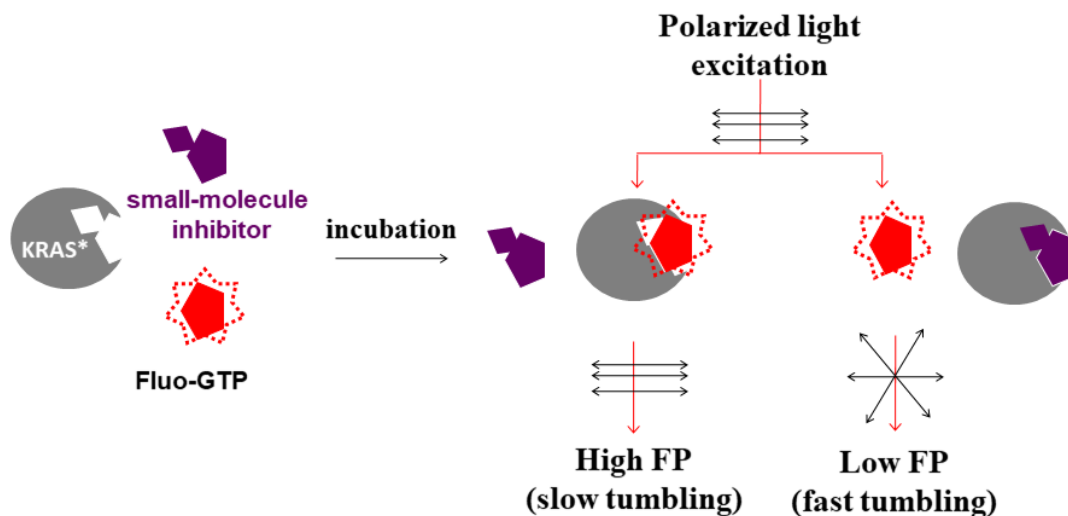


Figure 2. 9 Schematic principle of fluorescence polarization assay.

The binding of Fluo-GTP (BODIPY-GTP is used in this assay) to GTP-binding site yields a high fluorescence polarization (FP) value. With the displacement of small molecule inhibitors, Fluo-GTP is free in solution, thus having a fast tumbling and yielding a low FP value.

2.2.3 *in silico* design of inhibitors

A GDP-bound KRAS^{G12V} crystal structure (PDB: 4TQ9) was used to design compounds that covalently lock KRAS* in the GDP-bound state, inactivating its signaling function. KRAS^{G12V} was mutated *in silico* to KRAS*, and the engineered structure was refined by Schrödinger Protein Preparation Wizard for docking studies. A fragment-based design strategy was applied in the search for a covalent inhibitor¹¹⁹ and two series of covalent inhibitors were designed and synthesized. 177,911 fragments were screened using the Schrödinger Glide program and the top-ranked fragments were used as scaffolds for further design. The first series of inhibitors harbor a carboxylic acid group, which is predicted to interact with the magnesium ion and multiple residues in the GTP-binding pocket, thus giving a high predicted

binding affinity (as good as -12 for Glidescore). These inhibitors had high predicted binding affinity to the KRAS* protein, but low cellular activity, making it difficult to study the KRAS therapeutic index in cells. Esterification one carboxylic acid groups improved the compounds' cell-membrane-permeable but didn't increase the cellular activity. The low cellular activity might thus derive from their inability to block KRAS-effector interactions in cells.

We then found that the conserved aspartate residue D119 is a key residue determining the specificity for GTP over other nucleotides through hydrogen bonding. We reasoned that the discovery of a compound that can form hydrogen bonds with D119 is thus important for a successful design. H-bond constraints to D119 were applied in fragment screens for a second inhibitor design series. Top-ranked fragments without carboxylic acid groups were tested in a fluorescence polarization assay to measure binding affinity to KRAS*. We found that an indazole fragment G, with a docking score of -7.1, could compete with GTP binding for KRAS *in vitro* in the 100 micromolar range (**Figure 2.10**), and was chosen as a scaffold for further design.

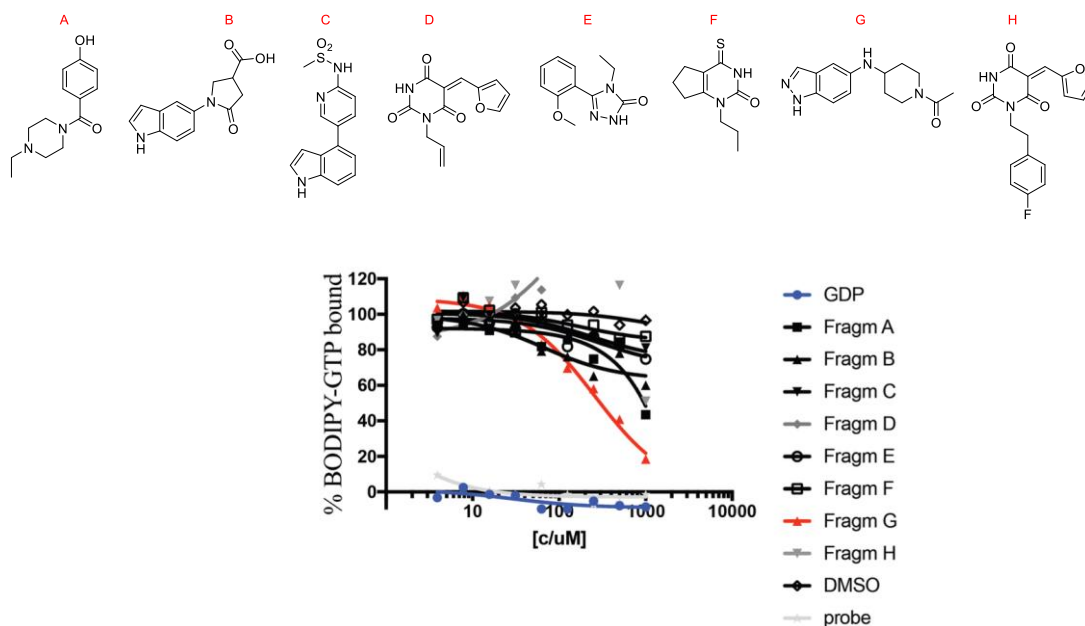
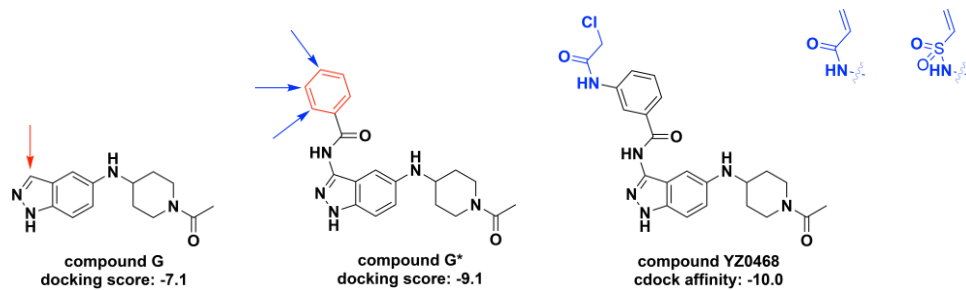


Figure 2. 10 Screen of fragments in biophysical assay.

8 fragments which have high predicted binding affinity for the GTP-binding site were tested in fluorescence-polarization (FP) assay. Fragment G showed highest binding affinity to GTP-binding site of KRAS^{G12V}.

As a next step, the hydrophobic pocket of the engineered allele was targeted by attaching a lipophilic group (**Figure 2.11**) to the appropriate site on fragment **G**. This produced compound **G***, which had a more favorable docking score of -9.1, compared to -7.1 for compound **G** (note that the Glide docking score is a log scale, so this predicted a 100-fold improvement in affinity). Based on the structure of compound **G**, a number of covalent inhibitors with electrophile warheads at different positions were designed and evaluated using Schrödinger's Covalent Docking program¹²⁰. This showed that having a 2-chloroacetamide electrophile at the *meta*-position (compound **YZ0468**) had the best-predicted affinity score *in silico* (docking structure showed in **Figure 2.11**).

A



B

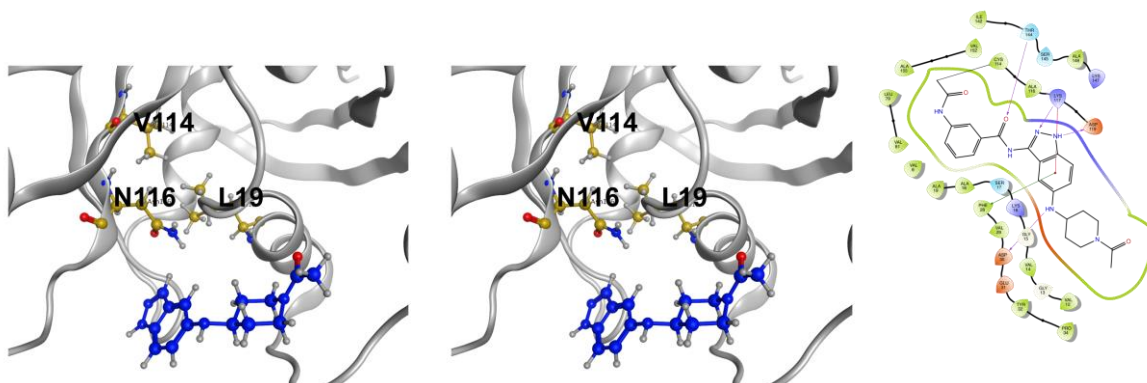


Figure 2. 11 Fragment-based small molecule design targeting KRAS* nucleotide binding site

Design of a second series of small molecule and representation of the proposed binding mode of compound **YZ0468** in KRAS*. Covalent docking of compound **YZ0468** in KRAS* showed favorable formation of covalent bond between C114 and the chloroacetyl moiety. The ligand interaction diagram showed possible non-covalent interactions between ligand and KRAS* (Purple: H-bond interaction, Red: Pi-Cation interaction, Green: Pi-Pi interaction). *N-1* is predicted to form H-bond with D119.

On the basis of this indazole scaffold, a customized compound library employing amide coupling, reductive aminations, and cross coupling reactions was created (**Figure. 2.12**) and evaluated using Schrödinger's Glide docking and Covalent Docking program. The top-scoring compounds were synthesized and tested in the fluorescence polarization assay to further assess inhibition activity.

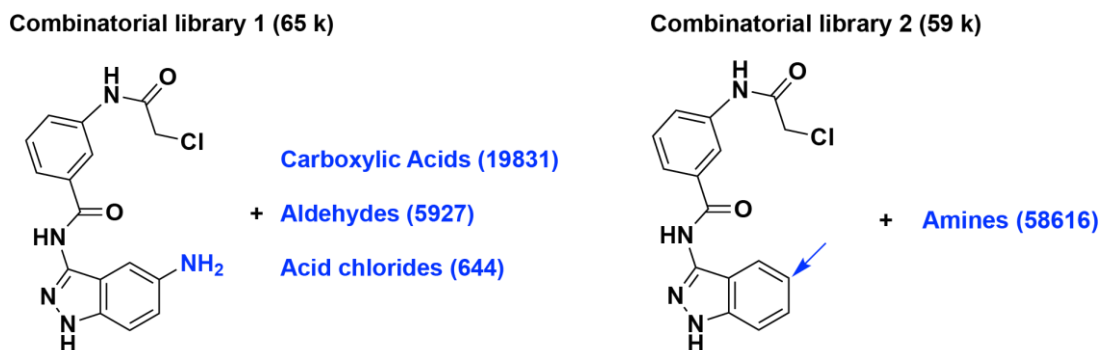


Figure 2. 12 Combinatorial library design

(created by MOE) (libraries of carboxylic acids, aldehydes, acid chlorides, and amines are collected from Sigma-Aldrich).

The combinatorial library (**Figure 2.12**) was screened using Glide Docking by removing the covalent warheads first followed by Covalent Docking of the top scoring compounds in the Glide Docking. To discover cell membrane permeable probes, the predicted Caco-2 cell permeability of top scoring compounds were calculated by Qikprop (**Schrödinger Release 2018-3**: QikProp, Schrödinger, LLC, New York, NY, 2018). The compounds with predicted-Caco-2 cells permeability larger than 25 nm/sec were synthesized (Caco-2 cells are a model for the gut-blood barrier. Predicted cell permeability value smaller than 25 nm/sec is considered as poor. Predicted cell permeability value larger than 500 nm/sec is considered as great). A compound with 3,4-(methylenedioxy)phenyl group (later named YZ0711) has the highest predicted Caco-2 permeability, 294 nm/sec, among all screened compounds. The predicted binding showed a favorable binding of Serine 17 residue with 3,4-(methylenedioxy)phenyl group (**Figure 2.13**).

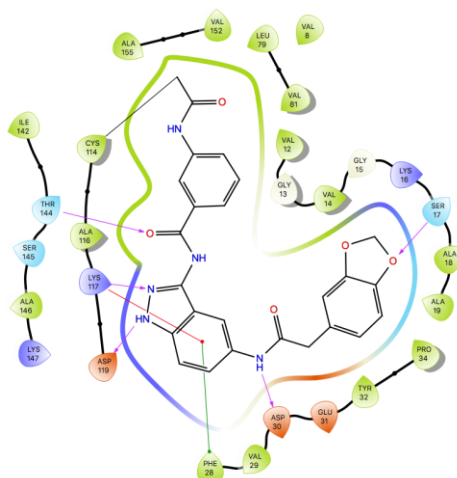
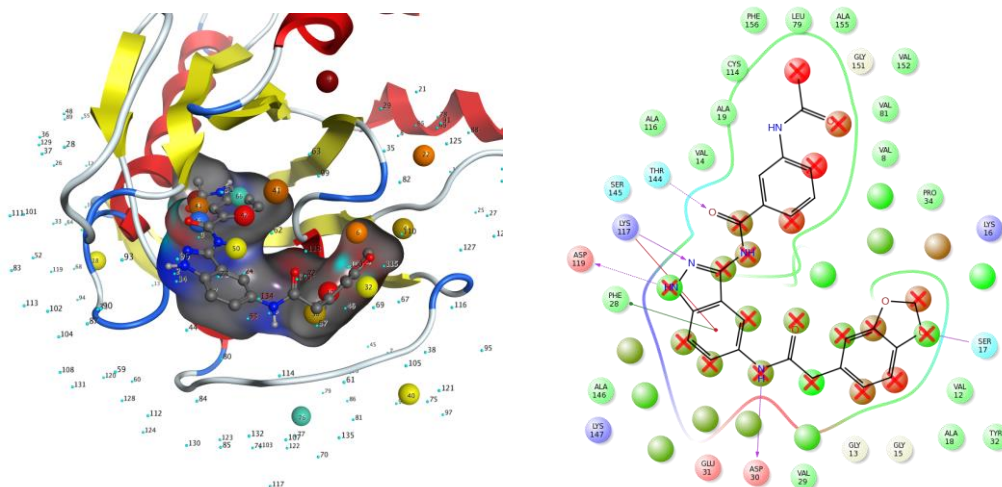


Figure 2. 13 YZ0711 ligand interaction diagram.

The ligand interaction diagram showed possible non-covalent interactions between ligand YZ0711 and KRAS* (Purple: H-bond interaction, Red: Pi-Cation interaction, Green: Pi-Pi interaction). *N-1* on indazole ring is predicted to form H-bond with D119.

WaterMap (**Schrödinger Release 2018-3**: WaterMap, Schrödinger, LLC, New York, NY, 2018), which calculates thermodynamics associated with water hydration sites in protein active sites¹²¹⁻¹²², was used here to check whether there is room to further optimize the compound. WaterMap showed that compound YZ0711 displaced nearly all high-energy hydration sites in the nucleotide binding site of KRAS* (**Figure 2.14**). This result indicated possible favorable binding between compound YZ0711 and KRAS* protein.

A



B

| Site | Occupancy | dH | -TdS | dG | Site | Occupancy | dH | -TdS | dG |
|------|-----------|------|------|------|------|-----------|-------|------|------|
| 34 | 0.74 | 6.45 | 2.36 | 8.81 | 30 | 0.78 | 1.33 | 2.44 | 3.77 |
| 66 | 0.48 | 5.62 | 1.46 | 7.08 | 4 | 1 | -1.06 | 4.82 | 3.76 |
| 3 | 1 | 1.42 | 5.33 | 6.75 | 18 | 0.86 | -0.08 | 3.51 | 3.43 |
| 10 | 0.96 | 2.09 | 3.72 | 5.81 | 32 | 0.74 | 0.96 | 2.47 | 3.43 |
| 42 | 0.64 | 3.24 | 2.05 | 5.29 | 76 | 0.44 | 1.93 | 1.22 | 3.15 |
| 41 | 0.66 | 2.41 | 2.29 | 4.7 | 50 | 0.6 | 1.23 | 1.86 | 3.09 |
| 43 | 0.64 | 2.48 | 2.15 | 4.63 | 40 | 0.67 | 1.05 | 2.01 | 3.06 |
| 6 | 0.99 | 0.36 | 4.08 | 4.44 | 99 | 0.34 | 1.97 | 1.02 | 2.99 |
| 22 | 0.82 | 1.44 | 2.7 | 4.14 | 19 | 0.85 | 0.17 | 2.71 | 2.88 |

Figure 2. 14 Watermap performed on YZ0711 bound KRAS*

WaterMap shows the thermodynamic-properties properties including enthalpy, entropy, and free energy of water occupying hydration sites of protein active site. (A) The interaction of compound YZ0711 with KRAS* protein and the overlay of compound YZ0711 with hydration sites showed favorable binding between the ligand and the protein. Hydrogen bond interaction is shown in purple. A cation- π interaction is shown in red. Stable hydration sites ($\Delta G < 3$ kcal/mol) are shown in green, significantly unstable hydration sites ($\Delta G > 5$ kcal/mol) are shown in red, and moderately unstable sites (3 kcal/mol $< \Delta G < 5$ kcal/mol) are shown in brown. (B) The thermodynamics of high-energy hydration sites in KRAS* is shown in table.

2.2.4 Synthesis of ligand library

A set of promising covalent small molecule inhibitors was thus synthesized (Methods). As an example, the synthetic route developed for compound **YZ0711** is illustrated in **Figure 2.15**. The indazole scaffold was synthesized by heating 2-fluoro-5-nitrobenzotrile and hydrazine monohydrate in refluxing ethanol followed by the selective BOC-protection of the *N*-1 position of the indazole and subsequent palladium-catalyzed hydrogenation¹²³. The resulting diaminoindazole could be acylated selectively at the *C*-5 amine using an acid chloride. In the next step, the *C*-3 amine was acylated in pyridine to yield compound **4**. Catalytic hydrogenation of the nitro group in compound **4** followed by acylation of the resulting aniline with chloroacetyl chloride and selective deprotection of the BOC-group provided the desired product.

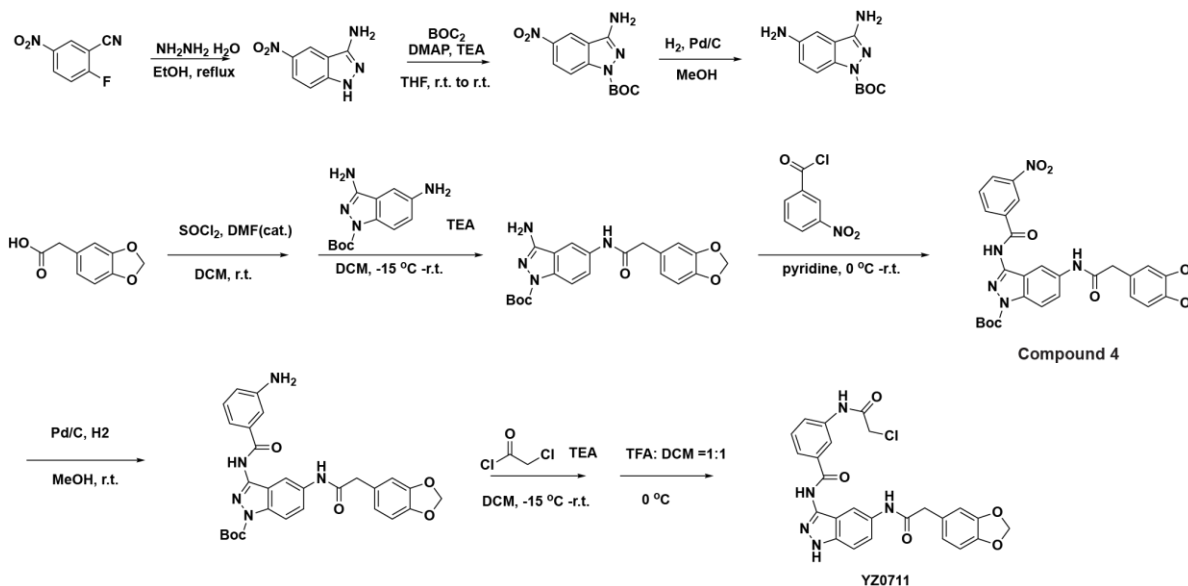


Figure 2. 15 Synthesis route of compound YZ0711

2.2.5 Evaluation of small molecule activities in biophysical assays

The designed covalent inhibitors and non-covalent inhibitors were able to compete with fluorescent GTP binding for the engineered mutant, but not for KRAS^{G12V} (Figure 2.16, 2.17), thus satisfying the selectivity criterion. Compared with compounds bearing acrylamide and vinyl sulfonate warheads, compounds bearing a chloroacetamide warhead had a better ability to bind to KRAS* (Figure 2.16). This might result from the relatively small pocket in KRAS*. Indeed, an extra chloro group on the benzyl moiety of YZ0571-1 decreased potency, consistent with a small available space in the binding site. In addition, a non-covalent analog (YZ0571-4) was not able to displace BODIPY-GTP. Based on this result, a series of covalent inhibitors incorporating chloroacetyl warheads were synthesized.

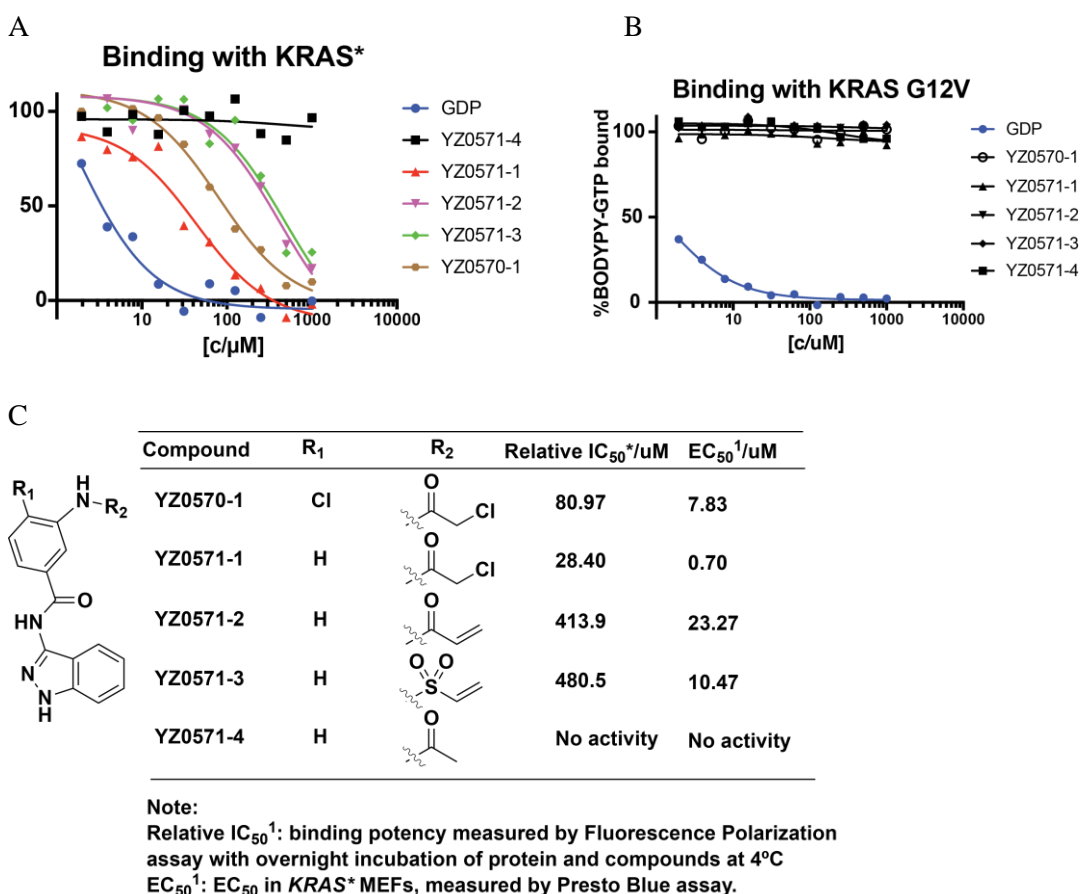


Figure 2. 16 The structure and activity relationship of selected covalent inhibitors.

Covalent inhibitor s selectively occupies GTP binding pocket of KRAS*, but not KRAS^{G12V} protein. Compound YZ0571-1, bearing a 2-chloroacetyl chloride moiety, has optimal activity in the fluorescence polarization assay and cell viability assays.

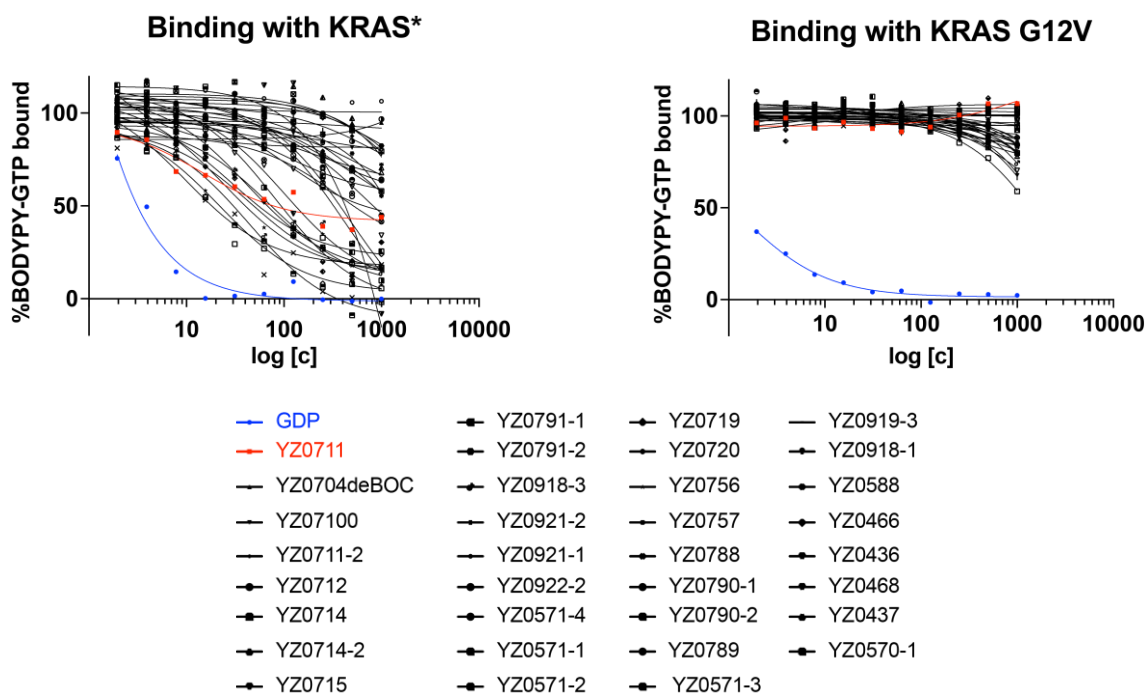


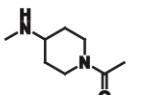
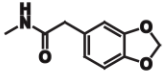
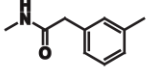
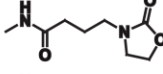
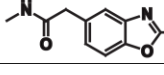
Figure 2. 17 Binding affinity test of covalent inhibitors in fluorescence polarization assay

Comparison of binding affinities of selected compounds for KRAS^{G12V} (left) and KRAS* (right) by fluorescence polarization assay. Covalent inhibitors selectively displace GDP from KRAS* protein, but not KRAS^{G12V} protein.

Compound YZ0714 and YZ0719 had comparable binding affinity to YZ0571-1 (**Figure 2.18**). Compound YZ0719 has low activity in a cell viability assay, which might result from its low cell membrane permeability. Compound YZ0711 had the best selectivity at inhibiting KRAS signaling among these electrophiles (data not shown) and was selected for further analysis.

In addition, inhibitor binding was catalyzed by ethylenediaminetetraacetic acid (EDTA) but not SOS1, a guanine nucleotide exchange factor that promotes guanine nucleotide exchange (**Figure 2.19**). EDTA can chelate the magnesium iron to facilitate nucleotide exchange in RAS.

A

| Compound | R | Relative IC ₅₀ ¹ /uM | EC ₅₀ ¹ /uM |
|----------|---|--|-----------------------------------|
| YZ0468 |  | 72.67 | 71 |
| YZ0711 |  | 52.07 | 39.85 |
| YZ0714 |  | 15.63 | 15.43 |
| YZ0719 |  | 24.87 | No activity |
| YZ0756 |  | 44.59 | 200 |

B

| | YZ0711 | YZ0712 | YZ0719 | YZ0756 |
|--|------------|------------|------------|------------|
| Cellular accumulation fold¹: | 1.4 | 0.4 | 0.1 | 1.2 |
| Predicted Caco-2 cell Permeability (nm/sec)² | 294 | 53 | 87 | 192 |

Figure 2. 18 Analysis of compounds' cellular activities and cell membrane permeabilities

(A) Summary of binding affinity and cellular activity of selected covalent inhibitors.

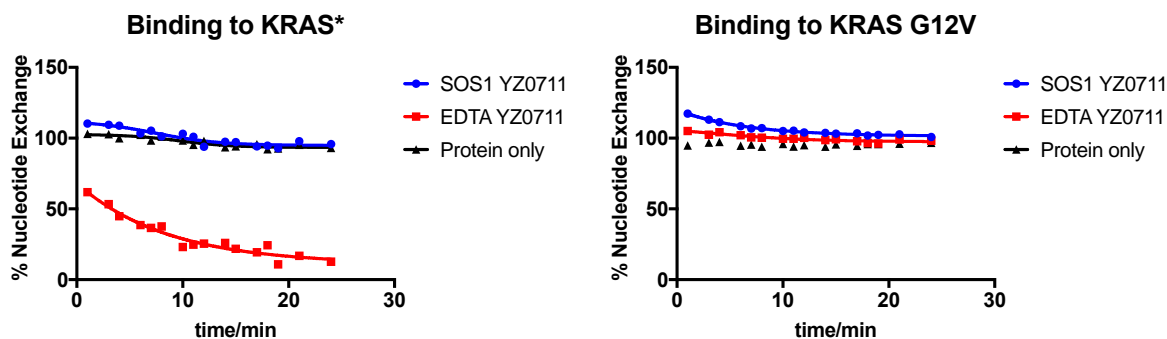
¹ Relative IC₅₀ is measured by fluorescence polarization assay through incubating the compounds with KRAS* protein overnight at 4 °C. ² EC₅₀ is measured by in KRAS* MEFs.(B) Summary of cellular accumulation and predicted Caco-2 cell. ¹ Accumulation fold was measured by treating KRAS* MEFs with 20uM compound for 4hs followed by LC-MS measurement. ² Predicted by Schrödinger Qikprop. Caco-2 cells are a model for the gut-blood barrier. Predicted permeability < 25 is considered as poor; > 500 is considered as great

Figure 2. 19 Exchange rate of BODIPY-GTP by small molecule YZ0711 in KRAS

Comparison of replacement of BODIPY-GTP by YZ0711 in KRAS* (left) and KRAS^{G12V} (right) as a function of time. EDTA catalyzed the replacement of BODIPY-GTP by YZ0711 in KRAS* but not in KRAS^{G12V}.

2.2.6 Evaluation of covalent binding of small molecules to KRAS*

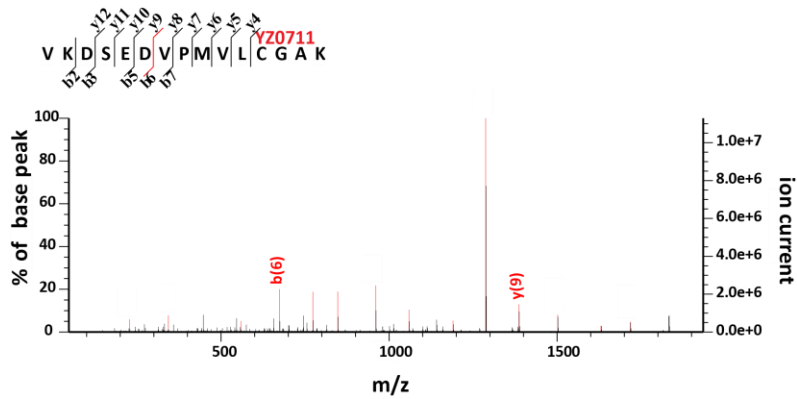
To determine whether compound YZ0711 could covalently bind to KRAS*, purified KRAS (20 μM) was incubated with 200 μM YZ0711 and 1 mM EDTA overnight at 4°C. The protein was then labeled with iodoacetamide and digested with trypsin. The resulting peptides were analyzed by nano LC/MS. LC/MS analysis revealed a modification of peptide (103-117) with YZ0711 at cysteine (C114) or lysine (K117) residues (**Figure 2.20**). A peptide (103-117) lacking cysteine but containing lysine in KRAS^{G12V} was not modified with YZ0711, indicating that YZ0711 modification was exclusive to C114 in KRAS*.

Besides, a pull-down assay was performed to prove whether the small molecule YZ0711 could covalently modify KRAS* in cells. Desthiobiotin-GTP, which can covalently modify conserved lysine residues in the nucleotide-binding site, was used to pull down KRAS in cell lysates. KRAS* MEFs treated with 50 μM YZ0711 have a decreased level of KRAS enrichment (**Figure 2.21**), suggesting that YZ0711 is able to penetrate the cell membrane and target the GTP/GDP-binding site.

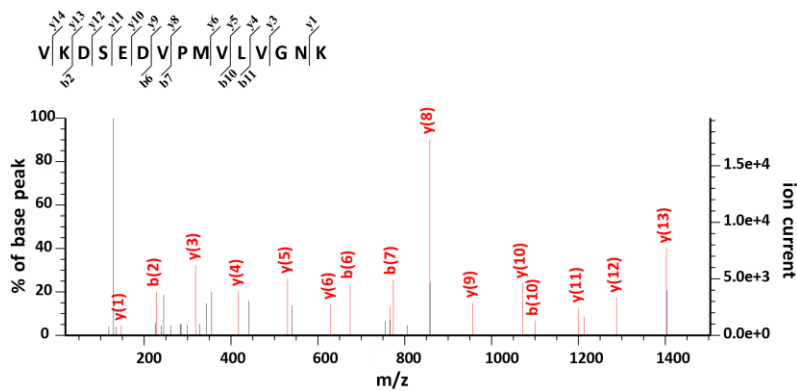
2.2.7 Inhibition effect of the compound on signaling pathway

In a cell growth inhibition assay, KRAS* MEFs and KRAS^{G12V} MEFs were treated with DMSO, 25 μM YZ0711, or 25 μM YZ0756 (a structurally similar compound as YZ0711) for 4 days and cell numbers were counted on a Vi-Cell XR Cell Viability Analyzer. Compound YZ0711 showed 80% inhibition of KRAS* MEF number and 50% inhibition to KRAS^{G12V} MEFs, indicating that YZ0711 exhibits some selectivity for KRAS* (**Figure 2.22**). Analog YZ0756 exhibited 25% inhibition in KRAS* MEFs and 15% inhibition to KRAS^{G12V} MEFs.

A



B



C

| | | |
|-----------|-----|--|
| KRAS G12V | 1 | MTEYKLVVVGAVGVGKSALTIQLIQNHFVDYDPTIEDSYRKQVVIDGETCLLDILD |
| KRAS* | 1 | MTEYKLVVVGAVGVGKSAATIQLIQNHFVDYDPTIEDSYRKQVVIDGETCLLDILD |
| KRAS G12V | 58 | TAGQEEYSAMRDQYMRTGEGFLCVINNTKSFEDIHHYREQIKRVKDSIEDVPMVL |
| KRAS* | 58 | TAGQEEYSAMRDQYMRTGEGFLCVINNTKSFEDIHHYREQIKRVKDSIEDVPMVL |
| KRAS G12V | 114 | VGNKCDLPSRTVDTKQAQDLARSYGIPFIETSAKTRQGVDDAFYTLVREIRKHKEK |
| KRAS* | 114 | CGAKCDLPSRTVDTKQAQDLARSYGIPFIETSAKTRQGVDDAFYTLVREIRKHKEK |

Figure 2. 20 YZ0711 covalently labels KRAS* but not KRAS G12V

(A) Liquid chromatography/mass spectrometry (LC/MS) analysis of cleaved peptides in KRAS* incubated with YZ0711. Peptide 103-117 in KRAS* was detected to be labeled by YZ0711 at either Lysine or Cysteine residue. (B) LC/MS analysis of cleaved peptides in KRAS^{G12V} incubated with YZ0711. No labeling was detected in peptide 103-117 in KRAS^{G12V}. (C) Sequence alignment between KRAS* and KRAS^{G12V}.

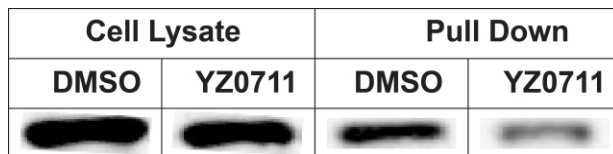


Figure 2. 21 Desthiobiotin-GTP pull down assay suggested YZ0711 occupied KRAS* nucleotide binding site covalently

The pull down assay was performed by treatment of KRAS* MEFs with 100 μ M YZ0711 or DMSO for 6hs prior to probing with desthiobiotin-GTP.

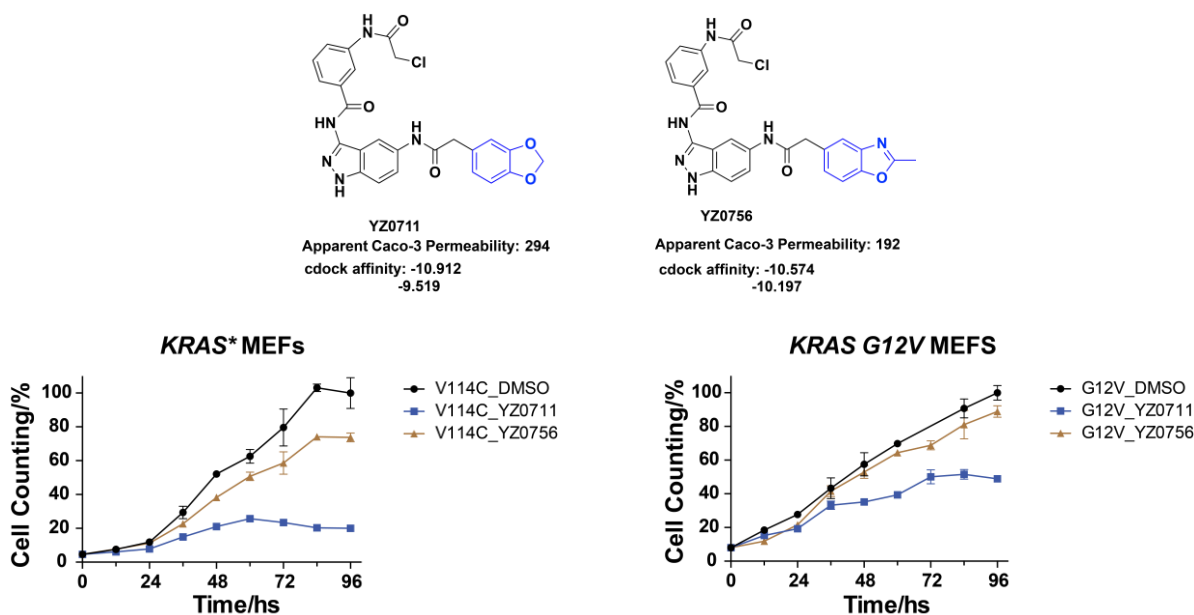


Figure 2. 22 YZ0711 specifically inhibited KRAS* MEFs proliferation

MEFs were treated with 25 μ M YZ0711, 25 μ M YZ0756, or DMSO for 4 days.

To test whether compound YZ0711 can disrupt KRAS*-effector binding, RAF RBD protein, which can selectively pull down GTP loaded KRAS*, was used. The GTP-loaded KRAS* protein was incubated with DMSO or YZ0711 (40 μ M) for 15 min and the reaction was stopped by adding MgCl₂ (65mM), then incubated with RAF RBD protein. Minimal KRAS* was observed for YZ0711-bound KRAS* compared with GTP-loaded KRAS* (DMSO control group) (**Figure 2.23 A**). Treatment of

*KRAS** MEFs with YZ0711 also resulted in decreased RAS-bound BRAF, suggesting YZ0711 can disrupt RAS signaling (**Figure 2.23 B**).

To further investigate whether compound YZ0711 can inhibit the RAS-RAF-MEK-ERK and RAS-PI3K-AKT signaling pathways in cells, the phosphorylation levels of ERK and AKT were analyzed by western blot (**Figure 2.24**). Treatment of *KRAS** MEFs with YZ0711 resulted in decreased pERK and pAKT levels. *KRAS*^{G12V} MEFs were more resistant to this effect.

A

| | DMSO | YZ0711 |
|---------------------|------|--------|
| Input <i>KRAS</i> * | | |
| anti-RAS | | |

B

| | Cell Lysate | | IP | |
|-------|-------------|--------|------|--------|
| | DMSO | YZ0711 | DMSO | YZ0711 |
| B-Raf | | | | |
| Ras | | | | |

Figure 2. 23 YZ0711 disrupted *KRAS**-BRAF interaction

(A) YZ0711 loaded *KRAS** was not able to bind with RAF-RBD. (B) *KRAS** MEFs cells treated with compound YZ0711 (100 μ M) or DMSO was lysed and immunoprecipitated by RAS-antibody followed by detection with BRAF antibody.

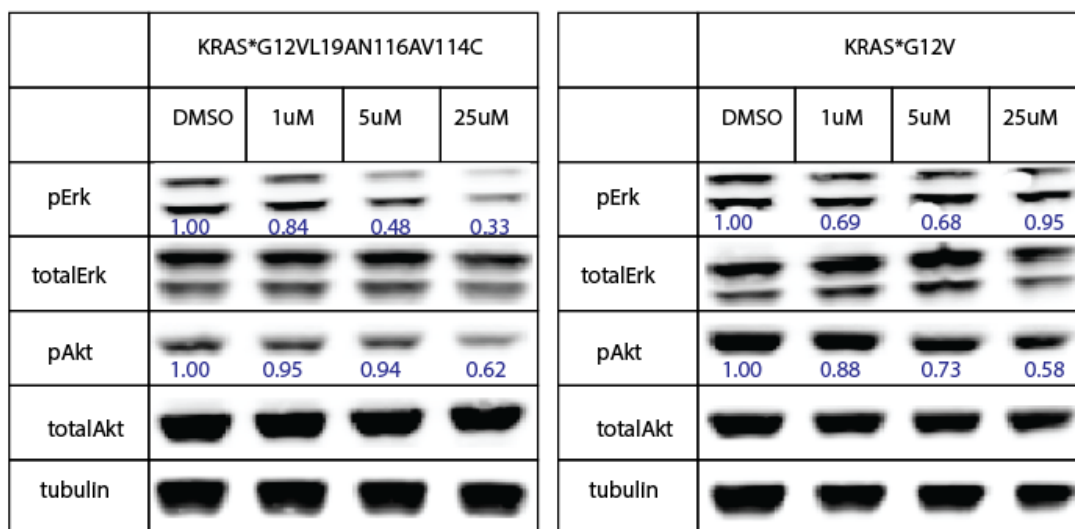


Figure 2. 24 YZ0711 inhibited RAS-MAPK pathway

MEFs were treated with DMSO, 1 μ M, 5 μ M, and 25 μ M YZ0711 for 24hs. The pERK and pAKT levels were decreased in *KRAS** MEFs but not *KRAS^{G12V}* MEFs with the treatment of YZ0711.

2.3 Conclusion and Discussion

Before embarking on a small molecule drug discovery project directed against a specific target protein, it is critical to first validate the therapeutic effectiveness of the target in a specific disease, as well as the therapeutic index associated with target inhibition¹²⁴. “Chemical” and “genetic” methods are two main approaches used in this target validation where small molecules or genetic tools are used to modulate the target function¹²⁵. Genetic methods including gene knockout and RNAi may have problems of generating null mutants for essential genes and lacking alignment between RNAi and inhibitor studies¹²⁵. Small molecule approaches can overcome above difficulties and provide additional information about druggability, toxicity, and safety of inhibiting a target.

KRAS is an essential gene and its gene product interacts with multiple upstream and downstream effectors. However, there is a lack of suitable chemical tools that can directly target *KRAS*. We developed a scalable system for testing the *in vitro* consequences of pharmacological inhibition of *KRAS*.

An enlarged binding pocket was engineered into GTP binding site of KRAS through mutation of two conserved residues to alanine. The engineered KRAS is functionally distinguishable from KRAS^{G12V} in cell. We have designed and synthesized a small-molecule probe that covalently binds to an engineered KRAS mutant with high affinity and displaces GTP from the binding pocket. The probe allows selective binding to the engineered protein, but not the wild-type protein. The probe is also cell membrane permeable and can selectively inhibit RAS signaling in cells.

There are two challenges facing in fragment-based small molecule design: identification of suitable fragment to develop and elaborating the initial fragment to a lead compound. In this chapter, by setting critical hydrogen bond interaction during docking, and carefully choosing fragments with suitable cell membrane permeability, structural modification possibility and binding affinity, an indazole piperidine was selected to be the initial fragment. By employing combinatorial library, a 124 k compounds library was generated which largely increased the screening space. Then, we synthesized top scoring compounds shown in Caco-2 cell permeability prediction, glide docking, and covalent docking programs, which saved a lot of time and resources. The covalent small molecule developed using this approach has improved selectivity to the target and exclusively modifies the engineered cysteine residue, which proved the success of this fragment based small molecule design approach.

While this covalent inhibitor showed specific on-target effect in cells, the cellular activity is not as high as expected. There could be many reasons. Firstly, GTP, the endogenous ligand of KRAS, has picomolar binding affinity with KRAS and around 0.5 mM concentration in cells. The potency and selectivity of small molecule could be dramatic decreased with such high concentration of endogenous ligands¹²⁶. Secondly, KRAS* has a quick turn over in cells comparing with KRAS^{G12V}, this quick turn over results in higher dosing of inhibitors. Thirdly, SOS1 could not effectively catalyze the exchange of GTP to the covalent inhibitor YZ0711, which might result in a low binding rate of YZ0711 to KRAS*.

Small GTPases contribute to multiple cellular processes and different stages of cancer development and progression^{24, 127-131}. They have conserved GTP/GDP binding pockets and share similar

activation/deactivation mechanisms. Guanine nucleotide exchange factors (GEFs) catalyze the exchange of GDP by GTP, while GTPase-activating proteins (GAPs) accelerate the intrinsic GTPase activity of small GTPases. In the active state (GTP-bound state), small GTPases associate with a variety of effectors and promote downstream signaling. The system we designed here can be expanded for the design of allele selective small molecule inhibitors of other proteins in small GTPase family, thus providing tools to validate small GTPases.

2.4 Methods

Software

Molecular docking and modeling was performed using Glide (versions 2012-2016, Schrödinger) and Molecular Operating Environment [MOE] (Chemical Computing Group). All chemical structures were drawn using ChemDraw Ultra version 10.0 (Perkin Elmer). All statistical analyses, potency determinations, and viability curves were produced using Prism 6.0 (GraphPad Software).

In-silico libraries

Libraries of commercially available molecules for general screening purposes were compiled from the inventories of Asinex, Enamine, Chembridge, ChemDiv, IBS, Life, Maybridge and TimTec. A fragment subset of ~200,000 compounds from the unfiltered library was selected using the following filter criteria: $\text{Log}(P) < 3$, hydrogen bond acceptors ≤ 3 , hydrogen bond donors ≤ 3 , molecular weight < 300 , aqueous solubility > 0.5 mM. Chemical descriptors were calculated using MOE (Chemical computing group). Designed libraries of synthetically accessible molecules were compiled using selected commercially available reagents from the inventory of Sigma-Aldrich and Chem-Impex using the Combigen application of MOE (chemical computing group).

Cloning

For cell transfection, mutagenesis was performed on human K-Ras^{G12V} pBabe puro vector (a gift from Dr. Nicole Fehrenbacher, NYU Cancer Institute) using a QuikChange XL site-directed mutagenesis kit from Agilent technologies according to the manufacturer's protocol. Primers were designed using the Agilent QuikChange Primer Design application and purchased from Integrated DNA Technologies. For protein expression and purification, the K-Ras constructs were cloned into in the pGEX-4T3 vector to obtain proteins with a Glutathione S-transferase (GST) tag and pET15b vector to obtain proteins with a His tag..

Expression and purification of KRAS*^{G12VL19AN116AV114C} and KRAS^{G12V}

For protein purification, an isolated colony was transferred to 5 mL LB media with 100 µg/mL ampicillin and the inoculated culture was incubated with shaking (225 rpm) at 37 °C for 3 h. The starter culture was added to 1 L fresh LB with 100 µg/mL ampicillin. The culture was incubated with shaking at 37 °C until the OD₆₀₀ reached 0.6. The temperature was then reduced to 30 °C or 15°C and shaking continued for 30 min. GST-tagged KRAS^{G12V} protein synthesis was induced by the addition of isopropyl β-D-thiogalactoside (500 µM) and the cells were incubated with shaking (225 rpm) at 15°C overnight. GST-tagged KRAS*^{G12VL19AN116AV114C} protein synthesis was induced by the addition of isopropyl β-D-thiogalactoside (100uM) and the cells were incubated with shaking (225 rpm) at 30°C overnight. His-tagged KRAS^{G12V} and His-tagged KRAS*^{G12VL19AN116AV114C} protein synthesis was induced by the addition of isopropyl β-D-thiogalactoside (500uM) and the cells were incubated with shaking (175 rpm) at 15°C overnight. The bacteria were harvested by centrifugation at 4,000 × g for 20 min at 4 °C and the obtained pellet was stored at -20°C.

Purification of GST-tagged KRAS*^{G12VL19AN116AV114C} and KRAS^{G12V}

The pellet was resuspended in 25 mL chilled lysis buffer (20 mM HEPES [pH 7.5], 75 mM KCl, 25 mM MgCl₂, 1 mM TCEP, 0.1 mM EDTA, 0.05% Triton X-100, and Roche protease inhibitor cocktail). The bacteria were lysed by sonication on ice for 3 min and the lysate was centrifuged at 15,000 × g for 45 min at 4 °C to remove cell debris. The clarified lysate was incubated with glutathione Sepharose beads on a rotator at 4°C for 2 hours. The beads were washed with lysis buffer once, and then with wash buffer (50

mM Tris-HCl [pH 7.5], 50 mM NaCl, 1 mM TCEP) three times. The protein was eluted with 10 mM glutathione in wash buffer (pH 7.5) and concentrated. Protein concentration was determined using absorbance at 280 nm with extinction coefficient of $55280 \text{ M}^{-1} \text{ cm}^{-1}$, and protein purity was assessed by gel electrophoresis.

Purification of His-tagged KRAS*^{G12VL19AN116AV114C} and KRAS^{G12V}

The pellet was resuspended in 25mL chilled lysis buffer (100mM NaPhosph Monobasic, 300mM NaCl, 20% Glycerol, 0.5% chaps (W/V), 15mM 2-mercaptoethanol, 5mM imidazole, pH 7.0, Roche protease inhibitor cocktail). The bacteria were lysed by sonication on ice for 3 min and the lysate was centrifuged at $15,000 \times g$ for 45 min at 4 °C to remove cell debris. The clarified lysate was incubated with Ni Sepharose 6 Fast Flow beads (GE Life Sciences) on a rotator at 4°C for 1 hour. The beads were washed with wash buffer (100mM NaPhosph Monobasic, 300mM NaCl, 20% Glycerol, 15mM 2-mercaptoethanol, 5mM imidazole, pH 7.0) and non-specific binding buffer (20mM imidazole in wash buffer). The protein was eluted with 250 mM imidazole in wash buffer. The eluted protein was desalted using 10DG-biorad-desalting column immediately. The protein was further purified using gel filtration Superdex 100 column in FPLC buffer containing 25 mM Tris-HCl pH 8, 100 mM NaCl, 5 mM MgCl₂, and 1 mM TCEP. The fractions containing KRAS^{G12D} were pooled together and verified by SDS-PAGE. Protein concentration was determined using absorbance at 280 nm with extinction coefficient of $11920 \text{ M}^{-1} \text{ cm}^{-1}$.

Fluorescence polarization assay

Small-molecule inhibitors (as 50 mM stocks in DMSO) were arrayed in an 10-points dilution series in 384-well polypropylene plates (reaction buffer: 50 mM Tris pH 7.5, 50 mM NaCl, 5 mM MgCl₂, 1 mM EDTA, 5 % glycerol, 1 mM TCEP). Compound solutions were transferred at a 1:2 dilution into the assay plates (Corning 384, #3821), followed by purified protein (GST-tagged KRAS, final concentration = 5 μM). The plates were incubated at room temperature for 30 minutes. Then BODIPY-GTP (final

concentration = 125 nM) was added to the plate. Trials were also run with GDP as a reference, no protein as a positive control and DMSO as a negative control. The plates were incubated at 4 °C overnight to allow for equilibration of the solution. The fluorescence intensity was measured on a Victor2 TMV plate reader (PerkinElmer, 485 nm excitation, 535 nm emission).

Nucleotide exchange assay

GST tagged KRAS*G12V^{L19AN116AV114C} (20uM) or KRAS^{G12V} (20uM) was incubated with BODIPY-GTP (200 μM) at room temperature for 1hour in Tris buffer (100 mM Tris, pH 7.5, 1 mM EDTA, 1 mM TCEP). The reaction was stopped by adding MgCl₂ (65 mM). NAP-5 column was equilibrated with reaction buffer (50 mM Tris, pH 7.5, 50 mM NaCl, 5 mM MgCl₂, 1mM TCEP). The protein was then run through a NAP-5 column to remove free nucleotide. The concentration of the obtained protein was determined by Nano-drop and diluted to desired concentration in reaction buffer. For the assay, 5 μL of the prepared protein (final concentration 1 μM) in reaction buffer was added to a well of a low volume black bottom plate (Corning, 3676). 5 μL of GDP (final concentration 4 μM), GTP (final concentration 4 μM), or compound YZ0711 (final concentration 4 μM) mixed with SOS1 (final concentration 1 μM), EDTA (final concentration 10 mM) in reaction buffer was added. The fluorescence polarization intensity was measured on a Victor2 TMV plate reader (PerkinElmer, 485 nm excitation, 535 nm emission).

Retroviral Transfection of Mouse Embryonic Fibroblasts

Phoenix Ampho packaging cells (ATCC: CRL-3213) were grown to 80% confluence in normal growth media (DMEM, 10% FBS, 1% Penicillin/Streptomycin, 2mM L-glutamine) (Invitrogen). 600,000 cells/well were seeded in 6-well dishes (Corning). After 20 hours, the media was aspirated and replaced with 800 μL Optimem (Life Technologies), and the cells were incubated for 20 minutes at 37°C. Meanwhile, 2.5 μg of pBabe puro vector was added to an eppendorf tube with 100 uL Optimem. 6μL of lipofectamine 2000 (Invitrogen) was added to 94μL of Optimem in a separate tube. The two solutions were mixed together, and the mixture was then incubated for 20 min at 25°C. The DNA/lipofectamine

emulsion was added dropwise to the Phoenix Ampho well, and the cells were incubated for 4 hours at 37°C. After 4 hours, 1mL of Optimem media with 20% FBS was added and the cells were incubated overnight at 37°C. After 24 hours, the transfection media was aspirated and replaced with normal growth media. The next day, 1.5 mL of virus supernatant was collected and kept at 4°C. The media was replaced, and the procedure was repeated after 4, 8, and 24 hours. The virus supernatants were combined and filtered through 0.45µm filter, and then polybrene was added. Meanwhile, Mouse Embryo Fibroblasts cells (*Kras*^{lox/lox}, *Hras*^{-/-}, *Nras*^{-/-} *RERTn*^{ert/ert} cells carrying an inducible Cre recombinase, Cre-ERT2) (DU315-6, gift from Mariano Barbacid) were seeded at 160,000 cells/well in 6-well dishes. After 14 hours, the media was removed and 2mL of filtered virus supernatant was added, and 2mL of virus supernatant was successively added at two-hour intervals until the total well volume was 6 mL. After 24 hours, the media was removed and replaced with selective media (DMEM, 10% HI-FBS, 1% Penicillin/Streptomycin, 1X Glutamax, and 1µg/ml puromycin). After 2 weeks of selection with puromycin, the cells were cultured in the presence of (Z)-4-hydroxytaoxifen (4OHT) (Sigma, 600nM) for another 2 weeks to ablate the endogenous *Kras*. Then the cells were analyzed for expression using western blot. KRAS expression was analyzed by western blot.

Viability assay in Mouse Embryonic Fibroblasts

KRAS^{*G12V/L19A/N116A/V114C} MEFs and *KRAS*^{*G12V} MEFs were trypsinized, counted, and seeded into 384-well plates at 1,000 cells/well in DMEM/10% HI-FBS/1% p-s/1X Glutamax medium. After 16 h, compounds (from 50 mM stocks in DMSO) were arrayed in a 10-point 2-fold dilution series in 384-well polypropylene plates. Compound solutions were transferred at a 1:5 dilution into assay plates. After 48 h, a 50% Presto blue solution was added to a final concentration of 10% Presto blue. After 6 h of incubation, fluorescence intensity was determined using a Victor3 plate reader (Perkin Elmer) with a 535 nm excitation filter and a 590 nm emission filter. All compound measurements were performed in duplicate.

Western blots for Analysis of Cell Line Transfection

0.25 million cells/well were seeded in DMEM with 1X Glutamax, 10% heat-inactivated FBS, and 1% P/S. After the cells grew to 80% confluence, the medium was changed to serum-free medium, and the cells incubated for 24 hr. The cells were stimulated with human EGF (10 ng/ml) for 15 min to stimulate RAS-dependent pERK and pAKT signaling. Then the cells were washed with cold PBS and lysed with RIPA lysis buffer (Thermo Fisher, catalog number: 89900) containing 1X protease inhibitor cocktail (Thermo Fisher, catalog number: 78430). Unlysed cells and debris were pelleted for 15 min at 13,000 rpm at 4°C. Samples were separated using SDS-PAGE and transferred to a natural cellulose membrane. Transfer was performed using the iBlot system (Invitrogen). Membranes were treated with Li-COR Odyssey blocking buffer for 20min at 25°C, then incubated with primary antibody (1:1000) in a 1:1 solution of PBS-T and Li-COR odyssey blocking buffer overnight at 4°C. Following three 5 min washes in PBS-T, the membrane was incubated with secondary antibodies (1:2000) in a 1:1 solution of PBS-T and Li-COR Odyssey blocking buffer for 1 hour at 25°C. Following three 5 min washes in PBS-T, the membrane was scanned using the Li-COR Odyssey Imaging System. Antibodies for pERK1/2, ERK1/2, pAKT ser473, AKT, pan-RAS, PI3Kgamma, c-RAF, b-RAF (Cell Signaling), and alpha-Tubulin (Santa Cruz) were detected using a goat anti-rabbit or goat anti-mouse IgG antibody conjugated to an IRdye at 800CW and 680CW conjugated, respectively (Li-COR Biosciences).

RAF-RBD pull down assay to test KRAS* switch function

His tagged KRAS*^{G12VL19AN116AV114C} (0.0042 µg/µL) was incubated with GDP (40 µM) or GTP (40 µM) at room temperature for 15 min in Tris buffer (100 mM Tris, pH 7.5, 1 mM EDTA, 1 mM TCEP). The reaction was stopped by adding MgCl₂ (65 mM). 0.42ug GDP loaded KRAS* or GTP loaded KRAS* was incubated with 7ug RAF RBD beads in 400 µL HEPES buffer (25 mM HEPES, pH 7.5, 150 mM NaCl, 5 mM MgCl₂, 10% glycerol, 1 mM TCEP, 0.1% Tween20, 0.5% Prionex) at 4°C for 1 hour. The beads were collected by centrifuging at 800 rpm for 2min and washed for 3 times with HEPES buffer. Then the beads was boiled with SDS sample buffer and analyzed by western blot.

RAF-RBD pull down assay to test whether compound YZ0711 can disrupt KRAS* effector binding

His tagged KRAS*^{G12VLI9AN116AV114C} (1 µg/µL) was incubated with GTP (400 µM) at room temperature for 1 hour in Tris buffer (100 mM Tris, pH 7.5, 1 mM EDTA, 1 mM TCEP). The reaction was stopped by adding MgCl₂ (65 mM). The protein was then run through a NAP-5 column to remove free nucleotide. The concentration of the obtained protein was determined by Nano-drop. GTP loaded KRAS* (0.0042 µg/µL) was incubated with DMSO or YZ0711 (40 µM) at room temperature for 15 min in Tris buffer. The reaction was stopped by adding MgCl₂ to a final concentration of 65 mM. 0.42ug GTP loaded KRAS* (DMSO control) or YZ0711 loaded KRAS* was incubated with 7ug RAF RBD beads in 400 µL HEPES buffer (25 mM HEPES, pH 7.5, 150 mM NaCl, 5 mM MgCl₂, 10% glycerol, 1 mM TCEP, 0.1% Tween20, 0.5% Prionex) at 4°C for 1 hour. The beads were collected by centrifuging at 800 rpm for 2min and washed for 3 times with HEPES buffer. Then the beads was boiled with SDS sample buffer and analyzed by western blot.

Gene expression analysis using RT-qPCR experiment

Cells from six-well plates were trypsinized and centrifuged at 3,000 rpm for 3 min. The cell pellet was then lysed and the RNA was extracted using the QIAshredder and RNeasy extraction kits (QIAGEN) according to the manufacturer's protocol. 2 mg of RNA from each sample was then converted to cDNA using the TaqMan RT Kit (Applied Biosystems). Primers for Quantitative PCR (qPCR) were designed with Primer Express. qPCR was performed using Power SYBR Green Master Mix (Applied Biosystems) in a 96-well format, in triplicate, using an Applied Biosystems 7300 Cyclor set to absolute quantification. Expression changes were computed using the $\Delta\Delta C_t$ method with Actin as an internal reference gene.

Western Blotting with Treatment of YZ0711

0.25 million cells/well were seeded in DMEM with 1X Glutamax, 10% heat-inactivated FBS, and 1% P/S. After the cells grew to 80% confluence, the medium was changed to serum-free medium containing DMSO or compound YZ0711 at indicated concentration, and the cells incubated for 24 hr. Then the cells were washed with cold PBS and lysed.

Desthiobiotin-GTP pulldown

KRAS^{*G12V L19A N116A V114C} MEFs were seeded 16 h prior to use in DMEM/10% HI-FBS/1% p-s/1X Glutamax medium. The medium was then aspirated and replaced with medium containing the inhibitors (from 50mM DMSO stocks) and cells were incubated for 6 hr. The medium was removed, washed with cold PBS, lysed and spun down at 13,000 rpm at 4°C to remove unlysed cells and debris. The lysate was buffer exchanged using DG10 columns to PBS. The lysate was added with protease inhibitor cocktail and diluted with PBS to 2mg/ml. 500uL (1mg) was transferred to a microcentrifuge tube. 1uL of 0.5M EDTA was added and incubated for 5 minutes at room temperature. 5uM ActiveX GTP-desthiobiotin (Thermo Scientific) and 20uM MgCl₂ were added, mixed and incubated for 10 minute at room temperature. 500uL of 8M Urea/IP Lysis Buffer and 50uL of 50% High Capacity Streptavidin Agarose resin slurry were added. After 2 hour incubation on rotator, the sample was centrifuged at 800 x g for 2 minute and washed 2X with 4M Urea/IP Lysis Buffer. The sample was then analyzed by western blotting procedure.

Immunoprecipitations

MEFs were seeded 16 h prior to use in 10% HI-FBS/1% p-s/1X Glutamax in DMEM. Media was aspirated and replaced with media containing YZ0711 (from a 50 mM DMSO stock). After 10h cells were washed 2X with ice cold buffer (25 mM tris, 100 mM NaCl, 1 mM TCEP, 5 mM MgCl₂, 0.1% tween-20 and 1 protease inhibitor/25 mL). Cells were scrapped, pelleted at 13,000 rpm for 10 min at 4 °C, then passed through a 26 gauge needle several times. The solution was spun down a second time at 13,000 rpm for 15 min at 4 °C, to remove unlysed cells and debris. Anti-RAS antibody (Abcam, EPR3255) was then added to the lysate (1:100) and the solution was rocked at 4 °C for 16 h. Protein A agarose beads were then added and the solution was rotated at 4 °C for an additional 6 h. The solutions were spun down at 1500xg for 2 min and the supernatant was removed by syringe. The beads were washed 2X by this process with buffer, then resuspended in 5X SDS.

Determining cellular concentrations of compounds

*KRAS**^{G12VLI9AN116AV114C} MEFs were grown in DMEM/10% HI-FBS/1% p-s/1X Glutamax medium and seeded in 6-well plates at a density of 0.4×10^6 cells/well, followed by overnight incubation. On the following day, the growth medium was removed and the cells were rinsed twice with PBS, then DMEM growth medium (without FBS) containing 20uM compounds was added. Cells were treated for 4 hours. After treatment, the growth media was removed and the cells were rinsed with PBS, trypsinized and suspended in DMEM/10% HI-FBS/1% p-s/1X Glutamax media. The cells were counted on a Vi-Cell XR Cell Viability Analyzer (Beckman Coulter), and the average diameter was recorded. An aliquot of the appropriate volume of cell suspension (1×10^6 cells per sample) was transferred to a 15 mL Falcon tube (3 samples each). The cells were pelleted at 1000 g for 5 minutes. The cells were washed twice with PBS and transferred to a 1.5 mL Eppendorf tube. The cells were pelleted at 3000 rpm for 3 minutes, after which the PBS was removed and the pellet was lysed by adding 150 μ L of methanol/acetonitrile (1:1). The suspension was mixed well by pipetting and the compound was extracted overnight at 4 °C. The samples were spun at 1400 g for 75 minutes at 4 °C, and the supernatant (75 μ L) was withdrawn and transferred to a sample vial with insert. The samples were analyzed by LC-MS. LC-MS analysis was performed on a platform comprising a Thermo Scientific Dionex Ultimate 3000 and a Bruker amaZon SL equipped with an electrospray ionization source controlled by Bruker Hystar 3.2. Chromatographic separation was performed by injecting the sample on an Agilent Eclipse Plus C18 column (2.1 x 50 mm, 3.5 μ m) at 20 °C. The flow rate was maintained at 400 μ L/min. The initial flow conditions were 60% solvent A (water containing 0.1% acetic acid) and 40% solvent B (methanol containing 0.1% acetic acid). Solvent B was raised to 60% over 0.25 minutes and to 70% by 6.75 minutes. Solvent B was raised to 95% by 7.00 minutes and lowered back to initial conditions (40%) by 8.00 minutes with a total run time of 9.00 minutes. The peak area was converted to a concentration using a standard curve and the intracellular concentration was determined using the following formula:¹

$$\text{Cellular Concentration} = \text{Sample Concentration} \times \frac{\text{Sample Volume}}{(\text{number of Cells})(\text{Cell Volume})}$$

(1) Colletti, L. M.; Liu, Y.; Koev, G.; Richardson, P. L.; Chen, C. M.; Kati, W. *Anal. Biochem.* 2008, 383 (2), 186.

Liquid chromatography/mass spectrometry sample preparation

20uM His-KRAS*G12V^{L19AN116AV114C} and His-KRAS^{G12V} were incubated with 200uM YZ0711 overnight at 4 °C in buffer (20mM Hepes, pH 7.5, 150mM NaCl, 1mM TCEP, 20% glycerol, 1mM EDTA). The reaction was stopped by adding MgCl₂ to a final concentration of 65mM. The sample was then purified by NAP-5 column and concentrated using Millipore spin column with 10kDa cut off filter. For each 70ul of protein sample, 0.4uL of dithiothreitol (75ug/uL) was added and the sample was heated at 60 °C for 30 minutes. Then the sample was cooled to room temperature and centrifuged briefly to bring down condensed droplets. 1.0uL iodoacetamide (110ug/uL) was added to the sample and the sample was placed in dark at room temperature for 30 minutes. Then the sample was separated by SDS PAGE gel for mass spectrometry analysis.

Synthesis of chemical materials

General information. All reactions were carried out under a nitrogen atmosphere under anhydrous conditions unless indicated otherwise. Anhydrous methylene chloride (DCM), tetrahydrofuran (THF), *N,N*-dimethylformamide (DMF) and pyridine were purchased from Sigma-Aldrich. Reactions were magnetically stirred and monitored by thin layer chromatography carried out by Merck pre-coated 0.25 mm silica plates containing a 254 nm fluorescence indicator. Flash chromatography was performed on a Teledyne combiflash companion automatic flash chromatography system. Preparative thin layer chromatography was performed on 1 mm. Proton nuclear magnetic resonance spectra (¹H NMR, 300 MHz, 400 MHz, 500 MHz) and proton decoupled carbon nuclear magnetic resonance spectra (¹³C NMR, 100 MHz, 125 MHz) were obtained on a Bruker DPX 300, 400, or 500 MHz instruments in deuteriochloroform (CDCl₃) with residual chloroform as internal standard. Other deuterated solvents that were used include *d*₄-MeOD and *d*₆-DMSO.

Abbreviations: TEA = triethyl amine, EtOAc = ethyl acetate, HCl = hydrochloric acid, MeOH = methanol, EtOH= ethanol, NaHCO₃ = sodium bicarbonate, Na₂SO₄ = sodium sulfate, NH₄Cl = ammonium chloride, rt = room temperature, TFA = trifluoroacetic acid, THF = tetrahydrofuran. BOC = *tert*-butyloxycarbonyl, SOCl₂ = thionyl chloride, DMAP = 4-dimethylaminopyridine, NH₂NH₂·H₂O = hydrazine monohydrate.



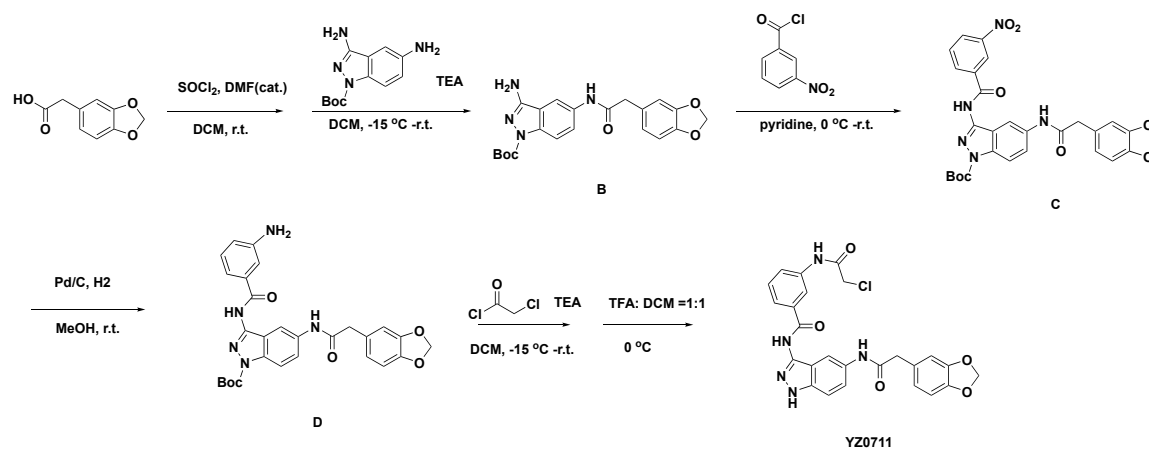
Compound A synthesis

1,750mg 2-fluoro-5-nitrobenzonitrile (1.0 equiv.) were dissolved in 29mL EtOH (0.36 M), the reaction as protected with N₂ and heated to 50 °C, then 661uL Hydrazine monohydrate (2.0 equiv.) was added. The reaction was refluxed for 1.5 hours, and then cooled to room temperature. The precipitate was filtered and the filtrate was collected and concentrated. The resulting residue was dissolved in EtOAc and washed with saturated ammonium chloride. The organic phase was separated, dried with anhydrous Na₂SO₄, and concentrated to yield indazole. The crude product of indazole was used directly in the next step without purification.

602mg indazole (1.0 equiv.), 729mg *tert*butyldicarbonate (1.0 equiv.), 103mg DMAP (0.25 equiv.), and 470uL triethylamine (1.0 equiv.) were dissolved in 16mL THF (0.2M) at room temperature under nitrogen. After stirring for 30min, the reaction was concentrated and the residue was dissolved in EtOAc, then washed with saturated ammonium chloride. The organic phase was separated, dried with anhydrous Na₂SO₄, and concentrated to yield indazole. The crude product of BOC-indazole was used directly in the next step without purification.

1.0g BOC-indazole (1.0 equiv.) and 90mg 10% Pd/C (0.2 equiv.) were dissolved in 30mL MeOH (0.12M). The mixture was gas exchanged with H₂ then stirred under H₂ overnight. The reaction was filtered through celite and concentrated under vacuo. The resulting mixture was purified by combiflash 0-

10% MeOH/DCM to afford compound A (86% yield over three steps). ^1H NMR (400 MHz, Chloroform-*d*) δ 7.61 (s, 1H), 6.76 (d, $J = 8.9$ Hz, 1H), 6.66 (s, 1H), 5.06 (s, 2H), 3.84 (s, 2H), 1.54 (s, 9H).



Compound B synthesis

720.8mg 3,4-(Methylenedioxy)phenylacetic acid (1.0 equiv.) and 435uL thionyl chloride (1.5 equiv.) were dissolved in 12mL dichloromethane (0.33M) at room temperature. Then 3 drops of dimethylformamide was added to the solution. After 2 hours, the reaction mixture was concentrated to provide 3,4-(Methylenedioxy)phenylacetyl chloride. 790 mg compound A (0.8 equiv.) and 557uL triethyl amine (1.0 equiv.) were dissolved in 60mL anhydrous dichloromethane and cooled to -15°C . 3,4-(Methylenedioxy)phenylacetyl chloride in 1mL anhydrous dichloromethane was slowly added to the reaction. After 1 hour, the reaction was washed with brine. The organic phase was separated, dried with anhydrous Na_2SO_4 , and concentrated. The product was purified by combiflash 0-5% MeOH/DCM to afford compound B (86% yield). ^1H NMR (400 MHz, DMSO-*d*₆) δ 10.20 (s, 1H), 8.20 – 8.14 (m, 1H), 7.88 (d, $J = 8.9$ Hz, 1H), 7.51 (dd, $J = 8.9, 2.0$ Hz, 1H), 6.94 (d, $J = 1.6$ Hz, 1H), 6.90 – 6.78 (m, 2H), 6.24 (s, 2H), 5.99 (s, 2H), 3.57 (s, 2H), 1.58 (s, 9H).

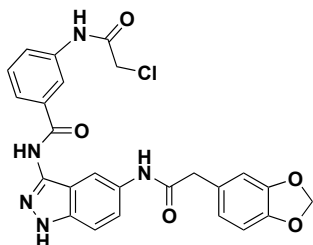
Compound C synthesis

641mg compound B (1.0 equiv.) was dissolved in 7mL anhydrous pyridine and cooled to 0°C . 581mg 3-nitrobenzoyl chloride (2.0 equiv.) was dissolved in 4mL anhydrous pyridine and was added to the reaction dropwise. The reaction was then warmed to room temperature and stirred overnight under N_2 .

After completion, 20mL EtOAc was added to the reaction, the reaction was washed with saturated ammonium chloride for several times. The organic phase was separated, dried with anhydrous Na₂SO₄, and concentrated. The product was purified by combiflash 0-5% MeOH/DCM to afford compound C (70% yield). ¹H NMR (400 MHz, Chloroform-*d*) δ 9.31 (s, 1H), 8.85 (t, *J* = 2.0 Hz, 1H), 8.42 (ddd, *J* = 8.3, 2.3, 1.0 Hz, 1H), 8.30 (ddd, *J* = 7.7, 1.8, 1.0 Hz, 1H), 8.11 (d, *J* = 2.0 Hz, 1H), 8.03 (d, *J* = 9.1 Hz, 1H), 7.68 (ddd, *J* = 9.8, 7.7, 5.0 Hz, 2H), 7.38 (s, 1H), 6.81 (td, *J* = 8.1, 7.4, 4.1 Hz, 3H), 5.98 (s, 2H), 3.67 (s, 2H), 1.68 (s, 9H).

Compound D synthesis

813mg compound C (1.0 equiv.) and 36mg 10% Pd/C (0.2 equiv.) was dissolved in 30mL 1:1 ratio of MeOH and EtOAc (0.05M). The mixture was gas exchanged with H₂ then stirred under H₂ overnight. The reaction was filtered through celite and concentrated under vacuo. The resulting mixture was purified by combiflash 0-10% MeOH/DCM to afford compound D (80% yield).

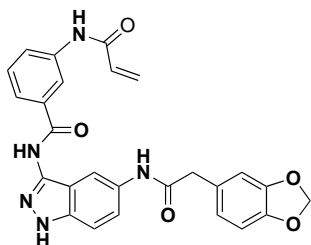


YZ0711

Compound YZ0711 synthesis

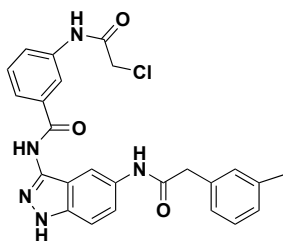
81.3mg compound D (1.0 equiv.) and 27uL dimethyl-isopropyl amine (1.1 equiv.) were dissolved in 20mL anhydrous dichloromethane (0.008M), and cooled to -15°C. 13.5uL chloroacetyl chloride (1.1 equiv.) dissolved in 1mL dichloromethane was added dropwise to the reaction. After 2 hours, the reaction was washed with brine. The organic phase was separated, dried with anhydrous Na₂SO₄, and concentrated. The crude product was dissolved in 1.6ml anhydrous dichloromethane and 0.8ml trifluoroacetic acid at 0°C. then the reaction was slowly warmed to room temperature and stirred under N₂ for 2 hours. After completion, the reaction was concentrated. The product was purified by combiflash 0-

10% MeOH/DCM to provide compound YZ0711 (40% yield). ^1H NMR (400 MHz, DMSO- d_6) δ 12.71 (s, 1H), 10.70 (s, 1H), 10.48 (s, 1H), 10.07 (s, 1H), 8.20 (t, $J = 1.9$ Hz, 1H), 7.93 (d, $J = 1.8$ Hz, 1H), 7.88 – 7.77 (m, 2H), 7.59 – 7.46 (m, 2H), 7.43 (d, $J = 8.9$ Hz, 1H), 6.93 – 6.75 (m, 3H), 5.97 (s, 2H), 4.29 (s, 2H), 3.52 (s, 2H). MS (APCI) m/z : $[\text{M} + \text{H}]^+$ Calcd for $\text{C}_{25}\text{H}_{20}\text{ClN}_5\text{O}_5$ 506.12, found 506.4



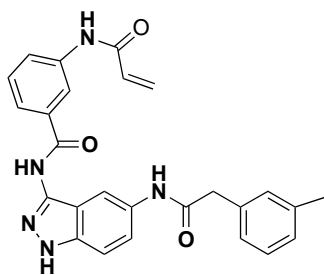
YZ0712

^1H NMR (400 MHz, DMSO- d_6) δ 12.70 (s, 1H), 10.67 (s, 1H), 10.32 (s, 1H), 10.07 (s, 1H), 8.26 (d, $J = 2.1$ Hz, 1H), 7.99 – 7.90 (m, 1H), 7.93 (s, 1H), 7.78 (d, $J = 7.8$ Hz, 1H), 7.59 – 7.39 (m, 3H), 6.93 – 6.75 (m, 3H), 6.46 (dd, $J = 17.0, 10.1$ Hz, 1H), 6.30 (dd, $J = 17.0, 2.0$ Hz, 1H), 5.96 (s, 2H), 5.79 (dd, $J = 10.1, 2.0$ Hz, 1H), 3.52 (s, 2H).



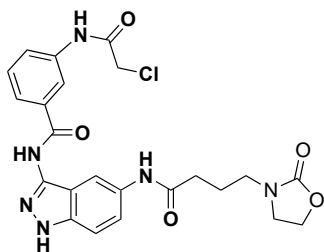
YZ0714

^1H NMR (400 MHz, DMSO- d_6) δ 12.71 (s, 1H), 10.69 (s, 1H), 10.48 (s, 1H), 10.12 (s, 1H), 8.20 (t, $J = 1.9$ Hz, 1H), 7.95 (d, $J = 2.0$ Hz, 1H), 7.88 – 7.77 (m, 2H), 7.60 – 7.45 (m, 2H), 7.43 (d, $J = 8.9$ Hz, 1H), 7.24 – 7.09 (m, 3H), 7.04 (d, $J = 7.4$ Hz, 1H), 4.29 (s, 2H), 3.57 (s, 2H), 2.28 (s, 3H). MS (APCI) m/z : $[\text{M} - \text{H}]^-$ Calcd for $\text{C}_{25}\text{H}_{22}\text{ClN}_5\text{O}_3$ 474.14, found 474.3



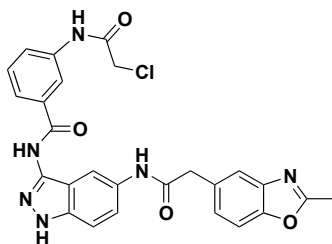
YZ0715

^1H NMR (400 MHz, $\text{DMSO-}d_6$) δ 12.71 (s, 1H), 10.67 (s, 1H), 10.33 (s, 1H), 10.12 (s, 1H), 8.26 (t, $J = 2.0$ Hz, 1H), 7.95 (dd, $J = 5.3, 2.1$ Hz, 2H), 7.82 – 7.75 (m, 1H), 7.60 – 7.39 (m, 3H), 7.24 – 7.09 (m, 3H), 7.04 (d, $J = 7.5$ Hz, 1H), 6.46 (dd, $J = 17.0, 10.1$ Hz, 1H), 6.30 (dd, $J = 17.0, 2.1$ Hz, 1H), 5.79 (dd, $J = 10.0, 2.1$ Hz, 1H), 3.58 (s, 2H), 2.28 (s, 3H). MS (APCI) m/z : $[\text{M} + \text{H}]^+$ Calcd for $\text{C}_{26}\text{H}_{23}\text{N}_5\text{O}_3$ 454.18, found 454.4



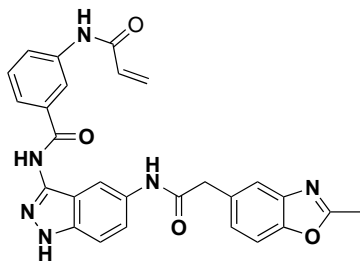
YZ0719

^1H NMR (400 MHz, $\text{DMSO-}d_6$) δ 12.71 (s, 1H), 10.70 (s, 1H), 10.50 (s, 1H), 9.90 (s, 1H), 8.23 (t, $J = 2.0$ Hz, 1H), 7.95 (d, $J = 1.8$ Hz, 1H), 7.88 – 7.78 (m, 2H), 7.57 – 7.39 (m, 3H), 4.29 (s, 2H), 4.27 – 4.18 (m, 2H), 3.57 – 3.50 (m, 2H), 3.23 – 3.15 (m, 2H), 2.32 (t, $J = 7.4$ Hz, 2H), 1.81 (q, $J = 7.2$ Hz, 2H).



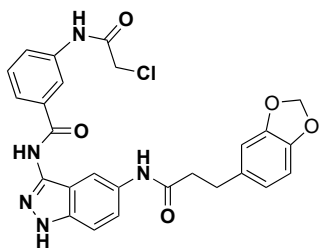
YZ0756

^1H NMR (400 MHz, $\text{DMSO-}d_6$) δ 12.76 (s, 1H), 10.74 (s, 1H), 10.53 (s, 1H), 10.21 (s, 1H), 8.20 (s, 1H), 7.94 (s, 1H), 7.88 – 7.77 (m, 2H), 7.63 – 7.40 (m, 6H), 7.30 (d, $J = 8.4$ Hz, 1H), 4.29 (s, 2H), 3.72 (s, 2H), 2.59 (s, 3H). MS (APCI) m/z : $[\text{M} + \text{H}]^+$ Calcd for $\text{C}_{26}\text{H}_{21}\text{ClN}_6\text{O}_4$ 517.13, found 517.4



YZ0757

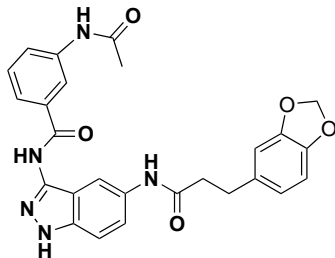
^1H NMR (400 MHz, $\text{DMSO-}d_6$) δ 12.75 (s, 1H), 10.72 (s, 1H), 10.36 (s, 1H), 10.21 (s, 1H), 8.25 (s, 1H), 7.95 (dd, $J = 7.4, 2.0$ Hz, 2H), 7.78 (d, $J = 7.7$ Hz, 1H), 7.63 – 7.40 (m, 5H), 7.30 (dd, $J = 8.4, 1.7$ Hz, 1H), 6.46 (dd, $J = 16.9, 10.0$ Hz, 1H), 6.29 (dd, $J = 17.0, 2.0$ Hz, 1H), 5.79 (dd, $J = 10.0, 2.1$ Hz, 1H), 3.72 (s, 2H), 2.59 (s, 3H).



YZ0788

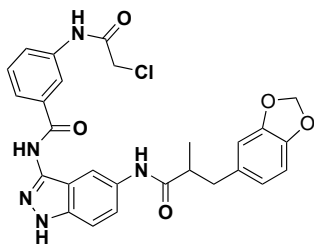
^1H NMR (400 MHz, $\text{DMSO-}d_6$) δ 12.71 (s, 1H), 10.70 (s, 1H), 10.50 (s, 1H), 9.86 (s, 1H), 8.23 (d, $J = 1.9$ Hz, 1H), 7.92 (s, 1H), 7.88 – 7.79 (m, 2H), 7.58 – 7.47 (m, 2H), 7.43 (dd, $J = 8.9, 0.8$ Hz, 1H), 6.85 – 6.77 (m, 2H), 6.70 (dd, $J = 7.9, 1.7$ Hz, 1H), 5.95 (s, 2H), 4.30 (s, 2H), 2.83 (t, $J = 7.6$ Hz, 2H), 2.57 (t, J

= 7.7 Hz, 2H). MS (APCI) m/z: $[M + H]^+$ Calcd for $C_{26}H_{22}ClN_5O_5$ 520.13, found 520.5



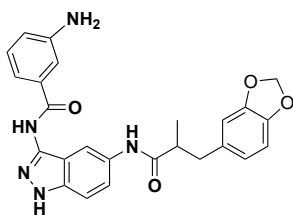
YZ0790-2

1H NMR (400 MHz, $DMSO-d_6$) δ 12.70 (s, 1H), 10.65 (s, 1H), 10.12 (s, 1H), 9.86 (s, 1H), 8.20 (s, 1H), 7.91 (s, 1H), 7.84 (d, $J = 8.2$ Hz, 1H), 7.76 (d, $J = 7.8$ Hz, 1H), 7.58 – 7.39 (m, 3H), 6.85 – 6.77 (m, 2H), 6.74 – 6.67 (m, 1H), 5.95 (s, 2H), 2.83 (t, $J = 7.6$ Hz, 2H), 2.57 (t, $J = 7.7$ Hz, 2H), 2.08 (s, 3H). MS (APCI) m/z: $[M + H]^+$ Calcd for $C_{26}H_{23}N_5O_5$ 486.17, found 486.3



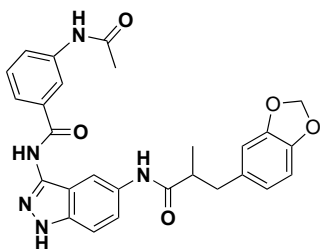
YZ0789

1H NMR (400 MHz, $DMSO-d_6$) δ 12.70 (s, 1H), 10.70 (s, 1H), 10.50 (s, 1H), 9.80 (s, 1H), 8.23 (t, $J = 1.9$ Hz, 1H), 7.94 – 7.79 (m, 3H), 7.57 – 7.47 (m, 2H), 7.42 (d, $J = 9.0$ Hz, 1H), 6.82 – 6.75 (m, 2H), 6.66 (dd, $J = 7.9, 1.7$ Hz, 1H), 5.93 (s, 2H), 4.30 (s, 2H), 2.88 (dd, $J = 13.3, 7.6$ Hz, 1H), 2.73 (p, $J = 6.9$ Hz, 1H), 2.57 – 2.52 (m, 1H), 1.08 (d, $J = 6.7$ Hz, 3H). MS (APCI) m/z: $[M + H]^+$ Calcd for $C_{27}H_{24}ClN_5O_5$ 534.15, found 534.5



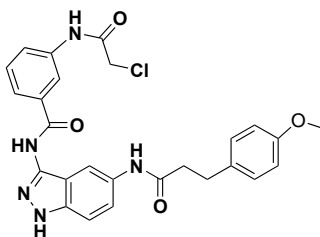
YZ0791-1

^1H NMR (400 MHz, $\text{DMSO-}d_6$) δ 12.69 (s, 1H), 10.62 (s, 1H), 9.80 (s, 1H), 7.94 (d, $J = 1.8$ Hz, 1H), 7.66 – 7.54 (m, 2H), 7.52 – 7.35 (m, 3H), 7.14 (dd, $J = 7.8, 2.3$ Hz, 1H), 6.82 – 6.75 (m, 2H), 6.66 (dd, $J = 7.9, 1.7$ Hz, 1H), 5.93 (s, 2H), 2.88 (dd, $J = 13.3, 7.7$ Hz, 1H), 2.73 (p, $J = 6.8$ Hz, 1H), 2.55 (s, 1H), 1.08 (d, $J = 6.7$ Hz, 3H). $[\text{M} + \text{H}]^+$ Calcd for $\text{C}_{25}\text{H}_{23}\text{N}_5\text{O}_4$ 458.18, found 458.4



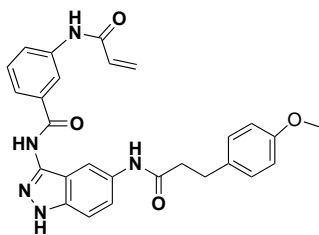
YZ0791-2

^1H NMR (400 MHz, $\text{DMSO-}d_6$) δ 12.68 (s, 1H), 10.65 (s, 1H), 10.13 (s, 1H), 9.80 (s, 1H), 8.20 (s, 1H), 7.93 – 7.80 (m, 2H), 7.76 (d, $J = 7.8$ Hz, 1H), 7.56 – 7.38 (m, 3H), 6.78 (d, $J = 7.9$ Hz, 2H), 6.66 (d, $J = 7.9$ Hz, 1H), 5.93 (s, 2H), 2.88 (dd, $J = 13.3, 7.6$ Hz, 1H), 2.73 (p, $J = 7.0$ Hz, 1H), 2.52 (d, $J = 19.4$ Hz, 1H), 2.09 (s, 3H), 1.08 (d, $J = 6.7$ Hz, 3H). $[\text{M} + \text{H}]^+$ Calcd for $\text{C}_{27}\text{H}_{25}\text{N}_5\text{O}_5$ 500.19, found 500.4



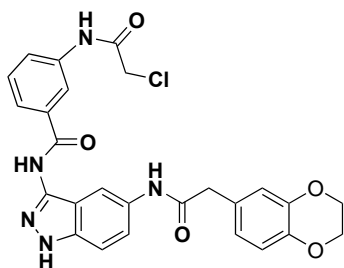
YZ0918-3

^1H NMR (400 MHz, $\text{DMSO-}d_6$) δ 12.71 (s, 1H), 10.70 (s, 1H), 10.50 (s, 1H), 9.87 (s, 1H), 8.23 (s, 1H), 7.92 (s, 1H), 7.83 (t, $J = 8.0$ Hz, 2H), 7.57 – 7.47 (m, 2H), 7.42 (d, $J = 8.9$ Hz, 1H), 7.16 (d, $J = 8.5$ Hz, 2H), 6.84 (d, $J = 8.6$ Hz, 1H), 6.49 (s, 1H), 4.29 (s, 2H), 3.70 (s, 3H), 2.85 (t, $J = 7.7$ Hz, 2H), 2.71 – 2.64 (m, 2H). $[\text{M} + \text{H}]^+$ Calcd for $\text{C}_{26}\text{H}_{24}\text{ClN}_5\text{O}_4$ 506.15, found 506.5



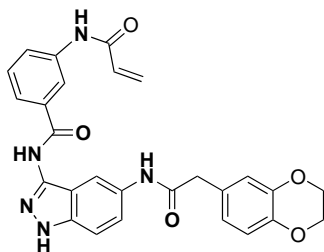
YZ0919-3

$^1\text{H NMR}$ (400 MHz, $\text{DMSO-}d_6$) δ 12.71 (s, 1H), 10.68 (s, 1H), 10.35 (s, 1H), 9.87 (s, 1H), 8.28 (t, $J = 1.9$ Hz, 1H), 7.99 – 7.90 (m, 2H), 7.80 (d, $J = 7.8$ Hz, 1H), 7.59 – 7.47 (m, 2H), 7.43 (dd, $J = 8.9, 0.8$ Hz, 1H), 7.19 – 7.12 (m, 2H), 6.90 – 6.77 (m, 2H), 6.47 (dd, $J = 17.0, 10.1$ Hz, 1H), 6.31 (dd, $J = 17.0, 2.0$ Hz, 1H), 5.80 (dd, $J = 10.1, 2.0$ Hz, 1H), 3.70 (s, 3H), 2.85 (t, $J = 7.6$ Hz, 2H), 2.64 – 2.52 (m, 2H). $[\text{M} + \text{H}]^+$ Calcd for $\text{C}_{27}\text{H}_{25}\text{N}_5\text{O}_4$ 484.19, found 484.4



YZ0921-2

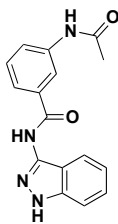
$^1\text{H NMR}$ (400 MHz, $\text{DMSO-}d_6$) δ 12.72 (s, 1H), 10.70 (s, 1H), 10.49 (s, 1H), 10.07 (s, 1H), 8.20 (s, 1H), 7.93 (s, 1H), 7.83 (dd, $J = 15.1, 7.9$ Hz, 2H), 7.58 – 7.40 (m, 3H), 6.83 (d, $J = 1.4$ Hz, 1H), 6.78 (d, $J = 1.2$ Hz, 2H), 4.29 (s, 2H), 4.20 (s, 4H), 3.48 (s, 2H). $[\text{M} - \text{H}]^-$ Calcd for $\text{C}_{26}\text{H}_{22}\text{ClN}_5\text{O}_5$ 518.13, found 518.3



YZ0922-2

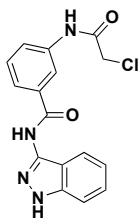
$^1\text{H NMR}$ (400 MHz, $\text{DMSO-}d_6$) δ 12.72 (s, 1H), 10.68 (s, 1H), 10.34 (s, 1H), 10.07 (s, 1H), 8.25 (t, $J = 1.9$ Hz, 1H), 7.95 (d, $J = 9.9$ Hz, 2H), 7.78 (d, $J = 8.0$ Hz, 1H), 7.59 – 7.40 (m, 3H), 6.83 (d, $J = 1.3$ Hz,

1H), 6.78 (d, $J = 1.2$ Hz, 2H), 6.47 (dd, $J = 17.0, 10.1$ Hz, 1H), 6.30 (dd, $J = 17.0, 2.0$ Hz, 1H), 5.80 (dd, $J = 10.1, 2.0$ Hz, 1H), 4.20 (s, 4H), 3.48 (s, 2H). $[M + H]^+$ Calcd for $C_{27}H_{23}N_5O_5$ 498.17, found 498.4



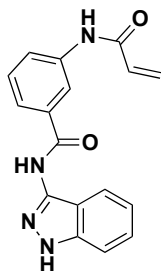
YZ0571-4

1H NMR (400 MHz, $DMSO-d_6$) δ 12.75 (s, 1H), 10.68 (s, 1H), 10.10 (s, 1H), 8.16 (d, $J = 2.0$ Hz, 1H), 7.92 (s, 0H), 7.82 (dd, $J = 8.1, 2.1$ Hz, 1H), 7.71 (dd, $J = 19.8, 8.2$ Hz, 2H), 7.51 – 7.39 (m, 2H), 7.34 (ddd, $J = 8.3, 6.8, 1.1$ Hz, 1H), 7.06 (dd, $J = 8.0, 6.9$ Hz, 1H), 2.06 (s, 3H). $[M + H]^+$ Calcd for $C_{16}H_{14}N_4O_2$ 295.11, found 295.3



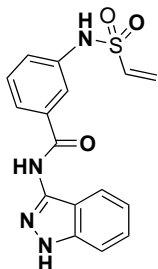
YZ0571-1

1H NMR (400 MHz, $DMSO-d_6$) δ 12.77 (s, 1H), 10.75 (s, 1H), 10.48 (s, 1H), 8.21 (t, $J = 1.9$ Hz, 1H), 7.83 (td, $J = 7.6, 7.1, 1.9$ Hz, 2H), 7.71 (d, $J = 8.2$ Hz, 1H), 7.50 (dd, $J = 9.6, 8.2$ Hz, 2H), 7.36 (ddd, $J = 8.3, 6.7, 1.1$ Hz, 1H), 7.08 (dd, $J = 8.1, 6.9$ Hz, 1H), 4.29 (s, 2H). $[M + H]^+$ Calcd for $C_{16}H_{13}ClN_4O_2$ 329.07, found 329.3



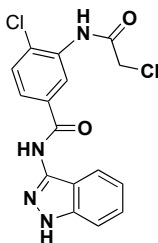
YZ0571-2

^1H NMR (400 MHz, $\text{DMSO-}d_6$) δ 12.78 (s, 1H), 10.73 (s, 1H), 10.34 (s, 1H), 8.27 (t, $J = 2.0$ Hz, 1H), 7.98 – 7.91 (m, 1H), 7.84 – 7.76 (m, 1H), 7.71 (dd, $J = 8.2, 1.1$ Hz, 1H), 7.54 – 7.45 (m, 2H), 7.36 (ddd, $J = 8.3, 6.7, 1.1$ Hz, 1H), 7.09 (ddd, $J = 8.0, 6.8, 0.9$ Hz, 1H), 6.47 (dd, $J = 17.0, 10.1$ Hz, 1H), 6.30 (dd, $J = 17.0, 2.0$ Hz, 1H), 5.79 (dd, $J = 10.0, 2.1$ Hz, 1H). $[\text{M} + \text{H}]^+$ Calcd for $\text{C}_{17}\text{H}_{14}\text{N}_4\text{O}_2$ 307.11, found 307.3



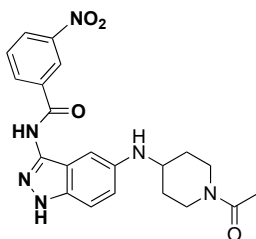
YZ0571-3

^1H NMR (400 MHz, $\text{DMSO-}d_6$) δ 12.76 (s, 1H), 10.74 (s, 1H), 10.17 (s, 1H), 7.83 – 7.75 (m, 2H), 7.69 (d, $J = 8.2$ Hz, 1H), 7.53 – 7.41 (m, 2H), 7.41 – 7.30 (m, 2H), 7.11 – 7.02 (m, 1H), 6.83 (dd, $J = 16.4, 10.0$ Hz, 1H), 6.13 (d, $J = 16.4$ Hz, 1H), 6.05 (d, $J = 10.0$ Hz, 1H). $[\text{M} + \text{H}]^+$ Calcd for $\text{C}_{16}\text{H}_{14}\text{N}_4\text{O}_3\text{S}$ 343.37, found 343.3



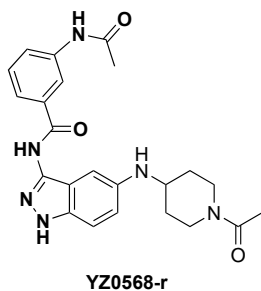
YZ0570-1

^1H NMR (400 MHz, $\text{DMSO-}d_6$) δ 12.80 (s, 1H), 10.89 (s, 1H), 10.05 (s, 1H), 8.40 (d, $J = 2.1$ Hz, 1H), 7.95 (dd, $J = 8.4, 2.1$ Hz, 1H), 7.71 (dd, $J = 8.3, 2.7$ Hz, 2H), 7.52 – 7.37 (m, 1H), 7.40 – 7.30 (m, 1H), 7.14 – 7.01 (m, 1H), 5.72 (d, $J = 8.3$ Hz, 0H), 5.56 (s, 0H), 4.41 (s, 2H).

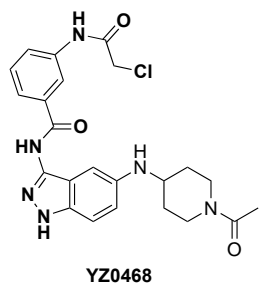


YZ0437

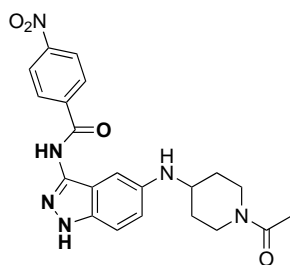
^1H NMR (400 MHz, $\text{DMSO-}d_6$) δ 12.42 (s, 1H), 10.91 (s, 1H), 8.87 (s, 1H), 8.52 – 8.41 (m, 2H), 7.85 (t, $J = 8.0$ Hz, 1H), 7.26 (d, $J = 8.9$ Hz, 1H), 6.89 (dd, $J = 8.9, 2.1$ Hz, 1H), 6.66 (d, $J = 2.0$ Hz, 1H), 5.22 (d, $J = 8.3$ Hz, 1H), 4.15 (d, $J = 13.3$ Hz, 1H), 3.75 (d, $J = 13.5$ Hz, 1H), 3.45 (dd, $J = 8.4, 3.5$ Hz, 1H), 3.17 (d, $J = 5.1$ Hz, 2H), 2.88 – 2.77 (m, 1H), 1.99 (s, 3H), 1.95 – 1.83 (m, 1H), 1.38 – 1.11 (m, 2H).



^1H NMR (400 MHz, $\text{DMSO-}d_6$) δ 12.33 (d, $J = 18.6$ Hz, 1H), 10.46 (s, 1H), 10.12 (s, 1H), 8.16 (d, $J = 1.9$ Hz, 1H), 7.82 (dd, $J = 8.1, 2.1$ Hz, 1H), 7.73 (d, $J = 7.7$ Hz, 1H), 7.44 (t, $J = 7.9$ Hz, 1H), 7.25 (dd, $J = 8.9, 3.7$ Hz, 1H), 6.87 (dt, $J = 9.0, 2.6$ Hz, 1H), 6.66 – 6.59 (m, 1H), 5.24 (d, $J = 25.1$ Hz, 1H), 4.14 (dd, $J = 11.4, 6.7$ Hz, 1H), 3.76 (dd, $J = 13.7, 4.5$ Hz, 1H), 3.43 (tt, $J = 11.8, 5.1$ Hz, 1H), 3.17 (ddd, $J = 13.6, 10.7, 2.9$ Hz, 1H), 2.54 (s, 1H), 2.07 (s, 2H), 2.05 – 1.84 (m, 5H), 1.42 – 1.15 (m, 2H).

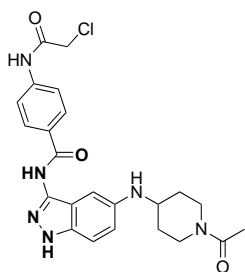


^1H NMR (400 MHz, $\text{DMSO-}d_6$) δ 13.02 (s, 1H), 10.88 (d, $J = 6.1$ Hz, 1H), 10.49 (s, 1H), 8.19 (d, $J = 21.4$ Hz, 1H), 7.92 – 7.78 (m, 2H), 7.68 (d, $J = 8.1$ Hz, 1H), 7.59 – 7.46 (m, 2H), 7.23 (dt, $J = 9.6, 1.9$ Hz, 1H), 4.65 (s, 1H), 4.42 (d, $J = 13.3$ Hz, 1H), 4.28 (s, 2H), 3.83 (dd, $J = 15.3, 13.1$ Hz, 2H), 3.10 (t, $J = 12.9$ Hz, 1H), 2.56 (t, $J = 12.7$ Hz, 1H), 1.99 (s, 1H), 1.88 (s, 3H), 1.81 (d, $J = 15.1$ Hz, 1H), 1.26 – 1.09 (m, 1H).
 MS (APCI) m/z : $[\text{M} + \text{H}]^+$ Calcd for $\text{C}_{23}\text{H}_{25}\text{ClN}_6\text{O}_3$ 469.94, found 469.4



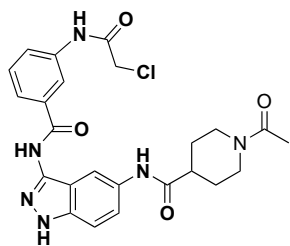
YZ0436

^1H NMR (400 MHz, $\text{DMSO-}d_6$) δ 12.42 (s, 1H), 10.86 (s, 1H), 8.37 (d, $J = 8.4$ Hz, 2H), 8.27 (d, $J = 8.4$ Hz, 2H), 7.26 (d, $J = 8.9$ Hz, 1H), 6.88 (dd, $J = 9.0, 2.1$ Hz, 1H), 6.65 (d, $J = 2.1$ Hz, 1H), 5.22 (d, $J = 8.3$ Hz, 1H), 4.15 (d, $J = 13.3$ Hz, 1H), 3.75 (d, $J = 13.8$ Hz, 1H), 3.50 – 3.38 (m, 0H), 3.22 – 3.11 (m, 2H), 2.83 (s, 1H), 1.99 (s, 3H), 1.91 (d, $J = 26.8$ Hz, 1H), 1.31 (q, $J = 13.6$ Hz, 1H), 1.25 – 1.11 (m, 1H). MS (APCI) m/z : $[\text{M} + \text{H}]^+$ Calcd for $\text{C}_{21}\text{H}_{22}\text{N}_6\text{O}_4$ 423.17, found 423.4



YZ0466

^1H NMR (400 MHz, $\text{DMSO-}d_6$) δ 13.01 (s, 1H), 10.78 (d, $J = 9.9$ Hz, 1H), 10.60 (s, 1H), 8.06 (d, $J = 8.8$ Hz, 2H), 7.71 (dd, $J = 25.1, 8.3$ Hz, 3H), 7.55 (d, $J = 8.8$ Hz, 1H), 7.23 (d, $J = 8.0$ Hz, 1H), 4.64 (s, 1H), 4.42 (d, $J = 13.4$ Hz, 1H), 4.31 (s, 2H), 3.85 (dt, $J = 17.0, 13.9$ Hz, 2H), 3.05 (s, 2H), 2.57 (d, $J = 13.2$ Hz, 1H), 1.88 (s, 3H), 1.83 (s, 2H).



YZ0588

^1H NMR (400 MHz, $\text{DMSO-}d_6$) δ 12.72 (s, 1H), 10.70 (s, 1H), 10.51 (s, 1H), 9.90 (s, 1H), 8.22 (t, $J = 1.9$ Hz, 1H), 7.96 (d, $J = 1.8$ Hz, 1H), 7.82 (td, $J = 7.4, 6.7, 1.8$ Hz, 2H), 7.57 – 7.45 (m, 2H), 7.43 (d, $J = 8.9$

Hz, 1H), 4.44 – 4.34 (m, 1H), 4.29 (s, 2H), 3.86 (d, $J = 13.6$ Hz, 1H), 3.61 (pd, $J = 6.6, 3.9$ Hz, 1H), 3.06 (td, $J = 13.5, 3.1$ Hz, 1H), 2.58 (ddd, $J = 15.5, 9.5, 3.8$ Hz, 2H), 2.00 (s, 3H), 1.79 (dt, $J = 13.6, 7.8$ Hz, 1H), 1.51 (dq, $J = 57.4, 12.3, 4.2$ Hz, 2H). MS (APCI) m/z : $[M + H]^+$ Calcd for $C_{24}H_{25}ClN_6O_4$ 497.16, found 497.4

Chapter 3: Pharmacokinetic and Pharmacodynamic Study of IKE²

3.1 Introduction

Ferroptosis is a type of regulated cell death driven by iron-dependent lipid peroxidation that can be inhibited by iron chelators and lipophilic antioxidants³³⁻³⁴. Ferroptosis has a role in regulating survival of some tumor cell types, such as lymphomas, renal cell carcinomas, and hepatocellular carcinomas⁷⁰⁻⁷². Ferroptosis inducers synergize with several chemotherapies, including cisplatin, temozolomide, and doxorubicin in cell culture studies⁷⁴⁻⁷⁷. The ferroptosis-suppressing cystine (Cys₂)/glutamate (Glu) antiporter system x_c⁻ is required in some cell contexts for providing cysteine^{34-35, 49}; inhibition of system x_c⁻ can induce ferroptosis through cysteine deprivation, subsequent glutathione (GSH) depletion, and ultimately inactivation of glutathione peroxidase 4 (GPX4)⁵¹⁻⁵². However, existing system x_c⁻ inhibitors, including sulfasalazine, glutamate, sorafenib, and erastin, are not suitable for *in vivo* evaluation due to the lack of potency, selectivity, and/or metabolic stability. IKE is an erastin analog with nanomolar potency, high metabolic stability and intermediate water solubility, thus potentially representing a suitable candidate for *in vivo* evaluation of the impact of ferroptosis driven through system x_c⁻ inhibition in mouse models of cancer⁵⁷.

Diffuse large B cell lymphoma (DLBCL) is an aggressive malignancy of B-lineage lymphocytes, accounting for 30-40% of non-Hodgkin's lymphoma. DLBCL cell lines are particularly sensitive to ferroptosis induced by system x_c⁻ inhibition^{5, 51, 67}, due to their inability to use the transsulfuration pathway to synthesize cysteine from methionine, making these cell lines dependent on uptake of cyst(e)ine from the micro-environment⁷¹. DLBCL is clinically heterogeneous, with 60% of patients curable with combination therapy, and the remainder succumbing to the disease¹³²⁻¹³³. Thus, therapies with distinct mechanisms of action may be beneficial for refractory patients, preventing disease relapse,

²This chapter is adapted from the manuscript submitted: Zhang, Y.; Tan, H.; Daniels J. D.; Zandkarimi, F.; Liu, H.; Brown, L. M.; Uchida, K.; O'Connor, O. A.; Stockwell, B. R., Imidazole ketone erastin nanoparticles induce ferroptosis and slow tumor growth in a mouse lymphoma model

and improving therapeutic outcomes. Here, we identified ferroptosis-sensitive and resistant DLBCL cell lines and established a subcutaneous DLBCL xenograft model to study the role of ferroptosis in treating DLBCL. We found that IKE exhibits antitumor activity in this DLBCL xenograft model and an associated increase in lipid peroxidation in tumors. These findings suggest that IKE can be effective as a novel potential therapeutic regimen for DLBCL.

Erastin is a useful small molecule for *in vitro* studies but is metabolically labile and has low water solubility and potency, which precludes its use *in vivo*. The small molecule IKE is an erastin analog incorporating a metabolically stable carbonyl (Figure 3.1), which can potentially form a reversible covalent interaction with proteins, resulting in >100x potency improvement comparing to erastin in some cell lines^{51, 57}. Substitution of an ethoxy moiety with isopropoxy resulted in improved metabolic stability, and the imidazole moiety in IKE helps increase water solubility, makes IKE soluble under acidic conditions.

In this chapter, the *in vitro* pharmacodynamics of IKE will be discussed.

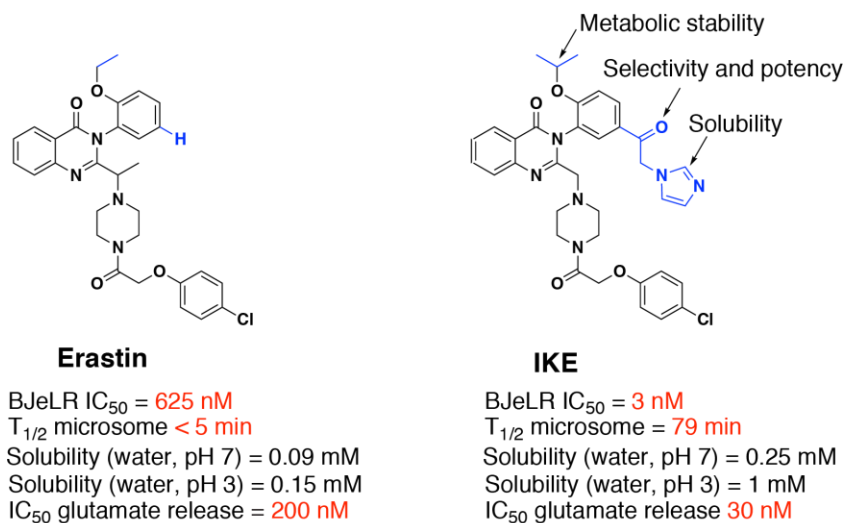


Figure 3. 1 Chemical structure of erastin and imidazole-ketone-erastin (IKE).

Small molecule IKE with isopropoxy, ketone, and imidazole substitutions is more potent than erastin and PE.

3.2 Result

3.2.1 DLBCL have differential sensitivity to IKE

Yang and colleagues have proved high sensitivity of DLBCL to ferroptosis inducer erastin by analyzing 127 cancer cell lines against diverse lethal compounds^{51, 67}. The extreme sensitivity of DLBCL to ferroptosis might come from the dysfunctional transsulfuration pathways in DLBCL making these cell lines rely on the uptake of cysteine from the microenvironment or culture medium (Figure 3.2).

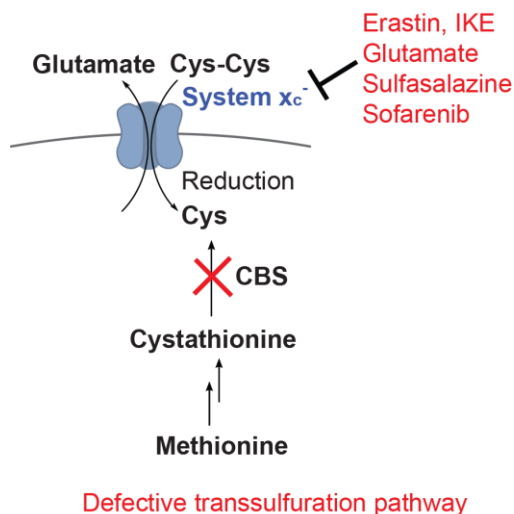


Figure 3. 2 Pathways regulating sensitivity of DLBCLs to IKE

DLBCLs have defective transsulfuration pathways resulting in disability to synthesis cysteine (Cys) thus heavily rely on the uptake of cysteine from the microenvironment.

We collected a panel of 18 DLBCL cell lines representing distinct DLBCL subtypes, including germinal center B cell-like (GCB), activated B cell like (ABC), and unclassified subgroups, to evaluate IKE sensitivity. The 18 DLBCL cell lines showed differential sensitivity to IKE inhibition, with cell lines exhibiting $IC_{50} < 20$ nM classified as sensitive cell lines, those with $IC_{50} > 10$ μ M classified as resistant cell lines, and those with IC_{50} values between 20 nM to 10 μ M classified as cell lines with intermediate

resistance (**Figure 3.3 A**). We further tested the degree of IKE-induced lethality upon co-treatment with the ferroptosis inhibitor ferrostatin-1 (fer-1)^{55, 67}, a radical-trapping antioxidant that inhibits lethal lipid peroxidation during ferroptosis. Co-treatment with fer-1 rescued cell death induced by IKE in DLBCL cell lines, indicating that IKE-induced lethality in these cell lines resulted from lipid peroxidation and ferroptosis (**Figure 3.3 B**). Among the most sensitive DLBCL cell lines, we selected SUDHL-6 for generating a subcutaneous xenograft model in 6-week-old male NCG mice, which will be discussed in the next chapter.

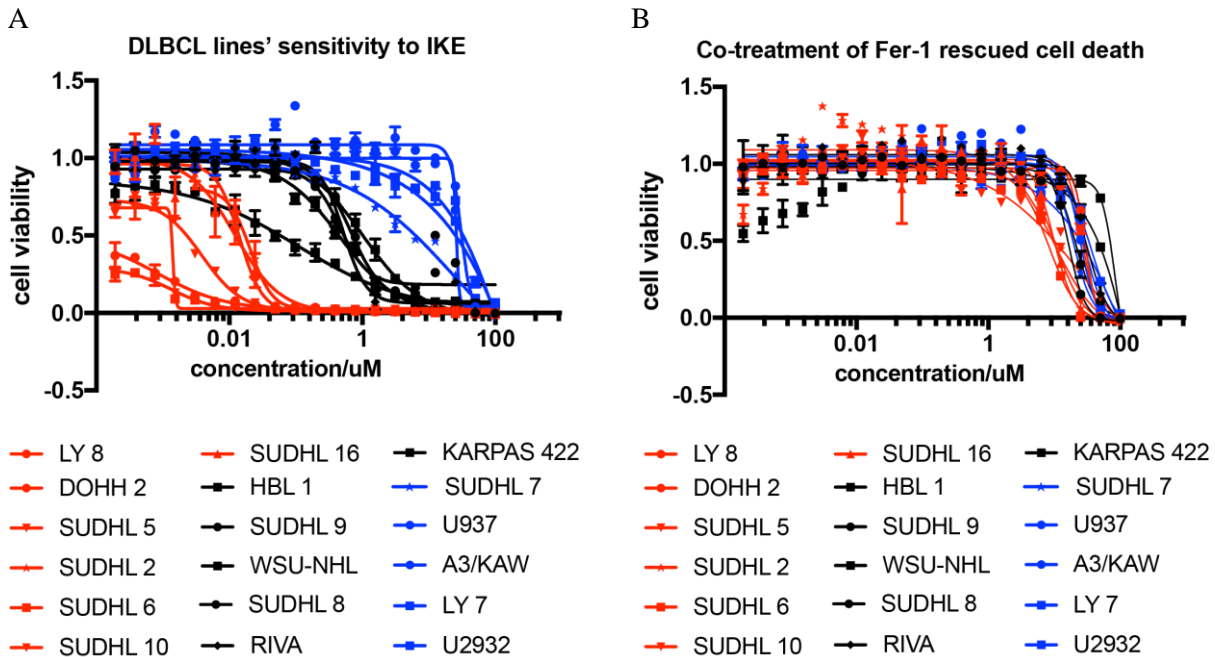


Figure 3. 3 Test of DLBCL sensitivity to IKE using cell viability assay

(A) DLBCL lines have differential sensitivity to IKE. The cell viability was measured by incubating cells with a two-fold series dilution of IKE (starting from 100 μ M) for 24 hours followed by a Cell Titor-Glo luminescent cell viability test. LY 8, DOHH 2, SUDHL 5, SUDHL 2, SUDHL 6, SUDHL 10, and SUDHL 16 were classified as sensitive classified lines (red color). HBL 1, SUDHL 9, WSU-NHL, SUDHL 8, RIVA, and KARPAS 422 were grouped as moderate resistant cell lines (black color). SUDHL 7, U937, A3/KAW, LY 7, and U2932 were classified as resistant cell lines (blue color). (B) Co-treatment with a two-fold series dilution of Fer-1 (starting from 200 μ M) rescued cell death induced by IKE. The x-axis shows the concentration of IKE.

Since DLBCL cell lines have differential sensitivity to IKE, there must be some intrinsic factors affecting DLBCL's sensitivity. We tried to explore the intrinsic biomarkers predicting DLBCL's sensitivity to ferroptosis by analyzing expression levels of ferroptosis-related genes by RT-qPCR. *ACSL4* and *LPCAT3*, which were identified to be overexpressed in ferroptosis resistant cell lines⁸⁶ didn't show differential expression across sensitive, medium resistant, and resistant DLBCL groups. Cystathionine-beta-synthase (*CBS*), system x_c^- light chain xCT (*SLC7A11*), and ferritin light chain (*FTL*) have higher average expression in resistant DLBCL groups comparing with sensitive and medium resistant DLBCL groups (**Figure 3.4**). *CBS* catalyzes cysteine biosynthesis from cystathionine, the high expression level of this protein would increase cysteine synthesis making cells less dependent on system x_c^- mediated cystine (Cys-Cys) import. Ferritin is an iron storage protein; the high expression level of this protein might decrease the free iron concentration in cells making cells less likely to have ferroptotic cell death. However, it is hard to predict the sensitivity or resistance of a specific DLBCL cell line using *CBS*, *SLC7A11*, and *FTL* because there were extensive expression variabilities within each DLBCL group.

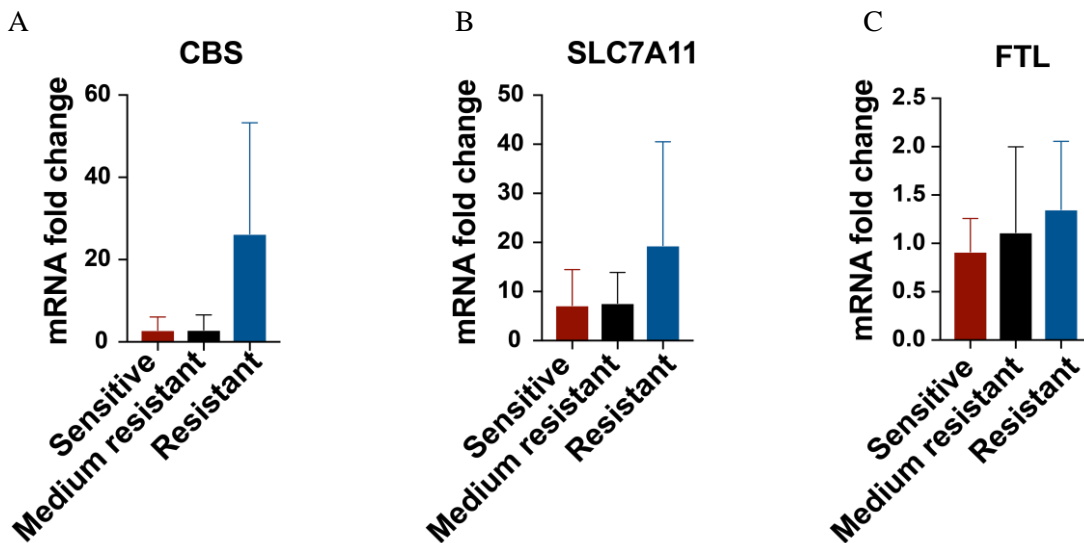


Figure 3. 4 *CBS*, *SLC7A11*, and *FTL* gene expression levels in different sensitivity groups of DLBCL. Cystathionine-beta-synthase (*CBS*) (A), system x_c^- light chain xCT (*SLC7A11*) (B), and ferritin light chain (*FTL*) (C) have higher average expression in resistant DLBCL groups comparing with sensitive and medium resistant DLBCL groups

3.2.2 Pharmacodynamics study of IKE *in vitro*

We aimed to investigate whether IKE specifically inhibited system x_c^- and induced ferroptosis in DLBCL cells. Inhibition of system x_c^- prevents cystine import and glutathione biosynthesis. A fluorometric method measuring reduced glutathione (GSH) concentration was used to evaluate IKE's inhibitory effect on system x_c^- . Dose-dependent GSH depletion by IKE was observed (**Figure 3.5A**); this effect was reversed by co-treatment with 10 μM β -mercaptoethanol (β -Me), which reduces cystine to cysteine, allowing its import into cells through system L, thus circumventing inhibiting of system x_c^- (**Figure 3.5B**). We observed that 250 nM IKE was able to deplete 94% of GSH in SUDHL-6 cells. The IC_{50} for GSH depletion by sulfasalazine was previously reported to be 1 mM^{134} , while, the IC_{50} of GSH depletion by IKE that we measured was 34 nM (**Figure 3.5A**), indicating that IKE is a potent inhibitor of system x_c^- .

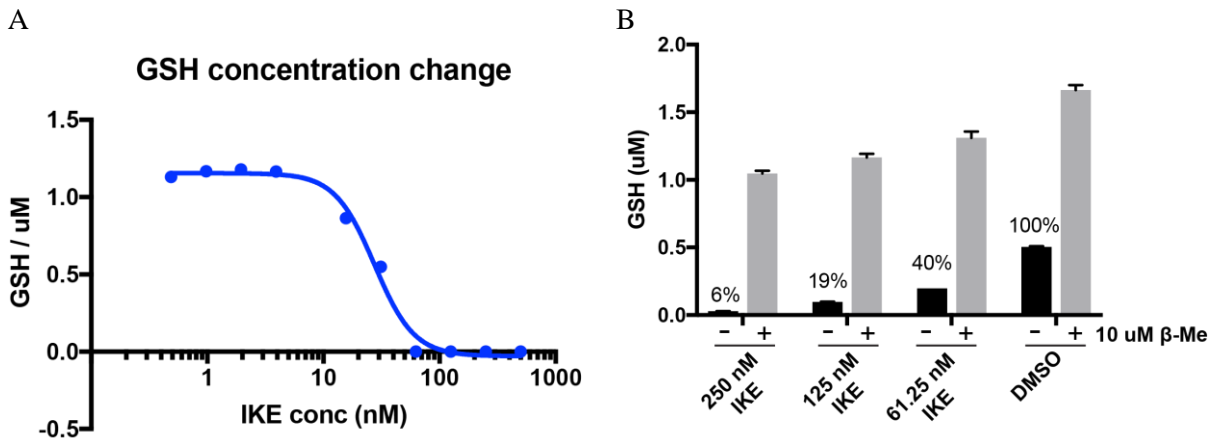


Figure 3. 5 Measurement of GSH level in IKE treated SUDHL-6 cells

GSH level was measured with a fluorometric-green probe in SUDHL6 cells treated with different concentration of IKE with or without 10 μM β -Me for 24 hours. (A) IKE induced glutathione depletion in a concentration-dependent way. The IC_{50} of glutathione depletion by IKE is 34 nM measured by three independent experiments. (B) Co-treatment of 10 μM β -ME inhibited IKE induced glutathione depletion by promoting cysteine uptake through L systems.

We next sought to evaluate whether IKE treatment caused lipid peroxidation in DLBCL cells, as a marker of ferroptosis. Analysis of lipid ROS by flow cytometry using the C11-BODIPY probe, a lipid

peroxidation sensor, revealed increased lipid ROS upon IKE treatment in SUDHL-6 cells in a dose-dependent manner (**Figure 3.6A**). Co-treatment with 10 μ M fer-1 inhibited this signal, as expected (**Figure 3.6B**).

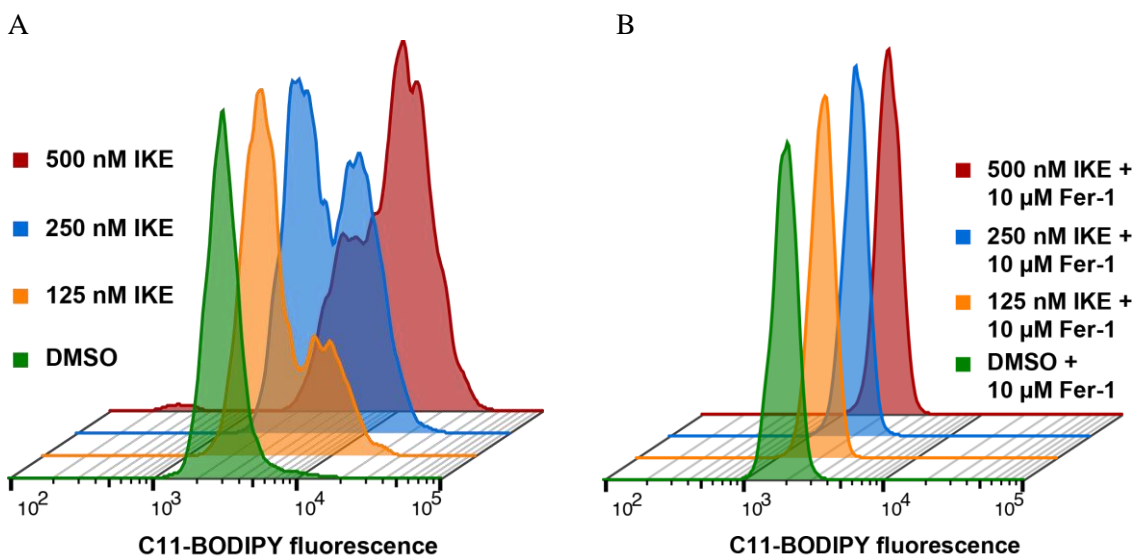


Figure 3. 6 Measurement of lipid peroxidation level in IKE treated SUDHL-6 cells using flow cytometry

Lipid-peroxidation level shown as C11-BODIPY fluorescence increase was measured in SUDHL6 cells treated with different concentration of IKE with or without 10 μ M Fer-1. (A) With increasing IKE concentration, there was increased lipid peroxidation. (B) Co-treatment of 10 μ M Fer-1 completely inhibited IKE induced lipid peroxidation.

We reasoned that lipo-oxidative stress markers, including lipid-peroxide-derived protein modifications and aldehyde-derived protein modifications might also be used as ferroptosis biomarkers. Malondialdehyde (MDA) is a naturally occurring reactive carbonyl compound that is derived from lipid peroxidation of polyunsaturated fatty acyl moieties. Immunofluorescence staining with an anti-MDA-lysine-adduct antibody (mAb 1F83), which specifically recognizes 4-methyl-1,4-dihydropyridine-3,5-dicarbaldehyde (MDHDC)¹³⁵⁻¹³⁶, revealed that MDA adduct abundance was increased upon IKE treatment (**Figure 3.7**).

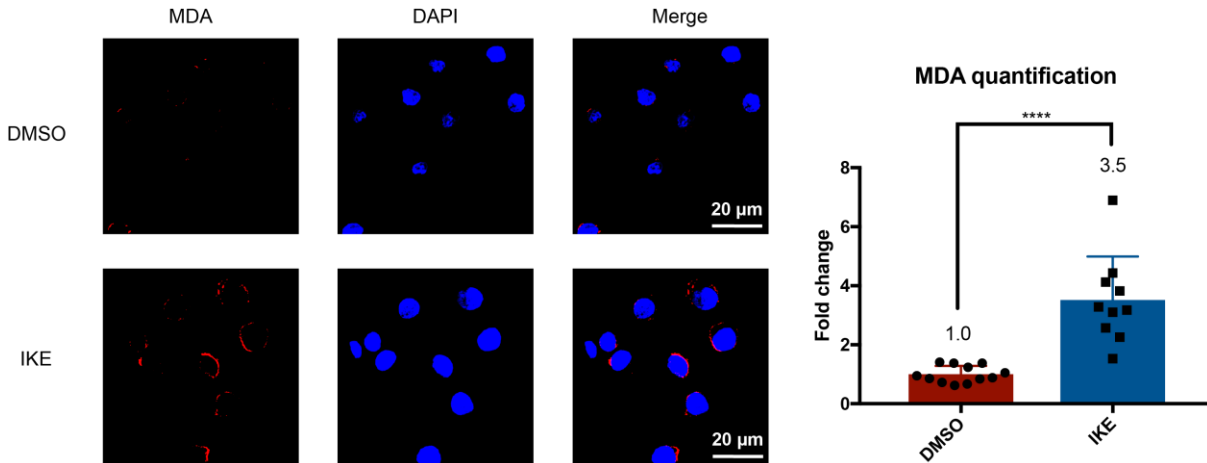


Figure 3. 7 Measurement of MDA level in SUDHL-6 cells using immunofluorescence

Immunofluorescence intensity of MDA in SUDHL6 cells with DMSO or 10 μ M IKE treatment for 6 hours indicated 3.4-fold increased MDA upon IKE treatment. **** P<0.0001 by t test.

To facilitate molecular characterization of ferroptosis induction in DLBCL cells, we analyzed gene expression biomarkers of ferroptosis in these cell lines by RT-qPCR. Expression of genes involved in ferroptosis³⁴, such as glutathione peroxidase 4 (*GPX4*), cystathionine beta-synthase (*CBS*), and acyl-CoA synthetase long-chain family member 4 (*ACSL4*) were analyzed upon IKE treatment. We determined that expression of the system x_c^- component *SLC7A11*, prostaglandin-endoperoxide synthase 2 (*PTGS2*, which encodes cyclooxygenase-2), and ChaC glutathione-specific gamma-glutamylcyclotransferase 1 (*CHAC1*) were significantly increased following IKE treatment in cultured SUDHL-6 cells (**Figure 3.8**). *SLC7A11*, the substrate-specific subunit system x_c^- , exhibited increased expression following 500 nM IKE treatment for more than 1 h. *PTGS2* was reported to be upregulated by the lipid peroxidation product 4-hydroxy-2-nonenal (4-HNE)¹³⁷ and by GPX4 depletion¹³⁸. *PTGS2* expression was increased following 500 nM IKE treatment, and co-treatment with fer-1 inhibited this upregulation, suggesting that *PTGS2* is a functional biomarker of ferroptosis (**Figure 3.9**). The mRNA level of *CHAC1* was increased following 500 nM IKE treatment, and fer-1 co-treatment did not inhibit its upregulation, as expected, indicating that *CHAC1* is a parallel downstream marker of system x_c^- inhibition not affected by lipid peroxidation (**Figure 3.9**). In addition, co-treatment with 10 μ M β -Me prevented IKE-induced upregulation of

SLC7A11, *PTGS2*, and *CHAC1*, suggesting that the upregulation of these genes was downstream of cysteine starvation. The upregulation of these three mRNAs was time-dependent (**Figure 3.8**), with increasing time of treatment, we observed increased gene expression, making these genes suitable for monitoring IKE pharmacodynamics.

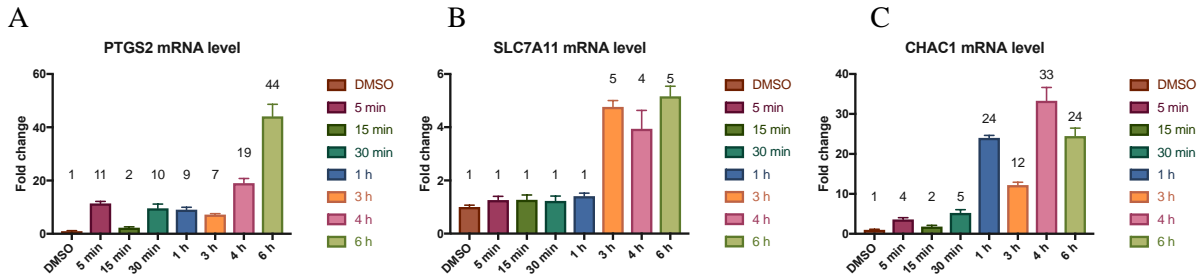


Figure 3. 8 IKE induced ferroptosis marker change in a time-dependent way.

RT-qPCR was performed in SUDHL-6 cells treated with 500 nM IKE for different time. (A) IKE induced *PTGS2* upregulation very quickly, starting from 5 minutes, there was over 10-fold increased *PTGS2* expression. (B) *SLC7A11* expression was induced by IKE starting from 3 hours incubation. (C) *CHAC1* expression was induced by IKE immediately, starting from 5 minutes, there was over 5-fold increased *CHAC1* expression. The highest mRNA change was 33 fold.

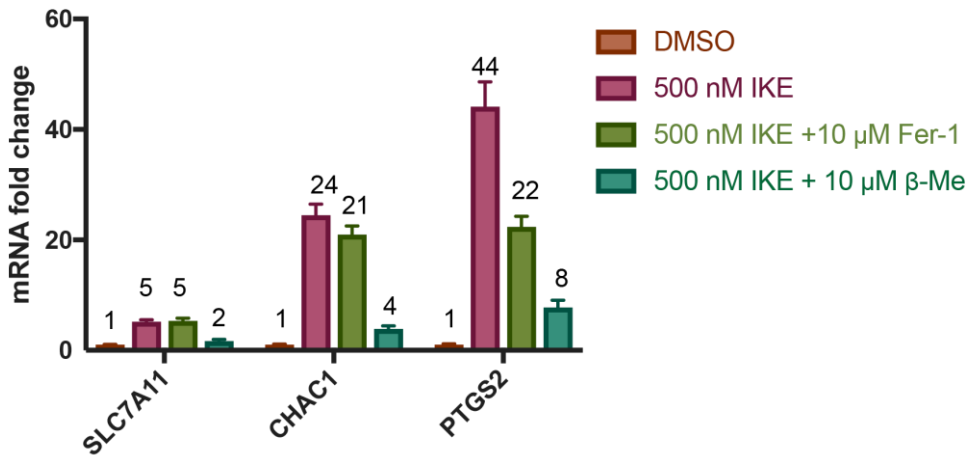


Figure 3. 9 *SLC7A11*, *CHAC1*, and *PTGS2* are specific for IKE-induced ferroptosis

RT-qPCR was performed in SUDHL-6 cells treated with indicated compounds for 6 hours. (A) 500 nM IKE treatment induced *SLC7A11*, *CHAC1*, and *PTGS2* upregulation. Co-treatment of 10 μM fer-1 inhibited *PTGS2* upregulation but not *SLC7A11* and *CHAC1*. Co-treatment of 10 μM β-Me inhibited all three genes upregulation.

While, IKE induced cell death through inhibiting system x_c^- resulting in GSH depletion and lipid peroxidation, a distinct cell death mechanism different from apoptosis, we are curious about whether there is increased caspase-3 activity in this process. An Apo-ONE homogeneous caspase-3/7 (Promega) assay was performed to measure the caspase-3/7 cleavage activity through detecting the fluorescent Rhodamine which is cleaved from a pro-fluorescent caspase-3/7 consensus substrate (**Figure 3.10A**). Caspase 3/7 activity was increased upon IKE treatment, which might result from the oxidative stress generated by system x_c^- inhibition because Fer-1 or β -Me cotreatment reduced caspase 3/7 activity resulted from IKE. A western blot measuring the abundance of cleaved-caspase 3 confirmed that IKE-induced oxidative stress would increase caspase-3 activity (**Figure 3.10B**).

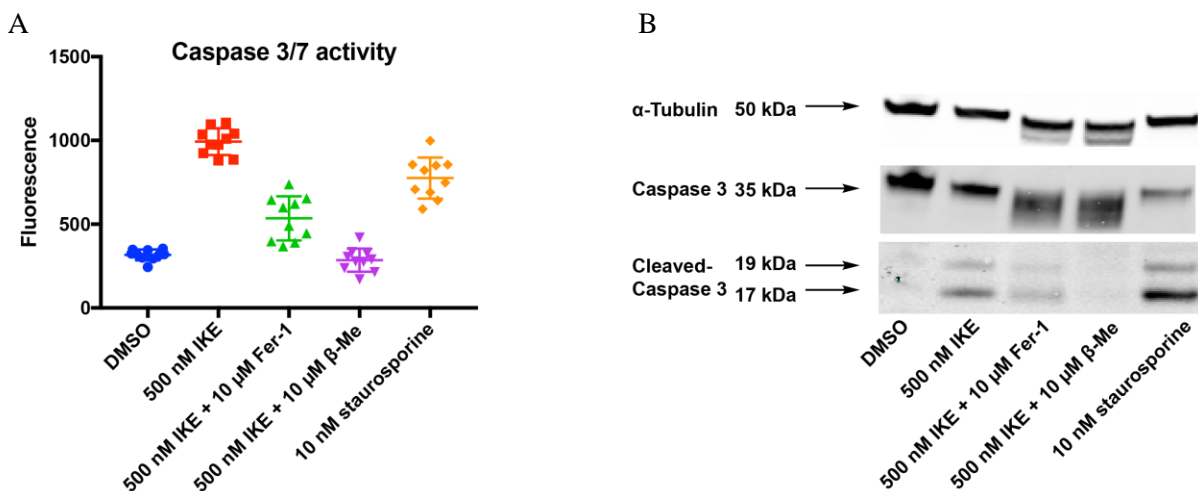


Figure 3. 10 Caspase-3 activity measurement using Apo-ONE assay and western blot

(A) Caspase 3/7 activity was measured by Apo-ONE homogenous caspase-3/7 assay in SUDHL-6 cells treated with 500 nM IKE, 500nM IKE with 10 μ M Fer-1 cotreatment, 500nM IKE with 10 μ M β -Me cotreatment, and 10 nM staurosporine for 24 hours. (B) Analysis of caspase and cleaved-caspase abundance by western blot.

3.3.3 Pharmacokinetics (PK) and pharmacodynamics (PD) study of IKE *in vivo*

To determine the suitability of IKE for *in vivo* studies, we first evaluated multiple dosage routes by administrating a single dose of IKE (50 mg/kg, 5% DMSO in HBSS) using IP, IV, and PO routes to

NOD/SCID mice. Determination of IKE concentration over a period of eight hours revealed IP to be the most effective and practical means of IKE administration (Table 3).

Next, IKE concentration in plasma and tumor samples was determined after single dose of IKE (50 mg/kg, 5% DMSO in HBSS, IP) to SUDHL-6-xenograft-bearing NCG mice over a period of 24 hours. IKE reached the highest plasma concentration of 5.2 $\mu\text{g/mL}$ at 2 h, and the highest tumor accumulation of 2.5 $\mu\text{g/mL}$ at 4 h (Table 4 and Figure 3.11A).

Table 3. 1 IKE distribution in plasma through IP, IV and PO administration routes

| | Tmax h | Cmax ng/mL | half-life h | Tlast h | Clast ng/mL | AUClast h*ng/mL |
|----|-----------|---------------|----------------|------------|----------------|--------------------|
| IP | 0.31 | 19515 | 1.82 | 8 | 1527 | 53898 |
| IV | 0 | 11384 | 1.31 | 8 | 16 | 16983 |
| PO | 0.72 | 5203 | 0.96 | 8 | 48 | 5723 |

Table 3. 2 IKE distribution in plasma and tumor tissue through IP administration

| | Tmax h | Cmax ng/mL | half-life h | Tlast h | Clast ng/mL | AUClast h*ng/mL |
|--------|-----------|---------------|----------------|------------|----------------|--------------------|
| Plasma | 1.35 | 5185 | 1.83 | 24 | 30 | 10926 |
| Tumor | 3.30 | 2516 | 3.50 | 24 | 283 | 9857 |

We collected tumor samples from each time point after a single dose of IKE (50 mg/kg, 5% DMSO in HBSS) and evaluated the abundance of ferroptosis biomarkers. There was significant GSH depletion upon IKE dosing starting from 4 h (Figure 3.11B). The GSH depletion in tumors induced by IKE was persistent at 24 h, as there was little IKE left in the bulk tumor sample, but up to 70% GSH depletion. Consistent with IKE accumulation kinetics in the tumor samples, *CHAC1*, *SLC7A11*, and *PTGS2* mRNAs were upregulated starting at 3 h. (3-5 fold for *PTGS2* and *SLC7A11*, and 2-fold for *CHAC1*) (Figure 3.12).

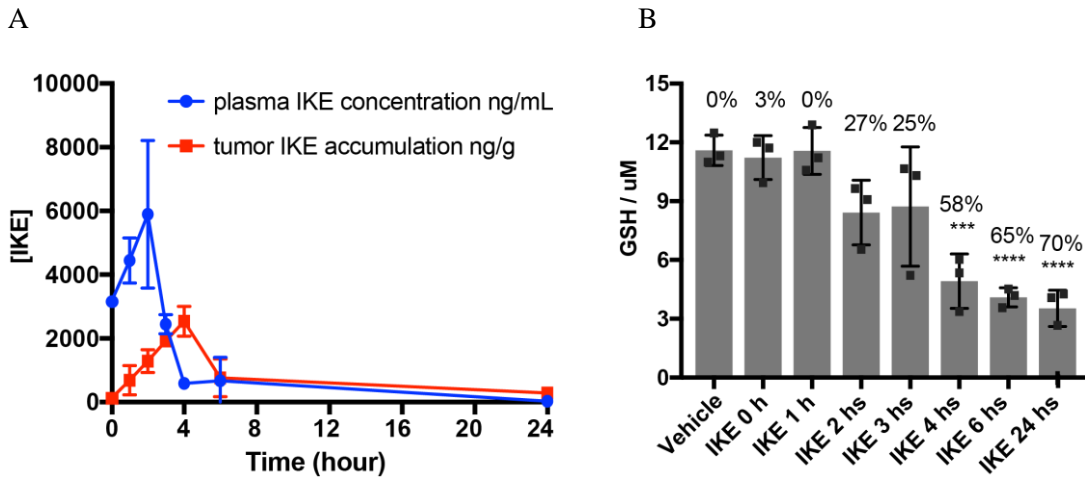


Figure 3. 11 PK/PD study of IKE in NCG mice bearing SUDHL-6 xenograft

(A) A pharmacokinetic study performed in SUDHL6 subcutaneously xenografted NCG mice measured IKE accumulation over time in plasma and tumor using LC-MS. (B) Analysis of GSH extracted from tumor tissue by fluorometric-green showed over 50% GSH depletion with IKE treatment starting at 4 hours. *** P<0.001, **** P<0.0001 by one-way ANOVA.

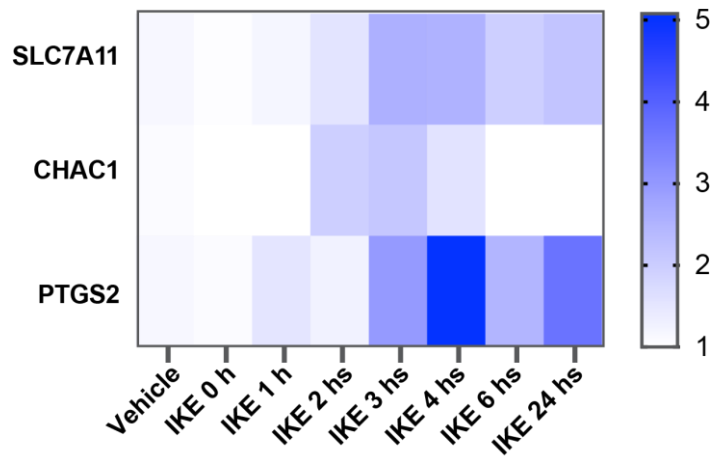


Figure 3. 12 Analysis of ferroptosis gene biomarkers in tumor tissues of IKE treated SUDHL-6 xenografts

RT-qPCR performed using RNA extracted from tumor tissue showed *PTGS2*, *SLC7A11*, and *CHAC1* mRNA increase starting from 3 hours, colored as blue in the heatmap.

Immunofluorescence analysis of samples at 4 h post-treatment showed that there was increased abundance of MDA adduct and 8-hydroxy-2'-deoxyguanosine (8-OHdG), a biomarker for free radical-induced oxidative lesions, indicating that IKE induced lipid peroxidation and DNA damage in these tumor samples (**Figure 3.13** and **3.14**).

3.3 Conclusion and Discussion

DLBCL cell lines have differential sensitivity to IKE-induced ferroptosis. The intrinsic factors determining DLBCL ferroptosis sensitivity remain to be explored to increase the understanding to ferroptosis and to enable patient selection. In summary, IKE has nanomolar cellular activity *in vitro*. The treatment of IKE induced GSH depletion, lipid peroxidation and ferroptosis. A series of biomarkers including lipid peroxidation level, oxidative stress, gene expression level of *PTGS2*, *CHAC1*, and *SL7A11* could be used to evaluate IKE-induced ferroptosis *in vitro* and *in vivo*.

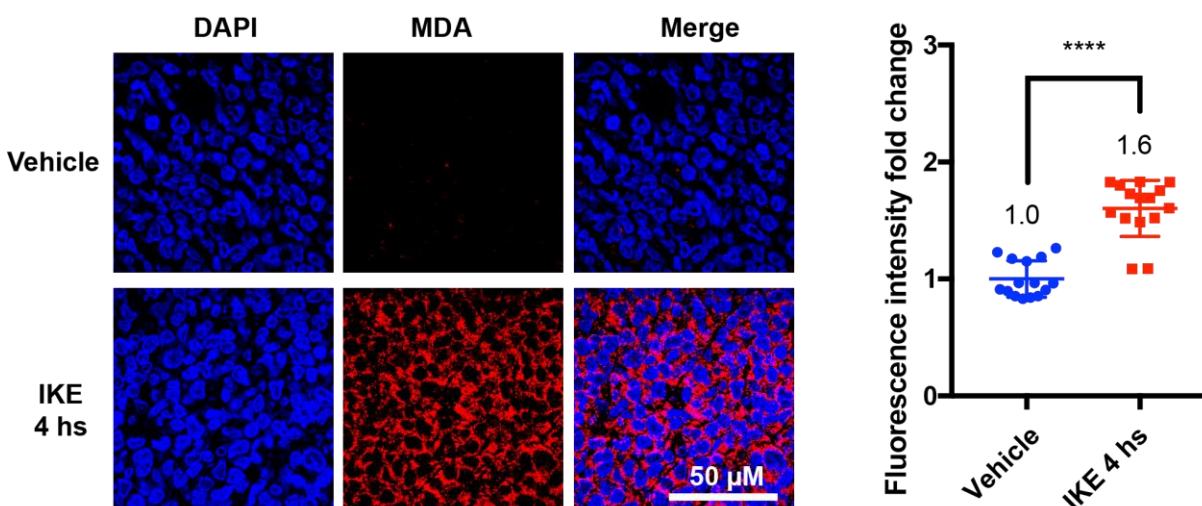


Figure 3. 13 Measurement of MDA level in tumor tissues of IKE treated SUDHL-6 xenografts using immunofluorescence

Immunofluorescence of MDA in paraffin-embedded tumor samples from mice treated with one dosage vehicle or IKE for 4 hours showed increased MDA-lysine adducts upon IKE treatment. Quantification of fluorescence intensity showed 1.6-fold increase of MDA-lysine adducts in IKE treated mice tumor tissue relative to the vehicle treated mice tumor tissue. (sections were cut from 3 mice in each group, five images from each section were captured on Zeiss LSM 800 63x/1.40 Oil DIC objective). *** $P < 0.001$, **** $P < 0.0001$ by t test.

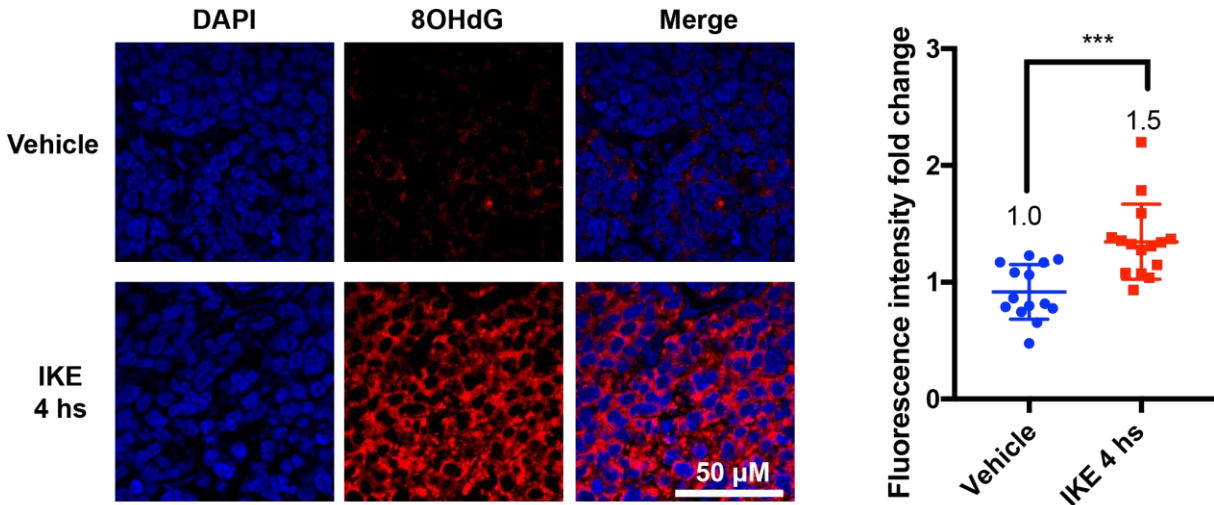


Figure 3. 14 Measurement of 8-OHdG level in tumor tissues of IKE treated SUDHL-6 xenografts using immunofluorescence

Immunofluorescence of 8-OHdG in paraffin-embedded tumor samples from mice treated with one dosage vehicle or IKE for 4 hours showed increased 8-OHdG upon IKE treatment. Quantification of fluorescence intensity showed 1.6-fold increase of 8-OHdG in IKE treated mice tumor tissue relative to the vehicle treated mice tumor tissue. (sections were cut from 3 mice in each group, five images from each section were captured on Zeiss LSM 800 63x/1.40 Oil DIC objective). *** $P < 0.001$, **** $P < 0.0001$ by t test.

3.4 Methods

Cell lines and media.

The SUDHL-5, SUDHL-6, SUDHL-16, and HT-1080 cell lines were obtained from ATCC. The DOHH-2 cell line was obtained from DSMZ. The HBL-1, U2932, SUDHL-7, SUDHL-9, A4/FUK, WSU-DHL, Ly18, Karpas422, SUDHL-1, SUDHL-2, SUDHL-8, SUDHL-10, A3/KAW, RIVA, Ly9, U937, and Ly7 cell lines were provided by Dr. Owen A. O'Connor (Columbia University) and the Columbia Genome Center. HT-1080 cells were grown in DMEM with glutamine and sodium pyruvate (Corning 10-013) supplemented with 10% heat-inactivated fetal bovine serum (FBS) (Life Technologies, 10437036) 1% non-essential amino acids (Thermo Fisher Scientific, 11140076) and 1% penicillin-streptomycin mix (pen-strep) (Thermo Fisher Scientific, 15140148). SUDHL-1, SUDHL-2, SUDHL-6, SUDHL-8, SUDHL-10, SUDHL-16, A3/KAW, RIVA, Ly8 and U937 cells were cultured in RPMI-1640 (ATCC 30-2001) with 10% FBS and 1% pen-strep. DOHH-2, HBL-1, U2932, SUDHL-7, SUDHL-9, A4/FUK,

WSU-NHL, and Ly8 were cultured in RPMI-1640 with 10% heat-inactivated FBS and 1% pen-strep. SUDHL-5 and Karpas422 were cultured in RPMI-1640 with 20% FBS and 1% pen-strep. Ly7 was cultured in IMDM (Thermo Fisher Scientific, 12440053) with 15% heat-inactivated FBS and 1% pen-strep. All cells were maintained in a humidified environment at 37 °C and 5% CO₂ in an incubator.

Animal studies

The animal studies reported in this manuscript adhere to the ARRIVE guidelines. All animal study protocols were approved by the Columbia University Institutional Animal Care and Use Committee (IACUC). Male NOD-*Prkdc*^{em26Cd52}*Il2rg*^{em26Cd22}/NjuCrl (NCG) mice (Charles River, strain code 572) mice and NOD.CB17-*Prkdcscid*/*J* (NOD SCID) mice (The Jackson Laboratory, stock number 001303) were acclimated after shipping for >3 days before beginning experiments. Mice were fed a standard diet (PicoLab 5053) and maintained with no more than 5 mice per cage.

Pharmacokinetic analysis in mice

NOD/SCID mice 12-weeks of age and ~28 g weight were weighed before injection and divided into groups of 3 mice per cage. IKE was dissolved in 5% DMSO/95% Hank's Balanced Salt Solution (HBSS) (Thermo Fisher Scientific, 14025076), pH 4, to create a 5 mg/mL solution. 5% DMSO/95% HBSS at pH 4 solution (Vehicle 1) without IKE was used as vehicle. The solution was sterilized using a 0.22 µm Steriflip filter unit (Thomas Scientific 1189Q46). Mice were dosed using three different routes, IP and PO with 50 mg/kg IKE, and IV with 17 mg/kg IKE. Samples were collected at 0, 1, 3, 4, and 8 h from three mice per time point. Additionally, three mice per group were used as control by administration with equivalent amount of vehicle 1 by IP, PO, and IV, and samples were collected at 8 h. At the appropriate time, mice were sacrificed by CO₂ asphyxiation for 3 min and ~0.5 mL of blood was collected via cardiac puncture. Blood was immediately put into K3 EDTA micro tube (SARSTEDT 41.1504.105) and placed on ice. Samples were centrifuged for 10 min at 2,100 x g at 4°C, then plasma was transferred to a clean tube. Plasma samples were flash frozen in liquid nitrogen and stored at -80°C. IKE was extracted from

plasma by adding 900 μL acetonitrile to 100 μL plasma. Samples were mixed for at least 5 min by rotating at room temperature and were sonicated prior to concentration for 10 min at 4,000 $\times g$ and 4°C. The supernatant was removed and dried on a GeneVac evaporator overnight on an HPLC setting. After drying, the samples were resuspended in 100 μL of methanol and analyzed on the liquid chromatography mass spectrometry (LC-MS), with each sample analyzed twice. Quality control standard samples were prepared by dissolving IKE in 100 μL water and extraction with the same procedures to ensure that the extraction was efficient. LC-MS analysis was performed on a platform comprising a Thermo Scientific Dionex Ultimate 3000RS controlled by Chromeleon (Dionex) and a Bruker amazon SL ESI ion-trap mass spectrometer.

Chromatographic separation was performed at 20°C on Agilent Eclipse Plus C18 column (2.1 \times 50 mm, 3.5 μm) at 20°C over a 12 minute gradient elution. Mobile phase A consisted of water with 0.1% acetic acid v/v and mobile phase B was methanol with 0.1% acetic acid v/v. After injection, the gradient was held at 80% mobile phase A for 1 min. The gradient was then ramped in a linear fashion to 80% mobile phase over 0.5 min. Over the next 3.5 min, the gradient was ramped in linear fashion to 100% mobile phase B and held at 100% mobile phase B for 3.25 min. The gradient was then ramped in a linear fashion to 80% mobile phase over 0.5 min and held there for the duration of the run. The flow rate was set to 400 $\mu\text{L}/\text{min}$ and injection volumes were 5 μL . The retention time for IKE in this gradient was 2.8 min.

Mass spectrometry analysis was performed on a Bruker Amazon SL (Billerica, MA) in positive ESI mode. Trap Control was used to control the ESI settings with the inlet capillary held at -4500 V and the end plate offset at -500 V. Nitrogen was used as the desolvation gas. Hystar v 3.2 was used to integrate the UHPLC and MS applications, and data analysis was performed with the Compass DataAnalysis software. The base peak chromatogram at m/z 655.2 with a width of ± 0.1 was integrated and peak area quantified by standard curve.

Pharmacokinetics (PK) of IKE were assessed using Prism fitted with lognormal of one phase exponential decay.

pharmacodynamic analysis in mice

IKE was dissolved in 5% DMSO/95% HBSS at pH 4 to create a 5 mg/mL solution or 3 mg/mL solution. 5% DMSO/95% HBSS at pH 4 was used as vehicle 1. IKE PEG-PLGA nanoparticles and unfunctionalized PEG-PLGA nanoparticles (without IKE) (vehicle 2) prepared with a NanoAssemblr were dialyzed with deionized water overnight, and the water was changed at least twice. Dialyzed IKE-PEG-PLGA nanoparticles and unfunctionalized PEG-PLGA nanoparticles were concentrated by Amicon Ultra-15 Centrifugal Filter Units to create a solution with 80 mg/mL PEG-PLGA nanoparticles. All above solutions were sterilized by filtering through a 0.2 μ m syringe filter.

NCG mice 6-weeks of age were injected with 10 million SUDHL-6 cells subcutaneously. Visible tumors appeared after 2 weeks. Tumor size was measured by electronic caliper every 2 days and calculated using the formula: $0.5 \times \text{length} \times \text{width}^2$. After another 2 weeks, mice were randomly separated into group of 3 mice per cage with roughly tumor size (1200 mm^3). Mice were dosed at 50 mg/kg IKE, 22 mg/kg IKE, 22 mg/kg IKE PEG-PLGA nanoparticles (equal to 600 mg/kg PEG-PLGA) using IP at one time and samples were collected at 0, 1, 2, 3, 4, 6, and 24 h with three mice per time point. Mice were dosed with Vehicle 1 and Vehicle 2 (600 mg/kg PEG-PLGA) by IP and samples were collected at 24 h. Mice were euthanized using a CO₂ gas chamber before xenograft dissection and cardio puncture. Plasma samples were collected and analyzed as described above. Tumors were dissected and divided into 6 segments, frozen on dry ice, and stored at -80°C. Before IKE extraction, tumor tissue samples were thawed at room temperature and weighed. A 2.5-fold ratio of volume of phosphate-buffered saline (PBS) (mL/g) was added to the sample and homogenized using Bead Ruptor 4 at speed 4 for 30 sec. The homogenization step was repeated until the samples were homogenized well (final weight/volume was 0.4 g/mL). 100 μ L of homogenized tissue

(equal to 40 mg) was added to a new microfuge tube, 900 μ L of acetonitrile was added. The samples were mixed for at least 5 minutes by rotating on a shaker and were sonicated for at least 30 sec prior to centrifugation for 10 min at 4,000 x *g* and 4°C. The supernatant was removed and dried on the GeneVac overnight on the HPLC setting. After drying, the samples were resuspended in 100 μ L of methanol and analyzed on the LC-MS with each sample analyzed twice. Technical replicates were averaged. The concentration of IKE in the sample was determined by comparison against a standard curve of IKE in the range of 25 to 2,500 ng/mL. Pharmacodynamic analysis of ferroptosis biomarkers is described in the RT-qPCR, glutathione, immunofluorescence, and lipidomics sections below. Pharmacokinetics parameters of IKE was assessed using Prism fitted with Lognormal of one phase exponential decay.

Measurement of DLBCL lines sensitivity to IKE

DLBCL cells were plated at 10,000 cells per well in white 384-well plates (32 μ L per well) in technical duplicates and incubated overnight. The cells were then treated with 8 μ L medium containing a two-fold dilution series of vehicle (DMSO), IKE (starting from 100 μ M) with or without Fer-1 (starting from 200 μ M). After 24 h incubation, 40 μ L of 50% CellTiter-Glo (Promega) 50% cell culture medium was added to each well and incubated at room temperature with shaking for 15 min. Luminescence was measured using a Victor X5 plate reader (PerkinElmer). All cell viability data were normalized to the DMSO vehicle condition. Experiments were performed three independent times with different passages for each cell line. From these data, dose-response curves and IC₅₀ values were computed using Prism 7.0 (GraphPad).

C-11 BODIPY lipid peroxidation measurement

0.20 million SUDHL-6 cells were seeded in six-well plates and treated with DMSO, IKE, or Fer-1 at specific concentration. The final cell density of 0.05 million cells/mL. After 24 h, cells were harvested by centrifuging at 300 x *g* for 5 min. Cells were resuspended in 500 μ L HBSS containing 2 μ M C11-BODIPY (BODIPY 581/591 C11) (Thermo Fisher Scientific, D3861) and incubated at 37 °C for 15 min.

Cells were pelleted and resuspended in HBSS. Fluorescence intensity was measured on the FL1 channel with gating to record live cells only (gate constructed from DMSO treatment group). A minimum of 10,000 cells were analyzed per condition.

Reduced glutathione measurement in cell culture

2.4 million cells incubated with DMSO, IKE, or β -mercaptoethanol (β -Me) at a density of 0.2 million cells/mL for 24 h. Cells were collected and washed with cold PBS once. Cell number was counted by Vi-Cell. Cells were resuspended in ice cold RIPA buffer (Thermo Fisher Scientific, 89900) with 100 μ L/one million cells. Samples were centrifuged for 15 min at 4°C at 17,000 x g. The resulting supernatant was deproteinized using a trichloroacetic acid and sodium bicarbonate solution and kept on ice. The sample was diluted with assay buffer provided in GSH/GSSG Ratio Detection Assay Kit (Abcam, ab13881) ten-fold. Reduced glutathione (GSH) levels were determined using Fluorometric-Green provided in the kit following the manufacture's protocol. 384-well (Corning) low volume black flat bottom polystyrene non-treated microplates 1230F99 were used in this experiment.

Reduced glutathione measurement in mouse tumor tissue

10 mg of tumor tissue was mixed with 400 μ L RIPA buffer, homogenized at speed 5 for 30 sec using a Bead Ruptor 4 (OMNI International). The sample was centrifuged at 17,000 x g for 5 min, then the above deprotenization and measurement steps performed.

qPCR analysis of gene expression

DLBCL cells were treated with 0-10 μ M IKE, Fer-1, or β -Me for the indicated times. RNA was extracted using the Qiashredder and Qiagen RNeasy Mini kits (Qiagen) according to the manufacture's protocol. 2 μ g RNA from each sample was reversed transcribed to cDNA using a High Capacity cDNA Reverse Transcription Kit (Thermo Fisher Scientific, 4368814). Quantitative PCR reactions were performed using Power SYBR Green PCR Master Mix (Applied Biosystems) with triplicate measurement on ViiA 7

Real-Time PCR instrument (Thermo Fischer). *HPRT1* was used as an internal reference. Differences in mRNA levels compared with *HPRT1* were computed between vehicle and experimental groups using the $\Delta\Delta C_t$ method. The primers used in the study was listed below.

| Genes | Foward | Reverse |
|----------------|------------------------------|------------------------------|
| <i>HPRT1</i> | 5'-GCCCTGGCGTCGTGATTAGTG-3' | 5'-GCCTCCCATCTCCTTCATCAC-3' |
| | | 5'- CGCAGCAAGTATTCAAGGTTGT- |
| <i>CHAC1</i> | 5'- GAACCCTGGTTACCTGGGC-3' | 3' |
| <i>SLC7A11</i> | 5'-GGTGGTGTGTTTGCTGTC-3' | 5'-GCTGGTAGAGGAGTGTGC-3' |
| | 5'- ATATGTTCTCCTGCCTACTGGAA- | |
| <i>PTGS2</i> | 3' | 5'-GCCCTTCACGTTATTGCAGATG-3' |

qPCR in mouse tumor tissue

~20 mg of tumor tissue was prepared and kept on dry ice. The frozen tissue was homogenized with Bead Ruptor 4 at speed 4 for 30 sec. The homogenization was repeated once if there remained unhomogenized tissue. Total mRNA was prepared from the cleared homogenate using Ribopure Kit (Thermo Fisher Scientific, am1924). RNA was reverse transcribed to cDNA then used in quantitative PCR experiment following the same steps used in cell qPCR experiment.

Immunofluorescence on cell and quantification

SUDHL-6 cells were treated with IKE. The cells were harvested by centrifugation and washed with PBS once. The cells were resuspended in PBS, fixed by adding equal volume of 4% paraformaldehyde (PFA), and incubated at room temperature for 15 min. The cells were washed with PBS/0.1% Tween 20 (PBST) twice, resuspended in 10% goat serum (ThermoFisher 50197Z) for 1 h. The cells were incubated with mouse mAb 1F83, which specifically recognizes malondialdehyde (MDA)-lysine adduct 4-methyl-1,4-dihydropyridine-3,5-dicarbaldehyde (MDHDC)¹³⁵⁻¹³⁶ (1:100 dilution) overnight at 4°C. The cells were

washed with PBS three times by centrifugation. The cells were incubated with goat anti-mouse IgG H&L (Alexa Fluor 647) (Abcam ab150115) (1:1000) at room temperature for 1 h. The cells were washed with PBST twice by centrifugation, then resuspended in PBS in 24-well plate with poly-lysine-(Sigma Aldrich P4832)-coated cover slips and centrifuged at 1,000 x *g* for 10 min. ProLong Diamond antifade mountant with DAPI (ThermoFisher P36962) was added to stain the nucleus. All images were captured on a Zeiss LSM 800 confocal microscope at Plan-Apochromat 63x/1.40 Oil DIC objective with constant laser intensity for all samples. When applicable, line-scan analysis was performed on representative confocal microscopy images using Zeiss LSM software to qualitatively visualize fluorescence overlap. The intensity above threshold of the fluorescent signal of the bound antibodies was analyzed using NIH ImageJ software. Data were expressed as fold change compared with the vehicle.

Immunofluorescence on paraffin-embedded tissue sections and quantification

Tumor tissue was fixed in 4% paraformaldehyde (PFA) for 24 h at 4°C followed by washing three times with PBS. The samples were fixed in paraffin. Six series of 5 µM sections were obtained with a sliding microtome. The serial sections were then mounted on gelatin-coated slide. The paraffin-embedded tissue sections were deparaffinized with xylene three times, 5 min each, followed by rehydrating in 100%, 90%, 70%, and 50% ethanol, two washes 5 min each, then rinsed with distilled water. Antigen retrieval was performed in Tris-EDTA buffer, pH 9.0, 95-100°C for 10 min. Then sections were rinsed in PBST, 2 min each. A hydrophobic barrier pen was used to draw a circle on each slide. The slides were permeabilized with PBS/0.4% Triton X-100 twice before non-specific-binding blocking by incubating the sections with 10% goat serum (ThermoFisher 50197Z) for 30 minutes at room temperature. The sections were separately incubated with mouse anti-MDA mAb 1F83 (1:1000 dilution), anti-cyclooxygenase 2 (COX 2, AKA PTGS2) antibody (Abcam, ab15191, 1:200 dilution), or anti-8-OH-dG (DNA/RNA damage) antibody (Abcam, ab62623, 1:200 dilution) overnight at 4°C in humidified chambers. Sections were washed with PBST for twice before incubating with goat anti-mouse IgG H&L (Alexa Fluor 647) (Abcam, ab150115, 1:1000 dilution) or goat anti-rabbit IgG H&L highly cross-absorbed secondary

antibody (Alexa Fluor488, Thermo Fisher Scientific, A-11034, 1:1000) at room temperature for 1 h. Slides were then washed twice with PBST. ProLong Diamond antifade mountant with DAPI (ThermoFisher P36962) was added onto slides, which were then covered with the coverslips, sealed by clear fingernail polish and observed under confocal microscopy. All images were captured on a Zeiss LSM 800 confocal microscope at Plan-Apochromat 63x/1.40 Oil DIC objective with constant laser intensity for all analyzed samples. The intensity above threshold of the fluorescent signal of the bound antibodies was analyzed using NIH ImageJ software. Data were expressed as fold change comparing with the vehicle

Caspase-3 activity measurement

Caspase-3/7 activity of SUDHL-6 cells treated with indicated compounds for 24 hours were measured by Apo-ONE homogeneous caspase-3/7 assay (Promega) followed by the reagent manual).

Western blot

SUDHL-6 cells treated with indicated compounds for 24 hours were lysed in ice cold RIPA buffer with cocktail protease inhibitor (Roche) followed by centrifugation. The supernatant was used in western blot analysis. Caspase-3 antibody (Cell Signaling Technology 12691) which could recognize both full-length caspase-3 and cleaved caspae-3 was used. α -Tubulin antibody was used as the reference.

Chapter 4: *in vivo* Study of IKE Nanoparticle Formulation in Xenograft Model³

4.1 Introduction

While small molecule system x_c^- inhibitors are promising agents for inducing ferroptosis in cancers that are addicted to cystine import, there are a number of potential concerns in translating such agents for therapeutic benefit. First, many compounds, including some system x_c^- inhibitors, do not accumulate sufficiently in target tumor tissues, resulting in a minimal pharmacodynamic effects; thus, improving delivery and accumulation of such compounds to tumors would be beneficial. Second, while system x_c^- inhibitors are expected to be largely tolerable based on the observation that SLC7A11 knockout mice have few phenotypes, it is possible that acute inhibition of system x_c^- would cause toxicity in normal tissues, or that off-target effects of system x_c^- inhibitors might cause undesirable toxicities. For these reasons, we hypothesized that improving the formulation and delivery of IKE to tumors might enhance its therapeutic index and translational potential.

Nanotechnology represents a potentially promising platform to address the above issues as well as others associated with conventional therapeutic agents, including poor water solubility, nonspecific distribution, inadequate accumulation, limited efficacious responses, and systemic toxicity⁹⁸⁻⁹⁹. We suspected that the enhanced permeability and retention (EPR) effect might increase DLBCL tumor targeting of IKE¹⁰⁰. We thus developed an IKE-loaded nanoparticle (NP) formulation using PEG-PLGA, a well-tolerated di-block copolymer, to achieve enhanced tumor tissue accumulation and improved *in vivo* delivery of IKE in a DLBCL xenograft model. The IKE PEG-PLGA NPs were formulated using a high flow microfluidic NanoAssemblr, with mean size of ~80 nm, polydispersity index of 0.2, and loading efficiency of 24% by weight. The IKE PEG-PLGA NPs have increased IC_{50} in SUDHL-6 cells, which might result from the increased internalization rate of NPs with cells. This IKE NP formulation achieved

³This chapter is adapted from the manuscript submitted: Zhang, Y.; Tan, H.; Daniels J. D.; Zandkarimi, F.; Liu, H.; Brown, L. M.; Uchida, K.; O'Connor, O. A.; Stockwell, B. R., Imidazole ketone erastin nanoparticles induce ferroptosis and slow tumor growth in a mouse lymphoma model

enhanced accumulation in xenograft tumor tissue, and inhibited tumor growth with less toxicity in mice compared to free IKE. In summary, we found that the small molecule ferroptosis inducer IKE is able to reduce tumor growth in a DLBCL xenograft model and that IKE PEG-PLGA NPs are suitable for inducing ferroptosis in mouse models.

In this chapter, the optimization of nanoparticle formulation, efficacy study of IKE and IKE PEG-PLGA NP efficiency, and characterization of IKE efficacy study biomarkers will be described.

4.2 Results

4.2.1 PLGA and PEG-PLGA nanoparticle system optimization

IKE is soluble to acidic aqueous conditions, but not to the same degree in neutral aqueous conditions (solubility in neutral water is 0.25 mM). To improve delivery of this compound and at the same time improve its tumor accumulation, we sought to use a nanoparticle formulation. We selected biocompatible and biodegradable PEG-PLGA di-block copolymer-based nanoparticle as an IKE carrier (**Figure 4.1**). The PEG block was used to create a deformable hydrating layer by tight associations with water molecules, which prevents clearance by the mononuclear phagocyte system (MPS), prolonging circulation lifetime. The PLGA block was used to form a hydrophobic core to incorporate IKE, which provides sustained release by diffusion and surface/bulk erosion.

To formulate <100 nm nanoparticles with a reproducible method, we employed the NanoAssemblr platform, which is equipped with a high flow microfluidic chip¹³⁹⁻¹⁴⁰. Self-assembly of nanoparticles by nanoprecipitation occurs when the organic phase containing IKE and the PEG-PLGA polymer combines with the aqueous phase in a micro channel (**Figure 4.1**).

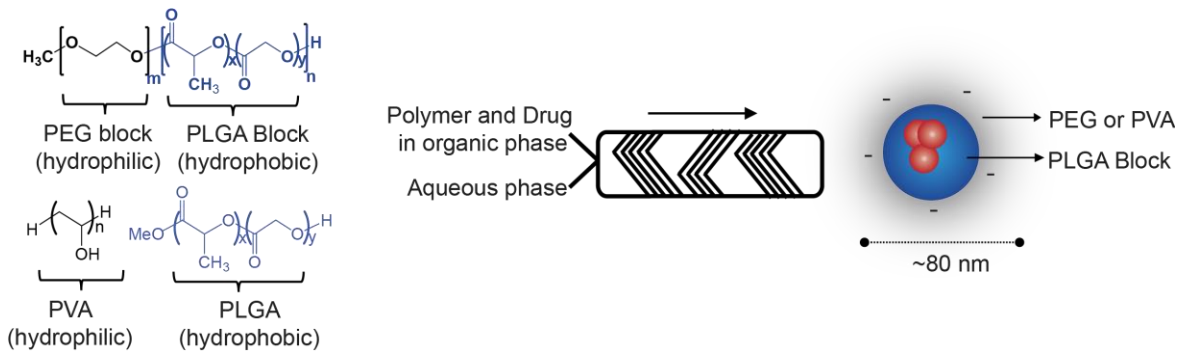


Figure 4. 1 Principles of nanoparticle formulation using microfluidic system

NanoAssemblr platform is a scalable system with multiple parameters to tune the formation of desired nanoparticles, which includes: (1) process parameters: total flow rate and flow rate ratio; (2) formulation parameters: polymer concentration, surfactants concentration, and drug concentration; (3) post-processing: purification and concentration. Upon optimizing these parameters, drug loaded nanoparticles with optimal particle size, polydispersity (PDI), and encapsulation efficiency could be achieved. As PLGA polymer is also widely used in drug delivery, a PLGA system is also described here as comparison with PEG-PLGA system.

At total flow rate of 8 mL/min, both PLGA and PEG-PLGA NPs have around 100 nm size, so we didn't optimize the total flow rate further. We tested flow rate ratios and found with increasing Aqueous:Organic ratio, the size of nanoparticles increased (**Figure 4.2A**). While increasing acetone percentage in organic phase decreased nanoparticle size a little, and with 25% of acetone in DMSO, the IKE PEG-PLGA NP has the highest encapsulation efficiency as indicated by IC50 measurement in SUDHL-6 cells (**Figure 4.2B**). While, during IKE PLGA NP formulation, increasing acetonitrile percentage in DMSO resulted in increased size and PDI, thus 100% DMSO as the organic phase was used in IKE PLGA NP formulation. Besides, since PLGA is hydrophobic, polyvinyl alcohol (PVA) a hydrophilic surfactant, was used to form the hydrophilic surface of PLGA NP.

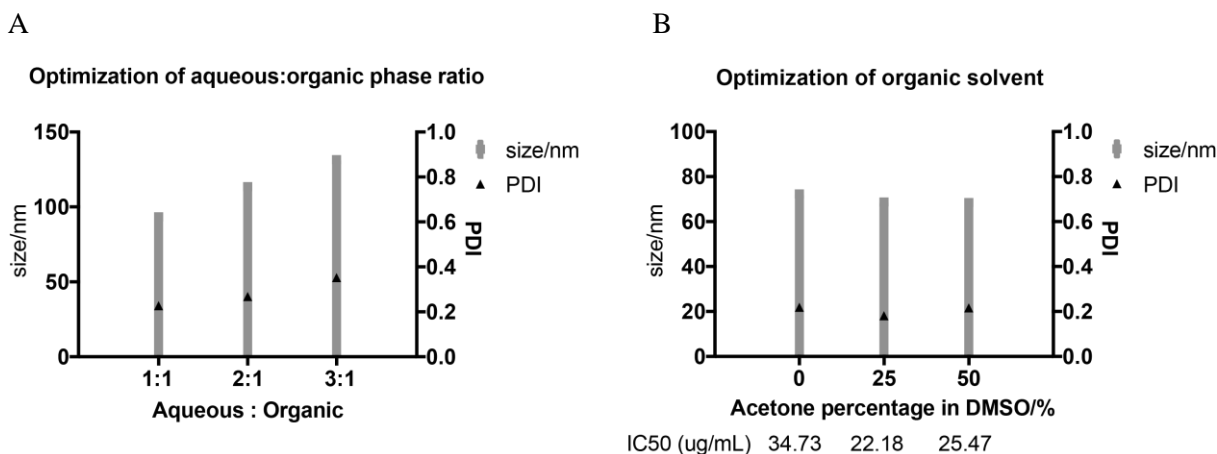


Figure 4. 2 Optimization of organic phase in PEG-PLGA nanoparticle formulation

(A) At a total flow rate of 8 mL/min and PEG-PLGA polymer concentration of 10 mg/mL in DMSO, with aqueous: organic (water: DMSO) ratio increases, the average diameter of PEG-PLGA nanoparticles formulated by NanoAssemblr increased. (B) At a total flow rate of 8 mL/min, PEG-PLGA polymer concentration of 10 mg/mL, and aqueous: organic ratio of 1: 1, IKE PEG-PLGA NP prepared from 25% acetone/DMSO has relatively smaller IC₅₀ comparing with 0% acetone/DMSO and 50% acetone/DMSO, indicating higher IKE encapsulation rate in 25% acetone/DMSO. All three solvents produced IKE PEG-PLGA NP with size smaller than 100 nm and polydispersity index (PDI) around 0.2

One of the problems with the use of nanoparticles as drug carriers *in vivo* is the low content of drug and low concentration of nanoparticles in suspension. We were able to achieve concentration factors up to 20 using centrifugal filter units without causing nanoparticle aggregation or dramatically decreasing IKE loading efficiency in IKE PEG-PLGA NP (**Figure 4.3A**). However, it was hard to concentrate PLGA NP, the main reason is that the PVA surfactants tend to clog the membrane of the filter units, as with increasing of PVA molecular weight, it was harder to concentrate the PLGA NP (**Figure 4.3B**).

To improve the final IKE loading in PEG-PLGA NPs, different IKE concentration used in the formulation was tried (**Figure 4.4**) With 15 wt% IKE in PEG-PLGA polymer, the final IKE loading is the highest as suggested in cellular activity test. Increasing IKE percentage further during the formulation didn't contribute to increasing final IKE loading. So 15wt% IKE was used in the *in vivo* study.

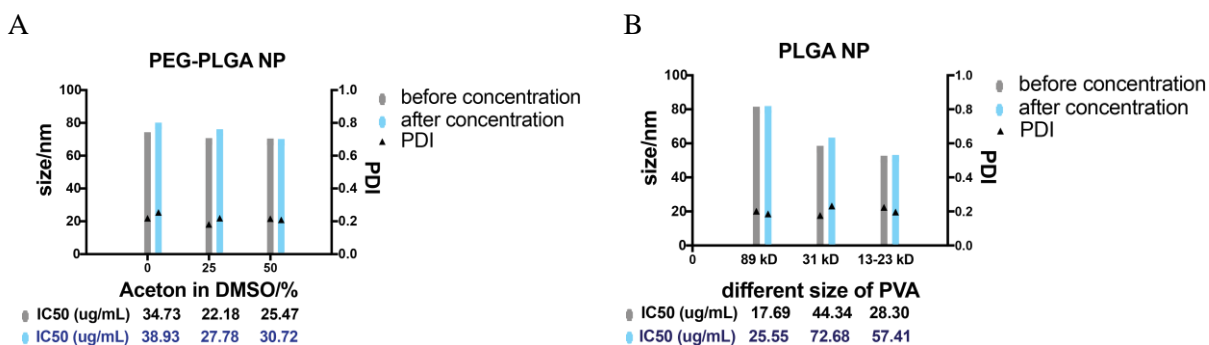


Figure 4. 3 Optimization of concentration step in PEG-PLGA and PLGA nanoparticle formulation

(A) After concentration using filter units with concentration factors up to 20, PEG-PLGA NP's average diameter, PDI, and IC₅₀ were not significantly increased. (B) PLGA NP formulated with different size of PVA as surfactants were concentrated using filter units. The concentration factors up to 5, 10, and 20 was achieved in 89 kD PVA, 31 kD PVA, and 13-23 kD PVA individually due to the clog of filter membranes by PVA.

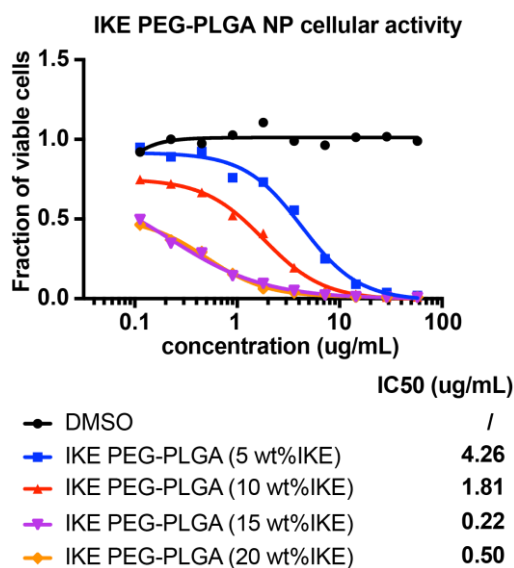


Figure 4. 4 Optimization of IKE loading in nanoparticles

IKE PEG-PLGA nanoparticle cellular activity with different percentage of IKE loaded in nanoparticles during formulation.

As a summary, the highest IKE loading efficiency with < 100 nm nanoparticle size was achieved by using 1:1 ratio of organic to aqueous phases, with 25% acetone / 75% dimethyl sulfoxide (DMSO) as the organic phase, and 15% (by weight) IKE to PEG-PLGA polymer in the organic phase. IKE PEG-PLGA nanoparticles (NPs) with a diameter as small as 80 nm and polydispersity index (PDI) of 0.17 were formulated using this approach. (Figure 4.5) The surface possessed a slightly negative charge with zeta potential of -17.0 mV to prevent nanoparticle aggregation. While, the PLGA NPs with diameter as small as 80 nm, PDI of 0.21, and zeta potential of -11 mV were formulated, it was not used in the *in vivo* study, partially due to the difficulty in concentration and less favored properties comparing with PEG PLGA NP, for example, deformability¹⁴¹.

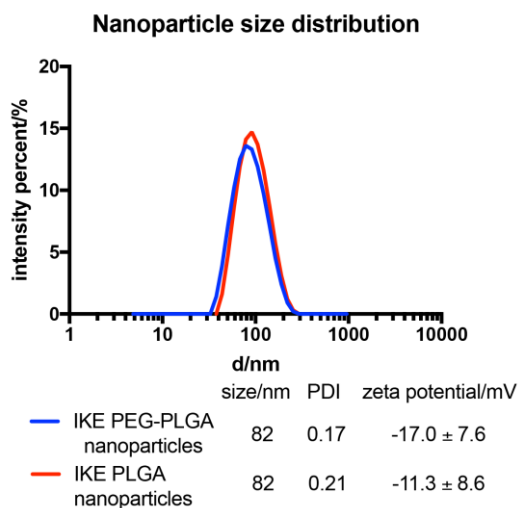


Figure 4. 5 Nanoparticles’ size and surface potential parameters

Nanoparticle size distribution of IKE PEG-PLGA nanoparticles and IKE PLGA nanoparticles. IKE PEG-PLGA nanoparticles formulated at a total flow rate of 8 mL/min, PEG-PLGA polymer concentration of 10 mg/mL in 25% acetone/DMSO (organic phase), and aqueous: organic ratio 1:1 has size of 82 nm, PDI 0.17, and zeta potential -17.0 ± 7.6 mV. IKE PLGA nanoparticles formulated at a total flow rate of 8 mL/min, PLGA polymer concentration of 10 mg/mL in DMSO (organic phase), 89 kD PVA as surfactant, and aqueous: organic ratio 1:1 has size of 82 nm, PDI 0.21, and zeta potential -11.3 ± 8.6 mV.

Comparing with free IKE, IKE PEG-PLGA NPs have enhanced cellular activity in SUDHL-6 cells, a sensitive DLBCL cell line to IKE, which might result from increased internalization of IKE NPs

to cell (**Figure 4.6**). However, IKE PLGA NPs didn't have the enhanced cellular activity effect, which is one of the factors making us eventually choose to use PEG-PLGA NP as the IKE carrier .

IKE content as high as 3 mg/mL (drug loading 3.65% by weight, encapsulation efficiency 24%) with PEG-PLGA NP was used for the *in vivo* study. Administration of 750 mg/kg PEG-PLGA NP daily for two weeks didn't result in any detectable weight loss or other observable signs of toxicity, suggesting that this NP system was suitable for *in vivo* drug delivery.

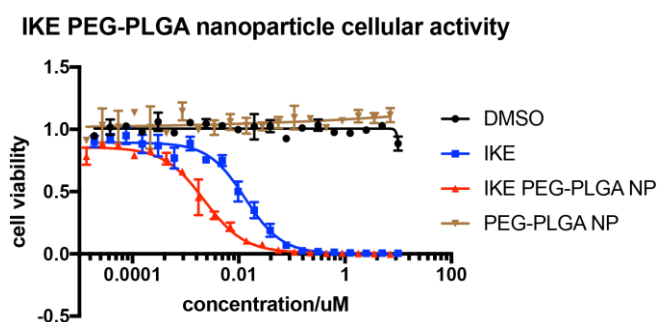


Figure 4. 6 IKE PEG-PLGA nanoparticles have enhanced cellular activity comparing with free IKE.

4.2.2 IKE PEG-PLGA NPs have suitable properties to be applied *in vivo*

We investigated the efficacy of IKE *in vivo* in NCG mice bearing SUDHL-6 subcutaneous xenografts. Once tumor volumes reached 100 mm³, mice were randomized into five groups and treated with vehicle (5% DMSO in HBSS at pH 4), unfunctionalized PEG-PLGA NPs in water, 40 mg/kg free IKE (5% DMSO in HBSS at pH 4), 23 mg/kg free IKE (5% DMSO in HBSS at pH 4), or 23 mg/kg IKE NP (IKE PEG-PLGA NPs in water) via intraperitoneal (IP) injection once daily. During the experimental period, mouse weight and tumor volume were measured daily to determine IKE's antitumor effect and possible toxicity. Tumor growth was calculated as the fold change to original tumor volume on day 0 before the first dose (**Figure 4.7A**). Administration of 40 mg/kg IKE, 23 mg/kg IKE, and 23 mg/kg IKE NPs caused a significant decrease in tumor growth starting from day 9 of treatment (**Table 5**). The tumor

growth inhibition effect was not significantly different between 23 mg/kg free IKE and 23 mg/kg IKE NP; however, IKE NPs showed less toxicity as evidenced by weight loss (**Figure 4.7B**). Compared to saline vehicle, free-IKE (5% DMSO in HBSS at pH 4) treated mice started losing weight from day 9, which might be caused by the accumulated low pH precipitation of IKE after administrated into the peritoneum, an environment with pH ranges of 7.5-8.0, causing damage to abdominal organs, or possible toxicity of systemic system x_c^- inhibition, or off-target toxicity of IKE. However, IKE NP-treated mice had a similar weight as the saline vehicle and the NP vehicle groups; the lower toxicity of the IKE NP formulation might derive from the NP EPR effect, which decreases the non-specific distribution and systemic toxicity associated with conventional hydrophobic drugs.

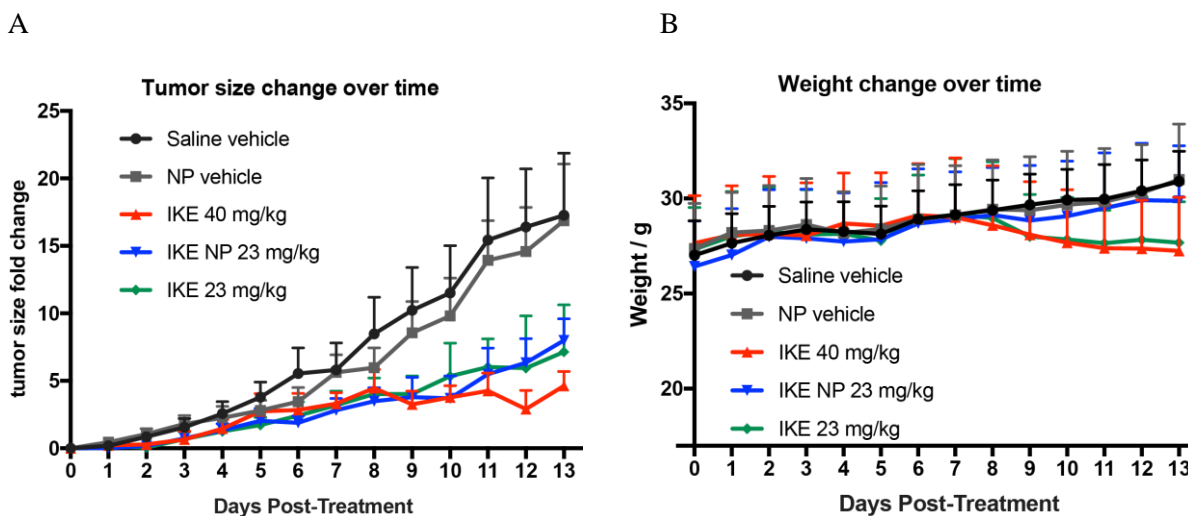


Figure 4. 7 IKE and IKE NPs inhibited tumor growth in NCG mice bearing SUDHL6 xenografts

(A) Tumor volume fold change compared with day 0, measured by electronic caliper daily and calculated using the formula $volume = 0.5 \times length \times width^2$, revealed a reduction of tumor growth by IKE 40 mg/kg (n=9), IKE 23 mg/kg (n=11), and IKE NP 23 mg/kg (n=13) treatment for 14 days comparing with vehicle (n=13) and NP vehicle (n=13) controls (data analyzed by two-way ANOVA). (B) Mouse weight was measured daily and indicated no weight loss upon NP and IKE NP treatments, but weight loss upon IKE 40 mg/kg and IKE 23 mg/kg treatment starting from day 9.

Table 4. 1 Percentage of tumor growth inhibition by IKE and IKE NP

| Days | 8 | 9 | 10 | 11 | 12 | 13 |
|-----------------------------------|------------|--------------|--------------|--------------|--------------|--------------|
| NP vehicle vs. Saline vehicle | ns * | ns **** | ns **** | ns **** | ns **** | ns **** |
| IKE 40 mg/kg vs. Saline vehicle | 0.47 ** | 0.68 **** | 0.67 **** | 0.72 **** | 0.82 **** | 0.73 **** |
| IKE 23.3 mg/kg vs. Saline vehicle | 0.53 ns | 0.61 *** | 0.54 **** | 0.61 **** | 0.64 **** | 0.59 **** |
| IKE NP 23.3 mg/kg vs. NP vehicle | 0.42 | 0.56 | 0.62 | 0.60 | 0.56 | 0.53 |

ns P > 0.05; * P < 0.05; ** P < 0.01; *** P < 0.001; **** P < 0.0001

By analyzing IKE tumor accumulation using LC-MS, we found that IKE NP at 23 mg/kg had slightly enhanced tumor accumulation compared with free IKE at 23 mg/kg and was comparable with the free IKE 40 mg/kg treatment (**Figure 4.8**). This suggests that IKE NPs likely accumulate in tumor tissue. Overall, PEG-PLGA NP formulation increased IKE's therapeutic window.

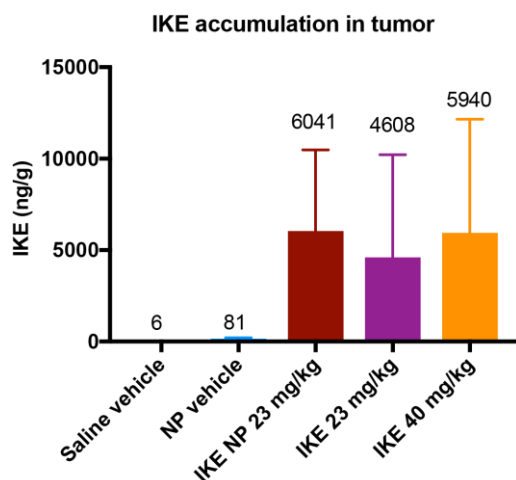


Figure 4. 8 Measurement of IKE accumulation in tumor tissues

LC-MS analysis of tumor IKE concentration showed IKE NP 23 mg/kg treated mice have higher tumor IKE accumulation comparing with IKE 23 mg/kg group. Tumor samples were from mice treated with saline vehicle, NP vehicle, IKE NP 23 mg/kg, IKE 23 mg/kg, and IKE 40 mg/kg daily for 14 days and sacrificed after 3 hours of the final dosage.

4.2.3 Investigation of ferroptosis biomarker expression in IKE and IKE PEG-PLGA efficacy study

Given the fact that *PTGS2* gene expression was upregulated during ferroptosis, we hypothesized that after IKE treatment, there might be increased level of PTGS2 protein in the tumor. Indeed, using immunofluorescence, we found PTGS2 protein expression was increased in IKE-treated tumor tissue (**Figure 4.9**). There was no significant PTGS2 protein increase in IKE NP treated tumor, which might be due to the slower release of IKE from PEG-PLGA NP, making the free IKE concentration less than with free-IKE-treated tumors.

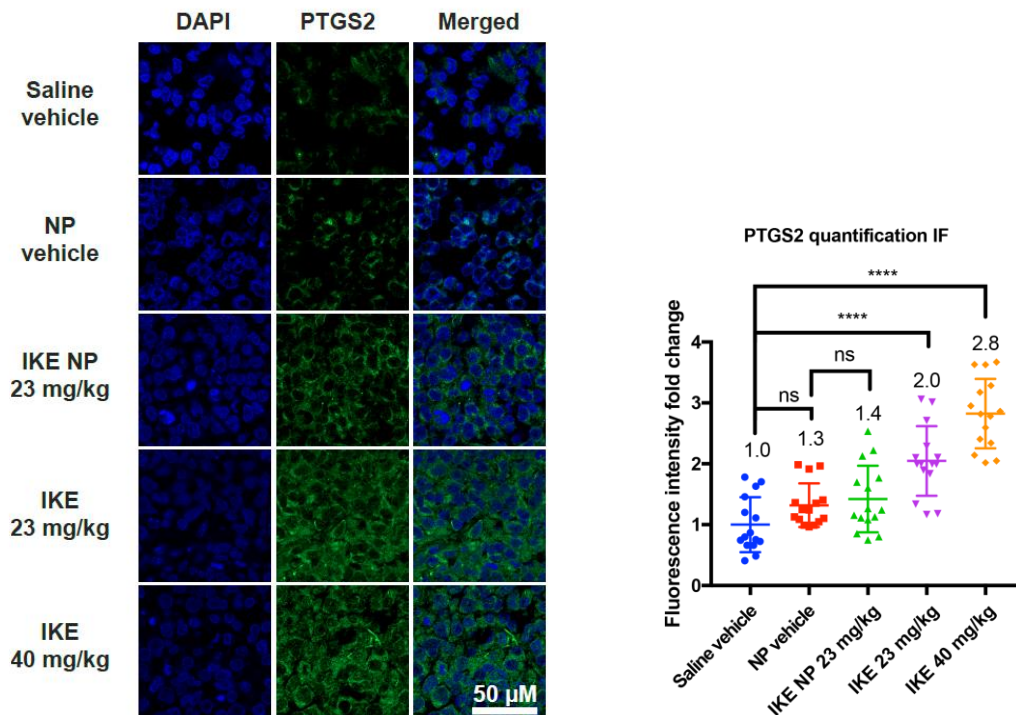


Figure 4. 9 Measurement of PTGS2 level in tumor tissues from efficacy study by immunofluorescence

Immunofluorescence of PTGS2 on frozen tumor sections showed 2.0 and 2.8-fold increase on PTGS2 intensity upon IKE 23 mg/kg and IKE 40 mg/kg treatment daily for 14 days. (sections were cut from 5 randomly chosen mice in each group, three images from each section were captured on Zeiss LSM 800 63x/1.40 Oil DIC objective)

We further characterized the lipid peroxidation level in tumor tissues in this efficacy study. Immunofluorescence analysis of tumor tissue from the five groups showed significantly increased MDA adduct levels in IKE-treated and IKE-PEG-PLGA-NP-treated groups, compared with the saline vehicle and NP vehicle groups (**Figure 4.10**). Compared to saline vehicle, the NP vehicle group had increased levels of MDA adduct, which might be caused by low level ferroptosis induction of ultrasmall (<10 nm in diameter) nanoparticles distributed in the sample, as observed in PEG-coated silica nanoparticles previously¹⁴². In addition, the Thiobarbituric Acid Reactive Substances (TBARS) assay, which measures fluorescence of MDA-TBA adducts formed also showed increased MDA levels in tumors from the free IKE and IKE PEG-PLGA NP groups (**Figure 4.11**). This assay is not as sensitive as immunofluorescence to detect small increases of MDA adducts, suggesting a possible explanation for our inability to detect this increase in the NP vehicle group. Immunofluorescence analysis of 8-OHdG showed increased oxidative DNA damage in IKE-treated and IKE-PEG-PLGA-NP-treated groups, confirming that IKE treatment induced free-radical-mediated-oxidative damages to tumor (**Figure 4.12**).

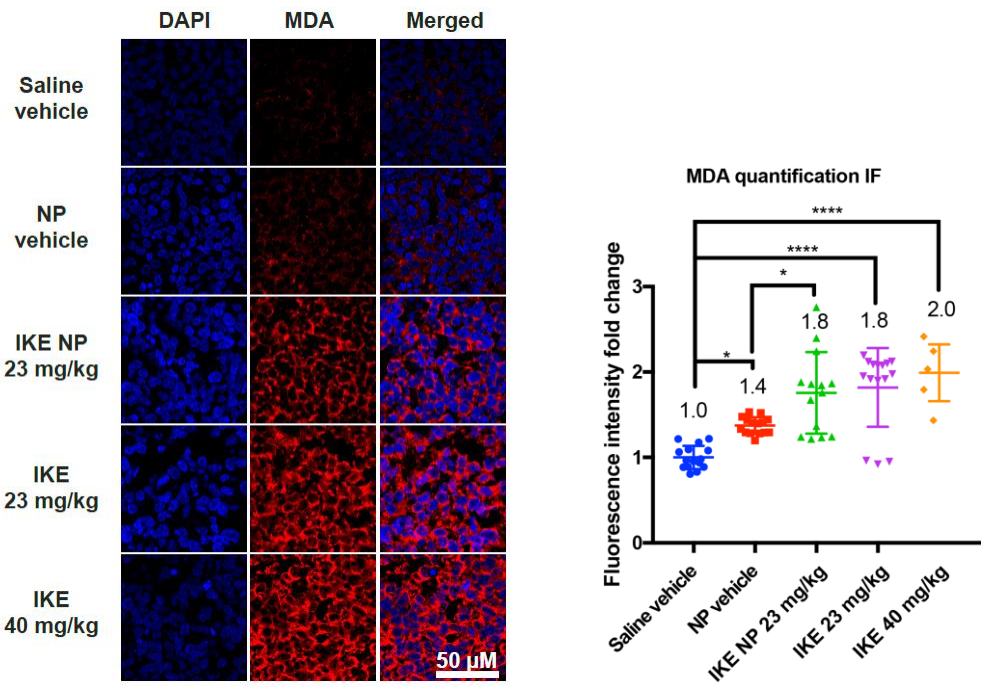


Figure 4. 10 Measurement of MDA level in tumor tissues from efficacy study by immunofluorescence

Immunofluorescence of MDA on frozen tumor sections measured by confocal microscopy showed 1.4, 1.8, 1.8, and 2.0-fold increase in MDA intensity upon NP vehicle, IKE NP 23 mg/kg, IKE 23 mg/kg, and IKE 40 mg/kg treatment daily for 14 days.

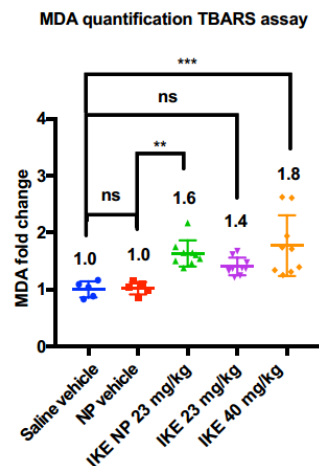


Figure 4. 11 Measurement of MDA level in tumor tissues from efficacy study by TBARS assay

TBARS assay measuring MDA-TBA adducts' fluorescence showed 1.6, 1.4, and 1.8-fold MDA increase upon IKE NP 23 mg/kg, IKE 23 mg/kg and IKE 40 mg/kg treatment. ns $P > 0.5$, * $P < 0.05$, ** $P < 0.01$, *** $P < 0.001$, **** $P < 0.0001$ by one-way ANOVA.

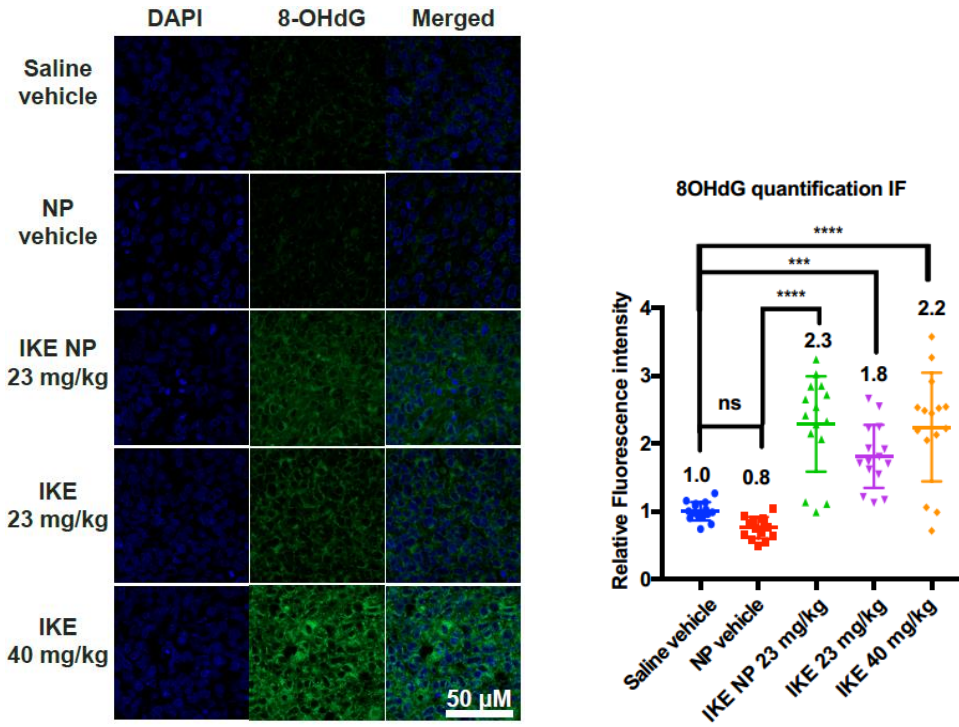


Figure 4. 12 Measurement of 8-OHdG in tumor tissues from efficacy study by immunofluorescence

Immunofluorescence of 8-OHdG on frozen tumor sections measured by confocal microscopy showed 2.3, 1.8, and 2.2-fold increase in 8-OHdG intensity upon IKE NP 23 mg/kg, IKE 23 mg/kg, and IKE 40 mg/kg treatment daily for 14 days.

Besides, there was no caspase-3 activity increase upon IKE treatment in tumor tissue, suggesting that the inhibition of tumor growth was not resulted by apoptosis (Figure 4.13).

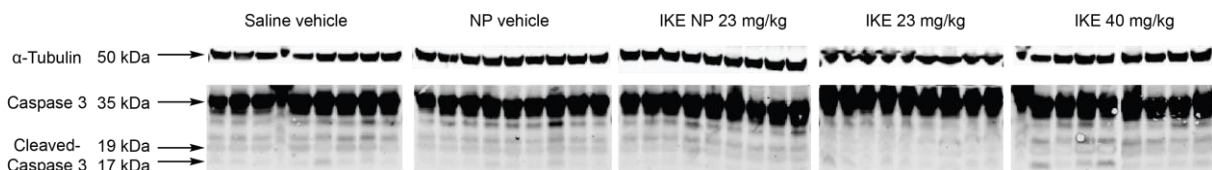


Figure 4. 13 Measurement of cleaved-caspase 3 abundance in tumor tissues from efficacy study

Western blot analysis of tumor tissue from the efficacy study showed there was no cleaved-caspase 3 increase upon IKE and IKE NP treatment for 14 days. Tumor samples of 9 individual mouse from each group were analyzed in western blot.

4.3 Discussion

Recent discoveries have suggested that ferroptosis inducers can have anti-tumor efficacy and may synergize with chemotherapy in some cell contexts. However, there is a lack of potent, selective, and metabolic stable tools to study ferroptosis *in vivo*. This study of the ferroptosis inducer IKE in an SUDHL-6 xenograft model demonstrated IKE and IKE NP's abilities to reduce tumor growth while causing ferroptosis. In addition, IKE PEG-PLGA NP formulation was suitable for *in vivo* use to increase IKE's therapeutic window by decreasing toxicity. The increased PTGS2 protein expression and oxidative biomarkers have been identified in IKE and IKE PEG-PLGA NP treated tumor tissues (Figure 4.14).

We partially addressed the observed toxicity associated with free IKE administration by formulating IKE in PEG-PLGA nanoparticles. The toxicity of high dose free IKE treatment might stem from systemic system x_c^- inhibition in normal tissues, or the possible precipitation of IKE after injecting into the peritoneal cavity. Targeted nanoparticles might further increase IKE tumor accumulation and without systemic toxicity.

There are various xenograft models used in preclinical assessment of anticancer drug development such as ectopic tumor xenograft model, orthotopic xenograft model, metastasis model, syngeneic models, humanized mouse, and patient derived xenografts. Here, we used the ectopic tumor xenograft model. Ectopic tumor xenograft model is the standard model of cancer used for validation and assessment in oncology studies. There are both pros and cons using this model. Firstly, the ectopic tumor xenograft model is reproducible, homogeneous, and amendable. Secondly, it is easy to monitor tumorigenicity and tumor growth rate. In addition, there are many parameters to assess drug efficiency including T/C ratio, tumor growth delay and tumor regression, and drug toxicity including drug-related death and body weight change. On the other hand, the ectopic tumor xenograft model is not applicable for tumors that show necrosis during tumorigenicity and non-solid tumors. Besides, the immunosuppressed mice represent a different microenvironment than that of human cancer, thus might not be able to mimic the human context. Another limitation is that it is hard to assess tumor invasion and metastasis. The efficacy of IKE in additional animal cancer models would be valuable to explore.

In summary, we have developed a suitable small molecule and formulation for inhibiting system x_c^- and inducing ferroptosis in mouse tumor models, which will be used in determining whether there are specific cancer contexts in which ferroptosis induction would be therapeutically beneficial.

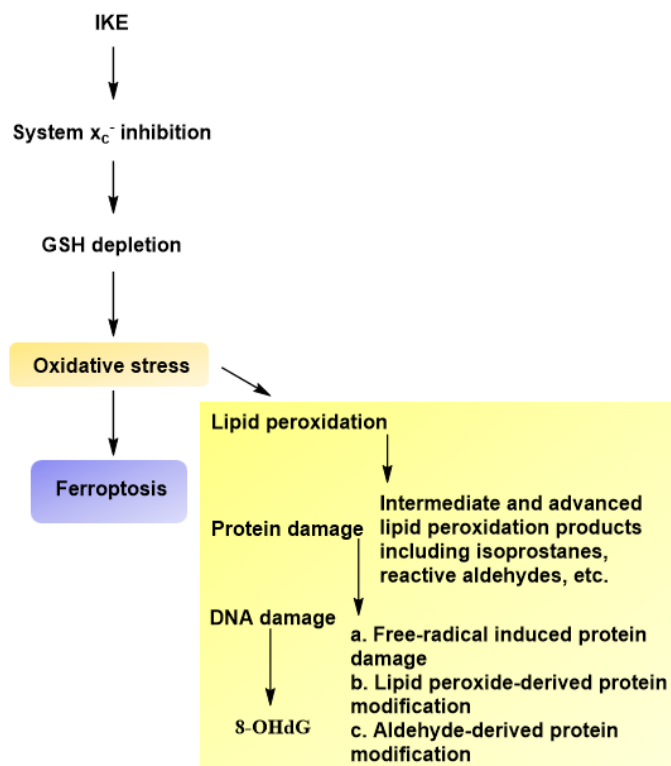


Figure 4. 14 Schematic overview of IKE-induced ferroptosis

4.4 Methods

IKE PEG-PLGA nanoparticle formulation

(Poly(ethylene glycol) methyl ether-*block*-poly(lactide-*co*-glycolide) (PEG-PLGA) with PEG average M_n 5,000, PLGA M_n 15,000, and lactide:glycolide 50:50 was purchased from Sigma-Aldrich (900948). PEG-PLGA nanoparticles were prepared using a microfluidic mixer with the NanoAssemblr Benchtop instrument (Precision NanoSystems Inc., Vancouver, BC) by mixing oil and aqueous phases. PEG-PLGA was dissolved in 25% acetone/75% DMSO at concentration of 10 mg/mL. Milli-Q water was used as aqueous phase. For synthesis of PEG-PLGA nanoparticles, two phases were injected through two inlets of the microfluidic mixer with a speed of 8 mL/min and a volume ratio of 1:1. Nanoparticles were

collected in the sample collection tube by discarding an initial and final waste volume of 0.25 and 0.05 mL. Samples were dialyzed in at least 500 x deionized water overnight using 10 kD cut-off dialysis bag (ThermoFisher, SnakeSkin Dialysis Tubulin, 68100) and the water was changed twice in between to remove organic solvent. Then the purified nanoparticles were concentrated by centrifuging using Amicon Ultra-15 Centrifugal Filter Units (Millipore, UF9050) at 2,168 x *g* to the desired concentration. For encapsulation of IKE, IKE was dissolved in a solution of PEG-PLGA in 25% acetone and 75% DMSO. The final concentration of PEG-PLGA was 10 mg/mL and IKE is 1.5 mg/mL. The process was the same with PEG-PLGA nanoparticles preparation. Nanoparticle size and potential were measured using a Malvern Zetasizer Nano ZS.

IKE quantification in PEG-PLGA nanoparticles

IKE concentration was determined in PEG-PLGA nanoparticles using Liquid Chromatography- Mass Spectrometry (LC -MS). IKE was extracted from nanoparticles by mixing 100 μ L of samples with 900 μ L of acetonitrile. After mixing for 1 h, the mixture was sonicated for 5 min and then centrifuged at 4000 rpm for 10 min. The supernatant was transferred to a new vial. The organic solvent was removed by Genevac evaporation. The residues were re-dissolved in 100 μ L MeOH in a LC-MS vial. Calibration standards and quality control samples were prepared spanning a range of 25 ng/ml to 1250 ng/ml IKE in MeOH. Peak integration and data analysis were performed. Using the standard curve, IKE concentration in the sample was determined.

Measurement of IKE PEG-PLGA cellular activity

DLBCL cells or HT-1080 cells were plated at 2,000 cells per well in white 384-well plates (32 μ L per well) in technical duplicates and incubated overnight. The cells were then treated with 8 μ L medium containing a two-fold dilution series of vehicle 1 (DMSO), IKE, Fer-1, vehicle 2 (unfunctional PEG-PLGA nanoparticles), or IKE PEG-PLGA nanoparticles. The final concentration of IKE in PEG-PLGA nanoparticles were measured by LC-MS as described in the sections below. After 24 h incubation with

compounds, 40 μ L of 50% CellTiter-Glo (Promega) 50% cell culture medium was added to each well and incubated at room temperature with shaking for 15 min. Luminescence was measured using a Victor X5 plate reader (PerkinElmer). All cell viability data were normalized to the DMSO vehicle condition. Experiments were performed in three independent times with different passages for each cell line. From these data, dose-response curves and IC₅₀ values were computed using Prism 7.0 (GraphPad).

IKE Efficacy study

IKE was dissolved in 5% DMSO/95% HBSS at pH 4 to create a 4 mg/mL solution. 5% DMSO/95% HBSS at pH 4 was used as vehicle 1. IKE PEG-PLGA nanoparticles and unfunctionalized PEG-PLGA nanoparticles (without IKE loading) (vehicle 2) prepared with a NanoAssemblr were dialyzed with deionized water overnight; the water was changed at least twice. Dialyzed IKE-PEG-PLGA nanoparticles and unfunctional PEG-PLGA nanoparticles were concentrated by Amicon Ultra-15 Centrifugal Filter Units to create a solution with 80 mg/mL PEG-PLGA nanoparticles. All above solutions were sterilized by filter through a 0.2 μ m syringe filter.

NCG mice, 6-weeks old, were injected with 10 million SUDHL0-6 cells subcutaneously. The mice were treated after the tumor size reached 100 mm³. Mice were separated randomly into treatment groups and dosed with 23 mg/kg IKE, 40 mg/kg IKE, 23 mg/kg IKE PEG-PLGA nanoparticles (equal to 700 mg/kg PEG-PLGA), vehicle 1 (based on volume), and vehicle 2 (700 mg/kg PEG-PLGA) once daily by IP for 14 days. Tumor volume was measured daily with electronic caliper and calculated using the formula: 0.5 x length x width². 3 h after the final dosage, mice were euthanized with CO₂ and tumor tissue was dissected, weighed, divided into 4-6 segments, frozen, and stored at -80°C. Tumor volume change was analyzed in Prism using one-way ANOVA. Tumor tissues were analyzed as described in the RT-qPCR, immunofluorescence, TBARS, and lipidomics sections below.

Immunofluorescence on frozen tissue sections and quantification

Tumor tissues were fixed in 4% paraformaldehyde (PFA) for 24 h at 4°C followed by washing with PBS three times. The tissues were perfused in 30% sucrose for 24 h at 4°C for cryo-protection. The samples were embedded in OCT cryostat sectioning medium, and then moved directly into a cryostat. After equilibration of temperature, frozen tumor tissues were cut into 5 µm thick sections. Tissue sections were mounted on to poly-L-lysine coated slides by placing the cold sections onto warm slides. Slides were stored at -80°C until staining. For staining, slides were warmed to room temperature followed by washing with PBS twice. A hydrophobic barrier pen was used to draw a circle on each slide. The slides were permeabilized with PBS/0.4% Triton X-100 twice before non-specific-binding blocking by incubating the sections with 10% goat serum (ThermoFisher 50197Z) for 30 minutes at room temperature. The sections were separately incubated with mouse anti-MDA mAb 1F83 (1:1000 dilution), anti-cyclooxygenase 2 (COX 2, AKA PTGS2) antibody (Abcam, ab15191, 1:200 dilution), or anti-8-OH-dG (DNA/RNA damage) antibody (Abcam, ab62623, 1:200 dilution) overnight at 4°C in humidified chambers. Sections were washed with PBST for twice before incubating with goat anti-mouse IgG H&L (Alexa Fluor 647) (Abcam, ab150115, 1:1000 dilution) or goat anti-rabbit IgG H&L highly cross-absorbed secondary antibody (Alexa Fluor488, Thermo Fisher Scientific, A-11034, 1:1000) at room temperature for 1 h. Slides were then washed twice with PBST. ProLong Diamond antifade mountant with DAPI (ThermoFisher P36962) was added onto slides, which were then covered with the coverslips, sealed by clear fingernail polish and observed under confocal microscopy. All images were captured on a Zeiss LSM 800 confocal microscope at Plan-Apochromat 63x/1.40 Oil DIC objective with constant laser intensity for all analyzed samples. The intensity above threshold of the fluorescent signal of the bound antibodies was analyzed using NIH ImageJ software. Data were expressed as fold change comparing with the vehicle.

Western blot

10-25 mg tumor tissue was placed into a 1.5 mL Eppendorf microfuge tube, and the sample was placed on dry ice until use. 20 µL/mg ice cold RIPA buffer with cocktail protease inhibitor (Roche) was added. The

tumor tissue was homogenized at speed 5 for 30 sec using Bead Ruptor 4. The sample was centrifuged at 4°C at 1,600 x *g* for 10 min. The sample was kept on ice and the supernatant used for analysis. Caspase-3 antibody which could recognize both full-length caspase-3 and cleaved caspase-3 was used. α -Tubulin antibody was used as the reference.

Quantification and statistical analysis

T-test, one-way ANOVA, and two-way ANOVA were performed in R (version 3.5.1) environment and GraphPad Prism7 with significance and confidence level 0.05 (95% confidence interval).

Chapter 5 Untargeted Lipidomics Study of IKE Induced Ferroptosis⁴

5.1 Introduction

Increased evidences have shown the involvement of lipid metabolism and the associated enzymes in ferroptosis. Acyl-CoA synthetase long-chain family member 4 (*ACSL4*) and lysophosphatidylcholine acyltransferase 3 (*LPCAT3*) were enriched in ferroptosis resistant cell lines⁸⁶. An independent genome-wide CRISPR-based genetic screen and microarray analysis also identified key function of *ACSL4* in ferroptosis⁶⁹. A quantitative redox global phospholipidomics revealed that doubly and triply oxygenated species of PE are significantly increased in ferroptosis⁸⁹. PEs containing arachidonoyl (AA) and adrenoyl moieties (AdA) were identified as the preferred substrates for oxidation in ferroptosis⁸⁹. In addition, inhibition of lipoxygenases (ALOXs) but not cyclooxygenases (COXs) and cytochrome P450 prevented RSL-3 induced ferroptosis^{82, 89}. However, the genes regulating change of different lipid species during ferroptosis, and lipidomics of *in vivo* ferroptosis have not been investigated. Here, we described the lipidomics in IKE-, and IKE in combination with Fer-1-, DFO-, or β -Me-treated SUDHL-6 cells to identify the lipids change during IKE-induced ferroptosis. Besides, a series of genes associated with lipid metabolism were identified to be upregulated with IKE treatment in SUDHL-6 cells. To our surprise, the lipids change in tumor samples of IKE treated NCG mice bearing subcutaneously SUDHL-6 xenograft is different than what in IKE-treated-SUDHL-6 cells.

⁴This chapter is adapted from the manuscript submitted: Zhang, Y.; Tan, H.; Daniels J. D.; Zandkarimi, F.; Liu, H.; Brown, L. M.; Uchida, K.; O'Connor, O. A.; Stockwell, B. R., Imidazole ketone erastin nanoparticles induce ferroptosis and slow tumor growth in a mouse lymphoma model

5.2 Results

5.2.1 Untargeted lipidomics study of IKE induced ferroptosis in cell culture

To investigate the effects of IKE on lipid composition and metabolites, we performed untargeted mass-spectrometry-based lipidomics and gene expression analysis of related enzymes during lipid biosynthesis and oxidation. SUDHL-6 cells treated with 1 μM IKE, and 500 nM IKE with or without 10 μM fer-1, 10 μM β -Me, and 10 μM deferoxamine (DFO) co-treatment, were subjected to UPLC-MS analysis. We observed significant (one-way ANOVA, $p < 0.05$) depletion in the relative abundance of 74 lipid ions including lysophosphatidylcholines (LPC), phosphatidylcholines (PC), phosphatidylethanolamines (PE), and triacylglycerols (TAG) mainly containing poly-unsaturated fatty acids (PUFAs) in IKE-treated groups, while co-treatment with β -Me or fer-1 reversed this effect and maintained the levels of these specific lipids near to baseline (**Figure 5.1**). The annotations of the lipid species were confirmed with LipoStar software (Version 1.0.4, Molecular Discovery, UK)¹⁴³. These results are consistent with the effects of piperazine erastin and erastin +/- fer-1 treated HT-1080 cells on lipid composition^{67, 82}. While the levels of monoacylglycerols (MAG), the hydrolysis product of TAG lipids were increased significantly in IKE-treated samples, fer-1 co-treatment decreased significantly the levels of these MAG lipids. The iron chelator DFO was not able to reverse IKE-induced lipidomic changes, although this may be due to the toxicity of DFO at concentrations that are needed to suppress ferroptosis.

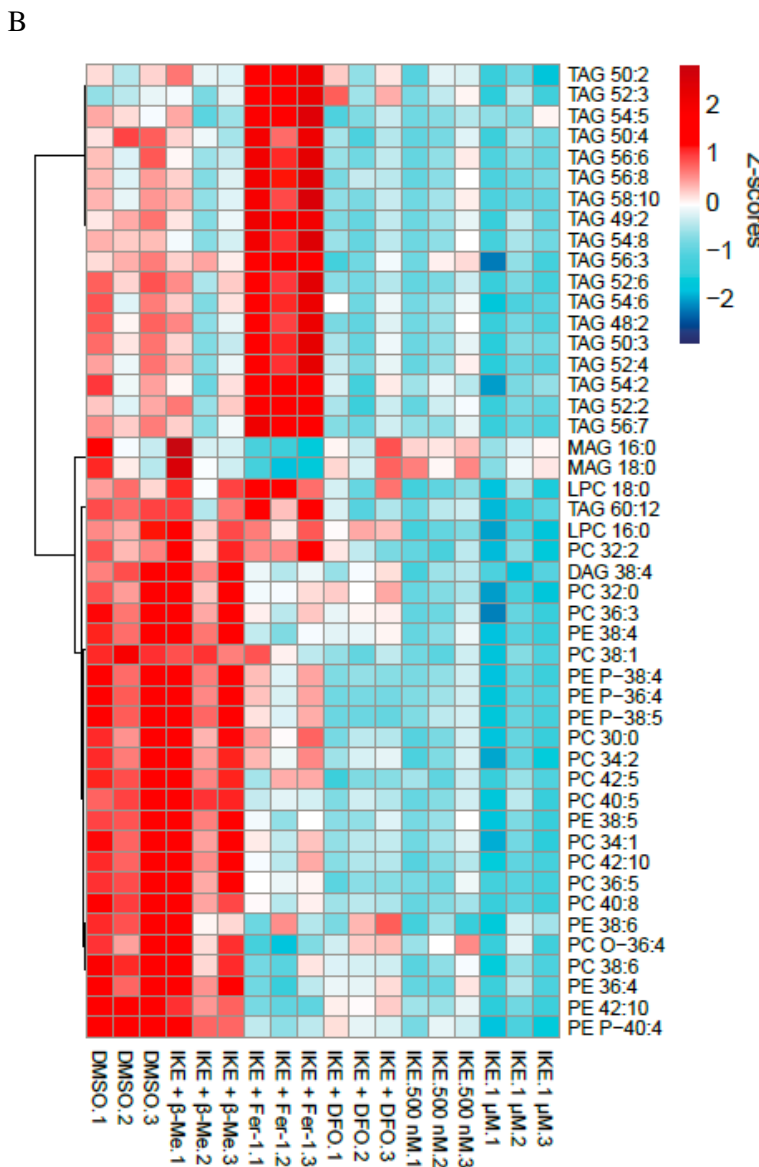
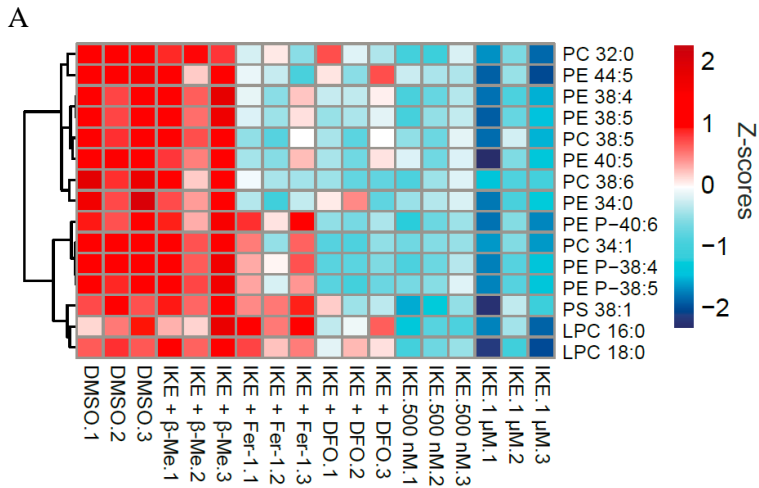


Figure 5. 1 Untargeted lipidomics study in SUDHL-6 cells

Heatmap of significantly changed (one-way ANOVA, $p < 0.05$) lipid species in SUDHL-6 cells treated with DMSO, 500 nM IKE, 1 μM IKE, 500 nM IKE with 10 μM fer-1 cotreatment, 500 nM IKE with 10 μM β-Me cotreatment, 500 nM IKE with 10 μM DFO cotreatment, measured by LC-MS. Each row represents z-score normalized intensities of the detected lipid species (A) in negative electrospray ionization mode and (B) in positive electrospray ionization mode. Each column represents an independent biological replicate. The lipid abundance is color coded with red indicating high signal intensity and dark blue indicating low signal intensity. Abbreviations: PC, phosphatidylcholine; PE, phosphatidylethanolamine; PS, phosphatidylserine; LPC, lysoPC; PE P-, plasmalogen PE; TAG, triacylglycerol; DAG, diacylglycerol, MAG, monoacylglycerol.

5.2.2 Investigation of enzymes relating to IKE induced lipids change

By measuring the mRNA levels of lipid biosynthesis enzymes upon IKE treatment, we found significant upregulation of acetyl-CoA carboxylase 1 (*ACCI*), which catalyzes the rate-limiting step of fatty acids biosynthesis from acetyl-CoA to malonyl-CoA, and elongation of very long chain fatty acids protein 7 (*ELOVL7*), which catalyzes the rate-limiting reactions of long-chain fatty acids elongation cycle especially the elongation of C18:3 (*n*-3) and C18:3 (*n*-6)-CoAs (**Figure 5.2**). The upregulation of these two mRNAs was partially reversed by co-treatment of 10 μ M fer-1 or 10 μ M β -Me, indicating that fatty acid biosynthesis was activated by cysteine depletion and lipid peroxidation during IKE-induced ferroptosis. Moreover, there was significant upregulation of adipose triglyceride lipase (*ATGL*), secretory phospholipase A2f (*sPLA2F*), lysophosphatidylcholine acyltransferase 4 (*LPCAT4*), and lysophosphatidylethanolamine acyltransferase 1 (*LPEAT1*), suggesting that phospholipid biosynthesis remodeling was activated with IKE treatment. Lipids peroxidation during ferroptosis is a deleterious process, and the best way to repair such damage is to selectively cleave the oxidized PUFA, replace with the native fatty acids, and subsequently reduce the lipid hydroperoxides by glutathione peroxidase¹⁴⁴. The activation of sPLA2, which selectively release arachidonic acid at the *sn*-2 position of phospholipids, ATGL, which hydrolyzes triacylglycerides, LPCAT4 and LPEAT1, which catalyze the conversion of LPC to PC and LPE to PE respectively, is thus important for this repair process. In addition to Fenton-chemistry-mediated lipid peroxidation, enzyme-mediated lipid peroxidation was also activated in IKE-induced ferroptosis as there were increased lipoxygenase 12 (*ALOX12*) and lipoxygenase 15 (*ALOX15*) expression.

Genes upregulated with IKE treatment were highlighted as red color in the schematic lipids biosynthesis overview (**Figure 5.3**). In summary, these lipidomic studies provides us with a detailed picture of IKE-induced ferroptosis in cell culture at the level of lipid metabolism.

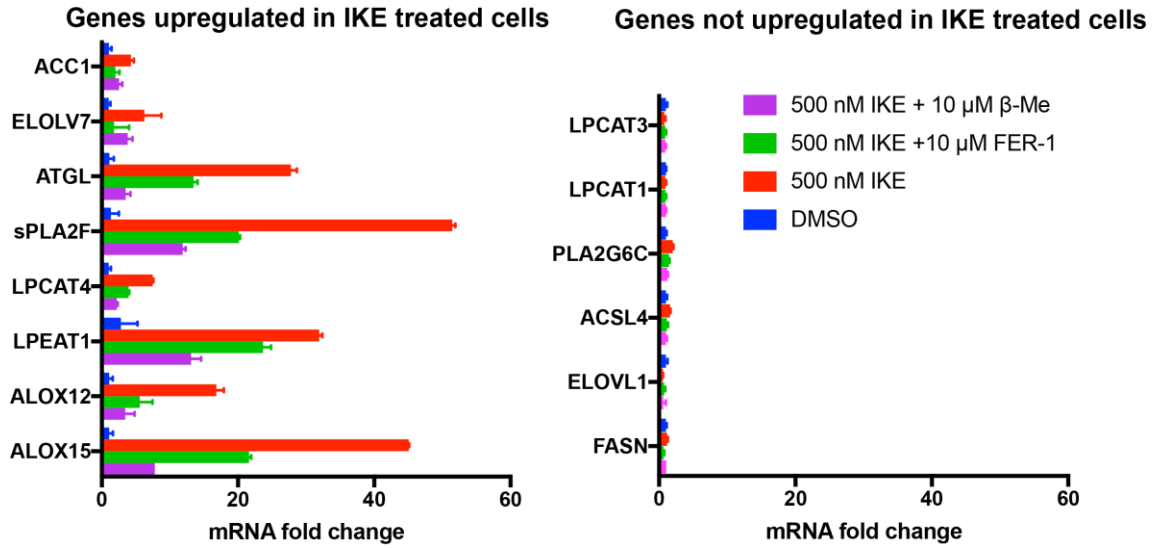


Figure 5. 2 Expression level of genes involving lipid metabolism

Fold change in expression of lipids biosynthesis and metabolism associated genes with 500 nM IKE treatment, 500 nM IKE with 10 μM fer-1 cotreatment, and 500 nM with 10 μM β-Me cotreatment comparing with DMSO control in SUDHL-6 cells. *ACC1*, *ELOVL7*, *ATGL*, *sPLA2F*, *LPCAT4*, *LPEAT1*, *ALOX12*, and *ALOX15* were upregulated in SUDHL-6 cells with IKE treatment. Cotreatment with fer-1 and β-Me partially reversed the effects (left). *FASN*, *ELOVL1*, *ACSL4*, *PLA2G6C*, *LPCAT1*, and *LPCAT3* were not upregulated in IKE treated SUDHL-6 cells (right).

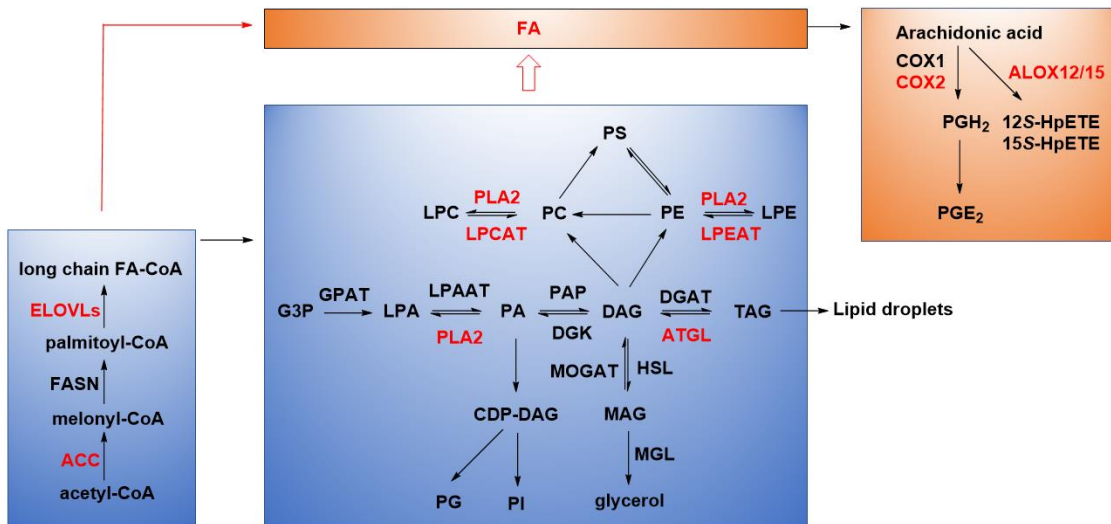


Figure 5. 3 Schematic view of fatty acid biosynthesis, lipids remodeling, and arachidonic acid oxidation

The genes upregulated in IKE treatment were labeled with red color.

5.2.3 Untargeted lipidomics study of IKE induced ferroptosis *in vivo*

While lipidomic study in SUDHL-6 cell culture helps us understand the mechanisms leading to the lipids change, we want to further investigate lipids change with IKE treatment *in vivo*, as the solid tumor has complex microenvironment which is hard to mimic by cell culture. We performed untargeted lipidomics on tumor tissue with a single dose of IKE across different time points. Different from the *in vitro* lipidomic results, we identified significant (one-way ANOVA $p < 0.05$) accumulation in the relative abundance of free fatty acids, phospholipids, and diacylglycerol (DAG) upon IKE treatment (**Figure 5.4**). This might stem from the different tumor microenvironment *in vivo*. The lipids identified were enriched in linoleic acid and arachidonic acid metabolism (**Figure 5.5**).

The significant increase in the levels of DAG and free fatty acids might result from the ATGL-mediated-TAG hydrolysis (**Figure 5.6**). We also observed accumulation of MAG lipids in IKE-treated cell (**Figure 5.1**). The increased fatty acids in turn promote phospholipid remodeling to synthesize specific types of phospholipids, including PC and PE.

To explore the free fatty acids effects on cells and ferroptosis, we performed a cell survival test of free fatty acids in the presence or absence of IKE. We found that high concentrations of PUFAs, including γ -linolenic acid, eicosapentaenoic acid, and arachidonic acid, were toxic to cells (**Figure 5.7A**), low concentration of free fatty acids sensitized to ferroptosis, while oleic acid and palmitoleic acid had protective effects on ferroptosis at low concentrations (**Figure 5.7B**)

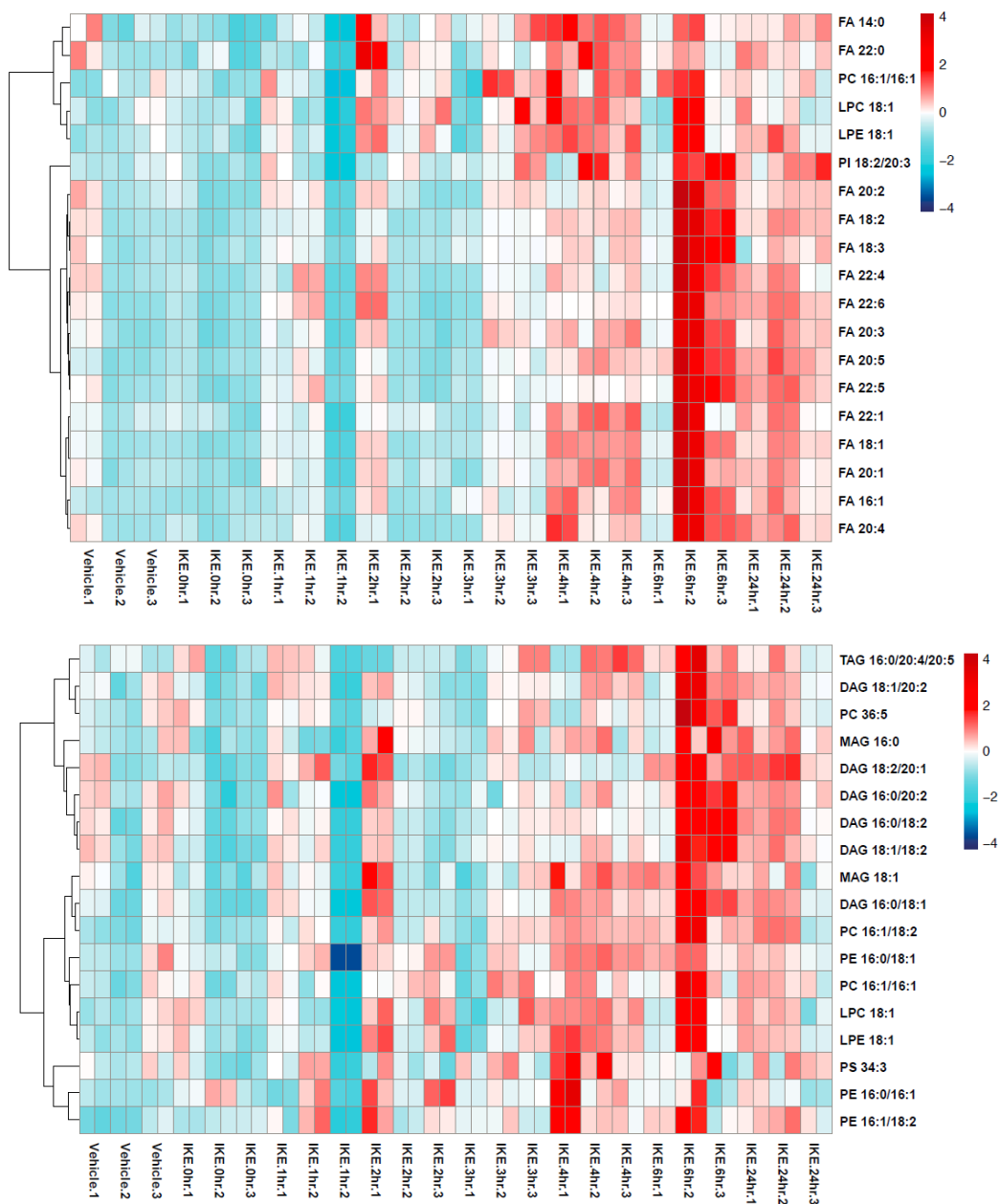


Figure 5. 4 Untargeted lipidomics study *in vivo*

Heatmaps of dysregulated lipids in SUDHL6 subcutaneously xenografted NCG mice treated with one dosage IKE for at 0, 4, and 24 hours or with vehicle, detected by untargeted UPLC-MS analysis. Data shown in heatmaps are lipid species that were identified as being statistically significant ($p < 0.05$) among the groups in negative electrospray ionization mode (Top) and positive electrospray ionization mode (Bottom). Each column represents an independent biological replicate. Each row represents z-score normalized intensity of a lipid feature. The relative abundance of each identified lipid is color coded with blue indicating low signal intensity and red indicating high signal intensity. Abbreviations: PC, phosphatidylcholine; PE, phosphatidylethanolamine; PI, Phosphatidylethanolamine; PS, phosphatidylserine, LPC, lysoPC; LPE, lysoPE; FA, free fatty acid; TAG, triacylglycerol; DAG, diacylglycerol, MAG, monoacylglycerol.

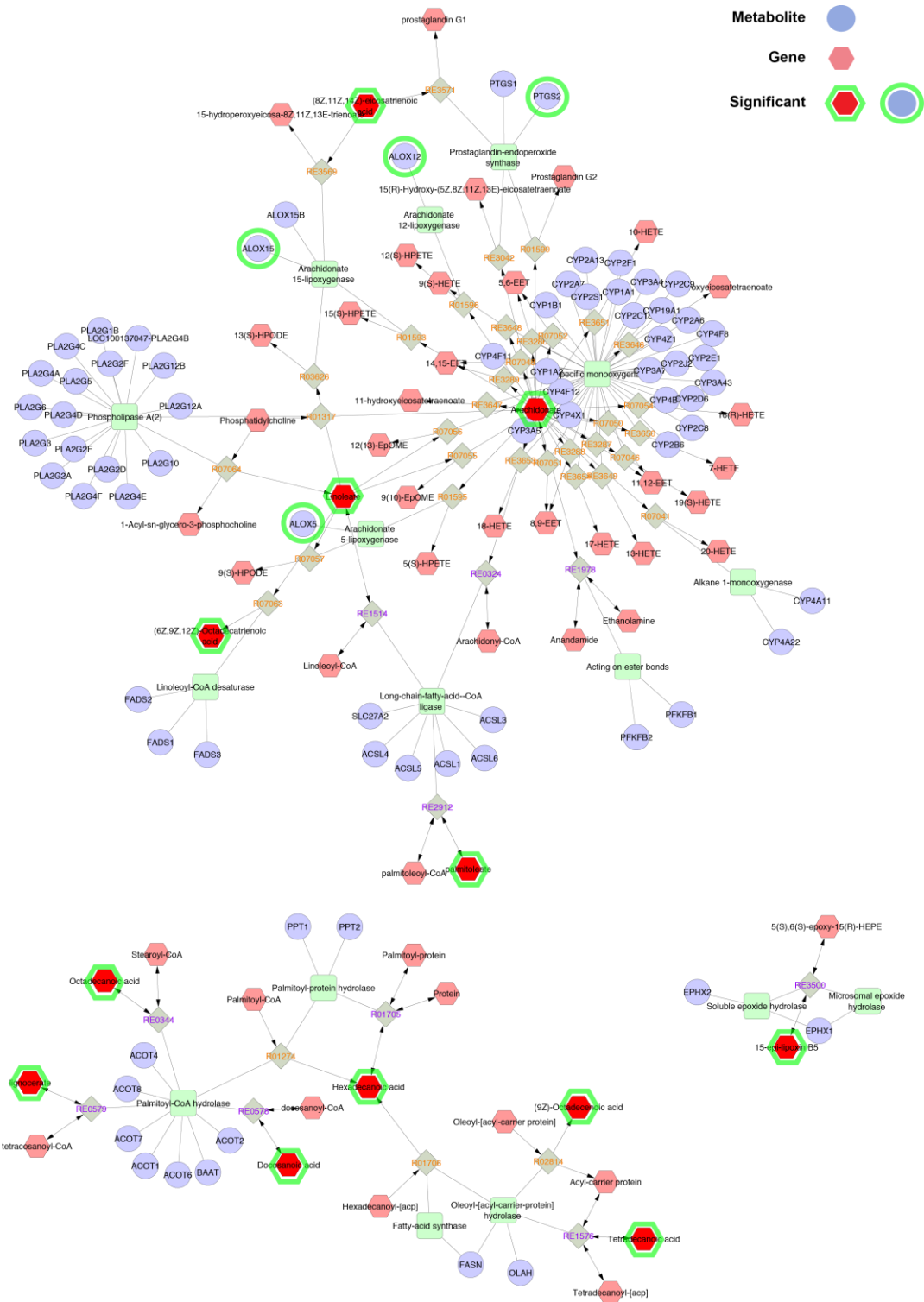


Figure 5. 5 Metscape network analysis of lipids identified in IKE treatment *in vivo*

Significant accumulated lipids *in vivo* and significant genes in ferroptosis are highlighted as green circle in the figure.

Genes expression analyzed by qPCR in tumor tissue

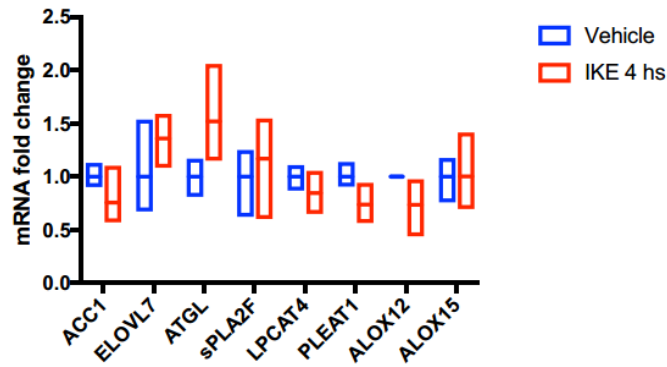


Figure 5. 6 Gene expression analysis *in vivo*

RT-qPCR analysis of gene expression related to lipids biosynthesis and peroxidation in tumor tissue samples from one dosage of IKE treatment comparing with vehicle treatment.

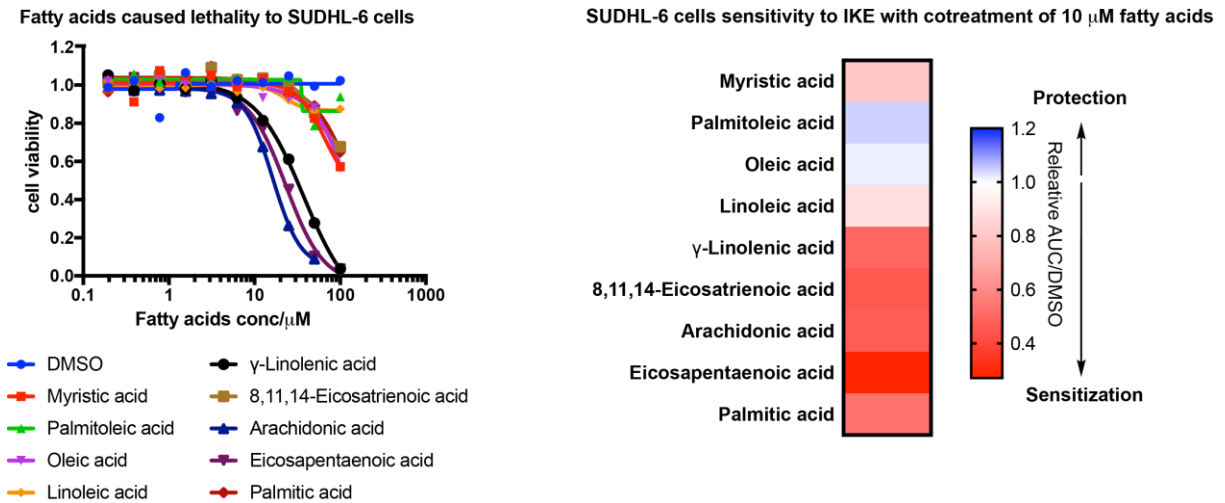


Figure 5. 7 Lethality and sensitivity effects evaluation of lipids

(A) Dose-response curves of SUDHL-6 cells was determined by adding free fatty acids in a 10-point, two-fold dilution series for 24 hours, followed by a Cell Titor-Glo luminescent cell viability test. γ -l-linolenic acid, eicosapentaenoic acid, and arachidonic acid are toxic to cells at high concentration. (B) Dose-response curves of SUDHL-6 cells was determined by treating with IKE in a 10-point, twofold dilution series in the presence of DMSO or free fatty acids. Relative Area Under Curve (AUC) to DMSO cotreatment was used to indicate the sensitization or protection effect of free fatty acids to IKE-induced ferroptosis.

5.3 Discussion

Lipidomics is an emerging area in biomedical research. By performing untargeted lipidomics study in IKE treated SUDHL-6 cells in combination with different ferroptosis inhibitors, we identified decreased PE, PC, and TAG upon IKE treatment. This might result from the cleavage of oxidized PUFA in PE, PC, and TAG to prevent the oxidative damage to cells induced by IKE treatment. The cotreatment of β -Me, which transport cysteine through L systems, completely reversed the lipids change resulted by IKE treatment. Besides, the antioxidant reagent Fer-1 partially prevented the phospholipids decrease in cells, but dramatically increased TAG. The increased TAG pool might serve as a buffer against lipotoxicity induced by IKE¹⁴⁵. In addition, the iron chelator DFO didn't prevent IKE induced phospholipids and TAG decrease, indicating that Fenton chemistry-mediated lipid peroxidation is not the driver of lipids change during ferroptosis.

A series of genes regulating lipid metabolism have been proved to participate in ferroptosis (**Table 6**). mRNA level of genes encoding lipid biosynthesis enzyme ACC1 and ELOVL7 were increased with IKE treatment, which might function to increase PUFA production to compensate the oxidized PUFA. *LPCAT4* and *LPEATI*, which encode enzymes to promote PC and PE synthesis, were dramatically upregulated upon IKE treatment. Given the evidence that PE peroxides were significantly increased in ferroptosis⁸⁹, and PE has important structural function in cell membrane⁸⁴, the upregulation of *LPEATI* is thus important for maintaining cellular PE concentration and integrity of cell membrane. Lipid peroxidation is lethal to cells, the most efficient way to remove this kind of oxidative damage is to cleave the oxidized PUFA and exchange with the natural ones. The upregulation of *ATGL* and *sPLA2F* strongly supports this hypothesis.

Lipidomics study *in vivo* proved a different landscape of lipids change. DAG were significantly increased in tumor tissue after IKE treatment, which might result from hydrolysis of TAG. The increased PUFA might come from the response of tumor microenvironment to protect tumor cells from the oxidative stress with IKE treatment.

In summary, we proved the involvement of different species of lipids and lipid metabolism genes in IKE-induced ferroptosis and the protective effect of different ferroptosis inhibitors to IKE-induced lipids change. More investigation could be done to study the execution roles of genes identified here.

Table 5. 1 Genes involved in reduced glutathione (GSH)-depletion induced ferroptosis

| Gene | Name | Function |
|---------------------------------|--|--|
| <i>SLC7A11</i> | Solute carrier family 7 member 11 (cystine/glutamate antiporter system x_c^- light chain, xCT) | Upregulated by system x_c^- inhibitors; Inhibition of system x_c^- leads to glutathione depletion and ferroptosis |
| <i>CHAC1</i> | ChaC glutathione-specific gamma- glutamylcyclotransferase 1 | Upregulated by system x_c^- inhibitors |
| <i>GPX4</i> | Glutathione peroxidase-4 | Function as phospholipid hydroperoxidase which reduces hydrogen peroxide and lipid peroxides by using reduced glutathione (GSH) to protect cells from lipid peroxidation; Inhibition or depletion of GPX4 leads to ferroptosis |
| <i>PTGS2</i> (<i>COX2</i>) | Prostaglandin-endoperoxide synthase 2 | Upregulated in ferroptosis |
| <i>ALOXs</i> | lipoxygenases | Involved in peroxidation of PUFA in GSH-depletion induced ferroptosis |
| <i>ACSL4</i> | Acyl-CoA synthetase long-chain family member 4 | Converts free fatty acids into fatty CoA ester, involved in GPX4-depletion induced ferroptosis |
| <i>PLA2</i> | Phospholipase 2 | Hydrolyzes polyunsaturated fatty acids and oxidized polyunsaturated fatty acids at the <i>sn</i> -2 position of |

| | | |
|----------------------------------|---|--|
| | | phospholipids |
| <i>sPLA2F</i> | Secretory phospholipase A2f | One isomer of PLA2 |
| <i>ATGL</i> (<i>PNPLA2</i>) | Adipose triglyceride lipase | Catalyzes the rate limiting step of lipolysis of triacylglycerol (TAG) |
| <i>LPCAT1</i> | Lysophosphatidylcholine acyltransferase 1 | Converts lysophosphatidylcholine (LPC) to phosphatidylcholine (PC), localize to the endoplasmic reticulum and lipid droplets |
| <i>LPCAT2</i> | Lysophosphatidylcholine acyltransferase 2 | Converts lysophosphatidylcholine (LPC) to phosphatidylcholine (PC), localize to the endoplasmic reticulum and lipid droplets |
| <i>LPCAT3</i> | Lysophosphatidylcholine acyltransferase 3 | Key enzyme to incorporate arachidonic acid into glycerophospholipids, critical for embryogenesis |
| <i>LPCAT4</i> | Lysophosphatidylcholine acyltransferase 4 | Acyl-CoA-dependent lysophospholipid acyltransferase, prefers long chain acyl-CoAs (C16, C18) as acyl donors. |
| <i>LPEAT1</i> | Lysophosphatidylethanolamine acyltransferase 1 | Preferentially acylates LPE with acyl-CoA |
| <i>ACC</i> | Acetyl-CoA carboxylase | Catalyzes the conversion of acetyl-CoA to malonyl-CoA |
| <i>ELOVL7</i> | Elongation of very long chain fatty acids protein 7 | Catalyzes the first and rate-limiting reaction of long-chain fatty acids elongation cycle, with higher activity toward C18 acyl-CoAs especially C18:3(<i>n</i> -3) and C18:3(<i>n</i> -6)-CoAs |

5. 4 Methods

qPCR in cells and mouse tumor tissue

The experiments followed the same steps used in Chapter 3 and 4. qPCR primers used in this chapter are listed below:

| Genes | Foward | Reverse |
|---------------|-----------------------------------|-----------------------------------|
| <i>ACSL4</i> | 5'-CCCCGCTATCT CTCAGACAC-3' | 5'-GGTGCTCCAACCTCTGCCAG-3' |
| <i>FASN</i> | 5'-CTTCCGAGATTCCATCCTACGC-3' | 5'-TGGCAGTCAGGCTCACAAACG-3' |
| | 5'- TCCCTCTACATTGTCTATGAGTTCC- | 5'- TTCAGTTGGCCTTGACCTTGGCAAT |
| <i>ELOVL1</i> | 3' | ACC-3' |
| | 5'- AGGATCCATGGCCTTCAGTGATCTT | 5'- AACCACCTGCAGCAAATTTGACTCC |
| <i>ELOVL7</i> | ACATCGAGG-3' | -3' |
| | 5'- AGAAAAGTTGACTAGTCCAGTGTG | 5'- AAAAGCTGTGCTAAACCAATTCCGA |
| <i>ALOX12</i> | GTGAA-3' | ACAGATTCTCA-3' |
| <i>ALOX15</i> | 5'-GGAGCCTTCCTAACCTACAGC-3' | 5'-CTCACGATTCCTTCCACATACC-3' |
| <i>LPCAT1</i> | 5'-CACAACCAAGTGGAATCGAG-3' | 5'-GCACGTTGCTGGCATAACA-3' |
| <i>LPCAT3</i> | 5'-ATCACTGCCGTCCTCACTAC-3' | 5'-AGTCAACAGCCAAACCAATC-3' |
| <i>LPCAT4</i> | 5'-GGTGGGAGAGAATGCCACTT-3' | 5'-ATGCAAGGGATGATGGCTGT-3' |
| <i>LPEAT1</i> | 5'-CTGAAATGTGTGTGCTATGAGCG- 3' | 5'- TGGAAGAGAGGAAGTGGTGTCTG-3' |
| <i>ACC1</i> | 5'-GAGGGCTAGGTCTTTCTGGAAG-3' | 5'-CCACAGTGAAATCTCGTTGAGA-3' |
| <i>sPLA2F</i> | 5'- TGACGACAGGAAAGGAAGCCGCAC | 5'- AGGGAAGAGGGGACTCAGCAACGA |

| | -3' | G-3' |
|----------------|-----------------------------|-------------------------------|
| <i>PLA2G6C</i> | 5'-CTGGAACCTGTGTTGGACCT-3' | 5'-CGGTGATATCTGTGGTCACG-3' |
| <i>ATGL</i> | 5'-CAACGCCACTCACATCTACGG-3' | 5'-GGACACCTCAATAATGTTGGCAC-3' |

Mass spectrometry-based untargeted lipidomics analysis

Sample preparation *in vitro* study

The lipids were extracted from each cell sample using a modified Matyash method¹⁴⁶ as described previously¹⁴⁷. 5 million cells treated with DMSO, 1 μ M IKE, 500 nM IKE with or without 10 μ M fer-1 and 10 μ M β -Me for 24 hours were homogenized in 250 μ L cold methanol containing 0.1% butylated hydroxyl toluene (BHT) with micro tip sonicator. Homogenized samples were transferred to fresh glass tubes containing 850 μ L of cold methyl-tert-butyl ether (MTBE) and vortex-mixed for 30 sec. To enhance extraction efficiency of lipids, the samples were incubated overnight at 4 °C on the shaker. On the next day, 200 μ L of cold water was added to each sample, and incubated for 20 min on ice before centrifugation at 3,000 rpm for 20 min at 4 °C. The organic layer was collected followed by drying under a gentle stream of nitrogen gas on ice and stored at -80 °C until LC-MS analysis. The protein pellet was used to measure protein concentration using Bio-Rad protein assay. The samples were re-constituted in a solution containing IPA/ ACN /water (4:3:1, v/v/v) containing mixture of internal standard for further MS analysis.

A quality control (QC) sample was prepared by combining 40 μ L of each sample to assess the reproducibility of the features through the runs.

Ultra-performance liquid chromatography analysis

Chromatographic separation of extracted lipids was carried out at 55 °C on Acquity UPLC HSS T3 column (2.1 \times 150 mm, 1.8 μ m) over a 17-min gradient elution. Mobile phase A consisted of ACN/water (60:40, v/v) and mobile phase B was IPA/ACN/water (85:10:5, v/v/v) both containing 10 mM ammonium

acetate and 0.1% acetic acid. After injection, the gradient was held at 60% mobile phase A for 1.5 min. For the next 12 min, the gradient was ramped in a linear fashion to 100% B and held at this composition for 3 min. The eluent composition returned to the initial condition in 1 min, and the column was re-equilibrated for an additional 1 min before the next injection was conducted. The flow rate was set to 400 $\mu\text{L}/\text{min}$ and Injection volumes were 5 μL using the flow-through needle mode in both positive and negative ionization modes.

The QC sample was injected between the samples and at the end of the run to monitor the performance and the stability of the MS platform. This QC sample was also injected at least 5 times at the beginning of the UPLC/MS run, in order to condition the column.

Mass spectrometry analysis

The Synapt G2 mass spectrometer (Waters, Manchester, U.K.) was operated in both positive and negative electrospray ionization (ESI) modes. For positive mode, a capillary voltage and sampling cone voltage of 3 kV and 32 V were used. The source and desolvation temperature were kept at 120 $^{\circ}\text{C}$ and 500 $^{\circ}\text{C}$, respectively. Nitrogen was used as desolvation gas with a flow rate of 900 L/hr. For negative mode, a capillary voltage of -2 kV and a cone voltage of 30 V were used. The source temperature was 120 $^{\circ}\text{C}$, and desolvation gas flow was set to 900 L/hr. Dependent on the ionization mode the protonated molecular ion of leucine encephalin ($[\text{M}+\text{H}]^+$, m/z 556.2771) or the deprotonated molecular ion ($[\text{M}-\text{H}]^-$, m/z 554.2615) was used as a lock mass for mass accuracy and reproducibility. Leucine enkephalin was introduced to the lock mass at a concentration of 2 $\text{ng}/\mu\text{L}$ (50% ACN containing 0.1% formic acid), and a flow rate of 10 $\mu\text{L}/\text{min}$. The data was collected in duplicates in the centroid data independent (MS^E) mode over the mass range m/z 50 to 1600 Da with an acquisition time of 0.1 seconds per scan.

The QC samples were also acquired in enhanced data independent ion mobility (IMS-MS^E) in both positive and negative modes for enhancing the structural assignment of lipid species. The ESI source settings were the same as described above. The traveling wave velocity was set to 650 m/s and wave height was 40 V. The helium gas flow in the helium cell region of the ion-mobility spectrometry (IMS)

cell was set to 180 mL/min to reduce the internal energy of the ions and minimize fragmentation. Nitrogen as the drift gas was held at a flow rate of 90 mL/min in the IMS cell. The low collision energy was set to 4 eV, and high collision energy was ramping from 25 to 65 eV in the transfer region of the T-Wave device to induce fragmentation of mobility-separated precursor ions.

Data pre-processing and statistical analysis

All raw data files were converted to netCDF format using DataBridge tool implemented in MassLynx software (Waters, version 4.1). Then, they were subjected to peak-picking, retention time alignment, and grouping using XCMS package¹⁴⁸ (version 3.2.0) in R (version 3.5.1) environment. For the peak picking, the CentWave algorithm¹⁴⁹ was used with the peak width window of 2-25 s. For peak grouping, bandwidth and m/z-width of 2 s and 0.01 Da were used, respectively. After retention time alignment and filling missing peaks, an output data frame was generated containing the list of time-aligned detected features (m/z and retention time) and the relative signal intensity (area of the chromatographic peak) in each sample.

Technical variations such as noise were assessed and removed from extracted features' list based on the ratios of average relative signal intensities of the blanks to QC samples (blank/QC >1.5). Also, peaks with variations larger than 30% in QCs were eliminated.

Multivariate and univariate analyses were performed using MetaboAnalyst¹⁵⁰ (version 4.0) and in R (version 3.5.1) environment. Group differences were calculated using VIP scores of PLS-DA model and one-way ANOVA ($p < 0.05$) and false discovery rate of 5% to control for multiple comparisons.

Structural assignment of identified lipids

Identification and structural characterization of significant lipid features were confirmed with LipoStar¹⁴³ (Version 1.0.4, Molecular Discovery, UK). Lipidomix standard (Avanti Polar Lipids, INC., Alabaster, AL, USA) and quality control samples were analyzed in LipoStar with the recommended data processing parameters¹⁴³ except MS/MS signal filtering threshold was set to 20 for both positive and negative

ionization mode. The precursor ion (MS) and fragment ion information obtained by data independent MS (MSE) were automatically annotated using LipoStar database library with mass tolerances of 5 ppm and 10 ppm, respectively. Annotated lipid species with the highest score and high-confidence identification (matches between experimental and theoretical MS/MS spectra) were approved, and the identified lipids with low-confidence matches were further evaluated manually using MS^E data viewer (Version 1.3, Waters Corp., MA, USA).

Untargeted lipidomics study *in vivo*

25 mg frozen tissue was homogenized in 15 $\mu\text{L}/\text{mg}$ pre-chilled methanol containing 0.1% butylated hydroxyl-toluene (BHT) at speed 5 for 30 secs using a Bead Ruptor 4 (OMNI International). Then, 300 μL of tissue lysate were transferred to a glass vials containing 1,000 μL ice-cold methyl-tert-butyl ether (MTBE) and vortex-mixed for 30 sec. The sample are stored in the $-20\text{ }^{\circ}\text{C}$ freezer overnight to enhance lipids extraction. In the following day, 250 μL of ice-cold methanol was added to each sample and vortex-mixed for 30 sec vigorously. Then, samples were incubated on dry ice for 20 min on the shaker followed by centrifuge at 3,000 rpm for 20 min at 4°C . Finally, 1,000 μL of upper phase containing lipids were transferred to fresh glass vials and evaporated to dryness under the stream of N_2 gas. The samples were re-constituted in a solution containing IPA/ ACN /water (4:3:1, v/v/v) containing mixture of internal standard for further MS analysis. The other steps including LC-MS analysis and data processing are the same as *in vitro* lipidomic analysis as mentioned above.

Chapter 6 Conclusions and Future Directions

This thesis examined the power of small molecule design to validate cancer targets and therapeutic mechanisms. In the second chapter, a fragment-based small molecule design strategy combined with protein engineering approach was applied to explore the potential of targeting the nucleotide-binding site of oncogenic KRAS. In the following three chapters, the nanocarrier strategy was exploited to deliver ferroptosis inducer IKE in diffuse large B-cell lymphoma (DLBCL) xenograft model and provided increased therapeutic index comparing with free IKE. The small molecule tools, reverse-transcription quantitative PCR (RT-qPCR) techniques, and untargeted lipidomic approaches employed herein greatly facilitated the characterization of ferroptosis therapeutic mechanism in DLBCL xenograft model.

6.1 Target validation using protein engineering strategy

6.1.1 Summary

KRAS mutations are prevalent in three of the most deadly cancers in the United States: pancreatic (71%), colon (35%), and lung (19%)¹². A variety of strategies including disruption of KRAS-GEF interaction, effector binding, blocking KRAS membrane-anchoring, targeting the nucleotide-binding site and adjacent allosteric pocket have been attempted to discover small molecules that target KRAS¹³. Despite the prevalence of *KRAS* mutations and enormous efforts attempted to target KRAS, no clinically useful KRAS therapy has been developed. In Chapter 2, our work provided a small molecule tool to investigate KRAS on-target inhibition mechanism in an engineered KRAS system. We engineered the oncogenic KRAS^{G12V} protein to a functionally indistinguishable but structurally more inhibitable allele, KRAS^{G12VL19AN116AV114C} (termed KRAS*). KRAS*-GTP form retains effective binding affinity with BRAF, and is fully function in cells. At the same time, these large-to-small mutations and cysteine

mutation of the gatekeeper residues in the nucleotide-binding site resulted in an enlarged hydrophobic pocket vulnerable for covalent inhibitor attacking.

Based on the engineered structure generated above, we used fragment-based small molecule design to develop a cell-membrane permeable and selective covalent inhibitor targeting KRAS*. This small molecule (YZ0711) could irreversibly modify KRAS* nucleotide binding site both *in vitro* and in cells. It selectively disrupts KRAS*-effector interactions, inhibits KRAS* downstream signaling, and prevents KRAS* mutant cell line proliferation. The system we developed here suggests the possibility of targeting the nucleotide-binding site of oncogenic RAS proteins by generating engineered RAS alleles, and the method could be expanded for the design of allele selective small molecule inhibitors for other small GTPases.

6.1.2 Significance

Developing a new drug from the original idea through clinical trials to FDA approval is a complex, expensive, and long process; to bring a drug to market it typically costs between \$500 million to more than \$2 billion per drug¹⁵¹ and takes more than 10 years of development. Therefore, it is critical to first identify and validate the therapeutic effectiveness of the target in specific diseases, which requires the use of both genetic and small molecule tools. The development of genetic techniques including RNA interference, conditional gene targeting (conditional gene knockout and knock-in), and gene editing tools has greatly improved the precision and efficiency of studying specific gene function in cells and organisms. However, RNA interference often results in a loss-of-function outcome that has the potential to impair the important localization or protein-protein interactions, limiting agreement with small molecule approaches. Conditional gene targeting is often difficult to apply to cell culture and requires intensive efforts to optimize *in vivo*. Gene editing tools, including CRISPR/Cas9, TALEN and zinc finger nucleases, provide an easy and concise method to generate gene mutations. Small molecule tools can both complement and supplement genetic approaches in target identification and validation. In addition, small

molecule tools have the advantage of allowing cells to have little time to compensate for the modulation of target activity and can have their actions optimized by adjusting the concentration and treatment duration.

Kras is an essential gene in mouse embryo development and has un-replaceable roles in cardiovascular system in mouse adulthood, making it impossible to generate a homozygous *Kras* knockout¹⁴⁻¹⁵. The alternative strategy is to create a conditional gene knockout, for example, using a Cre recombinase system that can remove floxed alleles of *Kras* in specific tissues or at a specific time¹⁵². The effects of *Kras* gene knockout, however, can be quite different from the results of small molecule inhibition due to disruption of important cellular localization and protein-protein interactions, leading to the demand of designing small molecule tools to elucidate KRAS function¹²⁵. Developing a small molecule directly targeting KRAS is challenging because of its high affinity for GTP (picomolar binding affinity) and lacking other druggable pockets on KRAS surface. We attempted to solve this challenge by developing a covalent small molecule based on shape and covalent complementarity to the engineered KRAS.

The strategy of creating an engineered allele amenable to small molecule inhibition has been widely used in kinases but not in small GTPases to study the phenotype of inhibitor occupancy^{105, 153-154}. Vincent *et al.* reported an engineered HRAS that cycles between the inactive state and active state upon binding with unnatural nucleotides (GDP and GTP analogs harboring a benzyl group), suggesting the capability of using small molecule modulator to control HRAS activity¹¹². However, the unnatural nucleotides with diphosphate or triphosphate groups are not cell-membrane permeable. Since the phosphate groups are critical for maintaining the high affinity of nucleotides to RAS by hydrogen bonding, reversible small molecules without phosphate or other polyatomic anions to form the hydrogen bonds might not be potent enough to replace GTP. We exploited a covalent targeting strategy to irreversibly modify the nucleotide-binding pocket. Computer-aided small molecule design was used to design small molecules that can form key hydrogen bond interactions with the nucleotide-binding pocket. The covalent inhibitor we designed is cell membrane-permeable; it can displace GTP; and can irreversibly

modify KRAS* in cells, leading to the accumulation of inactive KRAS* thereby preventing KRAS* signaling. This methodology could be applied to design useful cellular probes to understand functions of other small GTPases. In addition, the integration of glide docking, covalent docking, cell membrane permeability prediction, combinatorial library design, and biophysical assays employed in the design of the KRAS* inhibitor, represents an innovative fragment-based small molecule design pipeline for discovery of targeted-covalent inhibitors.

6.1.3 Future directions

The strategy of generating an engineered allele has greatly facilitated the understanding of the phenotype of target inhibition and the associated mechanisms, especially in undruggable targets or highly conserved protein families¹⁵⁴. The covalent inhibitor developed here showed selective target inhibition of KRAS in cells. A pharmacological tool with high target occupancy and metabolic stability to provide KRAS therapeutic index *in vivo* would be even more valuable. Possible strategies towards improving the system developed in this work are discussed below.

The design of the orthogonal engineering protein-small molecule system is often based on shape complementary (bump-and-hole) or covalent complementary (clamping). The nature of both endogenous proteins and endogenous ligands is critical for the selection of these two mechanisms to develop a high potency small molecule. KRAS shares a conserved nucleotide-binding site with the other two RAS isoforms (HRAS and NRAS) and has a picomolar binding affinity with GTP (0.5 mM cellular concentration). The potency and selectivity of small molecule could be dramatically decreased with such high binding affinity and high concentration of endogenous ligands¹²⁶. Hence, the combination of bump-and-hole and clamping mechanisms is required to assure selectivity and potency of small molecules. Protein engineering based on shape complementary often mutates conserved hydrophobic residues to alanine. In addition, proteins with a slow turnover rate are more suitable for covalent targeting. However,

the protein engineered in this work has an asparagine (N) to alanine (A) mutation, which disrupts the important hydrogen bonding interaction between asparagine and nucleotides and residues in KRAS, making the engineered KRAS less stable with an increased turnover rate compared to KRAS^{G12V}. This high turnover rate results in the quick removal of both covalent small molecule-modified KRAS* and unmodified KRAS*. Therefore, a high dosage of covalent inhibitor is required to modify the new generated KRAS*. Based on the above analysis, generating a structurally more stable KRAS allele by mutating hydrophobic residues but not polar or charged residues to alanine would be helpful to prevent turnover rate increase thus improve covalent inhibitor's cellular activity.

Structural biology information is crucial for computer-aided drug design. In this study, the crystal structure of KRAS^{G12V} was mutated *in silico* and minimized using Schrödinger Prime¹⁵⁵ to offer the engineered KRAS* structure. Although Schrödinger Prime is a powerful tool for accurate protein structure predictions, it might not fully represent the structure changes with triple residue mutations. Both the engineered KRAS* structure and KRAS*-covalent small molecule cocrystal structure would be valuable to facilitate the design of a more potent covalent inhibitor. Besides, developing a small molecule that can mimic nucleotides but has druglike properties could significantly improve target occupancy by capturing GEFs to catalyze the exchange of nucleotide to small molecule inhibitor.

6.2 Application of IKE *in vivo*

6.2.1 Summary

To use a small molecule tool *in vivo*, it needs to possess optimized absorption, distribution, metabolism, and excretion (ADME) and toxicity properties. Current small molecule tools to elucidate system x_c^- function and activity *in vivo* are limited. While, erastin has been extensively used *in vitro* to study system x_c^- and ferroptosis, it lacks the metabolic stability required for *in vivo* applications.

Sorafenib, a multi-kinase inhibitor approved by the FDA in the treatment of advanced renal carcinoma, hepatocellular carcinoma, and thyroid cancer, is metabolically stable but lacks sufficient specificity for system x_c^- , limiting its applicability for such approaches. The low potency of glutamate and sulfasalazine prevent their use in studies geared towards elucidating system x_c^- activity and function. In Chapters 3 and 4, we investigated the anti-tumor effect and the associated mechanisms of the first selective, potent, and metabolically stable erastin analog, IKE.

Diffuse large B-cell lymphoma (DLBCL) cell lines have defective transsulfuration pathway making them dependent on cystine import through system x_c^- and sensitive to IKE treatment⁴⁹. The *in vitro* study indicated that IKE is a highly potent system x_c^- inhibitor with an IC_{50} less than 20 nM in sensitive DLBCL cell lines, and EC_{50} of 34 nM on GSH depletion in SUDHL-6 cells (a sensitive DLBCL line). In addition, it induced lipid peroxidation and ferroptosis biomarker expression at low concentrations (125-500 nM). The pharmacokinetics study revealed that IKE has half-life of 1.83 hour in plasma and 3.50 hour in tumor tissue of DLBCL xenograft model through intraperitoneal (IP) administration. The pharmacodynamics study showed that IKE induced GSH depletion and ferroptosis gene biomarker upregulation, indicating that IKE inhibited system x_c^- function and induced ferroptosis in tumor tissue from DLBCL xenograft mice. In Chapter 4, we demonstrated that IKE inhibited tumor growth in a DLBCL xenograft model and showed that there was increased oxidative stress in tumor tissue upon IKE treatment. Collectively, our preliminary results support the utility of the small-molecule inhibitor IKE as an effective novel therapeutic option for DLBCL that requires further clinical evaluation.

6.2.2 Significance

DLBCL is an aggressive malignancy of mature B lymphocytes, accounting for 30-40% of non-Hodgkin's lymphoma¹³². It is a clinically and genetically heterogenous malignancy, which is classified into two main subgroups based on gene expression profiling, specifically, germinal centre B cell-like (GCB) and activated B cell like (ABC). Although most patients with DLBCL respond to chemotherapy and chemoimmunotherapy such as R-CHOP (Rituximab-Cyclophosphamide-Hydroxydaunorubicin-

Oncovin-Prednisone) regime, more than 30% of patients fail to respond or have disease relapse. Therefore, there is demonstrated need to develop novel drugs or therapies that can improve response rate and survival of DLBCL patients. We have shown that IKE inhibited tumor growth in a DLBCL xenograft model through inhibition of system x_c^- and induction of ferroptosis, indicating the potential application of IKE and ferroptosis inducers in anti-cancer therapy of DLBCL.

In addition to DLBCL, system x_c^- inhibitors have potential to inhibit tumor growth in other cancer models. For example, sulfasalazine, a low potency system x_c^- inhibitor, has shown tumor inhibition effect in xenograft models of prostate cancer (DU-145 and PC-3)¹⁵⁶, triple-negative breast tumor (M231), small-cell lung cancer (SCLC) (NCI-H69 and LU6-SCLC)¹⁵⁷, and pancreatic cancer (MIA PaCa-2, PANC-1, and Capan-1)¹⁵⁸⁻¹⁵⁹ without major side effects. LU6-SCLC was generated from a chemotherapy-resistant SCLC. The antitumor effect of sulfasalazine shown in this xenograft model indicates system x_c^- inhibition could be an option for cancers that are not responsive to other chemotherapeutic regimen¹⁵⁷. In addition, the efficacy of gemcitabine and etoposide chemotherapies could be markedly enhanced by combination with sulfasalazine in xenograft models of pancreatic cancer, suggesting the potential of applying system x_c^- inhibitor in combination chemotherapy¹⁵⁸⁻¹⁵⁹. Compared with sulfasalazine which inhibits glutamate release and depletes GSH at micromolar to millimolar range concentration^{134, 160}, IKE is a more potent system x_c^- inhibitor with IC_{50} of 30 nM on inhibition of glutamate release and 34 nM on GSH depletion. Therefore, IKE might have improved efficacy in DLBCL xenograft model and tumor models mentioned above. In addition, the pharmacokinetic and pharmacodynamic properties of IKE we presented here would be useful for future IKE *in vivo* studies.

6.2.3 Future directions

IKE is the first highly potent, selective, and metabolically stable erastin analog. However, there are opportunities to optimize its potency, selectivity, and ADME/toxicity properties by addressing the following challenges.

First, structure-based small molecule design would be useful if the system x_c^- structure information is available. System x_c^- , which belongs to the heterodimeric amino acid transporters family, is composed of a light chain, xCT, and a heavy chain, 4F2, with the transport activity located on xCT. xCT has 12 transmembrane domains consisting of 501 amino acids, however, no crystal structure of xCT is reported in the literature. Homology modeling might provide structural information for xCT; however, only two antiporters in the family have reported crystal structures: (i) amino acid-poly amine-and organocation transporter (ApcT) (PDB: 3GLA), a broad-specificity amino acid transporter, which has a sequence identity of 25% with xCT; and (ii) arginine agmatine antiporter (AdiC) (PDB: 3NCY), which has a sequence identity of 24% with xCT. Since a homology model based on protein with less than 30% sequence identity is not accurate, designing system x_c^- inhibitors through homology modeling would have limited success. A pharmacophore model based on all current system x_c^- inhibitors might provide some information on common features of system x_c^- inhibitors¹⁶¹, but such information is not precise enough to guide IKE analog design. Collectively, a crystal structure of xCT domain is required for a structure-based approach to design system x_c^- inhibitors. The development of new membrane crystallization strategies and the advancement of cryo-EM techniques has improved structural elucidation for proteins and could allow for the determination of the crystal structure of the xCT domain. A cocrystal structure of xCT with IKE as well as molecular dynamics (MD) simulation would be helpful for understanding the binding modes of IKE and allow for the development of more potent analogs.

Second, there are questions regarding the toxicity, off-targets, and tissue distribution of IKE to be addressed. The *in vivo* study of IKE described in Chapter 4 identified toxic effects of IKE to mice, with the mice losing weight starting at day 9 of treatment. However, the cause of toxicity is currently unknown and could result from systemic inhibition of system x_c^- , formulation issues resulting in drug precipitation *in vivo* causing damage to organs, or another unknown cause. Thus, further studies aimed towards determining the cause of toxicity, accounting for drug precipitation, systemic inhibition of system x_c^- , as well as metabolite toxicity is necessary to elucidate any deleterious side effect of IKE. In addition, little is known about off-target effects and tissue distribution of erastin and IKE. Identifying off-targets of IKE

and defining its exposure at site of action will help us understand the potential risks associated with IKE and its potential as a new class of chemotherapeutic agent¹⁶².

6.3 Nanoparticles as drug carriers

6.3.1 Summary

As system x_c^- is widely distributed in liver, kidney, brain, and macrophages, and acts as key regulator for cystine import and glutamate signaling¹⁶³, systematic inhibition could cause severe toxicity *in vivo*. In Chapter 4, a PEG-PLGA nanoparticle carrier, which takes advantage of the EPR effect, allowing for selective accumulation in tumor tissue over normal tissue, is designed and formulated. The IKE PEG-PLGA nanoparticle formulated in this work has suitable properties for *in vivo* application, specifically, the average size of 80 nm allows for extravasation, the surface charge of -17 mV prevents nanoparticle aggregation, and the PEG coating enables prolonged circulation time. Both free IKE and IKE PEG-PLGA nanoparticles showed efficacy in decreasing tumor growth rate in NCG mice subcutaneously xenografted with SUDHL-6 cells, however, the PEG-PLGA nanoparticle formulation of IKE had less toxic effects, highlighting the potential of this system in cancer therapy.

6.3.2 Significance

Nanoparticle carriers provide an effective way to improve drug efficacy and reduce systemic toxicity because of targeted localization in tumors. Despite the various nanocarrier systems available and numerous advantages of nanoparticle therapeutics, there are challenges to apply nanocarriers *in vivo*. One of the challenges is to manufacture uniform nanoparticles with high loading capacity at large scale. We utilized a scalable microfluidic platform, which allows for the precise engineering of specific sized PEG-PLGA nanoparticles with minimal batch to batch variability¹³⁹. This high-quality nanoparticle is critical

for the successful delivery of IKE in xenograft models. Given the rapid optimization process of the system and the commercial availability of PEG-PLGA and polymers, the nanoparticle system we investigated here could be employed by other researchers or applied to other drug delivery projects.

6.3.3 Future directions

The dual role of anti-oxidation and detoxification of xenobiotics to impede chemotherapy makes GSH an attractive target. However, glutathione synthesis inhibitors failed in clinical trials due to systemic toxicity resulting from GSH depletion¹⁶⁴. Targeting system x_c^- , which has more tumor specificity due to the differential expression and distribution in specific type of cells¹⁶⁵, is an alternative strategy to deplete GSH. Here, we chose the xenograft model of DLBCL, which is intrinsically sensitive to system x_c^- inhibitor due to a defective transsulfuration pathway, to explore IKE's potential as a chemotherapeutic. At the same time, we employed a PEG-PLGA nanoparticle carrier to allow for the accumulation of IKE in tumors. This passive targeting showed reduced systemic toxicity of IKE, which leads us to believe that the active targeting of nanocarriers by conjugation with molecules that recognize tumor cells, like antibodies, would further enhance targeting efficiency.

DLBCL has a range of surface markers which are overexpressed on DLBCL compared to normal cells that could be selectively targeted with commercially available antibodies¹⁶⁶. Specifically, the well characterized CD19 and CD20 antigens could be used depending on the tumor type and the drug mechanism of action. Binding of anti-CD19 antibody to CD19 antigens leads to receptor-mediated internalization¹⁶⁷, which will significantly increase the therapeutic outcome for nanoparticles that are designed to release drug inside the cell. While, anti-CD20 antibody is non-internalizing, targeting nanoparticles to CD20 antigen results in the release of drug at the cell surface¹⁰⁰. The non-internalizing receptors could be beneficial in solid tumors, as internalization can decrease the penetration of nanoparticles. At the same time, the non-internalizing nanoparticles allow for the release of drug on cell surface followed by diffusion into neighboring cells. However, for IKE delivery, it is hard to predict which antigen would be more advantageous. On one hand, IKE targets system x_c^- , which is a

cysteine/glutamate transporter on cell membrane, targeting the nanoparticle to CD20 would allow the release of IKE on cell surface. On the other hand, we have identified enhanced cellular activity effect of IKE PEG-PLGA nanoparticles comparing with free IKE (**Figure 4.6**), which might result from the increased internalization of IKE PEG-PLGA nanoparticles to cells compared free IKE to cells¹⁶⁸. This evidence indicates the potential benefit of targeting CD19 instead of CD20.

Besides, there are other nanoscale therapeutics that might be beneficial for IKE therapy. For example, PEG-conjugated chemotherapeutics are an attractive approach to increase drug circulation time by increasing hydrophilicity, evading immune system recognition, and reducing serum protein binding¹⁶⁹. Reversible PEGylation (PEG-prodrug), which attaches a drug to PEG through a cleavable linker, is used to minimize loss of activity. As the plasma half-life of IKE is only 1.8 hours, increasing the circulation life of IKE through PEGylation might help improve IKE's activity *in vivo*. In addition, designing a stimuli-response nanoparticle would enable controlled drug release in specific tissue. For example, tumors have a hypoxic and acidic microenvironment; an oxygen- or pH-sensitive nanoparticle would enable controlled drug release in tumor tissues.

6.4 Identification of ferroptosis biomarkers

6.4.1 Summary

A biomarker is a defined characteristic to indicate normal or pathogenic processes or responses to therapeutic interventions, which can be categorized into risk, predictive, diagnostic, monitoring, prognostic, response (pharmacodynamic), and safety biomarkers. Pharmacodynamic biomarkers are crucial to prove drugs' clinical benefits and guide dose-response studies. We employed untargeted lipidomics, immunofluorescence, and quantitative reverse transcription PCR (RT-qPCR) approaches to elucidate biomarkers of ferroptosis and characterize pharmacodynamics of IKE treatment in xenograft model. In Chapter 3 and 5, an untargeted lipidomics study, immunofluorescence experiments, and RT-

qPCR experiments are carried out on cell culture samples and tumor samples from treated mice to study IKE-induced changes in lipid composition and gene expression.

Previously unreported changes in lipid species were identified, including changes in triglycerides (TAG), diglycerides (DAG), monoglycerides (MAG) and free fatty acids (FA) following IKE treatment. In IKE-treated SUDHL-6 cells, TAG and phospholipids decreased, possibly resulting from the cleavage of oxidized polyunsaturated fatty acids (PUFA). TAG is largely increased with Fer-1 co-treatment in IKE treated SUDHL-6 cells, which indicates a possible protective role of TAG as a buffer against oxidative damage. However, the data from the tumor samples revealed that DAG, MAG and phospholipids are all significantly increased upon IKE treatment, possibly resulting from both the activation of TAG hydrolysis enzyme, ATGL, and the response of cancer cells to oxidative stress.

In addition, the RT-qPCR experiments identified a time-dependent upregulation of genes including *PTGS2*, *SLC7A11*, and *CHAC1* in IKE treated SUDHL-6 cells and tumor tissues xenografted with the same cell line. Besides, a series of genes encoding lipid metabolism enzymes are upregulated upon IKE treatment, specifically, the lipid biosynthesis enzymes ACC1 and ELOVL7, lipid metabolism remodeling enzymes ATGL, sPLA2F, LPEAT1 and LPCAT4, and lipid peroxidation enzymes ALOX12 and ALOX15. Co-treatment of Fer-1 or β -Me in IKE-treated cells prevent the upregulation of these genes, indicating the upregulation comes from system x_c^- inhibition and oxidative stress.

Moreover, we identified some histologic biomarkers of IKE-induced ferroptosis including PTGS2 protein and the oxidative stress biomarkers 8OHdG and MDA. The immunofluorescence experiments showed increased PTGS2, 8OHdG, and MDA in IKE and IKE PEG-PLGA nanoparticle treated tumor compared to vehicle, with no increased caspase-3 cleavage, biomarkers of apoptosis, in IKE and IKE PEG-PLGA nanoparticle treated tumor tissues. These data collectively suggest that the antitumor effects of IKE results from system x_c^- inhibition induced ferroptosis and not apoptosis.

The gene expression, lipids, and histologic biomarkers identified here would be useful to determine and monitoring ferroptosis *in vitro* and *in vivo*.

6.4.2 Significance

Emerging evidence has shown the potential antitumor effects of using ferroptosis inducers as single reagent or in combination with chemotherapies in cell culture and some types of xenografts^{34, 78}. It is thus important to identify biomarkers and understand the molecular mechanisms of ferroptosis inducers in both tumor cells and cancer models. Here we identify and establish pharmacodynamics of ferroptosis inducer IKE in a xenograft model for the first time. The pharmacokinetics and pharmacodynamics relationship established here would be beneficial for future study of ferroptosis therapeutic role in cancer and other pathological conditions.

In addition, previous lipidomics study have revealed depletion of PUFAs and phospholipids, and increase of lysophospholipids in erastin or erastin analog-treated HT1080 cells^{67, 82}. However, no one has characterized the genes that regulate these lipids change. The work presented here identified a range of genes that are upregulated by IKE treatment in SUDHL-6 cells and demonstrated that the upregulation of these genes is caused by inhibition of cysteine import and the increase in oxidative stress as illuminated following co-treatment with ferroptosis inhibitors. The upregulation of *sPLA2F* expression indicated that the increased lysophospholipids result from the cleavage of oxidized fatty acyl group from PC and PE to remove the detrimental oxidized PC and PE^{67, 82, 170}. Similarly, upregulation of *ATGL* indicates the increase of monoglycerides (MAG) might due to hydrolysis of oxidized fatty acyl group in triglycerides to minimize the pathology mediated by lipid peroxidation. The integration of small molecule tools, untargeted lipidomics, and RT-qPCR provides an efficient way to explore lipids change and lipid metabolism mechanisms during regulated cell death.

6.4.3 Future directions

Ferroptosis acts as an important regulator in specific physiological and pathological conditions³⁴. However, identifying biomarkers that determine ferroptosis sensitivity, therapeutic responses, and

progress remains an ongoing challenge. For example, DLBCL lines have differential sensitivity to IKE (**Figure 3.3**), making the identification of biomarkers predicting DLBCL sensitivity to system x_c^- a valuable pursuit for future pre-clinical studies as well as precision medicine approaches in the clinic. While, *ACSL4* and *LPCAT3* have previously been reported to be overexpressed in ferroptosis resistant cell lines^{69, 86}, these two genes could not predict DLBCL's differential sensitivity to IKE. Cystathionine-beta-synthase (*CBS*), ferritin light chain (*FTL*), and *SLC7A11* genes were found to have higher average expression levels in resistant DLBCL lines, however, the increased average expression level could not predict the sensitivity or resistance of a specific cell line due to extensive variability within each group. The 'omics' techniques (genomics, transcriptomics, proteomics, and metabolomics) in combination with bioinformatics, which allow for the collection of multidimensional information and identification of unknown targets, would help to identify targets regulating ferroptosis sensitivity. In addition, multiple cell lines including parental drug sensitive/resistant and derived drug resistant cell lines, are necessary to use for identifying intrinsic factors determining ferroptosis sensitivity^{69, 86, 171}.

One such biomarker, NADPH, was found to be a biomarker for ferroptosis sensitivity following transcriptome analysis in NCI-60 cell lines¹⁷¹. Identification of metabolite biomarkers like NADPH, however, presents unique challenges. First, the detection of significantly changed specific metabolites in a complex metabolite pool, where some metabolites are unstable or in low abundance, requires careful sample preparation and sample analysis. Second, metabolite biomarkers identified *in vitro* might not be translatable to *in vivo* as cell culture is a highly simplified and artificial system compared to humans and animals. For example, in Chapter 5, the results from the untargeted lipidomics experiments on the cell culture samples were conflicting with the results from the tumor samples, suggesting that different lipid metabolism pathways are active following IKE treatment *in vitro* and *in vivo*, limiting the overall applicability of the *in vitro* data. A similar finding is observed with GSH depletion following IKE treatment *in vitro* and *in vivo*. Tumors harvested from mice 24 hours after IKE administration had dramatically decreased GSH levels despite there being little IKE present. However, we didn't observe the persistent effect of GSH depletion upon IKE treatment in cell culture of SUDHL-6. This difference might

result from the faster uptake of cystine from the cell culture media than from the nutrient-poor tumor microenvironment. Thus, metabolomics analysis *in vitro* at conditions more representative of the *in vivo* environment, or directly from *in vivo* samples would be more beneficial for understanding ferroptosis role in physiology, pathology, and cancer therapy.

Reference

1. Maeder, M. L.; Gersbach, C. A., Genome-editing technologies for gene and cell therapy. *Molecular Therapy* **2016**, *24* (3), 430-446.
2. Bohacek, R. S.; McMartin, C.; Guida, W. C., The art and practice of structure-based drug design: a molecular modeling perspective. *Medicinal research reviews* **1996**, *16* (1), 3-50.
3. Hann, M. M.; Oprea, T. I., Pursuing the leadlikeness concept in pharmaceutical research. *Current opinion in chemical biology* **2004**, *8* (3), 255-263.
4. Scott, D. E.; Coyne, A. G.; Hudson, S. A.; Abell, C., Fragment-based approaches in drug discovery and chemical biology. *Biochemistry-Us* **2012**, *51* (25), 4990-5003.
5. Fink, T.; Bruggesser, H.; Reymond, J. L., Virtual exploration of the small-molecule chemical universe below 160 daltons. *Angewandte Chemie International Edition* **2005**, *44* (10), 1504-1508.
6. Murray, C. W.; Rees, D. C., The rise of fragment-based drug discovery. *Nature chemistry* **2009**, *1* (3), 187.
7. Souers, A. J.; Levenson, J. D.; Boghaert, E. R.; Ackler, S. L.; Catron, N. D.; Chen, J.; Dayton, B. D.; Ding, H.; Enschede, S. H.; Fairbrother, W. J., ABT-199, a potent and selective BCL-2 inhibitor, achieves antitumor activity while sparing platelets. *Nature medicine* **2013**, *19* (2), 202.
8. Oltersdorf, T.; Elmore, S. W.; Shoemaker, A. R.; Armstrong, R. C.; Augeri, D. J.; Belli, B. A.; Bruncko, M.; Deckwerth, T. L.; Dinges, J.; Hajduk, P. J., An inhibitor of Bcl-2 family proteins induces regression of solid tumours. *Nature* **2005**, *435* (7042), 677.
9. Delbridge, A. R.; Grabow, S.; Strasser, A.; Vaux, D. L., Thirty years of BCL-2: translating cell death discoveries into novel cancer therapies. *Nature reviews Cancer* **2016**, *16* (2), 99.
10. Pagadala, N. S.; Syed, K.; Tuszynski, J., Software for molecular docking: a review. *Biophys Rev* **2017**, *9* (2), 91-102.
11. Cromm, P. M.; Spiegel, J.; Grossmann, T. N.; Waldmann, H., Direct Modulation of Small GTPase Activity and Function. *Angewandte Chemie* **2015**.
12. Cox, A. D.; Fesik, S. W.; Kimmelman, A. C.; Luo, J.; Der, C. J., Drugging the undruggable RAS: Mission Possible? *Nature reviews. Drug discovery* **2014**, *13* (11), 828-51.
13. Ostrem, J. M.; Shokat, K. M., Direct small-molecule inhibitors of KRAS: from structural insights to mechanism-based design. *Nature reviews. Drug discovery* **2016**, *15* (11), 771-785.
14. Koera, K.; Nakamura, K.; Nakao, K.; Miyoshi, J.; Toyoshima, K.; Hatta, T.; Otani, H.; Aiba, A.; Katsuki, M., K-ras is essential for the development of the mouse embryo. *Oncogene* **1997**, *15* (10), 1151.
15. Johnson, L.; Greenbaum, D.; Cichowski, K.; Mercer, K.; Murphy, E.; Schmitt, E.; Bronson, R. T.; Umanoff, H.; Edelman, W.; Kucherlapati, R., K-ras is an essential gene in the mouse with partial functional overlap with N-ras. *Genes & development* **1997**, *11* (19), 2468-2481.
16. Potenza, N.; Vecchione, C.; Notte, A.; De Rienzo, A.; Rosica, A.; Bauer, L.; Affuso, A.; De Felice, M.; Russo, T.; Poulet, R., Replacement of K-Ras with H-Ras supports normal embryonic development despite inducing cardiovascular pathology in adult mice. *EMBO reports* **2005**, *6* (5), 432-437.
17. Appels, N. M.; Beijnen, J. H.; Schellens, J. H., Development of farnesyl transferase inhibitors: a review. *The oncologist* **2005**, *10* (8), 565-78.
18. Spiegel, J.; Cromm, P. M.; Zimmermann, G.; Grossmann, T. N.; Waldmann, H., Small-molecule modulation of Ras signaling. *Nat Chem Biol* **2014**, *10* (8), 613-22.
19. Lim, S. M.; Westover, K. D.; Ficarro, S. B.; Harrison, R. A.; Choi, H. G.; Pacold, M. E.; Carrasco, M.; Hunter, J.; Kim, N. D.; Xie, T.; Sim, T.; Janne, P. A.; Meyerson, M.; Marto, J. A.; Engen, J. R.; Gray, N. S., Therapeutic targeting of oncogenic K-Ras by a covalent catalytic site inhibitor. *Angewandte Chemie* **2014**, *53* (1), 199-204.
20. Evelyn, C. R.; Duan, X.; Biesiada, J.; Seibel, W. L.; Meller, J.; Zheng, Y., Rational Design of Small Molecule Inhibitors Targeting the Ras GEF, SOS1. *Chemistry & biology* **2014**, *21* (12), 1618-1628.

21. Patgiri, A.; Yadav, K. K.; Arora, P. S.; Bar-Sagi, D., An orthosteric inhibitor of the Ras-Sos interaction. *Nature Chemical Biology* **2011**, *7* (9), 585-587.
22. Leshchiner, E. S.; Bellairs, J.; Bird, G. H.; Opoku-Nsiah, K.; Godes, M.; Walensky, L. D., Direct inhibition of oncogenic KRAS by hydrocarbon- stapled SOS1 helices. *Molecular Cancer Research* **2014**, *12*.
23. Burns, M. C.; Sun, Q.; Daniels, R. N.; Camper, D.; Kennedy, J. P.; Phan, J.; Olejniczak, E. T.; Lee, T.; Waterson, A. G.; Rossanese, O. W.; Fesik, S. W., Approach for targeting Ras with small molecules that activate SOS-mediated nucleotide exchange. *Proceedings of the National Academy of Sciences of the United States of America* **2014**, *111* (9), 3401-3406.
24. Nassar, N.; Cancelas, J.; Zheng, J.; Williams, D. A.; Zheng, Y., Structure-function based design of small molecule inhibitors targeting Rho family GTPases. *Current topics in medicinal chemistry* **2006**, *6* (11), 1109-16.
25. Welsch, M. E.; Kaplan, A.; Chambers, J. M.; Stokes, M. E.; Bos, P. H.; Zask, A.; Zhang, Y.; Sanchez-Martin, M.; Badgley, M. A.; Huang, C. S.; Tran, T. H.; Akkiraju, H.; Brown, L. M.; Nandakumar, R.; Cremers, S.; Yang, W. S.; Tong, L.; Olive, K. P.; Ferrando, A.; Stockwell, B. R., Multivalent Small-Molecule Pan-RAS Inhibitors. *Cell* **2017**, *168* (5), 878-889 e29.
26. Athuluri-Divakar, S. K.; Vasquez-Del Carpio, R.; Dutta, K.; Baker, S. J.; Cosenza, S. C.; Basu, I.; Gupta, Y. K.; Reddy, M. R.; Ueno, L.; Hart, J. R., A small molecule RAS-mimetic disrupts RAS association with effector proteins to block signaling. *Cell* **2016**, *165* (3), 643-655.
27. Ostrem, J. M.; Peters, U.; Sos, M. L.; Wells, J. A.; Shokat, K. M., K-Ras(G12C) inhibitors allosterically control GTP affinity and effector interactions. *Nature* **2013**, *503* (7477), 548-51.
28. Gray, N., Potent and Selective Covalent Quinazoline Inhibitors of KRAS G12C. *Cell* **2017**.
29. Janes, M. R.; Zhang, J.; Li, L. S.; Hansen, R.; Peters, U.; Guo, X.; Chen, Y.; Babbar, A.; Firdaus, S. J.; Darjania, L.; Feng, J.; Chen, J. H.; Li, S.; Li, S.; Long, Y. O.; Thach, C.; Liu, Y.; Zariw, A.; Ely, T.; Kucharski, J. M.; Kessler, L. V.; Wu, T.; Yu, K.; Wang, Y.; Yao, Y.; Deng, X.; Zarrinkar, P. P.; Brehmer, D.; Dhanak, D.; Lorenzi, M. V.; Hu-Lowe, D.; Patricelli, M. P.; Ren, P.; Liu, Y., Targeting KRAS Mutant Cancers with a Covalent G12C-Specific Inhibitor. *Cell* **2018**, *172* (3), 578-589 e17.
30. Mirati Therapeutics, I., White Paper: Direct targeting of KRAS mutant cancers with a KRAS G12C mutant-selective inhibitor. **2018**.
31. Jain, M. V.; Paczulla, A. M.; Klonisch, T.; Dimgba, F. N.; Rao, S. B.; Roberg, K.; Schweizer, F.; Lengerke, C.; Davoodpour, P.; Palicharla, V. R., Interconnections between apoptotic, autophagic and necrotic pathways: implications for cancer therapy development. *Journal of cellular and molecular medicine* **2013**, *17* (1), 12-29.
32. Chaabane, W.; User, S. D.; El-Gazzah, M.; Jaksik, R.; Sajjadi, E.; Rzeszowska-Wolny, J.; Łos, M. J., Autophagy, apoptosis, mitoptosis and necrosis: interdependence between those pathways and effects on cancer. *Archivum immunologiae et therapiae experimentalis* **2013**, *61* (1), 43-58.
33. Galluzzi, L.; Vitale, I.; Aaronson, S. A.; Abrams, J. M.; Adam, D.; Agostinis, P.; Alnemri, E. S.; Altucci, L.; Amelio, I.; Andrews, D. W.; Annicchiarico-Petruzzelli, M.; Antonov, A. V.; Arama, E.; Baehrecke, E. H.; Barlev, N. A.; Bazan, N. G.; Bernassola, F.; Bertrand, M. J. M.; Bianchi, K.; Blagosklonny, M. V.; Blomgren, K.; Borner, C.; Boya, P.; Brenner, C.; Campanella, M.; Candi, E.; Carmona-Gutierrez, D.; Cecconi, F.; Chan, F. K.; Chandel, N. S.; Cheng, E. H.; Chipuk, J. E.; Cidlowski, J. A.; Ciechanover, A.; Cohen, G. M.; Conrad, M.; Cubillos-Ruiz, J. R.; Czabotar, P. E.; D'Angiolella, V.; Dawson, T. M.; Dawson, V. L.; De Laurenzi, V.; De Maria, R.; Debatin, K. M.; DeBerardinis, R. J.; Deshmukh, M.; Di Daniele, N.; Di Virgilio, F.; Dixit, V. M.; Dixon, S. J.; Duckett, C. S.; Dynlacht, B. D.; El-Deiry, W. S.; Elrod, J. W.; Fimia, G. M.; Fulda, S.; Garcia-Saez, A. J.; Garg, A. D.; Garrido, C.; Gavathiotis, E.; Golstein, P.; Gottlieb, E.; Green, D. R.; Greene, L. A.; Gronemeyer, H.; Gross, A.; Hajnoczky, G.; Hardwick, J. M.; Harris, I. S.; Hengartner, M. O.; Hetz, C.; Ichijo, H.; Jaattela, M.; Joseph, B.; Jost, P. J.; Juin, P. P.; Kaiser, W. J.; Karin, M.; Kaufmann, T.; Kepp, O.; Kimchi, A.; Kitsis, R. N.; Klionsky, D. J.; Knight, R. A.; Kumar, S.; Lee, S. W.; Lemasters, J. J.; Levine, B.; Linkermann, A.; Lipton, S. A.; Lockshin, R. A.; Lopez-Otin, C.; Lowe, S. W.; Luedde, T.; Lugli, E.; MacFarlane, M.; Madeo, F.; Malewicz, M.; Malorni, W.; Manic, G.; Marine, J. C.; Martin, S. J.; Martinou, J. C.; Medema,

- J. P.; Mehlen, P.; Meier, P.; Melino, S.; Miao, E. A.; Molkenkin, J. D.; Moll, U. M.; Munoz-Pinedo, C.; Nagata, S.; Nunez, G.; Oberst, A.; Oren, M.; Overholtzer, M.; Pagano, M.; Panaretakis, T.; Pasparakis, M.; Penninger, J. M.; Pereira, D. M.; Pervaiz, S.; Peter, M. E.; Piacentini, M.; Pinton, P.; Prehn, J. H. M.; Puthalakath, H.; Rabinovich, G. A.; Rehm, M.; Rizzuto, R.; Rodrigues, C. M. P.; Rubinsztein, D. C.; Rudel, T.; Ryan, K. M.; Sayan, E.; Scorrano, L.; Shao, F.; Shi, Y.; Silke, J.; Simon, H. U.; Sistigu, A.; Stockwell, B. R.; Strasser, A.; Szabadkai, G.; Tait, S. W. G.; Tang, D.; Tavernarakis, N.; Thorburn, A.; Tsujimoto, Y.; Turk, B.; Vanden Berghe, T.; Vandenabeele, P.; Vander Heiden, M. G.; Villunger, A.; Virgin, H. W.; Vousden, K. H.; Vucic, D.; Wagner, E. F.; Walczak, H.; Wallach, D.; Wang, Y.; Wells, J. A.; Wood, W.; Yuan, J.; Zakeri, Z.; Zhivotovsky, B.; Zitvogel, L.; Melino, G.; Kroemer, G., Molecular mechanisms of cell death: recommendations of the Nomenclature Committee on Cell Death 2018. *Cell Death Differ* **2018**, *25* (3), 486-541.
34. Stockwell, B. R.; Angeli, J. P. F.; Bayir, H.; Bush, A. I.; Conrad, M.; Dixon, S. J.; Fulda, S.; Gascón, S.; Hatzios, S. K.; Kagan, V. E., Ferroptosis: a regulated cell death nexus linking metabolism, redox biology, and disease. *Cell* **2017**, *171* (2), 273-285.
35. Dixon, S. J.; Lemberg, K. M.; Lamprecht, M. R.; Skouta, R.; Zaitsev, E. M.; Gleason, C. E.; Patel, D. N.; Bauer, A. J.; Cantley, A. M.; Yang, W. S., Ferroptosis: an iron-dependent form of nonapoptotic cell death. *Cell* **2012**, *149* (5), 1060-1072.
36. Yagoda, N.; Von Rechenberg, M.; Zaganjor, E.; Bauer, A. J.; Yang, W. S.; Fridman, D. J.; Wolpaw, A. J.; Smukste, I.; Peltier, J. M.; Boniface, J. J., RAS-RAF-MEK-dependent oxidative cell death involving voltage-dependent anion channels. *Nature* **2007**, *447* (7146), 865.
37. Yang, W. S.; Stockwell, B. R., Synthetic lethal screening identifies compounds activating iron-dependent, nonapoptotic cell death in oncogenic-RAS-harboring cancer cells. *Chemistry & biology* **2008**, *15* (3), 234-245.
38. Higuchi, Y., Polyunsaturated fatty acids promote 8-hydroxy-2-deoxyguanosine formation through lipid peroxidation under the glutamate-induced GSH depletion in rat glioma cells. *Arch Biochem Biophys* **2001**, *392* (1), 65-70.
39. Higuchi, Y.; Yoshimoto, T., Promoting effects of polyunsaturated fatty acids on chromosomal giant DNA fragmentation associated with cell death induced by glutathione depletion. *Free radical research* **2004**, *38* (6), 649-658.
40. Higuchi, Y.; Tanii, H.; Koriyama, Y.; Mizukami, Y.; Yoshimoto, T., Arachidonic acid promotes glutamate-induced cell death associated with necrosis by 12-lipoxygenase activation in glioma cells. *Life sciences* **2007**, *80* (20), 1856-1864.
41. Higuchi, Y., Glutathione depletion-induced chromosomal DNA fragmentation associated with apoptosis and necrosis. *Journal of cellular and molecular medicine* **2004**, *8* (4), 455-464.
42. Higuchi, Y., Chromosomal DNA fragmentation in apoptosis and necrosis induced by oxidative stress. *Biochemical pharmacology* **2003**, *66* (8), 1527-1535.
43. Higuchi, Y.; Yoshimoto, T., Arachidonic acid converts the glutathione depletion-induced apoptosis to necrosis by promoting lipid peroxidation and reducing caspase-3 activity in rat glioma cells. *Arch Biochem Biophys* **2002**, *400* (1), 133-140.
44. Yoshimoto, T.; Takahashi, Y., Arachidonate 12-lipoxygenases. *Prostaglandins & other lipid mediators* **2002**, *68*, 245-262.
45. Angeli, J. P. F.; Schneider, M.; Proneth, B.; Tyurina, Y. Y.; Tyurin, V. A.; Hammond, V. J.; Herbach, N.; Aichler, M.; Walch, A.; Eggenhofer, E., Inactivation of the ferroptosis regulator Gpx4 triggers acute renal failure in mice. *Nature cell biology* **2014**, *16* (12), 1180.
46. Jiang, L.; Kon, N.; Li, T. Y.; Wang, S. J.; Su, T.; Hibshoosh, H.; Baer, R.; Gu, W., Ferroptosis as a p53-mediated activity during tumour suppression. *Nature* **2015**, *520* (7545), 57-+.
47. Tarangelo, A.; Magtanong, L.; Bieging-Rolett, K. T.; Li, Y.; Ye, J. B.; Attardi, L. D.; Dixon, S. J., p53 Suppresses Metabolic Stress-Induced Ferroptosis in Cancer Cells. *Cell Rep* **2018**, *22* (3), 569-575.
48. Xie, Y. C.; Zhu, S.; Song, X. X.; Sun, X. F.; Fan, Y.; Liu, J. B.; Zhong, M.; Yuan, H.; Zhang, L.; Billiar, T. R.; Lotze, M. T.; Zeh, H. J.; Kang, R.; Kroemer, G.; Tang, D. L., The Tumor Suppressor p53 Limits Ferroptosis by Blocking DPP4 Activity. *Cell Rep* **2017**, *20* (7), 1692-1704.

49. Yang, W. S.; Stockwell, B. R., Ferroptosis: death by lipid peroxidation. *Trends in cell biology* **2016**, *26* (3), 165-176.
50. Feng, H.; Stockwell, B. R., Unsolved mysteries: How does lipid peroxidation cause ferroptosis? *PLoS biology* **2018**, *16* (5), e2006203.
51. Yang, W. S.; SriRamaratnam, R.; Welsch, M. E.; Shimada, K.; Skouta, R.; Viswanathan, V. S.; Cheah, J. H.; Clemons, P. A.; Shamji, A. F.; Clish, C. B., Regulation of ferroptotic cancer cell death by GPX4. *Cell* **2014**, *156* (1), 317-331.
52. Dixon, S. J.; Patel, D. N.; Welsch, M.; Skouta, R.; Lee, E. D.; Hayano, M.; Thomas, A. G.; Gleason, C. E.; Tatonetti, N. P.; Slusher, B. S., Pharmacological inhibition of cystine–glutamate exchange induces endoplasmic reticulum stress and ferroptosis. *Elife* **2014**, *3*.
53. Lachaier, E.; Louandre, C.; Godin, C.; Saidak, Z.; Baert, M.; Diouf, M.; Chauffert, B.; Galmiche, A., Sorafenib induces ferroptosis in human cancer cell lines originating from different solid tumors. *Anticancer Res* **2014**, *34* (11), 6417-22.
54. Wagner, B. A.; Buettner, G. R.; Burns, C. P., Free radical-mediated lipid peroxidation in cells: oxidizability is a function of cell lipid bis-allylic hydrogen content. *Biochemistry-U.S.* **1994**, *33* (15), 4449-4453.
55. Zilka, O.; Shah, R.; Li, B.; Friedmann Angeli, J. P.; Griesser, M.; Conrad, M.; Pratt, D. A., On the Mechanism of Cytoprotection by Ferrostatin-1 and Liproxstatin-1 and the Role of Lipid Peroxidation in Ferroptotic Cell Death. *ACS Cent Sci* **2017**, *3* (3), 232-243.
56. Hirschhorn, T.; Stockwell, B. R., The Development of the Concept of Ferroptosis. *Free Radical Biology and Medicine* **2018**.
57. Larraufie, M.-H.; Yang, W. S.; Jiang, E.; Thomas, A. G.; Slusher, B. S.; Stockwell, B. R., Incorporation of metabolically stable ketones into a small molecule probe to increase potency and water solubility. *Bioorganic & medicinal chemistry letters* **2015**, *25* (21), 4787-4792.
58. Hou, W.; Xie, Y.; Song, X.; Sun, X.; Lotze, M. T.; Zeh III, H. J.; Kang, R.; Tang, D., Autophagy promotes ferroptosis by degradation of ferritin. *Autophagy* **2016**, *12* (8), 1425-1428.
59. Alvarez, S. W.; Sviderskiy, V. O.; Terzi, E. M.; Papagiannakopoulos, T.; Moreira, A. L.; Adams, S.; Sabatini, D. M.; Birsoy, K.; Possemato, R., NFS1 undergoes positive selection in lung tumours and protects cells from ferroptosis. *Nature* **2017**, *551* (7682), 639.
60. Jenner, P., Oxidative damage in neurodegenerative disease. *The Lancet* **1994**, *344* (8925), 796-798.
61. Montine, T.; Beal, M.; Robertson, D.; Cudkowicz, M.; Biaggioni, I.; O'Donnell, H.; Zackert, W.; Roberts, L.; Morrow, J., Cerebrospinal fluid F2-isoprostanes are elevated in Huntington's disease. *Neurology* **1999**, *52* (5), 1104-1104.
62. Sayre, L. M.; Smith, M. A.; Perry, G., Chemistry and biochemistry of oxidative stress in neurodegenerative disease. *Current medicinal chemistry* **2001**, *8* (7), 721-738.
63. Chong, Z. Z.; Li, F.; Maiese, K., Oxidative stress in the brain: novel cellular targets that govern survival during neurodegenerative disease. *Progress in neurobiology* **2005**, *75* (3), 207-246.
64. Lee, J.; Kosaras, B.; Del Signore, S. J.; Cormier, K.; McKee, A.; Ratan, R. R.; Kowall, N. W.; Ryu, H., Modulation of lipid peroxidation and mitochondrial function improves neuropathology in Huntington's disease mice. *Acta neuropathologica* **2011**, *121* (4), 487-498.
65. Kim, G. H.; Kim, J. E.; Rhie, S. J.; Yoon, S., The role of oxidative stress in neurodegenerative diseases. *Experimental neurobiology* **2015**, *24* (4), 325-340.
66. Gutzmann, H.; Hadler, D., Sustained efficacy and safety of idebenone in the treatment of Alzheimer's disease: update on a 2-year double-blind multicentre study. In *Alzheimer's Disease—From Basic Research to Clinical Applications*, Springer: 1998; pp 301-310.
67. Skouta, R.; Dixon, S. J.; Wang, J.; Dunn, D. E.; Orman, M.; Shimada, K.; Rosenberg, P. A.; Lo, D. C.; Weinberg, J. M.; Linkermann, A., Ferrostatins inhibit oxidative lipid damage and cell death in diverse disease models. *Journal of the American Chemical Society* **2014**, *136* (12), 4551-4556.

68. Rudenko, E.; Kondratov, O.; Gerashchenko, G.; Lapska, Y.; Kravchenko, S.; Koliada, O.; Vozianov, S.; Zgonnyk, Y.; Kashuba, V., Aberrant expression of selenium-containing glutathione peroxidases in clear cell renal cell carcinomas. *Exp Oncol* **2015**, *37* (2), 105-10.
69. Doll, S.; Proneth, B.; Tyurina, Y. Y.; Panzilius, E.; Kobayashi, S.; Ingold, I.; Irmeler, M.; Beckers, J.; Aichler, M.; Walch, A.; Prokisch, H.; Trumbach, D.; Mao, G.; Qu, F.; Bayir, H.; Fullekrug, J.; Scheel, C. H.; Wurst, W.; Schick, J. A.; Kagan, V. E.; Angeli, J. P.; Conrad, M., ACSL4 dictates ferroptosis sensitivity by shaping cellular lipid composition. *Nat Chem Biol* **2017**, *13* (1), 91-98.
70. Yu, H. T.; Guo, P. Y.; Xie, X. Z.; Wang, Y.; Chen, G., Ferroptosis, a new form of cell death, and its relationships with tumourous diseases. *Journal of Cellular and Molecular Medicine* **2017**, *21* (4), 648-657.
71. Gout, P.; Buckley, A.; Simms, C.; Bruchovsky, N., Sulfasalazine, a potent suppressor of lymphoma growth by inhibition of the x^{c-} cystine transporter: a new action for an old drug. *Leukemia* **2001**, *15* (10), 1633.
72. Liu, D. S.; Duong, C. P.; Haupt, S.; Montgomery, K. G.; House, C. M.; Azar, W. J.; Pearson, H. B.; Fisher, O. M.; Read, M.; Guerra, G. R.; Haupt, Y.; Cullinane, C.; Wiman, K. G.; Abrahmsen, L.; Phillips, W. A.; Clemons, N. J., Inhibiting the system x^{c(-)}/glutathione axis selectively targets cancers with mutant-p53 accumulation. *Nat Commun* **2017**, *8*, 14844.
73. Zou, Y.; Palte, M. J.; Deik, A. A.; Li, H.; Eaton, J. K.; Wang, W.; Tseng, Y.-Y.; Deasy, R.; Alimova, M.; Dančik, V., HIF-2 α drives an intrinsic vulnerability to ferroptosis in clear cell renal cell carcinoma. *bioRxiv* **2018**, 388041.
74. Sato, M.; Kusumi, R.; Hamashima, S.; Kobayashi, S.; Sasaki, S.; Komiyama, Y.; Izumikawa, T.; Conrad, M.; Bannai, S.; Sato, H., The ferroptosis inducer erastin irreversibly inhibits system x^{c-} and synergizes with cisplatin to increase cisplatin's cytotoxicity in cancer cells. *Scientific reports* **2018**, *8* (1), 968.
75. Chen, L.; Li, X.; Liu, L.; Yu, B.; Xue, Y.; Liu, Y., Erastin sensitizes glioblastoma cells to temozolomide by restraining x^{CT} and cystathionine- γ -lyase function. *Oncology reports* **2015**, *33* (3), 1465-1474.
76. Yamaguchi, H.; Hsu, J. L.; Chen, C.-T.; Wang, Y.-N.; Hsu, M.-C.; Chang, S.-S.; Du, Y.; Ko, H.-W.; Herbst, R.; Hung, M.-C., Caspase-Independent Cell Death Is Involved in the Negative Effect of EGF Receptor Inhibitors on Cisplatin in Non-Small Cell Lung Cancer Cells. *Clinical cancer research* **2013**.
77. Yu, Y.; Xie, Y.; Cao, L.; Yang, L.; Yang, M.; Lotze, M. T.; Zeh, H. J.; Kang, R.; Tang, D., The ferroptosis inducer erastin enhances sensitivity of acute myeloid leukemia cells to chemotherapeutic agents. *Molecular & cellular oncology* **2015**, *2* (4), e1054549.
78. Lu, B.; Chen, X. B.; Ying, M. D.; He, Q. J.; Cao, J.; Yang, B., The role of ferroptosis in cancer development and treatment response. *Frontiers in pharmacology* **2018**, *8*, 992.
79. Fazzari, J.; Balenko, M. D.; Zacal, N.; Singh, G., Identification of capsazepine as a novel inhibitor of system x^{c-} and cancer-induced bone pain. *Journal of pain research* **2017**, *10*, 915.
80. Magtanong, L.; Ko, P. J.; Dixon, S. J., Emerging roles for lipids in non-apoptotic cell death. *Cell Death and Differentiation* **2016**, *23* (7), 1099-1109.
81. Mashima, T.; Seimiya, H.; Tsuruo, T., De novo fatty-acid synthesis and related pathways as molecular targets for cancer therapy. *British Journal of Cancer* **2009**, *100* (9), 1369-1372.
82. Yang, W. S.; Kim, K. J.; Gaschler, M. M.; Patel, M.; Shchepinov, M. S.; Stockwell, B. R., Peroxidation of polyunsaturated fatty acids by lipoxygenases drives ferroptosis. *Proceedings of the National Academy of Sciences* **2016**, *113* (34), E4966-E4975.
83. Gaschler, M. M.; Stockwell, B. R., Lipid peroxidation in cell death. *Biochem Biophys Res Commun* **2017**, *482* (3), 419-425.
84. Agmon, E.; Solon, J.; Bassereau, P.; Stockwell, B. R., Modeling the effects of lipid peroxidation during ferroptosis on membrane properties. *Scientific Reports* **2018**, *8* (1), 5155.
85. Shindou, H.; Shimizu, T., Acyl-CoA: lysophospholipid acyltransferases. *Journal of biological chemistry* **2009**, *284* (1), 1-5.

86. Dixon, S. J.; Winter, G. E.; Musavi, L. S.; Lee, E. D.; Snijder, B.; Rebsamen, M.; Superti-Furga, G.; Stockwell, B. R., Human haploid cell genetics reveals roles for lipid metabolism genes in nonapoptotic cell death. *Acs Chem Biol* **2015**, *10* (7), 1604-1609.
87. Milne, G. L.; Yin, H.; Hardy, K. D.; Davies, S. S.; Roberts, L. J., Isoprostane generation and function. *Chemical reviews* **2011**, *111* (10), 5973-5996.
88. Negre-Salvayre, A.; Coatrieux, C.; Ingueneau, C.; Salvayre, R., Advanced lipid peroxidation end products in oxidative damage to proteins. Potential role in diseases and therapeutic prospects for the inhibitors. *British Journal of Pharmacology* **2008**, *153* (1), 6-20.
89. Astarita, G.; Kendall, A. C.; Dennis, E. A.; Nicolaou, A., Targeted lipidomic strategies for oxygenated metabolites of polyunsaturated fatty acids. *Bba-Mol Cell Biol L* **2015**, *1851* (4), 456-468.
90. Kagan, V. E.; Mao, G.; Qu, F.; Angeli, J. P. F.; Doll, S.; St Croix, C.; Dar, H. H.; Liu, B.; Tyurin, V. A.; Ritov, V. B., Oxidized arachidonic and adrenergic PEs navigate cells to ferroptosis. *Nature chemical biology* **2017**, *13* (1), 81.
91. Li, L.; Han, J.; Wang, Z.; Liu, J. a.; Wei, J.; Xiong, S.; Zhao, Z., Mass spectrometry methodology in lipid analysis. *International journal of molecular sciences* **2014**, *15* (6), 10492-10507.
92. Han, X., Lipidomics for studying metabolism. *Nature Reviews Endocrinology* **2016**, *12* (11), 668.
93. Guo, S.; Wang, Y. M.; Zhou, D.; Li, Z. L., Significantly increased monounsaturated lipids relative to polyunsaturated lipids in six types of cancer microenvironment are observed by mass spectrometry imaging. *Scientific Reports* **2014**, *4*.
94. Cajka, T.; Fiehn, O., Comprehensive analysis of lipids in biological systems by liquid chromatography-mass spectrometry. *TrAC Trends in Analytical Chemistry* **2014**, *61*, 192-206.
95. Thomlinson, R.; Gray, L., The histological structure of some human lung cancers and the possible implications for radiotherapy. *British journal of cancer* **1955**, *9* (4), 539.
96. McDonald, D. M.; Baluk, P., Significance of blood vessel leakiness in cancer. AACR: 2002.
97. Minchinton, A. I.; Tannock, I. F., Drug penetration in solid tumours. *Nature Reviews Cancer* **2006**, *6* (8), 583.
98. Sun, T.; Zhang, Y. S.; Pang, B.; Hyun, D. C.; Yang, M.; Xia, Y., Engineered nanoparticles for drug delivery in cancer therapy. *Angewandte Chemie International Edition* **2014**, *53* (46), 12320-12364.
99. Blanco, E.; Shen, H.; Ferrari, M., Principles of nanoparticle design for overcoming biological barriers to drug delivery. *Nature biotechnology* **2015**, *33* (9), 941.
100. Peer, D.; Karp, J. M.; Hong, S.; Farokhzad, O. C.; Margalit, R.; Langer, R., Nanocarriers as an emerging platform for cancer therapy. *Nature nanotechnology* **2007**, *2* (12), 751.
101. Zhang, Y.; Larrauffie, M.-H.; Musavi, L.; Akkiraju, H.; Brown, L. M.; Stockwell, B. R., Design of small molecules that compete with nucleotide binding to an engineered oncogenic KRAS allele. *Biochemistry-Us* **2018**, *57* (8), 1380-1389.
102. Bishop, A.; Buzko, O.; Heyeck-Dumas, S.; Jung, I.; Kraybill, B.; Liu, Y.; Shah, K.; Ulrich, S.; Witucki, L.; Yang, F.; Zhang, C.; Shokat, K. M., Unnatural ligands for engineered proteins: new tools for chemical genetics. *Annual review of biophysics and biomolecular structure* **2000**, *29*, 577-606.
103. Alaimo, P. J.; Shogren-Knaak, M. A.; Shokat, K. M., Chemical Genetic Analysis of Protein Kinase Cascades. *The Scientific World Journal* **2002**, *2*, 108-110.
104. Specht, K. M.; Shokat, K. M., The emerging power of chemical genetics. *Current opinion in cell biology* **2002**, *14* (2), 155-9.
105. Denzel, A.; Hare, K. J.; Zhang, C.; Shokat, K.; Jenkinson, E. J.; Anderson, G.; Hayday, A., Cutting edge: a chemical genetic system for the analysis of kinases regulating T cell development. *Journal of immunology* **2003**, *171* (2), 519-23.
106. Bishop, A. C.; Zhang, X. Y.; Lone, A. M., Generation of inhibitor-sensitive protein tyrosine phosphatases via active-site mutations. *Methods* **2007**, *42* (3), 278-88.
107. Coward, P.; Wada, H. G.; Falk, M. S.; Chan, S. D.; Meng, F.; Akil, H.; Conklin, B. R., Controlling signaling with a specifically designed Gi-coupled receptor. *Proceedings of the National Academy of Sciences of the United States of America* **1998**, *95* (1), 352-7.

108. Peet, D. J.; Doyle, D. F.; Corey, D. R.; Mangelsdorf, D. J., Engineering novel specificities for ligand-activated transcription in the nuclear hormone receptor RXR. *Chemistry & biology* **1998**, *5* (1), 13-21.
109. Liberles, S. D.; Diver, S. T.; Austin, D. J.; Schreiber, S. L., Inducible gene expression and protein translocation using nontoxic ligands identified by a mammalian three-hybrid screen. *Proceedings of the National Academy of Sciences of the United States of America* **1997**, *94* (15), 7825-30.
110. Clemons, P. A.; Gladstone, B. G.; Seth, A.; Chao, E. D.; Foley, M. A.; Schreiber, S. L., Synthesis of calcineurin-resistant derivatives of FK506 and selection of compensatory receptors. *Chemistry & biology* **2002**, *9* (1), 49-61.
111. Rational design of orthogonal receptor-ligand combinations.
112. Vincent, F.; Cook, S. P.; Johnson, E. O.; Emmert, D.; Shah, K., Engineering unnatural nucleotide specificity to probe G protein signaling. *Chemistry & biology* **2007**, *14* (9), 1007-18.
113. Fletcher, T. M.; Cathers, B. E.; Ravikumar, K. S.; Mamiya, B. M.; Kerwin, S. M., Inhibition of human telomerase by 7-deaza-2'-deoxyguanosine nucleoside triphosphate analogs: potent inhibition by 6-thio-7-deaza-2'-deoxyguanosine 5'-triphosphate. *Bioorg Chem* **2001**, *29* (1), 36-55.
114. Cool, R. H.; Schmidt, G.; Lenzen, C. U.; Prinz, H.; Vogt, D.; Wittinghofer, A., The Ras mutant D119N is both dominant negative and activated. *Molecular and cellular biology* **1999**, *19* (9), 6297-305.
115. Walter, M.; Clark, S. G.; Levinson, A. D., The oncogenic activation of human p21ras by a novel mechanism. *Science* **1986**, *233* (4764), 649-52.
116. Wennerberg, K.; Rossman, K. L.; Der, C. J., The Ras superfamily at a glance. *Journal of cell science* **2005**, *118* (5), 843-846.
117. Hunter, J. C.; Manandhar, A.; Carrasco, M. A.; Gurbani, D.; Gondi, S.; Westover, K. D., Biochemical and Structural Analysis of Common Cancer-Associated KRAS Mutations. *Mol Cancer Res* **2015**, *13* (9), 1325-35.
118. Drosten, M.; Dhawahir, A.; Sum, E. Y.; Urosevic, J.; Lechuga, C. G.; Esteban, L. M.; Castellano, E.; Guerra, C.; Santos, E.; Barbacid, M., Genetic analysis of Ras signalling pathways in cell proliferation, migration and survival. *The EMBO journal* **2010**, *29* (6), 1091-104.
119. Singh, J.; Petter, R. C.; Baillie, T. A.; Whitty, A., The resurgence of covalent drugs. *Nature reviews. Drug discovery* **2011**, *10* (4), 307-17.
120. Zhu, K.; Borrelli, K. W.; Greenwood, J. R.; Day, T.; Abel, R.; Farid, R. S.; Harder, E., Docking covalent inhibitors: a parameter free approach to pose prediction and scoring. *Journal of chemical information and modeling* **2014**, *54* (7), 1932-40.
121. Abel, R.; Young, T.; Farid, R.; Berne, B. J.; Friesner, R. A., Role of the active-site solvent in the thermodynamics of factor Xa ligand binding. *Journal of the American Chemical Society* **2008**, *130* (9), 2817-31.
122. Young, T.; Abel, R.; Kim, B.; Berne, B. J.; Friesner, R. A., Motifs for molecular recognition exploiting hydrophobic enclosure in protein-ligand binding. *Proceedings of the National Academy of Sciences of the United States of America* **2007**, *104* (3), 808-13.
123. Krishnamurty, R.; Brock, A. M.; Maly, D. J., Protein kinase affinity reagents based on a 5-aminoindazole scaffold. *Bioorganic & medicinal chemistry letters* **2011**, *21* (1), 550-4.
124. Carney, S., Target validation. *Drug discovery today* **2012**, *17* Suppl, S1-2.
125. Weiss, W. A.; Taylor, S. S.; Shokat, K. M., Recognizing and exploiting differences between RNAi and small-molecule inhibitors. *Nature Chemical Biology* **2007**, *3* (12), 739-744.
126. Bunnage, M. E.; Gilbert, A. M.; Jones, L. H.; Hett, E. C., Know your target, know your molecule. *Nat Chem Biol* **2015**, *11* (6), 368-72.
127. Nishikimi, A.; Uruno, T.; Duan, X.; Cao, Q.; Okamura, Y.; Saitoh, T.; Saito, N.; Sakaoka, S.; Du, Y.; Suenaga, A.; Kukimoto-Niino, M.; Miyano, K.; Gotoh, K.; Okabe, T.; Sanematsu, F.; Tanaka, Y.; Sumimoto, H.; Honma, T.; Yokoyama, S.; Nagano, T.; Kohda, D.; Kanai, M.; Fukui, Y., Blockade of inflammatory responses by a small-molecule inhibitor of the Rac activator DOCK2. *Chem. Biol.* **2012**, *19* (4), 488-97.

128. Montalvo-Ortiz, B. L.; Castillo-Pichardo, L.; Hernandez, E.; Humphries-Bickley, T.; De la Mota-Peynado, A.; Cubano, L. A.; Vlaar, C. P.; Dharmawardhane, S., Characterization of EHop-016, novel small molecule inhibitor of Rac GTPase. *JBC* **2012**, *287* (16), 13228-38.
129. Shang, X.; Marchioni, F.; Sipes, N.; Evelyn, C. R.; Jerabek-Willemsen, M.; Duhr, S.; Seibel, W.; Wortman, M.; Zheng, Y., Rational Design of Small Molecule Inhibitors Targeting RhoA Subfamily Rho GTPases. *Chem. Biol.* **2012**, *19* (6), 699-710.
130. Vigil, D.; Cherfils, J.; Rossman, K. L.; Der, C. J., Ras superfamily GEFs and GAPs: validated and tractable targets for cancer therapy? *Nature reviews. Cancer* **2010**, *10* (12), 842-57.
131. Vega, F. M.; Ridley, A. J., Rho GTPases in cancer cell biology. *FEBS letters* **2008**, *582* (14), 2093-101.
132. Chapuy, B.; Stewart, C.; Dunford, A. J.; Kim, J.; Kamburov, A.; Redd, R. A.; Lawrence, M. S.; Roemer, M. G. M.; Li, A. J.; Ziepert, M.; Staiger, A. M.; Wala, J. A.; Ducar, M. D.; Leshchiner, I.; Rheinbay, E.; Taylor-Weiner, A.; Coughlin, C. A.; Hess, J. M.; Pedamallu, C. S.; Livitz, D.; Rosebrock, D.; Rosenberg, M.; Tracy, A. A.; Horn, H.; van Hummelen, P.; Feldman, A. L.; Link, B. K.; Novak, A. J.; Cerhan, J. R.; Habermann, T. M.; Siebert, R.; Rosenwald, A.; Thorner, A. R.; Meyerson, M. L.; Golub, T. R.; Beroukhi, R.; Wulf, G. G.; Ott, G.; Rodig, S. J.; Monti, S.; Neuber, D. S.; Loeffler, M.; Pfreundschuh, M.; Trumper, L.; Getz, G.; Shipp, M. A., Molecular subtypes of diffuse large B cell lymphoma are associated with distinct pathogenic mechanisms and outcomes. *Nat Med* **2018**, *24* (5), 679-690.
133. Alizadeh, A. A.; Eisen, M. B.; Davis, R. E.; Ma, C.; Lossos, I. S.; Rosenwald, A.; Boldrick, J. C.; Sabet, H.; Tran, T.; Yu, X.; Powell, J. I.; Yang, L.; Marti, G. E.; Moore, T.; Hudson, J., Jr.; Lu, L.; Lewis, D. B.; Tibshirani, R.; Sherlock, G.; Chan, W. C.; Greiner, T. C.; Weisenburger, D. D.; Armitage, J. O.; Warnke, R.; Levy, R.; Wilson, W.; Grever, M. R.; Byrd, J. C.; Botstein, D.; Brown, P. O.; Staudt, L. M., Distinct types of diffuse large B-cell lymphoma identified by gene expression profiling. *Nature* **2000**, *403* (6769), 503-11.
134. Narang, V. S.; Pauletti, G. M.; Gout, P. W.; Buckley, D. J.; Buckley, A. R., Sulfasalazine-induced reduction of glutathione levels in breast cancer cells: enhancement of growth-inhibitory activity of Doxorubicin. *Chemotherapy* **2007**, *53* (3), 210-7.
135. Yamada, S.; Kumazawa, S.; Ishii, T.; Nakayama, T.; Itakura, K.; Shibata, N.; Kobayashi, M.; Sakai, K.; Osawa, T.; Uchida, K., Immunochemical detection of a lipofuscin-like fluorophore derived from malondialdehyde and lysine. *J Lipid Res* **2001**, *42* (8), 1187-1196.
136. Hyvarinen, S.; Uchida, K.; Varjosalo, M.; Jokela, R.; Jokiranta, T. S., Recognition of Malondialdehyde-modified Proteins by the C Terminus of Complement Factor H Is Mediated via the Polyanion Binding Site and Impaired by Mutations Found in Atypical Hemolytic Uremic Syndrome. *Journal of Biological Chemistry* **2014**, *289* (7), 4295-4306.
137. Uchida, K., HNE as an inducer of COX-2. *Free Radical Biology and Medicine* **2017**, *111*, 169-172.
138. Sengupta, A.; Lichti, U. F.; Carlson, B. A.; Cataisson, C.; Ryscavage, A. O.; Mikulec, C.; Conrad, M.; Fischer, S. M.; Hatfield, D. L.; Yuspa, S. H., Targeted disruption of glutathione peroxidase 4 in mouse skin epithelial cells impairs postnatal hair follicle morphogenesis that is partially rescued through inhibition of COX-2. *Journal of Investigative Dermatology* **2013**, *133* (7), 1731-1741.
139. Gdowski, A.; Johnson, K.; Shah, S.; Gryczynski, I.; Vishwanatha, J.; Ranjan, A., Optimization and scale up of microfluidic nanolipomer production method for preclinical and potential clinical trials. *J Nanobiotechnol* **2018**, *16*.
140. Valencia, P. M.; Pridgen, E. M.; Rhee, M.; Langer, R.; Farokhzad, O. C.; Karnik, R., Microfluidic platform for combinatorial synthesis and optimization of targeted nanoparticles for cancer therapy. *ACS Nano* **2013**, *7* (12), 10671-80.
141. Yue, Z. G.; You, Z. X.; Yang, Q. Z.; Lv, P. P.; Yue, H.; Wang, B.; Ni, D. Z.; Su, Z. G.; Wei, W.; Ma, G. H., Molecular structure matters: PEG-b-PLA nanoparticles with hydrophilicity and deformability demonstrate their advantages for high-performance delivery of anti-cancer drugs. *J Mater Chem B* **2013**, *1* (26), 3239-3247.

142. Kim, S. E.; Zhang, L.; Ma, K.; Riegman, M.; Chen, F.; Ingold, I.; Conrad, M.; Turker, M. Z.; Gao, M.; Jiang, X.; Monette, S.; Pauliah, M.; Gonen, M.; Zanzonico, P.; Quinn, T.; Wiesner, U.; Bradbury, M. S.; Overholtzer, M., Ultrasmall nanoparticles induce ferroptosis in nutrient-deprived cancer cells and suppress tumour growth. *Nat Nanotechnol* **2016**, *11* (11), 977-985.
143. Goracci, L.; Tortorella, S.; Tiberi, P.; Pellegrino, R. M.; Di Veroli, A.; Valeri, A.; Cruciani, G., Lipostar, a comprehensive platform-neutral cheminformatics tool for lipidomics. *Analytical chemistry* **2017**, *89* (11), 6257-6264.
144. Chakraborti, S., Phospholipase A2 isoforms: a perspective. *Cellular signalling* **2003**, *15* (7), 637-665.
145. Listenberger, L. L.; Han, X. L.; Lewis, S. E.; Cases, S.; Farese, R. V.; Ory, D. S.; Schaffer, J. E., Triglyceride accumulation protects against fatty acid-induced lipotoxicity. *P Natl Acad Sci USA* **2003**, *100* (6), 3077-3082.
146. Matyash, V.; Liebisch, G.; Kurzchalia, T. V.; Shevchenko, A.; Schwudke, D., Lipid extraction by methyl-tert-butyl ether for high-throughput lipidomics. *J Lipid Res* **2008**, *49* (5), 1137-46.
147. Cajka, T.; Fiehn, O., Comprehensive analysis of lipids in biological systems by liquid chromatography-mass spectrometry. *Trac-Trend Anal Chem* **2014**, *61*, 192-206.
148. Smith, C. A.; Want, E. J.; O'Maille, G.; Abagyan, R.; Siuzdak, G., XCMS: Processing mass spectrometry data for metabolite profiling using Nonlinear peak alignment, matching, and identification. *Anal Chem* **2006**, *78* (3), 779-787.
149. Tautenhahn, R.; Bottcher, C.; Neumann, S., Highly sensitive feature detection for high resolution LC/MS. *Bmc Bioinformatics* **2008**, *9*.
150. Chong, J.; Soufan, O.; Li, C.; Caraus, I.; Li, S. Z.; Bourque, G.; Wishart, D. S.; Xia, J. G., MetaboAnalyst 4.0: towards more transparent and integrative metabolomics analysis. *Nucleic Acids Res* **2018**, *46* (W1), W486-W494.
151. Adams, C. P.; Brantner, V. V., Estimating the cost of new drug development: is it really \$802 million? *Health affairs* **2006**, *25* (2), 420-428.
152. Damnernsawad, A.; Kong, G.; Wen, Z.; Liu, Y.; Rajagopalan, A.; You, X.; Wang, J.; Zhou, Y.; Ranheim, E. A.; Luo, H. R., Kras is required for adult hematopoiesis. *Stem Cells* **2016**, *34* (7), 1859-1871.
153. Garske, A. L.; Peters, U.; Cortesi, A. T.; Perez, J. L.; Shokat, K. M., Chemical genetic strategy for targeting protein kinases based on covalent complementarity. *Proceedings of the National Academy of Sciences of the United States of America* **2011**, *108* (37), 15046-52.
154. Islam, K., The Bump-and-Hole Tactic: Expanding the Scope of Chemical Genetics. *Cell chemical biology* **2018**.
155. Jacobson, M. P.; Pincus, D. L.; Rapp, C. S.; Day, T. J.; Honig, B.; Shaw, D. E.; Friesner, R. A., A hierarchical approach to all-atom protein loop prediction. *Proteins: Structure, Function, and Bioinformatics* **2004**, *55* (2), 351-367.
156. Doxsee, D. W.; Gout, P. W.; Kurita, T.; Lo, M.; Buckley, A. R.; Wang, Y.; Xue, H.; Karp, C. M.; Cutz, J. C.; Cunha, G. R., Sulfasalazine-induced cystine starvation: Potential use for prostate cancer therapy. *The Prostate* **2007**, *67* (2), 162-171.
157. Guan, J.; Lo, M.; Dockery, P.; Mahon, S.; Karp, C. M.; Buckley, A. R.; Lam, S.; Gout, P. W.; Wang, Y.-Z., The x c- cystine/glutamate antiporter as a potential therapeutic target for small-cell lung cancer: use of sulfasalazine. *Cancer chemotherapy and pharmacology* **2009**, *64* (3), 463.
158. Lo, M.; Ling, V.; Low, C.; Wang, Y.; Gout, P., Potential use of the anti-inflammatory drug, sulfasalazine, for targeted therapy of pancreatic cancer. *Current oncology* **2010**, *17* (3), 9.
159. Muerkoeser, S.; Arlt, A.; Witt, M.; Gehrz, A.; Hays, S.; March, C.; Grohmann, F.; Wegehenkel, K.; Kalthoff, H.; Fölsch, U. R., Usage of the NF- κ B inhibitor sulfasalazine as sensitizing agent in combined chemotherapy of pancreatic cancer. *International journal of cancer* **2003**, *104* (4), 469-476.
160. Fazzari, J.; Lin, H.; Murphy, C.; Ungard, R.; Singh, G., Inhibitors of glutamate release from breast cancer cells; new targets for cancer-induced bone-pain. *Scientific reports* **2015**, *5*, 8380.

161. Bridges, R. J.; Natale, N. R.; Patel, S. A., System xc-cystine/glutamate antiporter: an update on molecular pharmacology and roles within the CNS. *British journal of pharmacology* **2012**, *165* (1), 20-34.
162. Baell, J.; Walters, M. A., Chemistry: Chemical con artists foil drug discovery. *Nature News* **2014**, *513* (7519), 481.
163. Lewerenz, J.; Hewett, S. J.; Huang, Y.; Lambros, M.; Gout, P. W.; Kalivas, P. W.; Massie, A.; Smolders, I.; Methner, A.; Pergande, M.; Smith, S. B.; Ganapathy, V.; Maher, P., The cystine/glutamate antiporter system x(c)(-) in health and disease: from molecular mechanisms to novel therapeutic opportunities. *Antioxid Redox Signal* **2013**, *18* (5), 522-55.
164. Hamilton, D.; Batist, G., Glutathione analogues in cancer treatment. *Current oncology reports* **2004**, *6* (2), 116-122.
165. Lewerenz, J.; Hewett, S. J.; Huang, Y.; Lambros, M.; Gout, P. W.; Kalivas, P. W.; Massie, A.; Smolders, I.; Methner, A.; Pergande, M., The cystine/glutamate antiporter system xc- in health and disease: from molecular mechanisms to novel therapeutic opportunities. *Antioxidants & redox signaling* **2013**, *18* (5), 522-555.
166. Visco, C.; Li, Y.; Xu-Monette, Z. Y.; Miranda, R. N.; Green, T. M.; Tzankov, A.; Wen, W.; Liu, W.; Kahl, B.; d'Amore, E., Comprehensive gene expression profiling and immunohistochemical studies support application of immunophenotypic algorithm for molecular subtype classification in diffuse large B-cell lymphoma: a report from the International DLBCL Rituximab-CHOP Consortium Program Study. *Leukemia* **2012**, *26* (9), 2103.
167. Wang, K.; Wei, G.; Liu, D., CD19: a biomarker for B cell development, lymphoma diagnosis and therapy. *Experimental hematology & oncology* **2012**, *1* (1), 36.
168. Pamujula, S.; Hazari, S.; Bolden, G.; Graves, R. A.; Chinta, D. D.; Dash, S.; Kishore, V.; Mandal, T. K., Cellular delivery of PEGylated PLGA nanoparticles. *Journal of Pharmacy and Pharmacology* **2012**, *64* (1), 61-67.
169. Davis, M. E.; Chen, Z. G.; Shin, D. M., Nanoparticle therapeutics: an emerging treatment modality for cancer. *Nat Rev Drug Discov* **2008**, *7* (9), 771-82.
170. Murakami, M.; Taketomi, Y.; Miki, Y.; Sato, H.; Hirabayashi, T.; Yamamoto, K., Recent progress in phospholipase A 2 research: from cells to animals to humans. *Progress in lipid research* **2011**, *50* (2), 152-192.
171. Shimada, K.; Hayano, M.; Pagano, N. C.; Stockwell, B. R., Cell-line selectivity improves the predictive power of pharmacogenomic analyses and helps identify NADPH as biomarker for ferroptosis sensitivity. *Cell chemical biology* **2016**, *23* (2), 225-235.